Title
A Gram-Scale low-Tc Low-Surface-Coverage Athermal-Phonon Sensitive Dark Matter Detector

Author
Fink, Caleb Wade

Publication Date
2022

Peer reviewed|Thesis/dissertation

A Gram-Scale low-T_c Low-Surface-Coverage Athermal-Phonon Sensitive Dark Matter Detector

by

Caleb Wade Fink

A dissertation submitted in partial satisfaction of the

requirements for the degree of

Doctor of Philosophy

in

Physics

in the

Graduate Division

of the

University of California, Berkeley

Committee in charge:

Assistant Professor Matt C. Pyle, Chair
Professor of the Graduate School Bernard Sadoulet
Professor Chung-Pei Ma

Summer 2022

A Gram-Scale low-T_c Low-Surface-Coverage Athermal-Phonon Sensitive Dark Matter Detector

Abstract

A Gram-Scale low-T_c Low-Surface-Coverage Athermal-Phonon Sensitive Dark Matter Detector

by

Caleb Wade Fink

Doctor of Philosophy in Physics

University of California, Berkeley

Assistant Professor Matt C. Pyle, Chair

In recent years, the dark matter direct detection community has become increasingly interested in dark matter below the mass scale of the WIMP. Often called 'low mass dark matter' or 'light dark matter', this refers to a collection of models for fermionic dark matter with masses typically in the range eV − GeV. Due to the slow relative velocity of the dark matter in the local halo, the dark matter is poorly kinematically matched to typical detector targets, leaving a detectable amount of energy that is orders of magnitude below the current state-of-the-art detector technology.

In this thesis, I will discuss the details of the athermal phonon sensor mediated detector technology used by the SuperCDMS and SPICE/HeRALD collaborations. I will motivate how this technology can be used to reach detector baseline energy thresholds of $\mathcal{O}$(meV). I then use these concepts in the design of the SPICE MELANGE detectors - the initial prototype dark matter detectors for the SPICE/HeRALD collaboration, with baseline energy resolutions expected to be sub-100 meV. I present the characterization from the testing of the initial fabrication on Si substrates. These Si versions are expected to be able to explore nuclear recoil dark matter parameter space for masses of $\mathcal{O}$(MeV−GeV). A future fabrication on Sapphire is planned, which will extend this mass range down easily into the keV range.

A major hurdle in the realization of ultra-low noise detector technology is the fact that the sensitivity to noise and backgrounds also increases. As such, much of this thesis is also dedicated to the characterization of ultra-sensitive cryogenic calorimeters and analysis of noise - from both intrinsic and environmental sources.

To Mia, Emma, and Isabel

Contents

Contents **ii**

I Introduction 1

1 Dark Matter **2**
1.1 Very Brief Overview of ΛCDM Model 2
1.2 The Argument for Dark Matter 4
1.2.1 Observations of the Modern Universe 4
1.2.2 Early Universe 6
1.2.3 Structure Formation 12
1.2.4 Alternatives to Dark Matter 14
1.3 Dark Matter Candidates 15
1.3.1 Properties of Dark Matter 15
1.3.2 Dark Matter Origins 19
1.3.3 Dark Matter Phenomenology 26
1.4 Dark Matter Direct Detection 30
1.4.1 Kinematic Matching 31
1.4.2 DM Detection Channels 32
1.4.3 Nuclear Recoil 33
1.4.4 Projected Reach of LDM Detectors 35
1.5 Chapter Conclusion and Looking Forward 38

II Detector Design 39

2 Micro-Calorimetry with Transition-Edge Sensors **40**
2.1 Ideal Calorimetry Model 40
2.1.1 Equilibrium Characteristics 42
2.1.2 Micro-Calorimeter Dynamics 44
2.1.3 Electrothermal Feedback TES 49
2.2 TES Stability and Thermal Phase Separation 52

2.3 TES Noise Sources . . . 52
2.3.1 Passive Johnson Noise . . . 53
2.3.2 TES Johnson Noise . . . 54
2.3.3 Thermal Fluctuation Noise . . . 56
2.3.4 Electronics Noise . . . 57
2.3.5 Total Noise Contribution . . . 58
2.4 TES based Micro-Calorimeter Energy Resolution . . . 58

3 Athermal-phonon Mediated Detector Design 61
3.1 Thermal vs Athermal Calorimetry . . . 61
3.1.1 Thermal Calorimeter . . . 61
3.1.2 Athermal Calorimeter . . . 62
3.2 Quasiparticle Trapping . . . 63
3.2.1 Signal Efficiency Losses in QETs . . . 65
3.3 QET Design . . . 68
3.3.1 Anatomy of a QET . . . 68
3.3.2 Heat Capacity Contributions of QET . . . 69
3.3.3 Al Fin Design . . . 71
3.3.4 W/Al Overlap Design . . . 79
3.3.5 Design of TES Fin Connector . . . 80
3.3.6 Number of QET Fins . . . 82
3.3.7 TES Dimensions . . . 84
3.3.8 QET Summary . . . 85
3.4 Optimization of QET based detector . . . 85
3.4.1 Phonon Lifecycle in Substrate . . . 86
3.4.2 Athermal Phonon Absorption . . . 88
3.4.3 Total Athermal phonon Collection Efficiency . . . 92
3.4.4 QET Layout . . . 92
3.4.5 Bandwidth Matching . . . 93
3.5 Chapter Summary . . . 101

4 Design of SPICE MELANGE and DEATH Detectors 102
4.1 Detector Goals and Overview . . . 103
4.2 Optimizing for R_N and n_{TES} . . . 103
4.3 Design of 4% Surface Coverage Device . . . 104
4.3.1 Design of Elliptical QET . . . 104
4.3.2 QET and Channel Layout . . . 107
4.4 Design of Ultra-Low Coverage Devices . . . 108
4.4.1 Design of 'Peanut' QET . . . 110
4.5 DEATH Detector . . . 110
4.5.1 Rectangular QET Design . . . 110
4.5.2 QET Layout . . . 111

4.6 Mask Layout and Fabrication . . . 112
4.6.1 Wafer Characterization Device . . . 113
4.7 Mounting and Thermalization of Detectors . . . 114
4.7.1 Detector Mounting . . . 115
4.8 Expected Performance . . . 117
4.9 Chapter Conclusion . . . 119

III Detector Testing 120

5 Experimental Techniques 121
5.1 Overview of Experimental Setup . . . 121
5.2 Experimental Techniques . . . 124
5.2.1 $I_B I_S$-Complex Admittance Sweeps . . . 124
5.2.2 Complex Admittance . . . 127
5.2.3 Noise Modeling . . . 133
5.3 Estimating Logarithmic Temperature Sensitivity . . . 137
5.4 Phonon Collection Efficiency . . . 137
5.5 Future Updates to Characterization Analysis . . . 138

6 Characterization of TES and QET Based Detectors 140
6.1 Characterizing TES Power Noise for Future Single Optical-Phonon and Infrared-Photon Detectors . . . 140
6.1.1 Abstract . . . 140
6.1.2 Introduction . . . 141
6.1.3 Experimental Setup and Data . . . 142
6.1.4 Parameter Estimation . . . 144
6.1.5 Noise Modeling and Energy Resolution . . . 145
6.1.6 Discussion . . . 150
6.1.7 Acknowledgements . . . 150
6.2 Performance of a Large Area Photon Detector for Rare Event Search Applications . . . 151
6.2.1 Abstract . . . 151
6.2.2 Introduction . . . 151
6.2.3 Experimental Setup and Data Acquisition . . . 152
6.2.4 Detector Characterization . . . 154
6.2.5 Energy Calibration and Resolution . . . 157
6.2.6 Discussion . . . 161
6.2.7 Acknowledgments . . . 162
6.2.8 Data Availability . . . 162

7 SPICE MELANGE Performance 163

7.1 Description of Devices . . . 163
7.2 Description of Data Sets . . . 163
7.2.1 Run 11 . . . 164
7.2.2 Run 14 . . . 165
7.2.3 Run 15 . . . 165
7.2.4 Run 16 . . . 166
7.3 Measurement of Basic Film Properties . . . 167
7.3.1 Resistivity . . . 167
7.3.2 Electron-Phonon Coupling . . . 168
7.3.3 Estimating Logarithmic Temperature Sensitivity α . . . 169
7.3.4 Effective Volume of W/Al Overlap . . . 169
7.3.5 T_c Gradient Across Wafer . . . 170
7.3.6 Measurements of Thermal Conductances . . . 171
7.4 Noise Analysis . . . 174
7.4.1 Noise Coupling Sources . . . 175
7.4.2 TESTR Devices in Run 11 . . . 176
7.4.3 Athermal Phonon Devices . . . 181
7.4.4 Estimated Energy Resolution for MELANGE Devices . . . 182
7.4.5 Infra-Red Loading . . . 183
7.4.6 Getting Rid of Pulse Tube Noise . . . 185
7.5 Future Studies . . . 187
7.5.1 Ballistic Athermal Phonon Lifetime Study . . . 187
7.5.2 Relative Energy Calibration . . . 189
7.6 Conclusions . . . 189

8 Conclusions and Looking Forward **191**
8.1 Increasing Athermal Phonon Collection Efficiency . . . 191
8.2 Final Thoughts . . . 195

Bibliography **196**

A Big-Bang Cosmology **218**
A.1 Intro to the ΛCDM Cosmological Model . . . 218
A.2 Thermal History of the Universe . . . 222

B TES Energy Resolution Derivation **232**

C TES Response to Square Wave Impulse **238**

D Design of Cryogenic Electronics **243**
D.1 Noise Modeling . . . 243
D.1.1 SQUID Feedback Resistor . . . 243
D.1.2 TES Shunt Resistor . . . 245

D.2 Heat Loads . . . 245
D.2.1 SQUID Feedback Resistor . . . 245
D.2.2 TES Shunt Resistor . . . 246
D.2.3 SQUID Arrays . . . 246
D.3 Wiring Layout . . . 247
D.3.1 Wiring . . . 247
D.4 PCB Designs . . . 248
D.4.1 300K Card . . . 250
D.4.2 4K Card . . . 251
D.4.3 SQUID Card . . . 251
D.4.4 Detector Card (DIB) . . . 252

E Noise studies of DCRC rev D.0 at SLAC **255**
E.1 Closed Loop Noise Model . . . 255
E.1.1 Calculation of Noise/Signal Transfer Function . . . 257
E.2 Identifying Dominant Noise Sources . . . 258
E.2.1 Vary Driver Gain (A_D) in Closed Loop . . . 258
E.2.2 Vary Feedback Gain (A_{FB}) in Closed Loop . . . 258
E.3 Open Loop Model . . . 258
E.3.1 Open Loop Transfer Function . . . 260
E.3.2 Closed loop vs Open loop noise . . . 260
E.3.3 Closed loop vs Open loop noise: δV_D . . . 261
E.3.4 Varying Squid Bias (G_{TES}) In Open Loop: Is Flux Coupled Noise Dominant? . . . 262
E.4 Conclusions . . . 263

F Estimation of Phonon Collection Time Constant **264**
F.1 Athermal Phonon Signal . . . 264
F.2 QET Signal . . . 264
F.3 Toy Model . . . 265
F.3.1 Pulse Fitting . . . 267
F.3.2 Results . . . 267
F.3.3 Accounting For TES Saturation . . . 268

G Event Reconstruction with a Variational Autoencoder **270**
G.1 Introduction . . . 270
G.2 Method . . . 271
G.2.1 Variational Autoencoder . . . 271
G.2.2 Data Processing . . . 274
G.2.3 Design of Model . . . 276
G.3 Training . . . 277
G.4 Results . . . 279

G.5 Conclusion and Future Work 280

Acknowledgments

There are just too many people to name who have helped me get to where I am now, so in no particular...

I'd like to thank my undergraduate advisor at UC Santa Cruz, Bruce Schumm. You gave me my first introduction to real research and taught me how to write good (kidding...). Your laid back attitude and love of science encouraged (maybe tricked?) me to pursue a PhD. I'm also thankful for your continued advice over the years, even though our scientific interests have drifted slightly, you've always been interested to catch up over beers.

I'd like to thank the whole CDMS crew at SLAC, where I spent probably the majority of my first two summers in graduate school trying to diagnose and fix noise sources in the DCRC electronics. I appreciate all the lab skills that I learned, and I'll never stop appreciating Paul's jokes and great sense of humor! Thanks Noah for filling in as the senior grad student when you were at Stanford. And thanks for always being one (or ten) steps ahead of me in your academic career and providing advice for each step of the way. I'm excited to continue working with you in this next step!

On a similar note, thanks to everyone I've interacted with as part of CDMS. There are far too many of you to name, but being a part of this collaboration has broadened my scientific interests and abilities so much. Also, none of my work would have been possible if it weren't for all the CDMSer's that pioneered this work before me. And while I am leaving the collaboration to join another group for my postdoc, I hope to stay connected to SuperCDMS in some regard in the future.

Obviously I am incredibly thankful to our Berkeley group. Bruno, our lab simply wouldn't exist without you. I've always appreciated your endless helpfulness - even after 6 years you've never hesitated to help me with even the most simple of tasks! Bernard, while it is unfortunate that I joined the group when you were in the process of retiring, I am incredibly grateful to have overlapped with you at least this much. I have appreciated every interaction we have had, and I always leave our conversations with either great advice, or at the very least a fun anecdotal story from your past!

As the first grad student to join the group, there aren't too many direct predecessors to thank, but to all the undergrads, engineers, postdocs who have come and gone, I couldn't have done this without you! To my fellow grad student Sam, thanks for joining the group and helping me get through the past 6 years. I'd like to say I'll miss sharing a windowless office, losing our minds re-deriving some silly TES property on the whiteboard together for the 100th time, playing hacky-sack, or sneaking off for lunch time beers when nothing seemed to be working... but I won't miss it, because we'll probably be doing the same thing in LANL as postdocs together haha. Here's to hoping there are some good death metal venues in New Mexico.

To my advisor Matt, being your first grad student in the group certainly presented a steep learning curve. While in many ways it would have been nice to have senior grad students around to learn from, I have come to appreciate how much one-on-one time we had. Very few grad students have had the opportunity to work so closely and learn from their advisor

the way I have. You've given me confidence and pushed me to become a better scientist. Of the many things I've learned from you, I feel most notably I've gained an appreciation for the power of back of the envelope calculations in order to guide intuition. Also, I'd like to thank you for being so flexible over the past few years. You've been understanding of the difficulties of having kids, especially in a pandemic over the past 2 years. I've appreciated our time working together and I'm sure our paths will cross plenty, its a small field. I look forward to our future collaborations and competitions!

To my family, thanks Mom, Dad, and Cassie. You've taught me the importance of work life balance, and that creating a life in which spending quality time with your family is the most important. You've always stressed the value in following your passions, and I've never felt pressure from you to do anything that didn't feel right for me. You've also taught me to always be curious about the world. Thanks for sticking with me as I've explored many paths and made quite a few questionable life decisions... And sorry dad, I guess I just couldn't hack it as an engineer haha.

To my in-laws John and Sharon, thanks for putting up with me all these years. I've lived with you too many times to count over the last 13 years! You've always been supportive of my education. John, your passion for electronics has definitely helped shape the direction of my pursuits - I still remember you explaining the difference in how a vacuum tube and transistor worked in a amplifier back before I understood anything about circuits. And to Becca, thanks for always taking the time to edit my research statements and proposals for grammar. Let me know when you've had a chance to finish editing this thesis, I know it sure needs it.

This one may sound out of place in a PhD thesis, but thanks to the crew of riders and diggers at Dirt World. Some of my happiest moments over the past 6 years have been stacking dirt and jumping bikes with you all. Thanks for providing an outlet to relieve stress and be a kid again, although let's be honest, I don't think I'm ever going to 'grow up'.

Finally, thanks to my wife Mia, daughter Emma, and very recent daughter Izzy. Mia, you have been the best partner and friend I could have ever asked for. You've always been supportive of me and never put any pressure or expectations on me. You've never placed importance on status or money, and that unwavering support has allowed me to purse this degree for simply the joy of learning. You've also always valued exercise and being outdoors in order to keep mentally healthy. Without you encouraging me to go ride my bike, I probably would have been consumed by stress!

Emma, it has been the greatest pleasure in my life being your dad over the last four and half years. Being with you is always the highlight of my day. You've helped me put my work into perspective, and certainly taught me time management skills! Izzy... I can't say that you arriving a month before submitting this thesis has made things easy, but I'm so happy you are here! I can't wait to watch you grow up into your own person and ask me basic questions about the universe that I should know but will somehow forget how to explain... I love you both so much, thanks for making my life so wonderful.

Part I

Introduction

Chapter 1

Dark Matter

"...Scientists, are you ready?
First question: dark matter
Oh, dark matter
Give me someone knows somethin' about space
... All right, what is it? Where is it? Can we get some?"

- Randy Newman, The Great Debate

While a full understanding of of dark matter (DM) is much beyond the scope of this thesis, this chapter hopefully serves to provide the reader with some of the more profound evidence we have for its existence. For the reader more interested in cosmology, I refer you to Appendix A in which I give an overview of the standard big bang cosmological model as well as discuss the thermal history of the universe. In this chapter I will lay out the existing evidence for dark matter, discuss what is known about it, and introduce some of the more popular theories to describe it.

1.1 Very Brief Overview of ΛCDM Model

To better appreciate the evidence for dark matter, we need to have at least a basic understanding of the standard cosmological model, also known as the Lambda cold dark matter model (ΛCDM). In this model, we live in an isotropic, homogeneous, expanding universe which can be either geometrically open, closed, or flat. The expansion of the universe is quantified by the 'scale factor' $a(t)$, and the curvature can be related to the total present day energy density Ω_0, in which $\Omega_0 = 1$ would imply a flat geometry. As shown in Appendix A, we can nicely describe the evolution of the universe with a modified form of the Friedmann equations with

$$H^2 = \left(\frac{\dot{a}}{a}\right)^2 = H_0^2 \left(\frac{\Omega_{0,m}}{a^3} + \Omega_{0,\Lambda} + \frac{\Omega_{0,r}}{a^4} + \frac{1 - \Omega_{0,m} - \Omega_{0,\Lambda} - \Omega_{0,r}}{a^2}\right). \tag{1.1}$$

where $\Omega_{0,m}$, $\Omega_{0,r}$, and $\Omega_{0,\Lambda}$ are the present day relative energy densities of all matter, radiation [1], and vacuum energy respectively, and H_0 is the present day value of the Hubble parameter.

Observationally these parameters can be constrained in many ways, but notably they have been measured by looking at a distance type metric of type 1A Supernovae as a function of cosmological redshift as shown in Fig. 1.1. From this, we see that $\Omega_0 \approx 1$ ($\Omega_{0,\Lambda} = 0.7, \Omega_{0,m} = 0.3$) and thus our universe is geometrically flat. At the time these results was published in the early 90's, the astronomy community was surprised to find out that our universe is dominated not by matter, but vacuum energy (Λ). This means that not only is the universe expanding, but at an accelerated rate! Understanding this vacuum energy, or 'dark energy', is one of the major unanswered questions in cosmology, the rest of this chapter will detail the other major mystery.

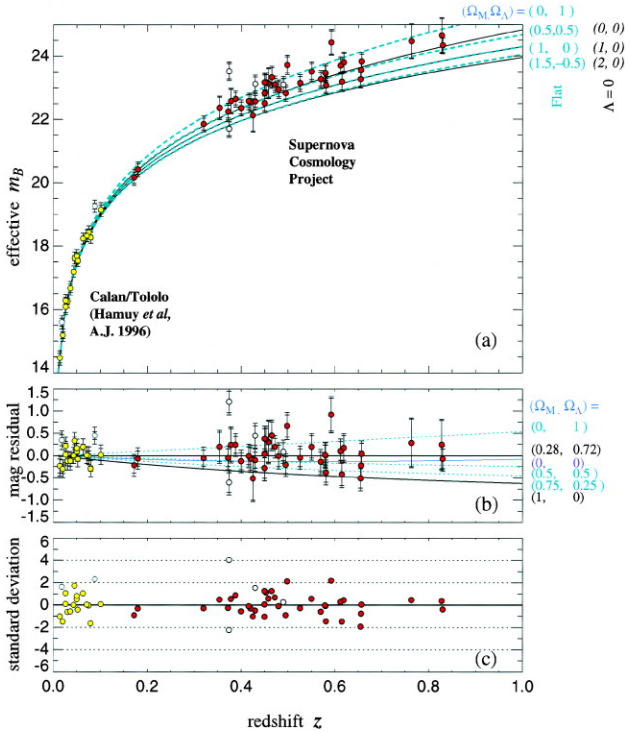

Figure 1.1: Hubble diagram for type 1A Supernovae, from Ref. [1]

[1] It is worth noting that the radiation density has been measured to be $\Omega_{0,r} \approx 10^{-4}$ and is often ignored in many calculations because of its low value.

1.2 The Argument for Dark Matter

As we just learned above, we live in a geometrically flat universe that is expanding at an accelerated rate, where the matter content only accounts for 30% of the total energy density. This section now takes a deeper look into what makes up that 30%. What follows is not an exhaustive list of all the evidence for DM, but provides hopefully enough evidence for the reader to paint a fairly complete picture for what DM could be. I split the evidence up into two categories, evidence from observations of the modern universe, and observations of the early universe.

1.2.1 Observations of the Modern Universe

Mass-to-Light Ratio of Galaxy Clusters

A common metric astronomers use to study galaxies and clusters of galaxies is the mass-to-light ratio (M/L), the ratio of the total mass of the astronomical object and the radiated electromagnetic power. This ratio is measured in units of solar mass ($M_\odot$) to the luminosity of the sun ($L_\odot$). So an astronomical object made of entirely sun-like stars would be expected to have a ratio of $M/L \approx 1$.

The mass of many 'non-irregular' clusters can be estimated from the Virial theorem, which states that the time averaged kinetic energy of a system of particles in equilibrium can be related to the average potential energy as

$$2T + V = 0. \tag{1.2}$$

For a galaxy cluster, the kinetic and potential terms can be written as

$$T = \frac{1}{2} M \left\langle v^2 \right\rangle \qquad\qquad V = -\frac{1}{2} G M^2 \left\langle \frac{1}{r} \right\rangle, \tag{1.3}$$

where $\langle v^2 \rangle$ in the mass weighted mean square velocity, $\left\langle \frac{1}{r} \right\rangle$ is the mean inverse separation (both referenced to the center of mass of the cluster), and M is the total mass. This gives a simple expression for the mass of the cluster:

$$M = \frac{2 \left\langle v^2 \right\rangle}{G \left\langle 1/r \right\rangle}. \tag{1.4}$$

The name dark matter is typically credited to Fritz Zwicky, who while studying the Coma Cluster in 1933 estimated the mass of the cluster by measuring the velocities of 7 galaxies at the edge of the cluster. When he compared this this to the luminosity of the cluster he measured a mass-to-light ratio of several hundred. This led him to conclude that the cluster must be made up of some 'dark matter' since the gravity of the visible matter alone could not explain the velocities seen [2]. Many years later astronomers are still measuring the M/L for larger clusters. More recently, a survey of 459 clusters resulted in $M/L \approx 348\, h\, M_\odot/L_\odot$ [3].

Galaxy Rotation Curves

Looking at the actual constituent stars and gas that make up galaxies, one can measure the radial velocities of these objects[2]. The Doppler shift of the light of the stars gives their radial velocity, and the emission of the 21 cm line from neutral hydrogen gives the radial velocity of the gas at larger radii.

From Kepler's laws, the velocity v of a star, orbiting a mass $M(r)$, enclosed by orbital radius r is given by,

$$v = \sqrt{\frac{GM(r)}{r}}. \tag{1.5}$$

It is therefor reasonable to expect that for objects at some radius beyond that of the bulk of the visible matter, the velocity would drop off as

$$v \propto \sqrt{\frac{1}{r}} \qquad\qquad r > R_{\text{luminous}} \tag{1.6}$$

as shown in the lower curve in Fig. 1.2 (Left). However as first demonstrated by Rubin and Ford, the velocity is approximately flat well beyond the visible matter [4]. For this to make sense with Newtonian mechanics, it requires that the true mass of the galaxy scales as $M(r) \propto r$, or equivalently the density should scale as $\rho(r) \propto 1/r^2$. This same effect is almost universally observed across all galaxies (see Fig. 1.2 (right) for example rotation curves.) Typically, the radius and mass of a dark matter halo is ~ 10 times radius and mass of the luminous matter [5].

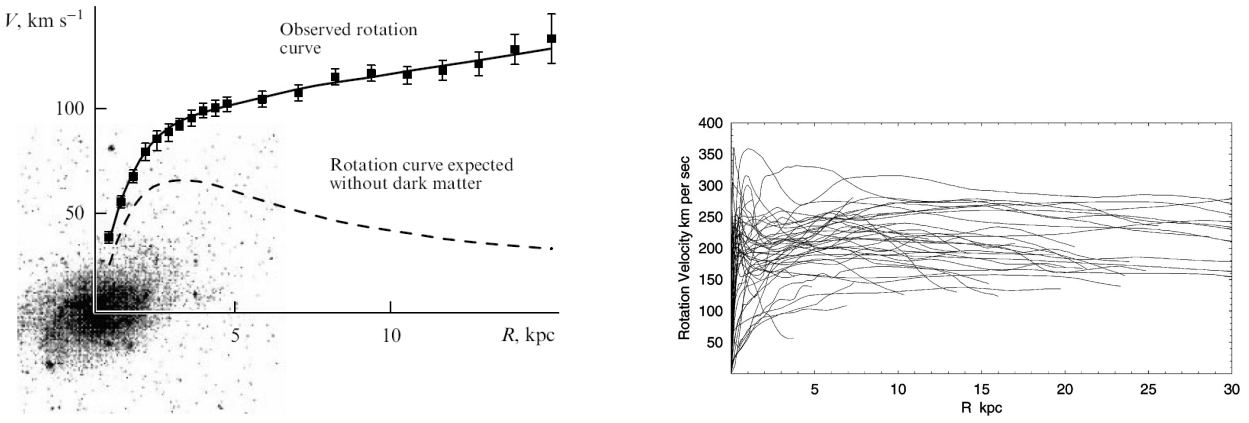

Figure 1.2: (Left) Rotation curve of the M 33 galaxy, shown with expected rotation curve without DM in dashed. Figure adapted from Ref. [6]. (Right) A sample of characteristic spiral galaxy rotation curves, from Ref. [7]

[2]Where in this case, the radial velocity is with respect to the observer on earth.

Gravitational Lensing

The mass of astronomical objects can be inferred by the gravitational bending and distortion of light of distant objects, known as gravitational lensing. In simple terms, an object in the foreground (galaxy, cluster, etc) acts as a lens that bends the light of a distant quasar or galaxy. See Fig. 1.3 (left) for a diagram of the lensing process, and Fig. 1.3 (right) for an image of a lensed galaxy. Gravitational lensing allows us to study mass distributions at $\mathcal{O}$(kpc) scales, which is crucial to understand the geometry and mass content of the universe. Gravitational lensing is yet another technique that confirms that most of the mass of astronomical objects is non-luminous [8].

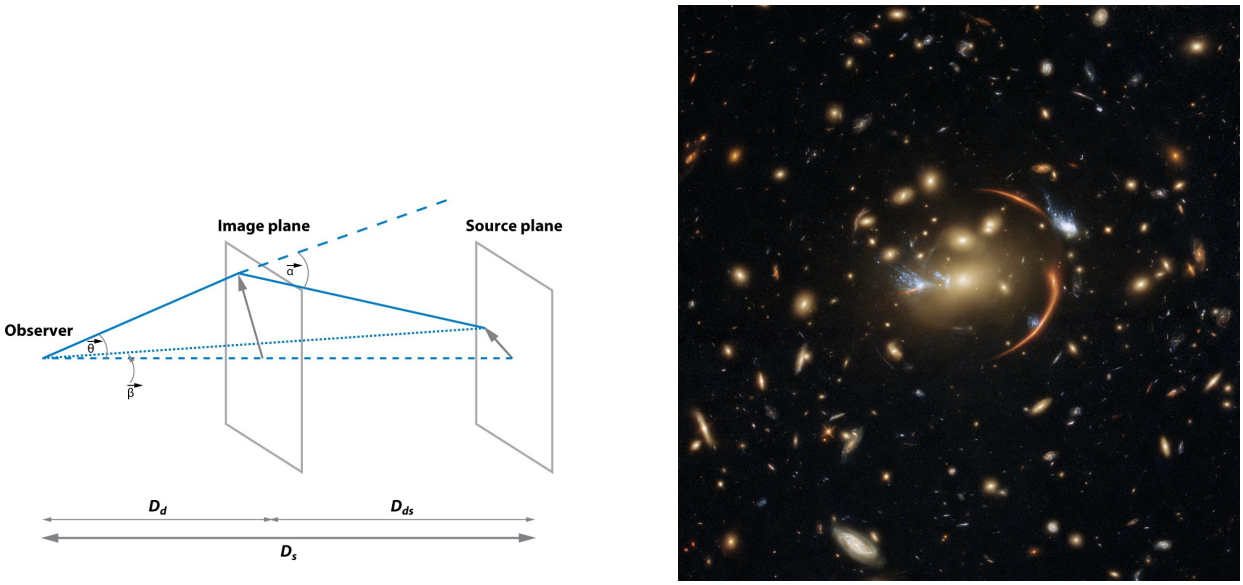

Figure 1.3: (Left) Schematic of gravitational lensing from [8]. (Right) Example image of strong gravitation lensing from Ref. [9]

1.2.2 Early Universe

The previous section of observational evidence for dark matter gives plenty of justification for it's existence, however probes of the early universe give estimates for how much DM in the universe there is.

To fully understand the following arguments, it is helpful to think a bit about the thermal history of the early universe. The universe began in a very dense energetic state. As it expands, the equilibrium temperature of the thermal radiation bath decreases. As this bath temperature decreases, different particle species will drop out of thermal equilibrium. Said another way, once the Hubble rate exceeds the particle interaction rate, that particle will no longer be thermally produced. Only a few key moments will be discussed below, but again, for a more complete explanation of the thermal history of the early universe, see Appendix A.

Big-Bang Nucleosynthesis

When the universe was about 3 min old, long after the thermal production of neutrons and protons had stopped and the neutrinos had frozen out, the stable production of Deuterium (or ^{2}H) began at a temperature of roughly $k_B T = 0.272\,\mathrm{MeV}$. This started the formation of the light elements (D, He, Li, Be) known as Big-Bang Nucleosynthesis or BBN[3].

After light element production froze out, their quantities remained relatively unchanged. The relic abundances of these elements can be used to probe the BBN. In order to quantify the light-element population, parts of the sky with little stellar production are needed. Since there are no processes occurring after the big bang that are able to produce large quantities of Deuterium, the relic Deuterium abundance provides the best metric to test the BBN. Deuterium abundance can be measured by looking at its absorption signature of light from distant quasars.

A common figure of merit is the ^{4}He mass fraction Y

$$Y \equiv \frac{4 m_{\mathrm{p}} n_{^4\mathrm{He}}}{m_{\mathrm{p}} n_B}, \tag{1.7}$$

which quantifies the amount of Helium-4 relative to the total amount of baryons. Measures of this give insight into the baryon content, and consequently the non-baryon content of the universe. There are three important parameters that play a major role in the evolution of the BBN:

1. **The baryon-to-photon ratio**

$$\eta \equiv \frac{n_B}{n_\gamma} = \frac{n_n + n_p}{n_\gamma}. \tag{1.8}$$

   Using statistical mechanics, one can show that the present day baryon density parameter can be related to η via,

$$\Omega_{0,B} h^2 = \eta \beta \tag{1.9}$$
$$\tag{1.10}$$

   where β is a unit-less factor made up of fundamental constants and the measurable CMB photon temperature and energy density (discussed later).

   For a larger η, deuterium would be more stable, the deuterium bottleneck would end sooner, and there would be a larger helium mass fraction.

2. **Neutron lifetime**. The lifetime of an unbound neutron (τ_n) is currently measured to be $\tau_n = 879.4 \pm 0.6\,\mathrm{sec}$ [10]. If τ_m was larger, more neutrons would survive and be converted into He and thus Y would increase.

[3] see Refs [10–12] for detailed reviews

3. **Number of neutrino species**. If a fourth neutrino species were to be discovered, this would increase the effective degrees of freedom g^* in Eq. A.18, which would in turn lead to a larger value for Y.

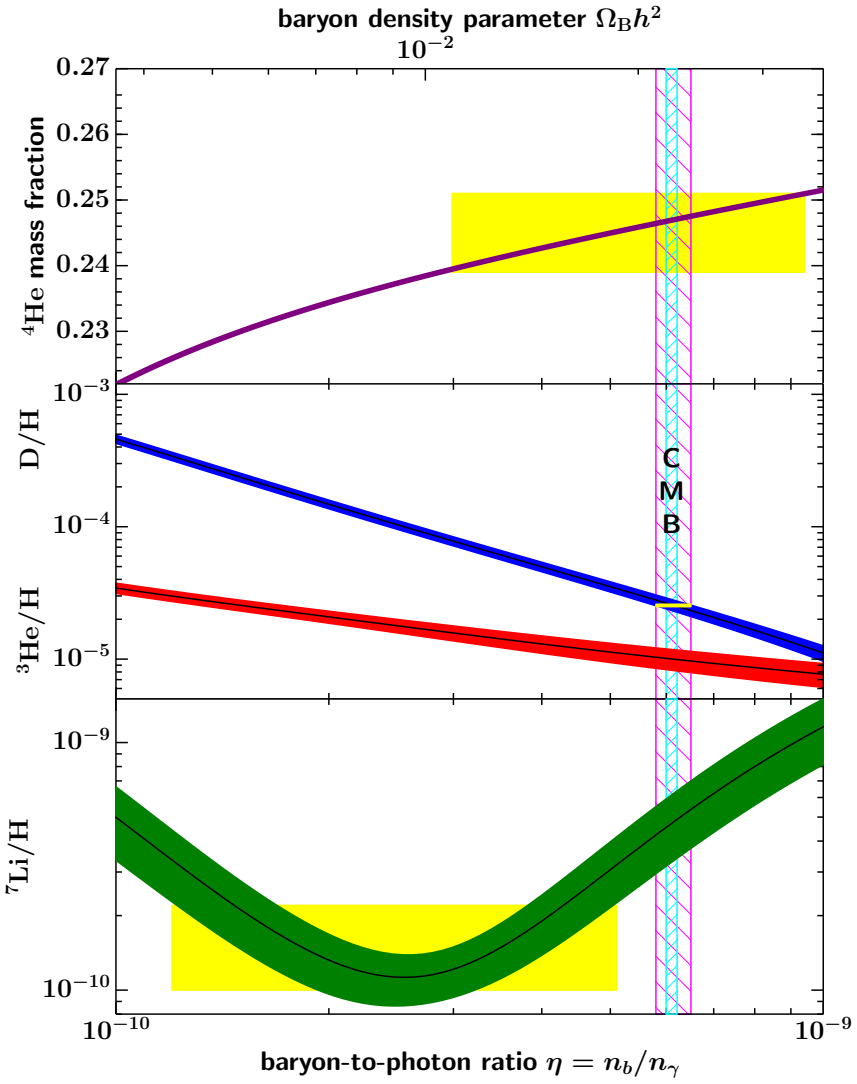

Figure 1.4: Predicted primordial abundances of the light elements as a function of baryon-to-photon ratio. The yellow regions indicate the observed abundances. The vertical band shows the baryon-to-phonon ratio as measured by the CMB. Figure adapted from Ref [13].

Using the measured free neutron lifetime and assuming the standard model (SM) physics (three neutrino species), the light element abundances are modeled as a function of baryon-to-photon ratio in Fig. 1.4. Given the observed primordial abundances, the baryon-to-photon

ratio is measured in Ref [13] to be

$$5.8 \times 10^{-10} \leq \eta \leq 6.5 \times 10^{-10} \quad (95\% \text{ CL}). \tag{1.11}$$

Using Eq. 1.10 we can relate the measured values of η to the present day baryon density

$$0.021 \leq \Omega_{0,B} h^2 \leq 0.024 \quad (95\% \text{ CL}). \tag{1.12}$$

However, we already know from Ref [1] that $\Omega_{0,m} \approx 0.3$, meaning that $\Omega_{0,B}$ accounts for only approximately $4 - 5\%$ of the total matter energy density[4]. We refer to the remaining non-baryonic component of the matter as **dark matter**.

CMB

About 300,000 years later, the universe has cooled to the point that it becomes energetically favorable for the electrons and nuclei to form neutral atoms. At this point, the Thomson scattering rate decreases below the Hubble rate and the photons decouple from the thermal bath. These photons have been red-shifted to a temperature of 2.7 K and essentially form a snapshot of the universe at the time of photon decoupling. This is called the cosmic microwave background, or CMB, and can be seen in Fig. 1.5.

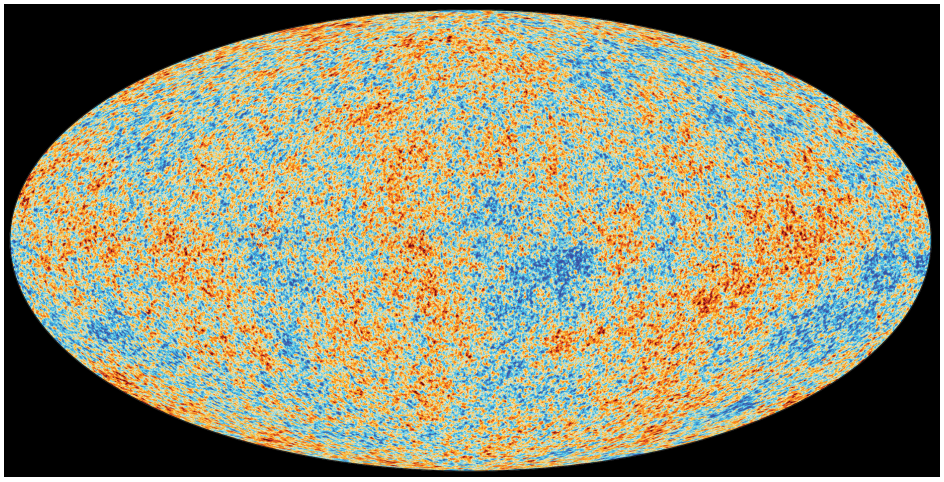

Figure 1.5: Picture of the CMB sky from [14] with data from [15, 16]. The color gradient represents temperature. No scale is given, this is simply to illustrate the temperature anisotropies.

The cosmic microwave background is the most information rich cosmological probe we have. From Fig. 1.5 it is apparent that the temperature is not perfectly uniform. In fact,

[4] Assuming $h = 0.7$

small temperature fluctuations exist [5] on the order of 10 μK. There are observed anisotropies in the CMB that arise from effects related to the modern universe, one due to the relative motion of the earth to the CMB [17], and another from the CMB scattering off of electrons within galaxy clusters known as the *Sunyaev–Zel'dovich effect* [18]. For the purpose of this thesis, these effects can be ignored, as we are only discussing the physics of the early universe. There is another set of anisotropies are caused by the state of the universe at the time the CMB photons were released. These anisotropies are imprints of the small over-densities and under-densities left over at the end of inflation.

Before recombination had finished, electrons, baryons, and photons were all in thermal equilibrium, forming the 'photon-baryon plasma'. Slight over-dense regions would begin to collapse due to gravitational attraction, and this same region would be repelled by the radiation pressure. This effect creates acoustic oscillations much like a driven harmonic oscillator [5]. However, as the universe is expanding and neutral atoms are forming, the mean free path of photons is increasing. Because of this, higher energy photons are able to travel from hotter over-dense regions to cooler under-dense regions which results in damping of these oscillations [19].

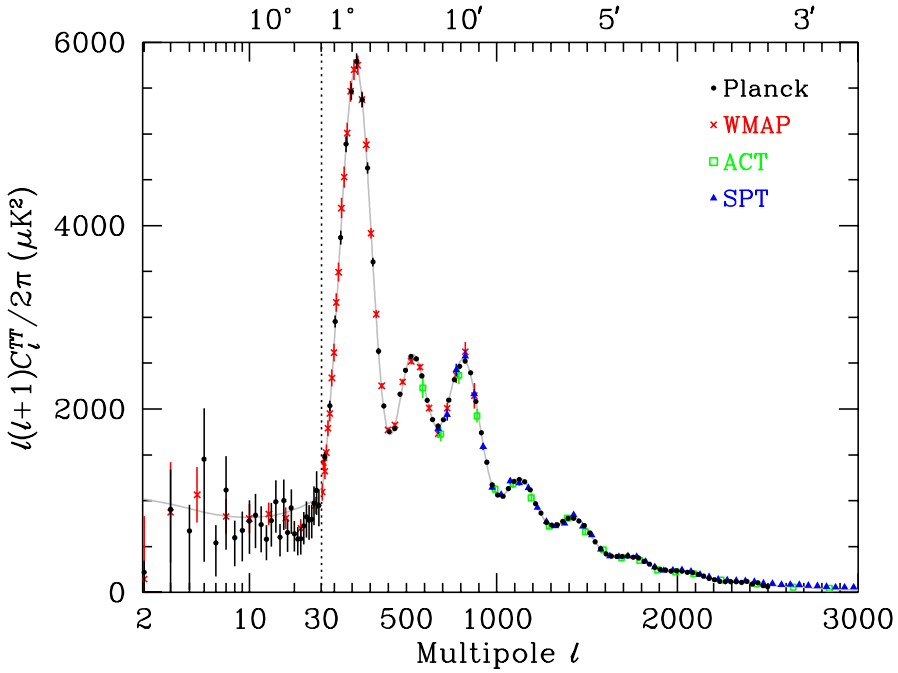

Figure 1.6: CMB temperature anisotropy band-power estimates from the Planck [15], WMAP [20], ACT [21], and SPT [22] experiments. The curve represents the best-fit Planck ΛCDM model. Figure from Ref. [10].

[5] polarization fluctuations also exist, but not shown.

Cosmological parameters are extracted from observation by looking at the angular power spectrum of the CMB, which is effectively the the 2-point correlation function of the sky, as shown in Fig. 1.6. The dependence of the cosmological parameters in the theoretical models is quite complex, but a rough intuition is as follows (see Fig. 1.7):

- **Curvature:** If you imagine the acoustic oscillations in the early universe as a standing plane wave, the observed angular variation arises from the fact that we are viewing light from far away parts of the universe that has taken longer to reach our viewing point [6]. So a spatial homogeneity is mapped to a an angular one. The curvature of the universe is highly related to how the oscillations would depend as a function of ℓ. It turns out that the observed ℓ of the first peak allows us to measure the curvature of the universe.

- **Baryonic Matter:** We can think about the universe at the time of the CMB with a smiple toy model of a mass hanging on a spring. The mass and the gravitational potential represent the over-dense baryon regioins, and the springs represent the radiation pressure. If we take two such systems, but one with larger mass (i.e. more baryons) and release them both from the same height, the larger mass system will stretch further than the smaller mass, yet they both return to the same height. In the CMB angular power spectrum, the odd numbered peaks correspond to point of maximum compression, i.e. gravitation wells from over dense regions of baryons, and the even numbered peaks correspond to the places of rarefaction, i.e. the springs returning the mass to the starting point.

  In this case, the addition of more baryonic matter into the universe would essentially increase the magnitude of the odd numbered peaks relative to their neighboring even peak.

- **Cold Dark Matter:** As discussed previously, the radiation-matter equality time depends strongly on the matter content of the universe. If the matter content was too low, then recombination would occur in the radiation dominated era which would noticeably effect the power spectrum. In particular, small-scale anisotropies would increase if the matter density was low.

[6] A great simplified animation of this can be seen here

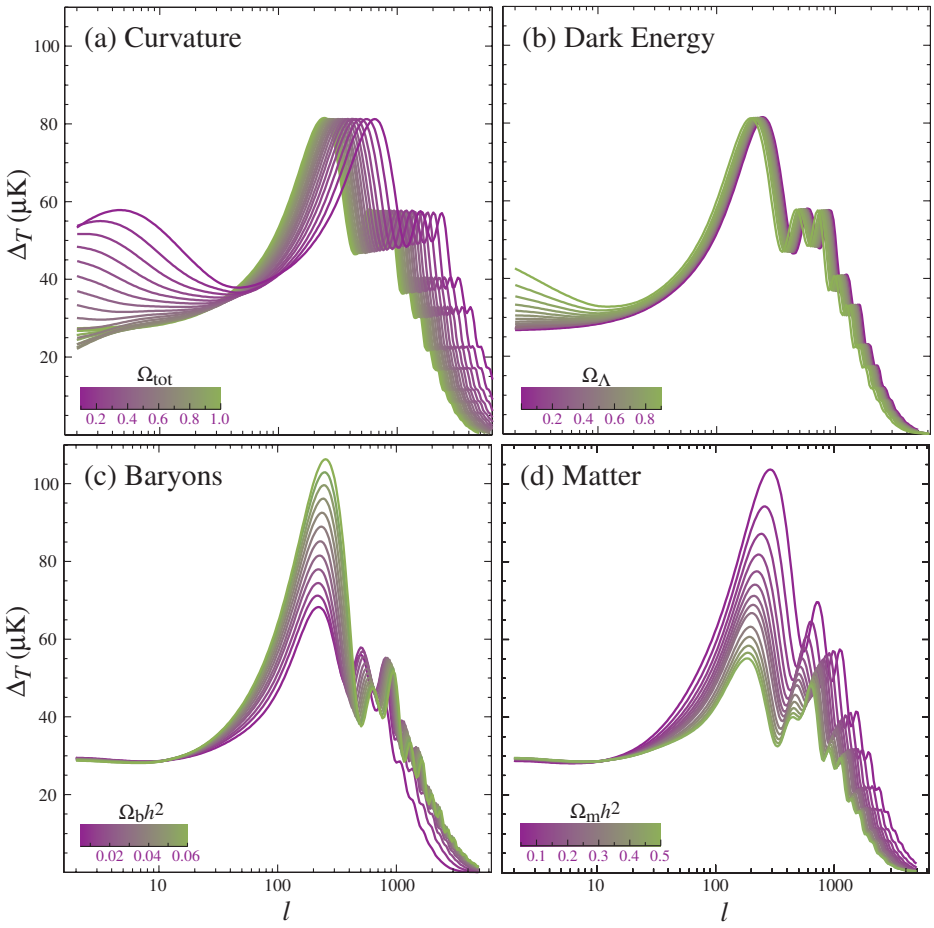

Figure 1.7: Modeling how how the characteristic acoustic temperature spectrum changes when varying the for main cosmological parameters. Figure adapted from Ref. [23].

The most recent results from *Plank* [15] give $\Omega_{0,b}h^2 = 0.02242 \pm 0.00014$ and $\Omega_{0,\mathrm{cdm}}h^2 = 0.11933 \pm 0.00091$. Measurements of the CMB and BBN both support the dark matter hypothesis, but what is most striking about this is that both of these measurable phenomenon manifest from very different physics! These are truly two *independent* confirmations for the existence of dark matter.

1.2.3 Structure Formation

So far, the big-bang model has a serious problem: how does a homogeneous universe form the structure of the very 'lumpy' universe we live in today? I've already mentioned that quantum fluctuations of energy density are left over at the end of inflation, however these inhomogeneities observed at the time of the CMB are simply not large enough to grow into the structures we see today.

Dark matter solves this problem; since it is not effected by the radiation pressure, it can begin gravitational collapse of over-dense regions much earlier than recombination. After photon decoupling, the baryons can then fall into the gravitational wells made by the dark matter. Modeling how such systems evolve into the modern universe is incredibly complex, and left to large N-body simulations. See [24] for a thorough review, but as a basic description they work by considering small perturbations in the dark matter density

$$\delta = \frac{\delta\rho}{\rho}, \tag{1.13}$$

where $\delta\rho$ is the difference in the dark matter density and the average density of the universe (ρ), and δ is a time dependent quantity. These perturbations are then evolved with the collisionless Boltzmann equation coupled with the Poisson equation. The power spectrum of the density perturbations from simulation can be compared with measurement to constrain models. Visualizations of these simulations and resultant power spectra can be see in Figs. 1.8 and 1.9. These N-body simulations tell us lots of information about the rich inner structures of dark matter halos and other astronomical objects.

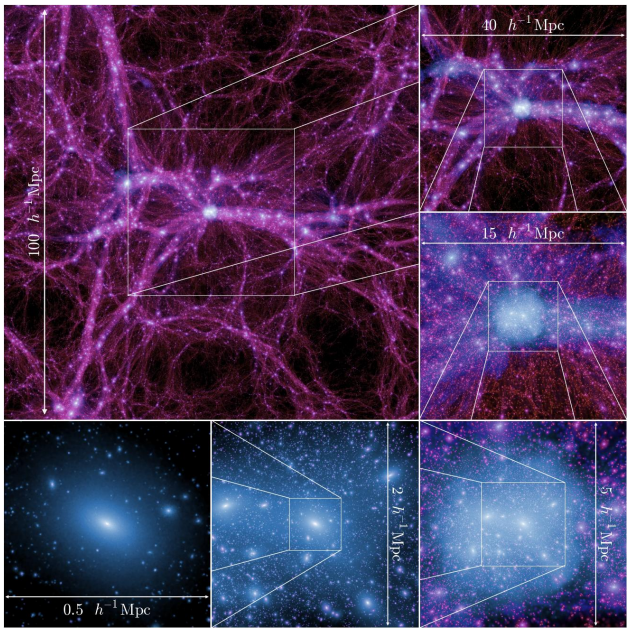

Figure 1.8: Zooming in on a massive halo from the Millennium-II Simulation [25]

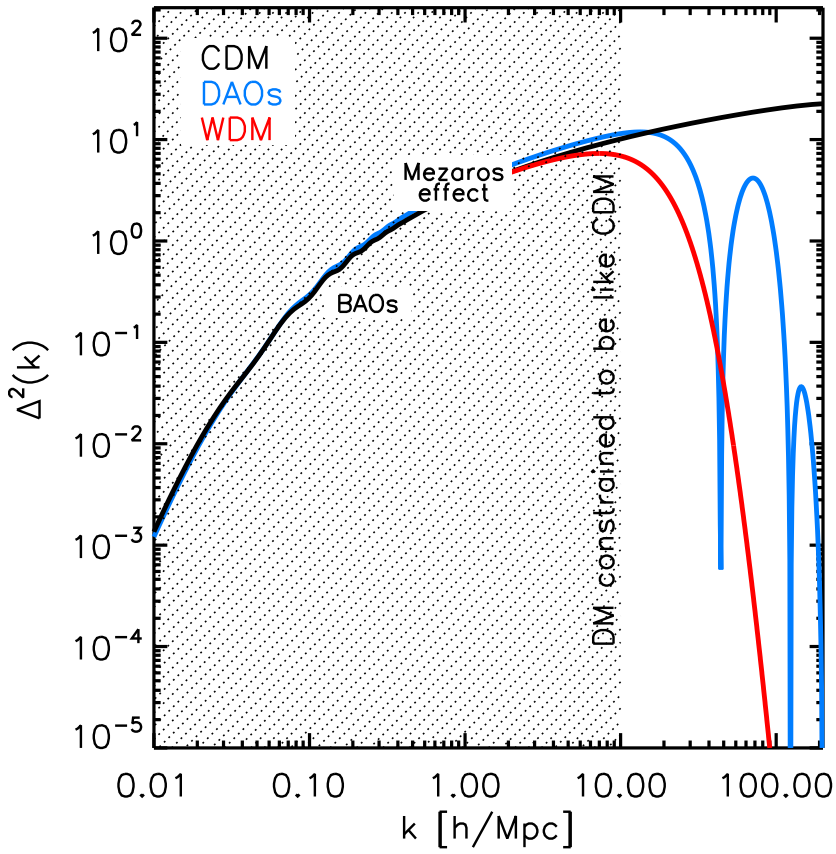

Figure 1.9: Linear dark matter power spectrum (dimensionless) in different dark matter models: Cold Dark Matter (CDM), Warm Dark matter (WDM), and Interacting Dark Matter (DAOs). The black hashed area constrains the DM behaviour from the observed large-scale distribution of galaxies and the Ly$-\alpha$ forest constraints on WDM to behave as CDM. Figure adapted from Reg. [26]

1.2.4 Alternatives to Dark Matter

While I have presented much 'evidence' for dark matter in this section, what makes us so sure that it is some new type of matter and not some other type of exotic effect? Indeed, observations from the modern universe do not alone necessarily conclude the existence of dark matter.

Many of the above arguments for DM can be explained by modifying Newtonian gravity, with a general theory (and variations of) know as modified Newtonian gravity, or MOND [9]. The general idea is that Newton's laws only apply to 'high acceleration' environments, and

MOND proposes a modified law of

$$F = m\mu\left(\frac{a}{a_0}\right)a, \tag{1.14}$$

where $\mu(a/a_0)$ is an unknown function, and a_0 is a new fundamental constant which sets the scale for MOND vs regular Newtownian dynamics. To be consistent with observation, it must have the limiting cases of

$$\mu \to 1, \quad \text{for } a \gg a_0 \quad \text{Newtonian Dynamics} \tag{1.15}$$

$$\mu \to \frac{a}{a_0}, \quad \text{for } a \ll a_0 \quad \text{MOND} \tag{1.16}$$

While this does a good explaining the observed galaxy rotation curves (among other phenomena in the observed modern universe) MOND struggles to explain many phenomena of the early universe. Also problematic is that MOND is a non-relativistic theory. A relativistic version of the theory was formulated, called TeVeS [27]. However, for any MOND-like theory to be able to explain all of the evidence for dark matter, it ends up requiring an incredible amount of fine tuning. And while this does not in-and-of-itself make the theory wrong, the main argument behind MOND originally was to have a simpler explanation for the universe than the dark matter hypothesis. There are still proponents of MOND, but it is largely disfavored by the astrophysics community compared to the ΛCDM model.

1.3 Dark Matter Candidates

There are a multitude of theories to explain the evidence for dark matter presented previously, however I will only focus on the most actively pursued theories, highlighting the ones that pertain most to this thesis. When discussing dark matter as a particle, it is typically represented by the symbol χ, for example, the mass of a dark matter candidate would be represented as m_χ.

1.3.1 Properties of Dark Matter

So what do we actually know about dark matter? Spoiler alert, we haven't found any direct laboratory evidence for DM, all of our evidence is astronomical. The evidence provided in the previous section does however allow us to constrain a few parameters about the DM.

- *Electric Charge*

  Implied by its name, dark matter is... dark. But how dark? From observations of the modern universe, the dark matter could simply be 'non-luminous' baryonic matter such as very faint starts or planets, etc. The BBN and CMB are what truly constrain the electric charge of dark matter. If DM was charged, it would effect the baryon-photon

fluid and alter the baryon acoustic oscillations at the time of recombination. Also, if DM were charged, structure formation would be effected, as the density perturbations would be sensitive to radiation pressure. Both of these effects would be present in the CMB power spectrum. Upper limits of the allowed DM charge have been placed by [28] (see Fig. 1.10) to be

$$\epsilon\,[e] \leq \begin{cases} 3.5 \times 10^{-7} \left(\frac{m_\chi}{\mathrm{GeV}}\right)^{0.58} & m_\chi > 1\,\mathrm{GeV} \\ 4.0 \times 10^{-7} \left(\frac{m_\chi}{\mathrm{GeV}}\right)^{0.35} & m_\chi < 1\,\mathrm{GeV}. \end{cases} \tag{1.17}$$

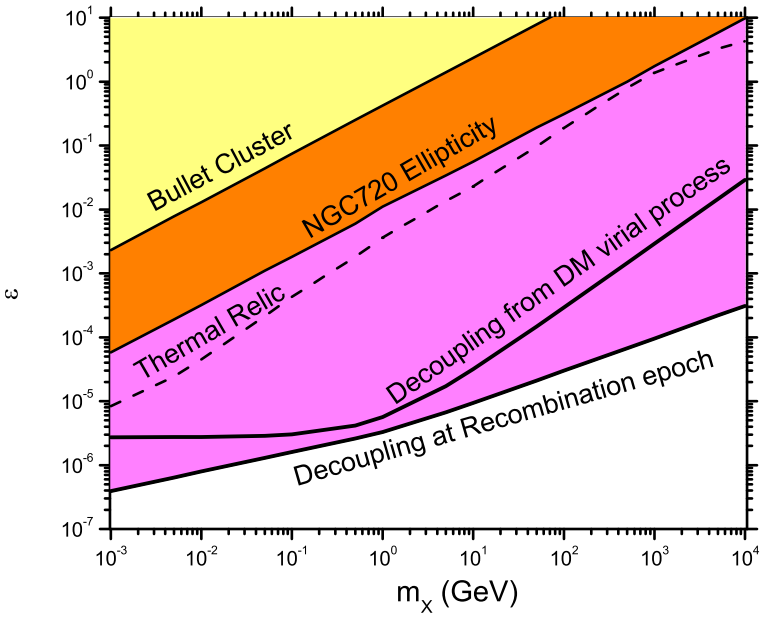

Figure 1.10: Limits on the charge of DM from various data sources. Figure adapted from Ref. [28]

- *Dark Matter Self Interactions*

  Cluster Collisions have been used to place limits on the self-interactions of DM. Perhaps one of the most impressive illustrations of this is the 'Bullet cluster', which was formed from the collision of two large galaxy clusters passing through each other, shown in Fig. 1.11. Using gravitational lensing techniques astronomers were able to reconstruct the mass density of the cluster (shown via the contours in the image). Through the observation of X-ray emissions, the hot baryonic gas content of the cluster could be seen (shown in blue and red in the right image). The gas in each cluster was slowed

by drag forces during collision creating shock waves. It is clear the bulk of the matter of the two clusters passed right through each other with little interaction as compared to the baryonic gas. This is completely consistent with the idea that majority of the mass of a cluster is 'dark', however this now confirms that the dark matter itself is 'collision-less'.

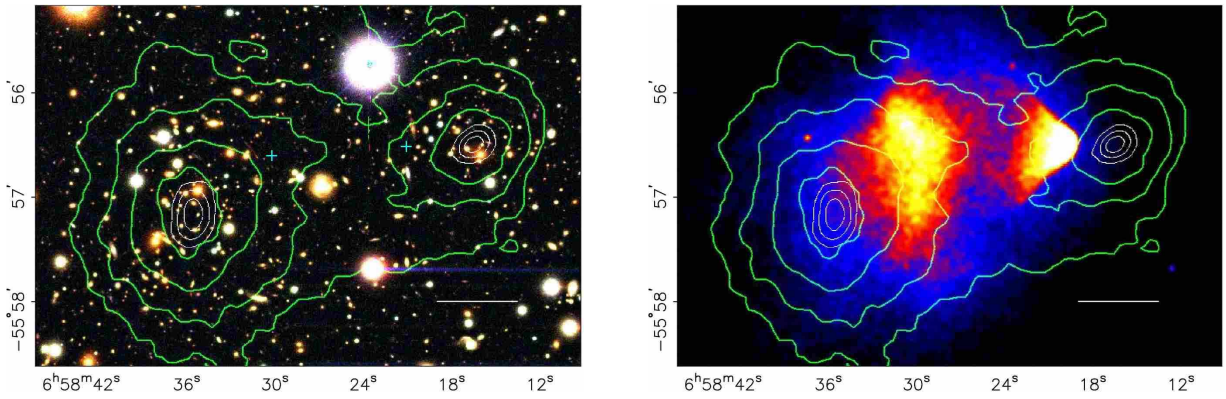

Figure 1.11: Left: Image of the bullet cluster shown with mass distributions shown in green contours via weak gravitation lensing. Right: The mass distribution of the baryonic matter via X-rays shown over the total mass contours from weak gravitation lensing. [29]

The current limits on self interaction from cluster collisions [30, 31] as well as from the tri-axial shape of galactic DM halos [32] are

$$\sigma_{\chi\chi}/m_\chi < 0.47\,\frac{\mathrm{cm}^2}{g} \approx 0.84\,\frac{\mathrm{barn}}{\mathrm{GeV}}. \tag{1.18}$$

- *Dark Matter Mass Lower Limit*

  The lower limit of DM mass depends on if the particle is assumed to be bosonic or fermionic. For fermionic DM, the Pauli exclusion principle places a strict (DM model independent) lower limit on the mass, requiring that phase-space density of the DM does not exceed that of the degenerate Fermi gas [33]. Consider a spherically symmetric DM halo of total mass M at radius r, internal degrees of freedom g, with a Fermi velocity of

$$v_F = \left(\frac{9\pi}{2g}\frac{\hbar^3 M}{r^3 m_\chi^4}\right)^{\frac{1}{3}} \tag{1.19}$$

  The escape velocity for this gravitationally bound system is thus,

$$v_{esc}^2 = \frac{2GM}{r}. \tag{1.20}$$

In order for this to be a stable system, we require that the Fermi velocity is less than the gravitational escape velocity

$$v_F \leq v_{esc} \implies m_\chi \geq \frac{9\pi\hbar^3}{4\sqrt{2M}g\,(rG)^{3/2}}. \tag{1.21}$$

A similar form of this argument is ofter referred to as the 'Tremaine-Gunn bound' [34].

Using dwarf galaxies, Ref. [35] bounds fermionic dark matter mass at

$$m_\chi > 70\,\text{eV} \quad \text{(fermionic DM - model independent)}. \tag{1.22}$$

Using measurements of Lyman-α even tighter constraints can be achieved, although these rely on assumptions about the DM thermal history [35]

$$m_\chi > 400\,\text{eV} \quad \text{(fermionic DM - from Ly-}\alpha\text{)}. \tag{1.23}$$

From this, we can easily rule out neutrinos as the source of DM, as their mass has been constrained to $m_\nu \approx \mathcal{O}(\text{eV})$ [36].

Bosonic DM does not face the issue of degenerate pressure, however it is physically limited in mass by the size of its de-Broglie wavelength; too small of mass would result in too large of a de-Broglie wavelength and wash out small scale structure. Constraints from CMB [37], Ly-α observations [38], and observations of satellites in the milky way [39] set the lower limit on bosonic DM mass to

$$m_\chi > 10^{-22}\,\text{eV} \quad \text{(Bosonic DM)}. \tag{1.24}$$

- *Dark Matter Mass Upper Limit*

  Very massive DM would be in the form of large astronomical objects, typically referred to as a massive astrophysical compact halo object or MACHO. The current strictest limits on mass are found from the stability of the ultra-faint dwarf galaxy Eridanus II in Ref. [40] and looking at tidal disruptions in halo binaries in Ref. [41]. If we assume that all of the DM is comprised of point-like MACHOs, these results combined bound the MACHO mass to be

$$m_\chi < 5\,M_\odot. \tag{1.25}$$

- *Stability of Dark Matter*

  We know that dark matter is crucial for structure formation, both for small scales in the early universe, and complex structures in the late universe, therefor we know that it must be stable from the time of decoupling. From Ref. [42] we can say that the lifetime of DM is

$$\tau_\chi > 200\,\text{Gyr}, \tag{1.26}$$

  making it at least an order of magnitude longer than the age of the universe.

- *Dark Matter Interactions*

  Observationally, the only force that we know DM interacts with is gravity. There are however many clues that suggest it *might* interact with other standard model forces.

Is that *really* all we know about dark mater!? Well, yes and no. These are the properties of DM that we *do* understand, but there have been 30+ years of active searching that have taught us a lot about what we know DM *isn't*. Moving forward, we now move into the hypothetical realm.

1.3.2 Dark Matter Origins

Before we talk too much about specific models, it is worth discussing different mechanisms in which the relic DM density manifests.

- *Freeze-Out Dark Matter*

  Perhaps one of the most popular explanations for the DM relic abundance is analogous to the thermal production of the standard model particles. In the early universe, we assume there was some abundance of dark matter and anti-dark matter ($\overline{\chi}$) in thermal equilibrium, with an self-annihilation rate $\Gamma_{\chi\overline{\chi}} = n_\chi \langle\sigma v\rangle$, where n_χ is the DM number density and $\langle\sigma v\rangle$ is the thermally-averaged pair-annihilation cross section times relative velocity [43]. In the same fashion as discussed above, the annihilation of the DM will 'freeze-out' when $\Gamma_{\chi\overline{\chi}} < H$. Intuitively this can be understood as: when the universe is small, the DM and anti-DM particles will eventually collide and destroy each other. However as the universe expands beyond the mean-free-path of the DM, the DM and anti-DM will no longer interact and the amount of DM will stay essentially fixed. Since we can measure the relic DM abundance today, this allows us to predict the temperature/time the DM froze out, as shown in Fig. 1.12.

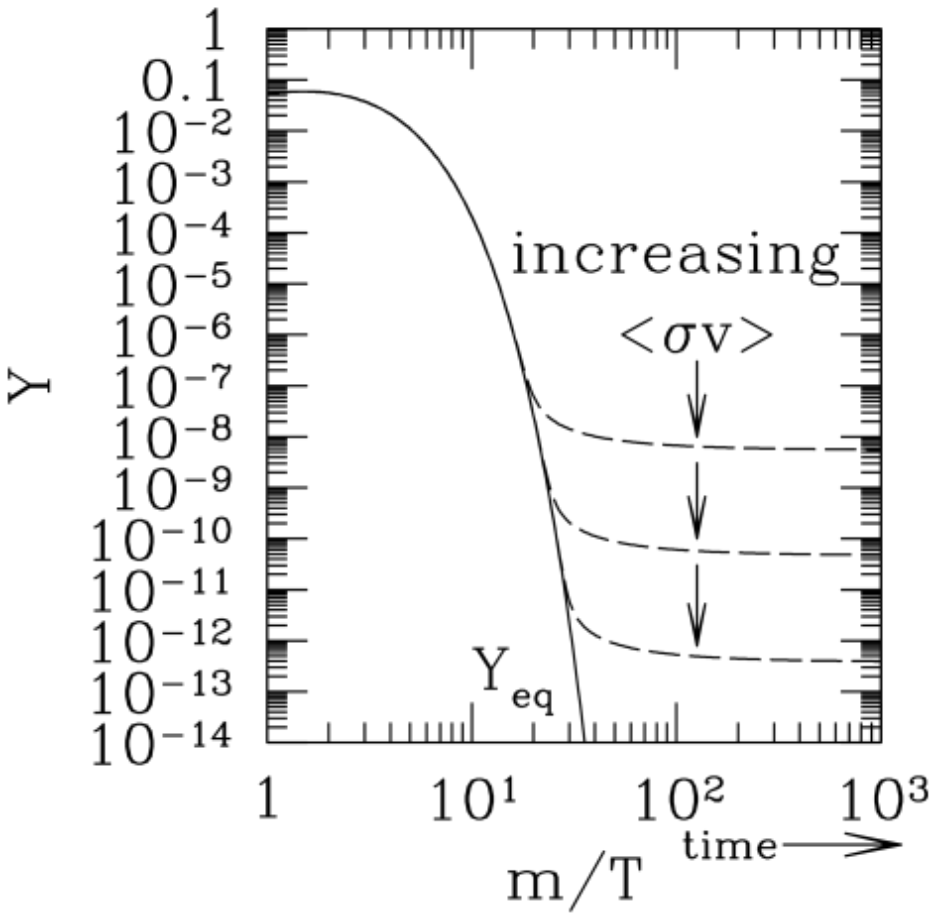

Figure 1.12: Co-moving number density of a WIMP in the early Universe. The dashed curves are the actual abundance, and the solid curve is the equilibrium abundance [44]

A full calculation of the relic DM abundance comes from solving the Boltzmann equation,

$$\frac{dn_\chi}{dt} = -3Hn - \langle \sigma v \rangle \left(n_\chi^2 - n_{eq}^2 \right). \tag{1.27}$$

However for out purposes, more intuition can be gained from simplified models. What follows is an example of two DM freeze-out models, as detailed in [45].

For a given point in the thermal history of the universe, considering all the relativistic particles contributing to the radiation energy density, we can write the radiation density as

$$\rho_{\text{rad}} = \frac{\pi^2}{30} g_{\text{eff}} T^4 \tag{1.28}$$

where g_{eff} is the effective degrees of freedom of the relativistic particles. For the radiation dominated universe (see Fig. A.5) we can write the Hubble parameters as

$$H^2 \approx \frac{8\pi G}{3}\rho_{\text{rad}} \approx \frac{T^2}{M_P}, \tag{1.29}$$

where $M_P \approx 10^{19}\,\text{GeV}$ is the Planck mass.

A particle's interaction rate is given by

$$\Gamma = n\sigma v \tag{1.30}$$

where n is the number density, σ is the cross-section, and v is the relative velocity. When the interaction rate is roughly equal to the Hubble expansion rate, then the particle interactions are highly suppressed and the particles are said have frozen out. Let us now consider two limiting cases:

1. **Hot Thermal Relics**
   When the temperature of freeze-out T_f is much greater than the mass of the particle then the freeze-out happens when the particles are still highly relativistic, these are referred to as hot thermal relics.
   Consider as an example the question 'could neutrinos make up the DM?' We begin with the condition $\Gamma_\nu = H$,

$$n_\nu \sigma v = H. \tag{1.31}$$

   Since we know the neutrinos are relativistic, their relative velocity is $v = 1$ [7] and from [46] the number density is $n_\nu \approx T_v^3$. Since the interaction is mediated by the weak force, we know

$$\sigma \approx G_F^2 T_v^2, \tag{1.32}$$

   where $G_F \approx 1.17 \times 10^{-5}\,\text{GeV}^{-2}$ is the Fermi constant [47]. Combining this with Eq. 1.29 and solving for the temperature,

$$T_f \approx \frac{1}{\left(G_F^2 M_P\right)^{1/3}} \approx 1\,\text{MeV}. \tag{1.33}$$

   With this temperature we can now determine the relic abundance. We define the co-moving number density (or Yield), $Y = n/s$, where s is the entropy density. Due to the conservation of co-moving entropy density, we can equate

$$Y_{\text{freeze out}} = Y_{\text{present day}}. \tag{1.34}$$

[7] using natural units like a civilized person

Thus,

$$n_{\nu,0} = \frac{n_\nu(T_f)}{s_\nu(T_f)} s_0 \tag{1.35}$$

$$\Omega_{\nu,0} = m_\nu \frac{n_\nu(T_f)}{s_\nu(T_f)} s_0 \tag{1.36}$$

Where everything on the RHS of the equation is either measured or is easily calculated (except the mass). Evaluating this expression gives,

$$\Omega_{\nu,0} h^2 \approx \frac{m_\nu}{93\,\mathrm{eV}}. \tag{1.37}$$

From cosmological surveys [48], we know that the sum of all 3 neutrinos favor masses must be $m_\nu < 0.3\,\mathrm{eV}$. This means that at most, neutrinos can only account for less that 3% of the DM mass. Furthermore, we know from the Fermi-degenerate pressure limit that Fermionic DM mass must be greater than $\sim \mathcal{O}(100\,\mathrm{eV})$.

2. **Cold Thermal Relics**

We now consider the opposite limit, $m_\chi \gg T_f$. In this limit, the number density is approx [46]

$$n_\chi \approx (m_\chi T)^{3/2} e^{-m_\chi/T}. \tag{1.38}$$

Applying the freeze-out condition, we have

$$\sigma v (m_\chi T)^{3/2} e^{-m_\chi/T} \approx \frac{T^2}{M_P} \tag{1.39}$$

$$\sqrt{x_f} e^{-x_f} \approx \frac{1}{M_P \sigma_{\chi\chi} v}, \tag{1.40}$$

where we have defined $x_f = m_\chi/T_f$, and the freeze-out temperature is determined by solving this expression.

Let us now turn to the energy density of DM,

$$\Omega_{\chi,0} = \frac{\rho_{\chi,0}}{\rho_c} = \frac{n_{\chi,0} m_\chi}{\rho_c} \tag{1.41}$$

We now want to express this in terms of the freeze-out number density and temperature. Recall from above from the conservation of entropy density, that $n_{\chi,0}/s_0 = n_{\chi,f}/s_f$. Also note that $s \propto T$, thus,

$$\frac{n_{\chi,0}}{T_0^3} \approx \frac{n_{\chi,f}}{T_f^3}. \tag{1.42}$$

Using this expression and multiplying Eq. 1.41 by T_0^3/T_0^3 we get

$$\Omega_{\chi,0} = \frac{m_\chi T_0^3}{\rho_c} \frac{n_{\chi,f}}{T_f^3}. \tag{1.43}$$

Substituting in the definition of x_f and $n_{\chi,f} \approx T_f^2/M_P \sigma_{\chi\chi} v$,

$$\Omega_{\chi,0} = x_f \left(\frac{T_0^3}{\rho_c M_P} \right) \frac{1}{\sigma_{\chi\chi} v}. \tag{1.44}$$

Plugging in measured values this becomes

$$\Omega_{\chi,0} = \frac{x_f}{100} \left(\frac{10^{-8}\,\mathrm{GeV}^{-2}}{\sigma_{\chi\chi} v} \right), \tag{1.45}$$

where a factor of 1/100 has been pulled out for reasons that will soon be clear. From Fig. 1.12, we can see that the freeze-out temperature is determined as the cross-section and mass that result in the measured DM energy density. If the annihilation cross-section is too large, not enough DM remains today, and if too small, then there is an over-abundance of DM. The $10^{-8}\,\mathrm{GeV}$ in the above expression suggests that a cross section on the weak scale would be a reasonable choice. And thus values of $\sigma_{\chi\chi} \approx 10^{-8}\,\mathrm{GeV}^{-2}$ with DM masses in the range $10 - 100\,\mathrm{GeV}$ ($x_f \approx 30$) would give the correct DM abundance. Because of this nice form, a particle of this type is known as a WIMP (Weakly Interacting Massive Particle) [44]. There is a strict lower bound on the WIMP mass of $m_\chi > 2\,\mathrm{GeV}^{-2}$ from the fact that a mass lower than this would result in a relic abundance of DM that would close the universe (*i.e.* $\Omega_\chi \geq 1$), this is knows as the Lee-Weinberg bound [49]. The upper bound of the mass comes from the requirement of unitarity of the scattering matrix, and results in $m_\chi < 120\,\mathrm{TeV}$ [50].

3. **Warm Dark Matter**

   Ignoring any particle physics model dependencies, structure formation sets the lower bound for thermal dark matter mass at $m_{\mathrm{warm}\chi} > 2\,\mathrm{keV}$.

- *Freeze-In DM*

  While freeze-out dark matter is appealing since it is analogous to how most SM particles manifest in the hot big-bang model, it is not necessary to explain the DM abundance. We now turn to essentially the opposite case. Proposed by [51], the basic premise of freeze-in is as follows: In the early universe assume there is a small abundance of a long lived particle X that has interactions with the bath that are so small that these particles are essentially thermally decoupled from the bath. This particle is knows as a FIMP, or 'Feebly-Interacting-Massive Particle'. Also assume that there is a set of SM 'bath particles' that are in thermal equilibrium with the bath. For large temperatures,

X particles are produced from collisions or decays of bath particles. The production of X is at its maximum when $T \approx m_X$, and at freeze-in the yeild is fixed and given by

$$Y_{FI} \approx \lambda^2 \frac{M_P}{m_X}, \tag{1.46}$$

where $\lambda << 1$ is the coupling. Contrasting with freeze-out, we can write the cross section as $\sigma_{\chi\chi} v \approx \lambda_\chi^2 / m_\chi^2$, and the freeze-out yeild is

$$Y_{FO} \approx \frac{1}{\lambda_\chi^2} \frac{m_\chi}{M_P}, \tag{1.47}$$

showing that freeze-in and freeze-out are effectively inverses of each other. A large interaction rate for freeze-in results in an overabundance of DM, while it results in an under-abundance in freeze-out, as is schematically shown in Fig. 1.13.

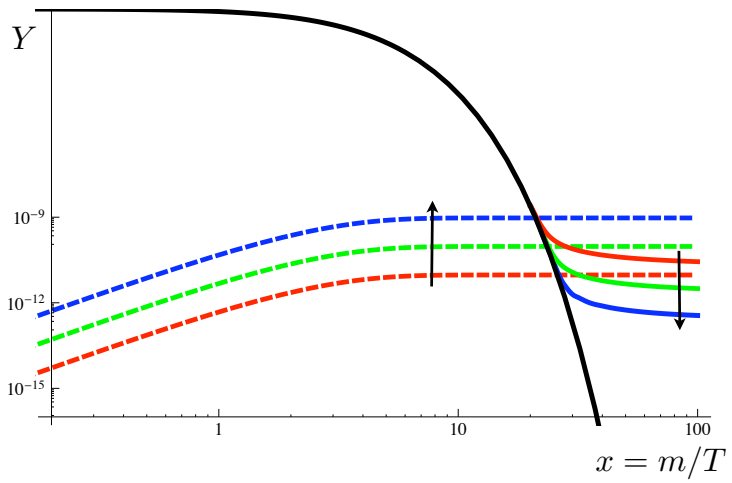

Figure 1.13: Comparison of freeze-out (solid colored) vs freeze-in v (dashed colored). Arrows represent the effect of increasing coupling strength for the two processes. Figure from [51]

Freeze-in theories require two particles (as apposed to freeze-out DM requiring only the WIMP), the FIMP, and the 'lightest particle in the thermal bath that carries the symmetry' or LOSP. The relic DM abundance could then be explained via 4 different scenarios as detailed in Fig. 1.14.

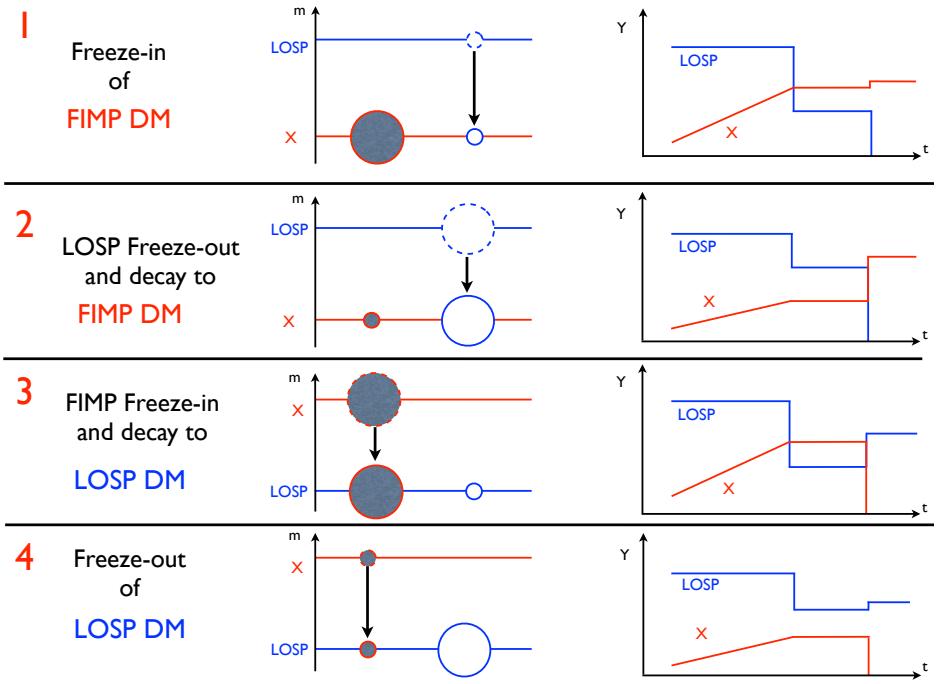

Figure 1.14: Four possible scenarios of the freeze-in mechanism. Left-side figures show the LOSP/FIMP spectrum. The circles represent cosmologically produced abundances. Large/small circles represent the dominant/sub-dominant mechanism for producing the dark matter abundance, the dotted/solid circles represent unstable/stable particles. The filled/open circle corresponds to production by freeze-in/freeze-out.. Right side figures show LOSP and FIMP abundances as a function of time. Figure from [51]

- *Asymmetric DM*

  In cosmological terms, the baryon density and dark matter density are quite close to each other, at least within the same order of magnitude. The standard WIMP model treats this as a coincidence, rather than a fundamental connection between the DM and baryonic matter. There is a class of models that connect the baryonic matter with the DM to explain the baryon matter/anti-matter asymmetry, called Asymmetric Dark Matter, or ADM [52]. The general class of models assumes that an asymmetry is created in either the baryonic/leptonic sector and communicated to the DM sector somehow, or vise versa. The process that communicates the asymmetry decouples at some temperature, separately freezing in the asymmetry for each sector. Lastly, if the DM was thermalized in the process of asymmetry generation, the excess symmetric population must have a mechanism in which it can annihilate itself.

- *Primordial Black Holes*

Primordial black holes (PBH) are the result of gravitational collapse of DM density fluctuations in the early universe [53, 54]. Since they are not made predominately from baryonic matter, they are able to have masses much less than $M_\odot$. They are considered part of the DM class of MACHOs.

- *Number changing processes*

  The abundance of DM can deplete itself via an $n \to 2$ number changing process, known as 'cannibalism' [55]. If DM is in thermal contact with the thermal bath, then the relic DM abundance can be driven by these $n \to 2$ processes, as in the case of SIMPs (strongly interacting massive particles) [56].

- *Non-thermal Processes*

  There are also ways in which DM can be produced non-thermally, as will be discussed with the case of the axion.

1.3.3 Dark Matter Phenomenology

As shown in Fig. 1.15, there is a multitude of DM models across a vast mass range. Some of these models have been mentioned or introduced in the previous section about mechanisms describing their abundance. In this next section I will highlight a few of the more popular models, focusing specifically on the models that are relevant to this thesis.

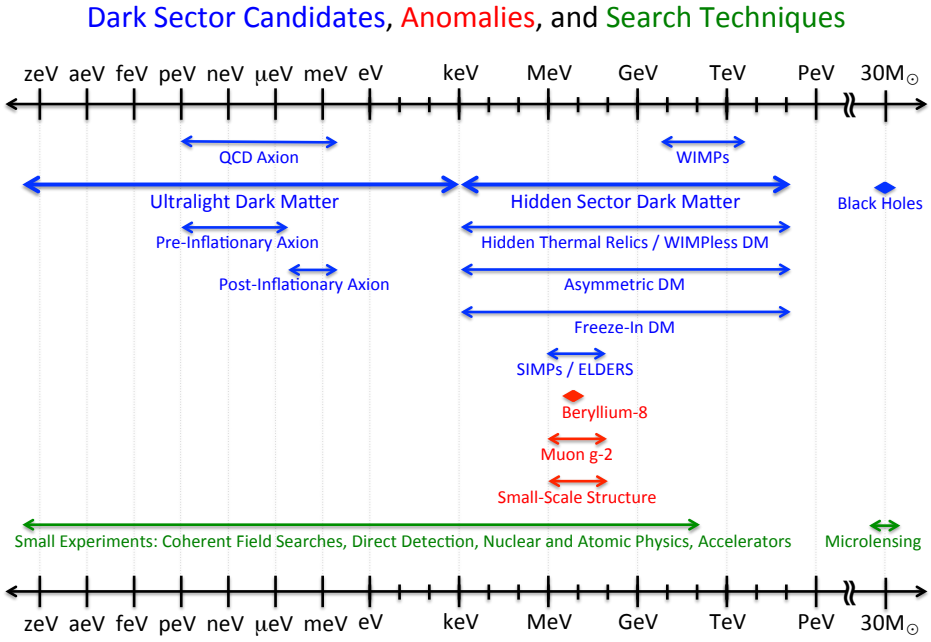

Figure 1.15: Rough mass ranges for dark matter and mediator particle candidates, experimental anomalies, and search techniques. Figure from Ref. [57].

- **WIMPs**

  Unrelated to cosmological arguments presented in the 'freeze-out' section, new physics at the weak scale was predicted in supersymmetric extensions of the SM [58] to solve the hierarchy problem. For both these reasons, the WIMP was a tantalizing solution to many open problems in physics. As noted above, the expected WIMP mass is roughly

  $$10\,\mathrm{GeV} \leq m_{\mathrm{WIMP}} \leq 10\,\mathrm{Tev}. \tag{1.48}$$

  While WIMPs have been the most popular DM particle candidate for about the past 30 years, they are beginning to lose popularity after null results from both collider/accelerator searches and direct detection experiments as shown in Fig.1.16.

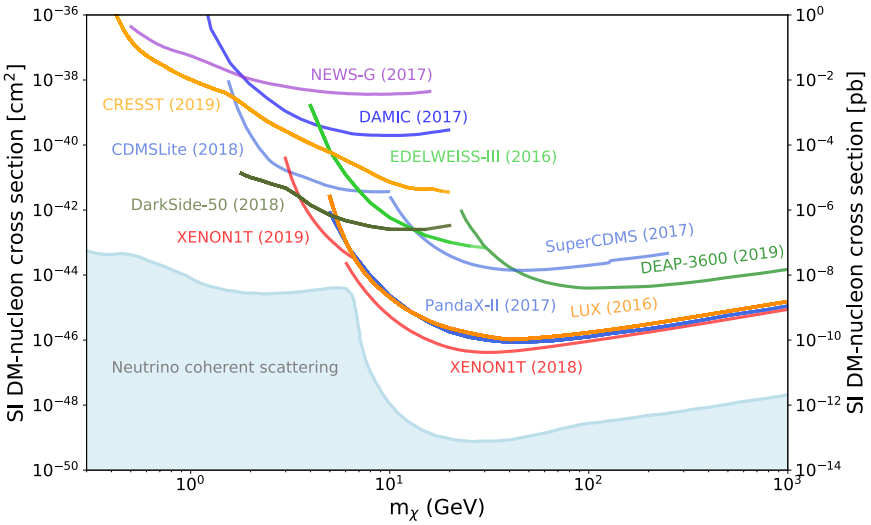

Figure 1.16: Current upper limits of the spin independent DM-nucleon cross section [10]

- **Axions and Axion-Like Particles (ALPs)**

  Originally proposed as a solution to the 'strong CP problem' [59] in QCD, it was soon realized the resulting pseudo-Nambu-Goldstone boson would make a potential DM candidate. Much like the WIMP, a particle that would solve the DM problem as well as an open problem in particle physics makes for an attractive solution.

  The axion should have a mass of

  $$m_A \approx 5.7 \left(\frac{10^9\,\mathrm{GeV}}{f_A} \right) \mathrm{meV}, \tag{1.49}$$

  where $f_A > 10^9\,\mathrm{GeV}$ is the coupling constant, and the typical expected mass range of roughly $10^{-12}\,\mathrm{eV}$ to $10^{-3}\,\mathrm{eV}$ [10].

ALPs are produced 'non-thermally' in the early universe. They are created as a non-relativistic condensate via the misalignment mechanism [60]. The axion field coherently oscillates around the minimum of the potential during the QCD phase transition (160 MeV). In this way, they still behave as 'cold' dark matter, despite their very low mass.

Axions can be detected in a number of ways, but the primary searches rely on the conversion of axions to photons in the presence of a strong magnetic field, known as the Primakoff effect [61]. The two photon decay is given by

$$\Gamma_{A\to\gamma\gamma} = \frac{g^2_{A\gamma\gamma} m^3_A}{64\pi} \tag{1.50}$$

where $g_{A\gamma\gamma} \propto \alpha/2\pi f_A$ is the axion two photon coupling constant. Current limits on $g_{A\gamma\gamma}$ and m_A are shown in Fig. 1.17.

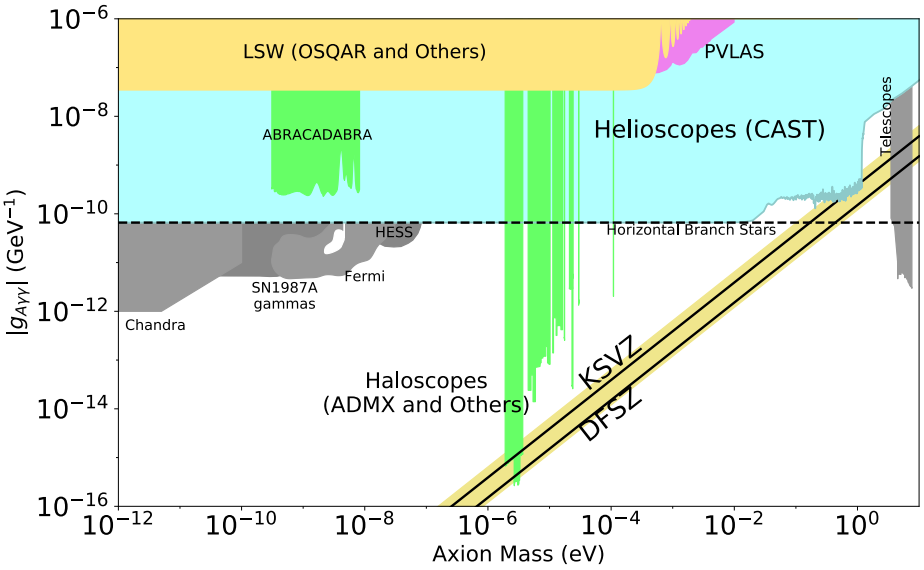

Figure 1.17: Current upper limits of the ALP to two photon coupling as a function of ALP mass [10]

- **Sterile Neutrinos**

  At first glance, neutrinos may present as a perfect DM candidate; long-lived, massive, and are electrically neutral. From the arguments presented in the freeze-out mechanism section, we know that SM neutrinos could only make up less than 1% of the DM density. Furthermore, from the Tremaine-Gunn bound we know that the mass of fermionic DM must be greater than a few hundred eV. A natural hypothetical DM candidate would

be a neutrino of much larger mass $\mathcal{O}$(keV), with even weaker interactions, known as *sterile neutrinos* [62].

The most relevant (detectable) decay mode is a sterile neutrino into a nuetrino and a photon, where the photon energy would be half the mass of the sterile neutrino. This decay would provide a strong astrophysical signal from galactic clusters at 3.5 keV as observed by [63, 64]. However the validity of the excess of this signal is these analyses is debated [65], as well as the absence of the signal in other galaxies [66–68] cast doubt on the sterile neutrino hypothesis.

- **Hidden Sector DM**

  The lack of any WIMP signal with SM forces in the expected mass range has pushed the DM search community to explore other models. It is interesting to ask "is DM charged under a new force?" With the addition of new force carriers, one can greatly extend the 'WIMP-like' mass range down to roughly keV [57]. While this hidden sector could be arbitrarily complex, I will focus on what the DM search community commonly refers to as *Light Dark Matter* (LDM) or *sub-GeV Dark Matter*.

  A popular model is the minimal kinetically mixed dark photon A', where the dark photon is either the DM itself, or is the mediator for the DM. We can think about this model in multiple regimes, as detailed in [57]

  1. Secluded freeze-out ($m_\chi > m_{A'}$):
     In this case, the mediator particles are lighter than the DM, so the DM annihilates to mediator particles, which freeze out. These mediator particles

     $$\langle \sigma v \rangle \propto \frac{g_D^4}{m_\chi^2}, \tag{1.51}$$

     where g_D is the DM-mediator coupling.
  2. Direct freeze-out ($m_\chi < m_{A'}$):
     DM directly annihilates to SM particles via a heavy mediator with cross section

     $$\langle \sigma v \rangle \propto \frac{g_D^2 g_{\mathrm{SM}}^2 m_\chi^2}{m_{\mathrm{MED}}^4} \tag{1.52}$$

  3. Freeze-in ($m_{A'} \ll \alpha m_e$):
     In this case, the coupling is so small the DM would not thermalize with the SM particles. Rather, the DM abundance would be populated by rare SM particle annihilations to DM until the temperature drops below the mass of the source particle.

1.4 Dark Matter Direct Detection

At this point, we have discussed astronomical evidence for dark matter, and discussed many different hypothetical models for particle-like DM. It is now time to return to earth and talk about how to actually detect dark matter. The focus of this section will be on the detection of *Light Dark Matter*. There are three avenues that one can look to find dark matter.

1. **Production:** DM is produced from SM particles interacting, e.g. from collisions at the LHC. The DM can be accounted for as 'missing mass' by keeping track of the momentum and energy of all particles created in an interaction.

2. **Indirect Detection:** DM and anti-DM particles from astronomical sources can interact and create SM particles in the form of high energy gamma rays. These gamma ray signals can be measured as signatures of DM. These experiments are typically satellites or ground based gamma ray observatories.

3. **Direct Detection:** DM interacts directly with SM particles. These experiments are typically condensed matter systems underground looking for signals of DM from the local DM halo. This type of detection is the only was to conclusively make a claim of discovery.

I will focus on the method of direct detection, not because it is necessarily better[8], but because that is what pertains to this thesis. To put it in simple terms, direct detection experiments are looking for kinetic energy deposited in a target material (detector) via either an elastic or in-elastic scattering processes. Since the earth is conveniently located in a DM halo, there is a constant flux of DM to use as the DM source. The local DM density and velocity in our galaxy are well known [69] to be

$$\rho_\chi = n_\chi m_\chi = 0.3 - 0.5\,\mathrm{GeV/cm^3}, \quad \text{and} \quad v_\chi \approx 10^{-3}. \tag{1.53}$$

Basic Nuclear Recoil Model

We first start with a very basic model to help with intuition. Considering the case of DM-nuclear scattering, the expected DM scattering rate-per-nucleus is

$$R_\chi = n_\chi v_\chi \sigma_{\chi-N} = \rho_\chi v_\chi \frac{A^2 \alpha_W^2}{m_\chi}, \tag{1.54}$$

where A is the atomic mass number and $\alpha_W \approx 0.03$ is the coupling constant of the weak nuclear force [10]. We can plug in a few numbers to start to get a feel for the requirements of a DM detector. For a typical WIMP mass of $m_\chi = 100\,\mathrm{GeV}$ and the atomic mass number for Xe of $A \approx 130$, the scatting rate is

$$R_\chi \approx 10^{-26}\,[\mathrm{s^{-1}}], \quad m_\chi = 100\,\mathrm{GeV}. \tag{1.55}$$

[8] I think it is...

This is a very small number. To have any hope of detecting DM in a reasonable time scale, lots of exposure is needed (target mass $\times$ time length of recorded data). This requires either huge detector volumes, or incredibly dense targets, which is exactly the trend that is happening with the Xe based experiments which are racing to design multi-ton Liquid Xe targets. However note the dependence on m_χ in Eq. 1.54, this offers a huge advantage for experimental searchers for *light dark matter*. By searching for DM masses of say $m_\chi = 100\,\text{keV}$ once can get the same exposure as a experiment looking for WIMPs, but with 6 orders of magnitude less mass!

1.4.1 Kinematic Matching

As was seen in the previous section, the DM scattering rate for nuclear recoils depends on the atomic mass number A. This can be thought of as, the DM is scattering of all of the nucleons in the nucleus coherently. Thus from a scattering rate perspective, having a target with larger nuclei is preferable. However, from an energy transfer perspective this is not necessarily good. This can be understood by looking the maximum energy transfer from an elastic collision

$$E_R(\text{max}) = 2v_\chi^2 \frac{m_\chi^2 m_T}{(m_\chi + m_T)^2}, \tag{1.56}$$

where m_N is the target nuclear mass. A plot of this recoil energy can be seen as a function of DM mass for some common detector materials in Fig. 1.18. Right away the problem should be evident; for DM masses below $\mathcal{O}(100\,\text{GeV})$ the recoil energy imparted in the detector becomes vanishing small. For $\mathcal{O}(100\,\text{keV})$ mass DM, the detectable energy becomes sub-eV. Also evident in the plots, is the fact that the lines are truncated around 100 keV or so. This is because the approximation of treating the nucleus as a free particle is no longer valid.

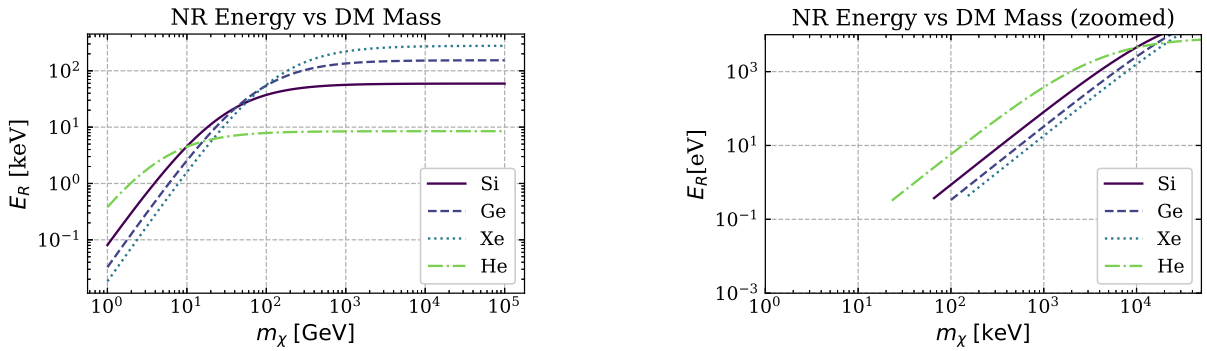

Figure 1.18: Left: Recoil energy in detector after elastic DM-nuclear scattering as a function of DM mass shown for Si, Ge, He, and Xe. Right: Same plot as left but zoomed in on lower DM masses. Note the different units on the x-axis between the plots.

1.4.2 DM Detection Channels

We can see that when searching for LDM, it will become exceedingly difficult to detect DM down to keV masses with standard nuclear recoil channels, if not impossible. Luckily the situation is not so grim, as we have other channels in which to detect DM. I will (briefly) discuss two other channels: in-elastic electron scattering, and single-phonon scattering. Before talking about a specific channels, I will give a brief overview of the general framework as detailed in Ref. [70]. This section is by no means comprehensive and is only meant to give a short introduction into the DM signal modeling to better motivate the design of LDM detectors. For a great summary of the concepts introduced here, see Ref. [71] or Ref. [70].

The DM event rate per target mass is given by[9]

$$R_\chi \frac{1}{\rho_T}\frac{\rho_\chi}{m_\chi}\int d^3v f_\chi(\boldsymbol{v})\Gamma(\boldsymbol{v}), \tag{1.57}$$

where $f_\chi(\boldsymbol{v})$ is the DM particle's velocity distribution in the lab frame and $\Gamma(\boldsymbol{v})$ is the event rate for a DM particle with velocity $\boldsymbol{v}$. The material response from the target medium can be accounted for in the scattering rate for spin-independent dark matter with the dynamic structure factor $S(\boldsymbol{q},\omega)$. The event rate can be written as

$$\Gamma(\boldsymbol{v}) = \frac{\pi\bar{\sigma}}{\mu^2}\int \frac{d^3q}{(2\pi)^3}\mathcal{F}^2_{\text{med}}(q)S(\boldsymbol{q},\omega_q) \tag{1.58}$$

where $\boldsymbol{q}$ is the momentum transfer, and

$$\omega_q = \boldsymbol{q}\cdot\boldsymbol{v} - \frac{q^2}{2m_\chi}. \tag{1.59}$$

The mediator form factor $\mathcal{F}^2_{\text{med}}(q)$ is given by

$$\mathcal{F}^2_{\text{med}}(q) = \begin{cases} 1 & \text{heavy mediator} \\ q_0^2/q^2 & \text{light mediator} \end{cases} \tag{1.60}$$

And $\bar{\sigma}$ is a reference cross section based on the particle level scattering matrix element

$$\bar{\sigma} = \begin{cases} \bar{\sigma}_n \equiv \frac{\mu^2_{\chi n}}{\pi}\overline{|\mathcal{M}_{\chi n}(q_0)|^2}_{q_0=m_\chi v_0} & \text{DM - nucleon scattering} \\ \\ \bar{\sigma}_e \equiv \frac{\mu^2_{\chi e}}{\pi}\overline{|\mathcal{M}_{\chi e}(q_0)|^2}_{q_0=\alpha m_e} & \text{DM - electron scattering} \end{cases} \tag{1.61}$$

where μ is the reduced mass for either the DM-nucleon or DM-electron interaction. Lastly the dynamic structure factor can be calculated for an arbitrary material and interaction

$$S(\boldsymbol{q},\omega_q) \equiv \frac{1}{V}\sum_f \left|\langle f|\,\mathcal{F}_T(\boldsymbol{q})\,|i\rangle\right|^2 2\pi\delta(E_f - E_i - \omega), \tag{1.62}$$

[9]Note that this is a generalized expression for the rate, where as what was done in the previous section was an limiting case shown for intuition.

where $|i\rangle$ and $|f\rangle$ are the initial and final states of the target, and $\mathcal{F}_T$ is the operator for the DM coupling. By factoring the DM scatting rate in this way, the same general framework can be used for all target material types and DM models.

1.4.3 Nuclear Recoil

For the case of DM scattering off of nucleons in a target, e.g. WIMPS, the dynamic structure factor is given by

$$S(\boldsymbol{q}, \omega_q) = 2\pi \frac{\rho_T}{m_N} \frac{f_N^2}{f_n^2} F_N^2(q) \delta\left(\frac{q^2}{2m_N} - \omega\right), \tag{1.63}$$

where f_n and f_N are the DM-neutron and DM-nucleon couplings, and $F_N^2(q)$ is the Helm form factor

$$F_N^2(q) = \frac{3j_1(qr_n)}{qr_n} e^{-(qs)^2/2}, \tag{1.64}$$

where $r_n \approx 1.14 A_n^{1/3}\,\text{fm}$ and $s \approx 0.9\,\text{fm}$. It is worth noting that in the limit that $q \to 0$, this form factor goes to unity.

Finally, the differential scattering rate for nuclear recoil DM is

$$\frac{dR}{d\omega} = \frac{\rho_\chi}{m_\chi} \frac{\bar{\sigma}_n}{2\mu_{\chi n}^2} \frac{1}{\sum_N A_N} \left[\sum_N A_N \frac{f_N^2}{f_n^2} F_N^2 \mathcal{F}_{\text{med}} \eta(v_{\text{min}})\right]_{q^2 = 2m_N\omega}, \tag{1.65}$$

where $\eta(v_{\text{min}})$ is the velocity integral for an isotropic target. This expression is valid only for for energies that are much grater than the phonon energies in the material, typically $\omega \gg \omega_{ph} \approx \mathcal{O}(100\,\text{meV})$.

Electronic Transitions

Electromagnetically interacting DM can excite an electron from the valence band of an insulator or semiconductor across the gap to the conduction band. This dynamic structure factor is written as

$$\begin{aligned} S(\boldsymbol{q}, \omega_q) = 2 \sum_{i_1, i_2} \int_{1\text{BZ}} \frac{d^3k_1 d^3k_2}{(2\pi)^6} 2\pi \delta(E_{i_2, \boldsymbol{k}_2} - E_{i_1, \boldsymbol{k}_1} - \omega) \\ \times \sum_{\boldsymbol{G}} (2\pi)^3 \delta^3(\boldsymbol{k}_2 - \boldsymbol{k}_1 + \boldsymbol{G} - \boldsymbol{1}) |f_{[i_1 \boldsymbol{k}_1, i_2 \boldsymbol{k}_2, \boldsymbol{G}]}|^2, \end{aligned} \tag{1.66}$$

where $i, \boldsymbol{k}$ are the band index and wave vector, $\boldsymbol{G}$ encapsulates the reciprocal primitive vectors $\boldsymbol{b}_i$, and $f_{[i_1 \boldsymbol{k}_1, i_2 \boldsymbol{k}_2, \boldsymbol{G}]}$ is the crystal form factor. The full definitions of these terms are well beyond the scope of this thesis, and I refer the reader to Ref. [71] for further explanation. The total rate is then,

$$R = \frac{2}{\rho_T}\frac{\rho_\chi}{m_\chi}\frac{\pi\bar{\sigma}_e}{\mu_{\chi e}^2}\sum_{i_1,i_2}\int_{1\text{BZ}}\frac{d^3k_1 d^3k_2}{(2\pi)^6}\times\sum_{\boldsymbol{G}} g(\boldsymbol{q},\omega)\mathcal{F}_{\text{med}}^2(q)|f_{[i_1\boldsymbol{k}_1,i_2\boldsymbol{k}_2,\boldsymbol{G}]}|^2. \tag{1.67}$$

where the momentum vector is given by $\boldsymbol{q} = \boldsymbol{k}_2 - \boldsymbol{k}_1 + \boldsymbol{G}$ and the energy $\omega = E_{i_2,\boldsymbol{k}_2} - E_{i_1,\boldsymbol{k}_1}$. Also note the $g(\boldsymbol{q},\omega)$ function accounts for the fact that when considering electronic transition, the material is no longer isotropic in general and the $\eta(v_{\text{min}})$ can not be used for the velocity.

Single Phonon Excitations

As mentioned in the previous section on nuclear recoils, the rate equation presented is only valid for energies well above the typical phonon energies of the system. This is because in this limit, the nuclei are treated as independent. This can be treated more generally by considering the the crystalline lattice of the target.

A three dimensional crystal has n ions (or atoms) in its primitive cell, each with 3 phonon branches. There are dispersions $\omega_{\nu,\boldsymbol{k}}$, with $\nu = 1,\ldots,3n$. The most generalized dynamic structure factor for this case is given by

$$S(\boldsymbol{q},\omega_q) = \frac{\pi}{\Omega}\sum_\nu \delta(\omega-\omega_k)\frac{1}{\omega_{\nu,k}}\left|\sum_j \frac{e^{-W_j(\boldsymbol{q})}}{\sqrt{m_j}}e^{i\boldsymbol{G}\cdot\boldsymbol{x}_j^0}\left(\boldsymbol{Y}_j\cdot\boldsymbol{\epsilon}_{\nu,k,j}^*\right)\right|^2 \tag{1.68}$$

where Ω is the volume of the primitive cell, $\boldsymbol{\epsilon}_{\nu,k,j}$ are the phonon polarization vectors, $j = 1,\ldots,n$ goes over all ions in the primitive cell, with masses and equilibrium positions given by m_j and $\boldsymbol{x}_j^0$ respectively [70]. The variable $\boldsymbol{Y}_j$ is a DM model specific parameter that contains the DM-ion couplings. $W_j(\boldsymbol{q})$ is the Debye-Waller factor, which suppresses the the dynamic structure factor for larger values of q, which is why single phonon interaction can be ignored in the larger mass nuclear recoil model presented previously. Plugging this into the rate equation we get

$$R = \frac{1}{m_{\text{cell}}}\frac{\rho_\chi}{m_\chi}\frac{\pi\bar{\sigma}}{\mu^2}\int\frac{d^3q}{(2\pi)^3}\mathcal{F}_{\text{med}}^2(q)\sum_\nu g(\boldsymbol{g},\omega_{\nu,k})\frac{1}{\omega_{\nu,k}}\left|\sum_j \frac{e^{-W_j(\boldsymbol{q})}}{\sqrt{m_j}}e^{i\boldsymbol{G}\cdot\boldsymbol{x}_j^0}\left(\boldsymbol{Y}_j\cdot\boldsymbol{\epsilon}_{\nu,k,j}^*\right)\right|^2. \tag{1.69}$$

Where notice now that $\bar{\sigma}$ was used rather than $\bar{\sigma}_n$ or $\bar{\sigma}_e$. This is because this generalized phonon excitation model can be applied to both the case of nuclear recoil, or electron recoil DM models.

Recall that phonons are quantized lattice vibrations. In-phase oscillations of ions in the same primitive cell are known as **Acoustic phonons**. There are 3 branches of acoustic phonons, and their dispersion relationship is linear in the long wavelength limit, $\omega_{\nu,k} \propto c_s|\boldsymbol{k}|$. The remaining phonon branches consist of out of phase oscillations called **Optical phonons**,

of which there are $3(n-1)$ branches. In the case of polar materials (materials with oppositely charged ions in the primitive cell), these optical phonons form an oscillating dipole.

The distinction between these two phonon branches becomes important when considering the coupling to different DM models. for the kinetically mixed dark photon, there is a very strong coupling to the dipole in polar materials, efficiently exciting optical phonons. For a DM model in which the DM couples to nucleons via a scalar of vector mediator, acoustic phonons can be excited from the DM coupling coherently to all the ions.

1.4.4 Projected Reach of LDM Detectors

The remaining work to be done at this step is to answer the question: "Given DM model 'X' from section 1.3.3, how does material 'Y' respond to it?" Many particle physics and computational condensed matter theorists have worked very hard on answer this question. Given certain assumptions about various background spectra, DM scattering cross section sensitivity projections can be made for different materials. Fig. 1.19 shows the current expected limits from a variety of detector materials for dark photon models and hadrophilic scalar mediated DM models in Fig. 1.20.

We can see that when considering detection channels beyond that of the traditional nuclear recoil model, vast amounts of unexplored DM parameters space opens up. For the case of hadrophilic scalar mediated DM, traditional solid-state materials such as Si and CVD diamond perform very well. However, to probe new parameter space using phonon excitations for dark photon models, one needs to use a polar material. Probing this new parameter space with polar materials is goal of the SPICE collaboration [72], of which much of the work in this thesis is deadicated.

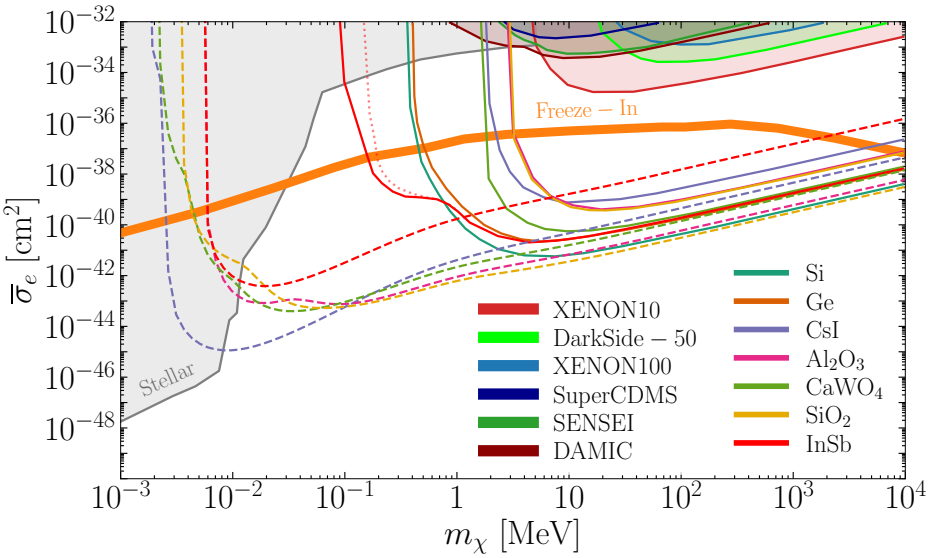

Figure 1.19: Sensitivity projections for electronic transitions (solid) and single phonon excitations (dashed) for the kinetically mixed dark photon DM model shown for various materials. The detector threshold is assumed to be 1 meV. Shown as shaded regions are the excluded regions from existing experiments. An exposure of 1 kg yr was assumed in this plot. Figure adapted from Ref. [73]

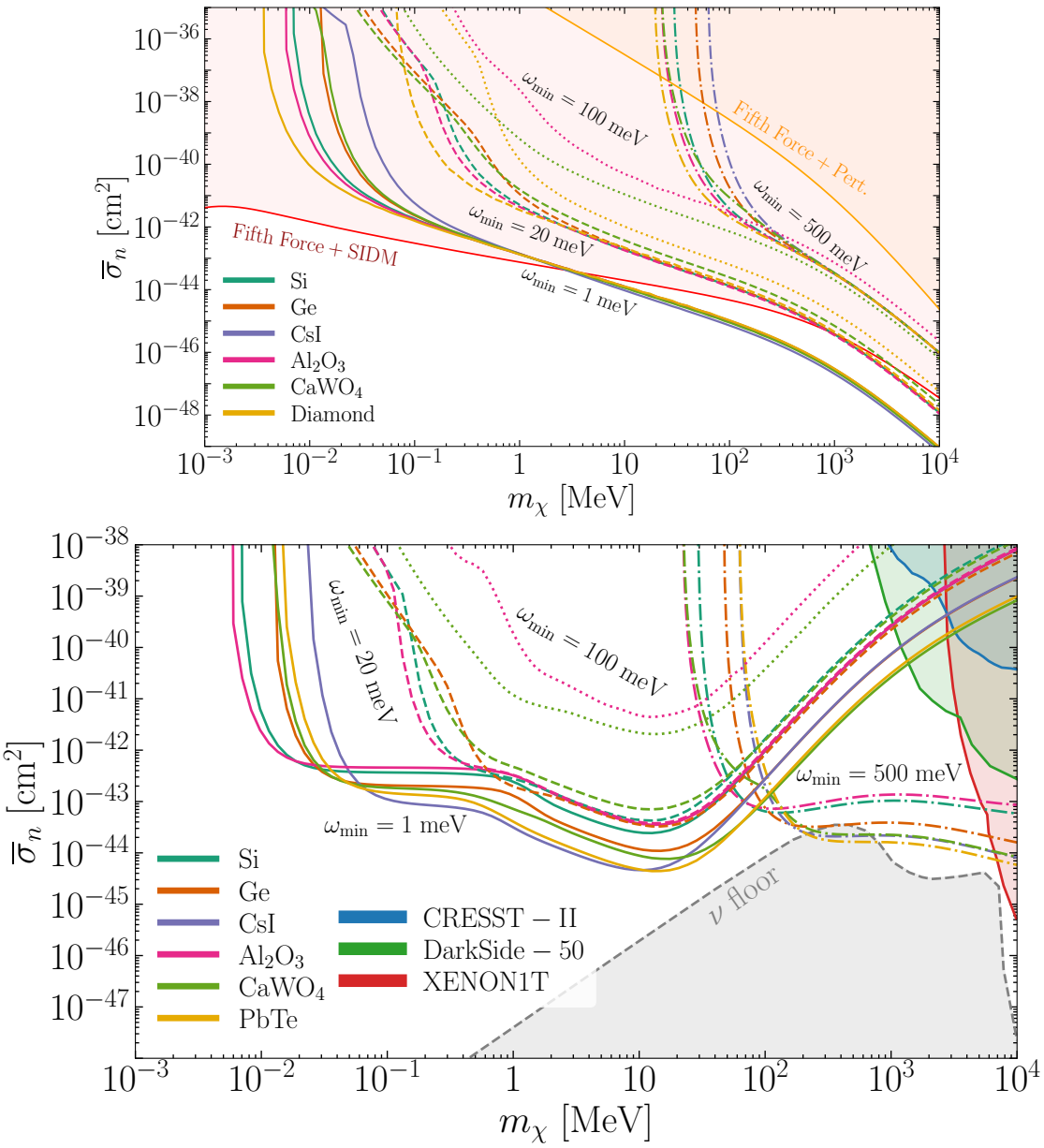

Figure 1.20: Sensitivity projection from light ($m_\phi = 1$) hadrophilic scalar mediator (top) and heavy ($m_\phi \geq 400$) hadrophilic scalar mediator (bottom) for single phonon and nuclear recoils for various materials. The Nuclear recoil reach is shown with the assumed detector threshold of $\omega_{\rm min} = 500\,$meV, while the remiaing lines correspond to single phonon excitations. An exposure of 1 kg yr was assumed in this plot. Figure adapted from Ref. [73]

1.5 Chapter Conclusion and Looking Forward

In this chapter we have motivated the existence of dark matter, what we currently know about it, and discussed methods of detection. We have highlighted the class of models known as light dark matter, and discussed the most promising techniques for its detection based on solid-state based detectors.

A *crucial* part of realizing these projected sensitivities is very low detector thresholds. The current state of the art solid-state detectors currently have detector thresholds of $\mathcal{O}(1-10\,\mathrm{eV})$. Thus, to truly reach these goals, 3-4 orders of magnitude in detector baseline energy sensitivity needs to be achieved. The remainder of this thesis is dedicated to the development and testing of protype DM detectors working towards the goals of $\mathcal{O}(\mathrm{meV})$ sensitivity. Specifically, chapters 2 and 3 detail the detector technology used in this thesis, chapter 4 details the design of a set of R&D detectors I designed for the SPICE collaboration, chapter 5 discusses analysis techniques in general for characterizing our detectors, chapter 6 is a version of two papers I published on the characterization of TESs and an athermal phonon mediated cryogenic photon detector, and finally chapter 7 discusses the (in progress) performance of the SPICE MELANGE detectors designed in chapter 4.

Finally, I feel that our understanding of dark matter can be summarized best by the great Randy Newman,

> "*... Let me get this straight: you don't know what it is*
> *You don't know where it is, and we can't get any?*"
>
> -Randy Newman

Part II

Detector Design

Chapter 2

Micro-Calorimetry with Transition-Edge Sensors

In this chapter I will give an overview of the ideal calorimeter model, introduce the transition-edge sensor (TES), and derive the dynamics and noise properties of the electrothermal feedback (ETF) TES. Much of this chapter is based on previous works (e.g. [74–77]), however various topics have been expanded upon. One potentially new result that the reader might find interesting is the derivation of how the effective noise bandwidth time constant (τ_*) depends on parasitic power in the TES. This chapter is mostly included for completeness, as it provides much of the background for the rest of the thesis. However a reader with a background in TESs could simply skip ahead to either the athermal phonon design in chapters 3- 4, or the experimental techniques and results in Chapters 5- 7.

2.1 Ideal Calorimetry Model

At the simplest level, all particle detectors work in the same fundamental way: an particle interacts with a target, either via a scattering or absorbing process, an amount of energy is transferred to the target in the form of an excitation, and this excitation is then measured via some type of sensor. In the case of a low-temperature micro-calorimeter, the excitation being absorbed is typically a phonon or a superconducting quasiparticle. The way in which these devices operate varies by technology, but for now we will simply think of a micro-calorimeter as a sensor which absorbs an energy of δE and leave the details to later chapters. Within the community of low temperature detectors, there are two highly related sensors: the calorimeter and the bolometer. In many cases, these can be physically quite similar and differ only in thier mode of operation. A bolometer measures a radiative flux, where as a calorimeter measures the total absorbed energy from an interaction. Said a different way, bolometer measure power, and calorimeters measure energy.

The ideal calorimeter model, originally described by Mather [78] for bolometers and McCammon [79] for calorimeters, consists of an absorber with heat capacity C, connected

to a fixed thermal reservoir[1] at temperature T_B via a thermal conductance G as shown in Fig. 2.1 (left). In this ideal model, it is assumed that there is a perfect resistive thermometer held at the temperature of the absorber. In a realistic calorimeter, the resistive sensor is thermally connected to an absorber, which is thermally coupled to the bath. In most designs, the thermal links can be designed such that the absorber is effectively at the temperature of the bath, and thus the model on the right side of Fig. 2.1 can still be approximated as the figure on the left. The design of the sensor/absorber/bath system will also depend on the intended purpose of the calorimeter: if the sensor itself is also the detector target, or if there is an absorber target, where a thermal or athermal excitation in the absorber is measured with the sensor. This will be discussed in more detail in later sections.

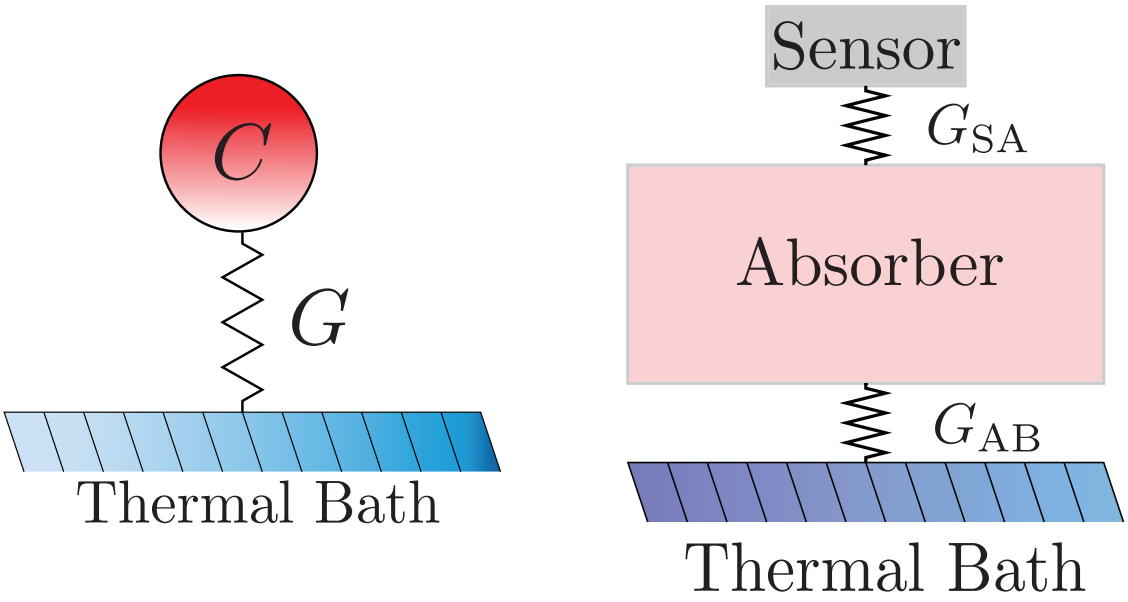

Figure 2.1: Left: Schematic for ideal calorimeter/bolometer model. Right: Realistic model for calorimeter/bolometer where the sensor is thermally connected to an absorber that is then connected to the thermal bath.

The resistance $R(I,T)$ of a resistive thermometer, or thermistor, typically changes as a function of temperature (T) and current (I), which are characterized by the dimensionless parameters

$$\alpha \equiv \left.\frac{T_0}{R_0}\frac{\partial R}{\partial T}\right|_{I_0} \qquad \beta \equiv \left.\frac{I_0}{R_0}\frac{\partial R}{\partial I}\right|_{T_0}, \tag{2.1}$$

where the '0' subscript represents the equilibrium values. The characteristics of α and β will depend on the material properties of the thermistor used. As will be discussed in fol-

[1]Also referred to as the thermal bath, or simply the 'bath'

lowing the sections, the sign of the temperature sensitivity determines the optimal operation scheme for the sensors. In particular, for $\alpha < 0$ the thermistor should be operated with a constant current bias, and for $\alpha > 0$ with a constant voltage. A schematic for an example biasing circuit is shown in Fig. 2.2 (left), where a current bias I_B is applied across a parallel combination of a shunt resistor R_{sh} and the resistor. If $R_{sh} \ll R(I,T)$, the voltage across $R(I,T)$ is approximately constant, and thus the thermistor is considered voltage biased. Conversely, if $R_{sh} \gg R(I,T)$, this becomes a constant current bias.

For some very low impedance current sensitive thermistors, the current through the resistor is typically read out via an input coil coupled to a SQUID array. In a realistic circuit there are parasitic resistances on both legs of the bias circuit, accounted for as R_p on the thermistor side. The parasitic line resistance on the shunt side of the circuit has been bundled into the definition of R_{sh}. Additionally, parasitic inductance in the sensor line is lumped together with the inductance of the input coil and labeled L. It will be made clear in later chapters that it is necessary to minimize the parasitics on the shunt side when designing the TES circuit, see Appendix D for discussion of how this is done in practice. For simplicity, a Thevinin equivalent circuit (see the right figure of Fig. 2.2) is often used, where the voltage bias is given by $V_B = I_B R_{sh}$ and the 'load resistance' is $R_\ell = R_{sh} + R_p$.

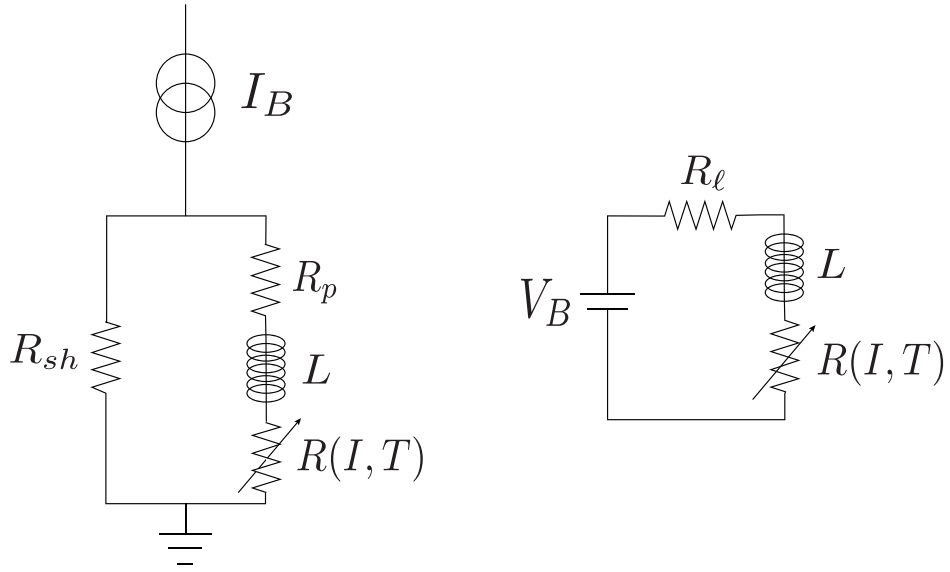

Figure 2.2: Left: Actual bias circuit. Right: Thevenin equivalent circuit, where $V_B = I_B R_{sh}$ and $R_\ell = R_p + R_{sh}$.

2.1.1 Equilibrium Characteristics

Before getting into the dynamics of the model, it is worth looking first at the characteristics of the system in equilibrium. With no additional input from the environment, we have two power sources to keep track of: the joule heating (P_J) from the applied bias and the cooling

power (P_{Bath}) from the heat flow to the thermal bath. In equilibrium these two powers are equal to each other, and commonly represented as P_0. The joule heating is simply,

$$P_J = V_0 I = I^2 R(I,T) = \frac{V_0^2}{R(I,T)} \tag{2.2}$$

where V_0 is the voltage across the thermistor. For the cooling power of the bath, a power law is assumed as per [80]

$$P_{\text{Bath}} = K(T^n - T_B^n), \tag{2.3}$$

where n is the thermal conductance exponent and K is a normalization factor, both of which are determined by the geometry and material of the calorimeter. The prefactor K can be re-written based on the definition of the thermal conductance,

$$G = \frac{\partial P}{\partial T} = nKT^{n-1} \implies K = \frac{G}{nT^{n-1}}, \tag{2.4}$$

$$P_{\text{Bath}} = \frac{G}{nT^{n-1}}(T^n - T_B^n) = \frac{GT}{n}\left(1 - \frac{T_B^n}{T^n}\right). \tag{2.5}$$

In equilibrium, the cooling power to the bath is equal to the joule heating from the applied bias plus any additional parasitic power incident on the calorimiter (P_{par}).

$$P_{\text{Bath}_0} = P_{J_0} + P_{\text{par}} \tag{2.6}$$

Since typically the resistance and bias voltage can be precisely known, in the limit of no parasitic power, the joule power can be used to estimate the thermal conductance in the case that the operating temperature can be known.

$$G = \frac{n}{T}(P_{J_0} + P_{\text{par}})\left(1 - \frac{T_B^n}{T^n}\right)^{-1} \tag{2.7}$$

$$G \approx \frac{nP_{J_0}}{T}, \quad P_{\text{par}} = 0, T_B \ll T \tag{2.8}$$

where the second line is the limiting case that the thermal bath temperature is much less than the operating temperature[2] and there is no parasitic power. As we will see in later sections, it is difficult to disentangle the effect of the parasitic power, as it is often degenerate with the measurement of operating temperature T. Note that depending on the sensor technology being used, T may not necessarily be known. For the case of a Transition-Edge Sensor, it is typically reasonable to approximate $T \approx T_c$.

[2]Note that due to the exponential factor of n, T_B typically need not be that much less than T for this to be true

2.1.2 Micro-Calorimeter Dynamics

The derivations in the following section are largely based on Lindeman [74] and Irwin and Hilton [81], reproduced here for completeness. We can describe the thermal and electrical circuits in Fig. 2.1 and Fig. 2.2 with a set of coupled differential equations. For the time being, we will ignore noise terms. For a given power signal[3] P, the thermal equation is given by

$$C\frac{dT}{dt} = -P_{\text{Bath}} + P_J + P, \tag{2.9}$$

which is basically saying, the change in energy per time in the calorimeter is equal to the power flowing in minus the power flowing out to the bath. The electrical equation, with current through the micro-calorimeter I, is given by

$$L\frac{dI}{dt} = V_B - IR_\ell - IR(I,T). \tag{2.10}$$

To solve this system of equations, we take the 'small-signal approximation' and expand about the equilibrium values T_0 and R_0. Starting with the thermal equation first, from Eq. 2.3 and Eq. 2.4 the cooling power from the bath can be written as

$$P_{\text{Bath}} \approx P_{\text{Bath}_0} + nKT^{n-1}\delta T \tag{2.11}$$

$$\approx P_{\text{Bath}_0} + G\delta T \tag{2.12}$$

where $P_{\text{Bath}_0} = P_{J_0} + P_{\text{par}} + P_{\text{Signal}_0}$, and the parasitic power term is assumed to be zero frequency. For simplicity, we can wrap the DC parasitic power term into the Joule power, and simply ignore it for now.

To approximate the joule heating power, recall that $P_J = I^2R(I,T)$, thus we must first expand $R(I,T)$ about I_0 and T_0.

$$R(I,T) \approx R_0 + \beta \left.\frac{\partial R}{\partial I}\right|_{T_0} \delta I + \alpha \left.\frac{\partial R}{\partial T}\right|_{I_0} \delta T \tag{2.13}$$

$$\approx R_0 + \beta\frac{R_0}{I_0}\delta I + \alpha\frac{R_0}{T_0}\delta T. \tag{2.14}$$

Using this result, we can now write the joule heating term as

$$P_J \approx P_{J_0} + 2I_0R_0\delta I + I_0^2\left(\beta\frac{R_0}{I_0}\delta I + \alpha\frac{R_0}{T_0}\delta T\right) \tag{2.15}$$

$$\approx P_{J_0} + I_0R_0(2+\beta)\delta I + \alpha\frac{I_0^2R_0}{T_0}\delta T \tag{2.16}$$

$$\approx P_{J_0} + I_0R_0(2+\beta)\delta I + \mathscr{L}G\delta T, \tag{2.17}$$

[3]Note that P here is simply a placeholder for signal power, noise, parasitic power, etc.

where the 'loopgain' has been defined as

$$\mathscr{L} \equiv \frac{P_{J_0}\alpha}{GT_0} = \frac{I_0^2 R_0 \alpha}{GT_0}. \tag{2.18}$$

The last term in Eq. 2.9 is the signal term and is simply

$$P = P_{\text{Signal}_0} + \delta P. \tag{2.19}$$

Combining these into Eq. 2.9, it becomes

$$C\frac{d\delta T}{dt} = - P_{J_0} - P_{\text{Signal}_0} - G\delta T \tag{2.20}$$

$$+P_{J_0} + I_0 R_0(2+\beta)\delta I + \mathscr{L} G\delta T + P_{\text{Signal}_0} + \delta P. \tag{2.21}$$

Combining terms and dividing by the heat capacity C we get

$$\frac{d\delta T}{dt} = \frac{I_0 R_0(2+\beta)}{C}\delta I - \frac{(1-\mathscr{L})}{\tau}\delta T + \frac{\delta P}{C}, \tag{2.22}$$

where we also defined the *natural thermal time constant*

$$\tau \equiv \frac{C}{G}. \tag{2.23}$$

We now turn to the electrical equation. Going term by term,

$$V_B \approx V_0 + \delta V = I_0\left(R_\ell + R_0\right) + \delta V, \tag{2.24}$$

$$IR_\ell \approx I_0 R_\ell + R_\ell \delta I, \tag{2.25}$$

and

$$IR(I,T) \approx I_0 R_0 + R_0\delta I + I_0\left(\beta\frac{R_0}{I_0}\delta I + \alpha\frac{R_0}{T_0}\delta T\right) \tag{2.26}$$

$$\approx I_0 R_0 + (1+\beta)R_0\delta I - \frac{\mathscr{L} G}{I_0}\delta T. \tag{2.27}$$

Combing these expressions into Eq. 2.10, we get

$$L\frac{d\delta I}{dt} = V_0 - I_0 R_\ell - I_0 R_0 - \left(R\ell + R_0(1+\beta)\right)\delta I - \frac{\mathscr{L} G}{I_0}\delta T + \delta V. \tag{2.28}$$

Simplifying we get that the linearized small signal thermal and electrical differential equations

$$\frac{d\delta T}{dt} = \frac{I_0 R_0(2+\beta)}{C}\delta I - \frac{(1-\mathscr{L})}{\tau}\delta T + \frac{\delta P}{C} \tag{2.29}$$

$$\frac{d\delta I}{dt} = -\frac{R_\ell + R_0(1+\beta)}{L}\delta I - \frac{\mathscr{L} G}{L I_0}\delta T + \frac{\delta V}{L}. \tag{2.30}$$

There are two limiting cases for Eq. 2.29 and Eq. 2.30 that are easily solved.

1. Zero loopgain limit: $\mathscr{L} = 0$. In this limit, Eq. 2.29 no longer has δT dependence. It can be integrated to give a solution of a single exponential with a time constant referred to as the *electrical time constant* given by

$$\tau_{el} \equiv \frac{L}{R_\ell + R_0(1+\beta)}. \tag{2.31}$$

2. Hard current bias limit: $\delta I = 0$. Similarly, in this case, Eq. 2.29 no longer has δI dependence and can be integrated to give a single exponential solution with the *constant current time constant* given by

$$\tau_I \equiv \frac{\tau}{1-\mathscr{L}}. \tag{2.32}$$

   We note in this case, that in order for this to be a stable mode of operation, the loopgain must be less than 1, i.e. $\alpha < 0$.

We now can use these time constants to simplify the coupled ODE's

$$\frac{d\delta T}{dt} = \frac{I_0 R_0(2+\beta)}{C}\delta I - \frac{1}{\tau_I}\delta T + \frac{\delta P}{C} \tag{2.33}$$

$$\frac{d\delta I}{dt} = -\frac{1}{\tau_{el}}\delta I - \frac{\mathscr{L}G}{LI_0}\delta T + \frac{\delta V}{L}. \tag{2.34}$$

The above equations can be more compactly written in matrix format,

$$\frac{d}{dt}\begin{pmatrix}\delta I\\ \delta T\end{pmatrix} = -\begin{pmatrix}\frac{1}{\tau_{el}} & \frac{\mathscr{L}G}{I_0 L}\\ -\frac{I_0 R_0(2+\beta)}{C} & \frac{1}{\tau_I}\end{pmatrix}\begin{pmatrix}\delta I\\ \delta T\end{pmatrix} + \begin{pmatrix}\frac{\delta V}{L}\\ \frac{\delta P}{C}\end{pmatrix}. \tag{2.35}$$

Eq. 2.35 can either be solved in the Fourier basis or by diagonalizing the matrix and finding the eigenvalues and eigenvectors in time domain. We will show both methods below, starting with the time domain solution to give more intuition into the micro-calorimeter dynamics.

We first consider only the homogeneous solution, setting δP and δV equal to zero. In this case, the solutions will be of the form,

$$\begin{pmatrix}\delta I\\ \delta T\end{pmatrix} = A_+ e^{-\lambda_+ t}\mathbf{v}_+ + A_- e^{-\lambda_- t}\mathbf{v}_-, \tag{2.36}$$

where $\lambda_\pm$ are the eigenvalues, $\mathbf{v}_\pm$ are the eigenvectors, and $A_\pm$ are the normalization constants. The eigenvalues are found to be

$$\lambda_\pm = \frac{1}{\tau_\pm} = \frac{1}{2\tau_{el}} + \frac{1}{2\tau_I} \pm \frac{1}{2}\sqrt{\left(\frac{1}{\tau_{el}} - \frac{1}{\tau_I}\right)^2 - 4\frac{R_0}{L}\frac{\mathscr{L}(2+\beta)}{\tau}}. \tag{2.37}$$

Micro-Calorimeter Response to Delta-Function Impuse

For calorimeter applications in which a discrete amount of energy is deposited in the detector, the most interesting solution to Eq. 2.35 is the case of a delta-function impulse of energy into the micro-calorimeter. We define the impulse of energy at $t = 0$ to be

$$\delta T(0) = E/C \equiv \Delta T. \tag{2.38}$$

As derived in Ref. [82], the current of the TES to an impulse of energy is given by

$$\delta I(t) = \left(\frac{\tau_I}{\tau_+} - 1\right)\left(\frac{\tau_I}{\tau_-} - 1\right)\frac{1}{(2+\beta)}\frac{C\Delta T}{I_0 R_0 \tau_I^2}\frac{\tau_+\tau_-}{\tau_- - \tau_+}\left(e^{-t/\tau_+} - e^{-t/\tau_-}\right). \tag{2.39}$$

It is worth noting the current response to an energy impulse is of the form of a 2-pole exponential with rise time τ_+ and fall time τ_-.

Micro-Calorimeter Responsivity

For the case of a bolometer, in which a constant flux of power incident on the detector is being read out, the power-to-current response of the sensor is the most important parameter. We consider the case of a sinusoidal power input of $\delta P = \mathrm{Re}\,(\delta P_0 e^{i\omega t})$. In this case Eq. 2.35 becomes

$$\frac{d}{dt}\begin{pmatrix}\delta I\\ \delta T\end{pmatrix} = -\begin{pmatrix}\dfrac{1}{\tau_{el}} & \dfrac{\mathscr{L}G}{I_0 L}\\ -\dfrac{I_0 R_0(2+\beta)}{C} & \dfrac{1}{\tau_I}\end{pmatrix}\begin{pmatrix}\delta I\\ \delta T\end{pmatrix} + \begin{pmatrix}0\\ \dfrac{\delta P_0}{C}\end{pmatrix}e^{i\omega t} \tag{2.40}$$

Again, from Ref. [82], we find that the current and temperature responsivities $\partial I/\partial P\,(\omega)$ and $s_T(\omega)$ respectively, are given by

$$\frac{\partial I}{\partial P}(\omega) = -\frac{1}{I_0 R_0}\frac{1}{(2+\beta)}\frac{(1-\tau_+/\tau_I)}{(1+i\omega\tau_+)}\frac{(1-\tau_-/\tau_I)}{(1+i\omega\tau_-)} \tag{2.41}$$

$$s_T(\omega) = \frac{1}{G}\frac{\tau_+\tau_-}{\tau^2}\frac{(\tau/\tau_+ + \tau/\tau_- + \mathscr{L} - 1 + i\omega t)}{(1+i\omega\tau_+)(1+i\omega\tau_-)}. \tag{2.42}$$

We can also express $\partial I/\partial P\,(\omega)$ in terms of thermal and electrical parameters using the definitions of $\tau_\pm$ from Eq. 2.37,

$$\frac{\partial I}{\partial P}(\omega) = -\frac{1}{I_0 R_0}\left[\frac{L}{\tau_{el} R_0 \mathscr{L}} + \left(1 - \frac{R_\ell}{R_0}\right) + i\omega\frac{L\tau}{R_0\mathscr{L}}\left(\frac{1}{\tau_I} + \frac{1}{\tau_{el}}\right) - \frac{\omega^2\tau}{\mathscr{L}}\frac{L}{R_0}\right]^{-1} \tag{2.43}$$

Complex Impedance

As will be clear in subsequent chapters, the complex impedance $Z(\omega)$ of the micro-calorimeter circuit can be a powerful tool in characterizing the device. This can most easily be calculated in the Fourier basis. Taking the Fourier transform of Eq. 2.35 we get

$$i\omega \begin{pmatrix} \delta I \\ \delta T \end{pmatrix} = - \begin{pmatrix} \frac{1}{\tau_{el}} & \frac{\mathscr{L} G}{I_0 L} \\ -\frac{I_0 R_0 (2+\beta)}{C} & \frac{1}{\tau_I} \end{pmatrix} \begin{pmatrix} \delta I \\ \delta T \end{pmatrix} + \begin{pmatrix} \frac{\delta V}{L} \\ \frac{\delta P}{C} \end{pmatrix}. \tag{2.44}$$

$$\begin{pmatrix} \frac{1}{\tau_{el}} + i\omega & \frac{\mathscr{L} G}{I_0 L} \\ -\frac{I_0 R_0 (2+\beta)}{C} & \frac{1}{\tau_I} + i\omega \end{pmatrix} \begin{pmatrix} \delta I \\ \delta T \end{pmatrix} = \begin{pmatrix} \frac{\delta V}{L} \\ \frac{\delta P}{C} \end{pmatrix}. \tag{2.45}$$

The matrix on the left is commonly written as $\mathbf{M}$ and the inverse is often called the 'generalized responsivity matrix' [83]. We simplify the expression by multiplying by the generalized responsivity matrix.

$$\begin{pmatrix} \delta I \\ \delta T \end{pmatrix} = \mathbf{M}^{-1} \begin{pmatrix} \frac{\delta V}{L} \\ \frac{\delta P}{C} \end{pmatrix}. \tag{2.46}$$

Before we can solve this, we must explicitly write out the generalized responsivity matrix

$$\mathbf{M}^{-1} = \left[\left(\frac{1}{\tau_{el}} + i\omega \right) \left(\frac{1}{\tau_I} + i\omega \right) + \frac{\mathscr{L} R_0 (1+\beta)}{L} \frac{1}{\tau} \right]^{-1} \begin{pmatrix} \frac{1}{\tau_I} + i\omega & -\frac{\mathscr{L} G}{I_0 L} \\ \frac{I_0 R_0 (2+\beta)}{C} & \frac{1}{\tau_{el}} + i\omega \end{pmatrix}. \tag{2.47}$$

We can now solve for the complex impedance by considering only a voltage excitation, i.e. $\delta P = 0$.

$$\left[\left(\frac{1}{\tau_{el}} + i\omega \right) \left(\frac{1}{\tau_I} + i\omega \right) + \frac{\mathscr{L} R_0 (2+\beta)}{L} \frac{1}{\tau} \right]^{-1} \left(\frac{1}{\tau_I} + i\omega \right) \frac{\delta V}{L} = \delta I \tag{2.48}$$

Simplifying and recalling the definition of τ_{el}, we get

$$Z(\omega) \equiv [Y(\omega)]^{-1} \equiv \frac{\delta V}{\delta I} = R_\ell + R_0 (1+\beta) + i\omega L + \frac{\mathscr{L} R_0 (2+\beta)}{(1-\mathscr{L})} \frac{1}{1+i\omega\tau_I}, \tag{2.49}$$

where we have also defined Y as the complex admittance. It is worth noting that the power to current responsivity can also easily be calculated in this same way, except you set $\delta V = 0$ rather than δP. It is clear from the form of the generalized responsivity matrix that the poles of the complex impedance will be the same as for the responsivity (the responsivity simply adds a zero). This is a very powerful fact, as the responsivity of a micro-calorimeter is often difficult to measure, where as measurement of the complex impedance is easy to perform. Due to their shared poles, the responsivity can be nicely written in terms of the complex impedance

$$\frac{\partial I}{\partial P}(\omega) = I_0 \frac{\mathscr{L} - 1}{\mathscr{L}} \left(1 + j\omega \frac{\tau}{1 - \mathscr{L}}\right) Z(\omega). \tag{2.50}$$

Plots of the inverse complex impedance and responsivity are plotted in Fig. 2.3, using experimental values from C. Fink and S. Watkins et al [84].

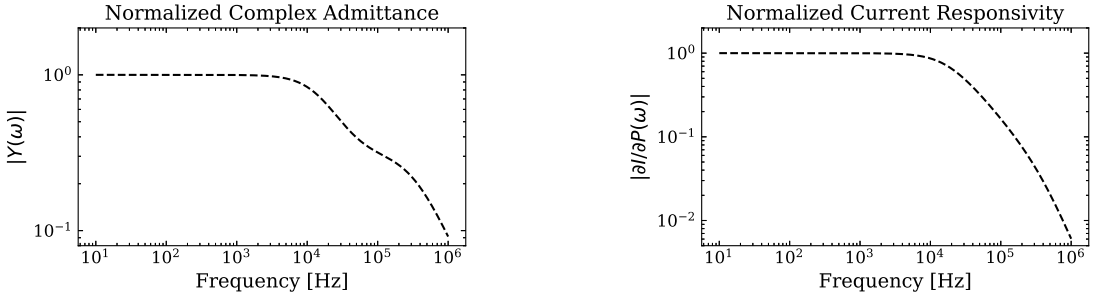

Figure 2.3: Left: Example of typical inverse complex impedance, or 'complex admittance'. Right: Example of typical current responsivity.

2.1.3 Electrothermal Feedback TES

Before going into more detail of the dynamics of Micro-Calorimeters, it is now worth focusing on the negative Electrothermal Feedback (ETF) Transition Edge Sensor (TES). It is important to mention that many of the following results still apply to many micro-calorimeters in general, but the derivations will be done in a more specific context.

A TES is a thin superconducting (SC) film that is biased in-between its SC and normal state regions. The details of the SC region will be discussed in more detail in later chapters, but for now this definition is sufficient. The negative ETF arises from the voltage biased condition: $R_\ell \ll R_{\text{TES}}$ in the biasing circuit in Fig. 2.2. This method was first demonstrated in [85] and is now the most common method of TES operation.

The negative ETF is necessary to stabilize the TES due to the fact that it has a positive temperature sensitivity, $\alpha > 0$. This stability of the ETF for $\alpha > 0$ can be intuitively understood as follows:

Voltage Bias: ($\alpha > 0$)

- Energy deposition raises temperature of TES
- Resistance of TES increases
- Joule heating lowers
- Temperature of TES is lowered
- Return to equilibrium

Current Bias: ($\alpha > 0$)

- Energy deposition raises temperature of TES
- Resistance of TES increases
- Joule heating increases
- Temperature of TES raised
- Thermal runaway

Thus it is clear that a voltage biased TES will remain stable, while a current bias will result in a positive feedback loop. Analogous to how negative feedback is used with an Op-amp or transistor, the negative electrothermal feedback in a TES serves to linearize the system. In this way, the small signal dynamical equations derived above will be valid for a TES, despite its intrinsic non-linear nature. The opposite would be true for a sensor with $\alpha < 0$ for say an NTD.

ETF TES Readout

The operating resistance of a TES is typically below $1\,\Omega$, sometimes as low as 10's of mΩ, therefor a SQUID[4] array must be used to measure the current through the TES. As shown in Fig. 2.2, an inductor L is placed in series with the TES, which is coupled to the SQUID array. The SQUID is then connected to a high impedance amplifier, and fed-back via a feedback resistor $R_{\rm FB}$ and feedback inductor $L_{\rm FB}$. Requiring a SQUID array introduces many complexities into the use of TESs, however their energy performance is so great it outweighs these difficulties.

The bandwidth of a modern SQUID array is typically much larger than that of the TES, and thus the overall bandwidth of the system is typically limited by the electronic time constant τ_{el}, typically denoted as 'L/R pole'.

$$\omega_{\text{read out}} \gtrsim \frac{1}{\tau_{el}} = \frac{R_\ell + R_0(1+\beta)}{L}. \tag{2.51}$$

For optimum signal-to-noise (discussed later) we want a small R_0, however this lowers our effective bandwidth. This limitation from R_0 can be ignored if a sufficiently low L can be achieved. We note that this L is really the combination of the input coil inductance plus any parasitic inductance in the TES biasing circuit. More about this will be discussed later when talking about experimental design.

[4]Superconducting Quantum Interface Device

ETF TES Dynamics

We now return to the time constants defined as the inverse eigenvalues in Eq. 2.37. As motivated above, we want the input inductance to be very small. In this limit, if $\tau_+ \ll \tau_-$, then

$$\tau_+ \to \tau_{el} \tag{2.52}$$

$$\tau_- \to \tau \frac{1+\beta+R_\ell/R_0}{1+\beta+R_\ell/R_0+(1-R_\ell/R_0)\mathscr{L}} \equiv \tau_{\rm ETF} \tag{2.53}$$

Where we have now introduced the effective electrothermal time constant $\tau_{\rm ETF}$ (which is also sometimes called τ_{eff} in the literature). Further still, in the limit of large loop-gain, or equivalently large α, $\tau_{\rm ETF}$ reduces to

$$\tau_{\rm ETF} \approx \frac{\tau}{1+\mathscr{L}} \quad (\mathscr{L} \gg 1). \tag{2.54}$$

When operated with negative electrothermal feedback, TESs are able to have $\mathscr{L} \gg 1$ and remain in stable operation. Typical values for $\mathscr{L}$ in modern TESs is between 100's and 1000's, thus the effective thermal fall time of an ETF TES is multiple orders of magnitude faster than the natural thermal time constant.

With this low inductance approximation, the responsivity becomes

$$\lim_{\text{small } L} \frac{\partial I}{\partial P}(\omega) = -\frac{1}{I_0 R_0}\frac{1}{(2+\beta)}\frac{(1-\tau_{el}/\tau_I)}{(1+i\omega\tau_{el})}\frac{(1-\tau_{\rm ETF}/\tau_I)}{(1+i\omega\tau_{\rm ETF})}. \tag{2.55}$$

In this limit, $\tau_{el} << \tau_{\rm ETF}$ and $\tau_{el} << \tau_I$. Thus for frequencies below $1/\tau_{\rm ETF}$, the responsivity can be approximated as

$$\frac{\partial I}{\partial P}(\omega) \approx -\frac{(1-\tau_{\rm ETF}/\tau_I)}{I_0 R_0(2+\beta)}\frac{1}{(1+i\omega\tau_{\rm ETF})}. \tag{2.56}$$

We can see that for low frequencies, the responsivity is essentially flat with a single pole roll off at $\tau_{\rm ETF}$.

Energy Removed From TES by ETF

In the strong ETF limit, for frequencies below $1/\tau_{\rm ETF}$ the current responsivity in Eq. 2.43 simply reduces to

$$\frac{\partial I}{\partial P}(0) = -\frac{1}{I_0(R_0-R_\ell)} \tag{2.57}$$

and low frequency power inputs are equal to the change in Joule heating

$$dP_J = -I(R_0 - R_\ell)dI. \tag{2.58}$$

Recalling that $R_0 = V_B/I - R_\ell$ this becomes

$$dP_J = -(V_B - 2IR_\ell)dI. \tag{2.59}$$

For a current excitation ΔI, we can calculate the the change in Joule heating ΔP by integrating the above expression

$$\Delta P_J = \int_{I_0'}^{I_0'+\Delta I} (V_B - 2IR_\ell)dI \tag{2.60}$$

$$\Delta P_J = (V_B - 2I_0R_\ell)\Delta I - \Delta I^2 R_\ell. \tag{2.61}$$

Finally, we can calculate the energy removed from the TES from electrothermal feedback by integrating the change in Joule heating

$$E_{\mathrm{ETF}} = \int \Delta P_J dt = \int_0^\infty \left[(V_B - 2I_0R_\ell)\Delta I(t) - \Delta I^2(t)R_\ell\right] dt, \tag{2.62}$$

Where I_0 is the baseline current, and $\Delta I(t)$ is the time dependent current pulse.

2.2 TES Stability and Thermal Phase Separation

Up to this point, the TES has been thought of as a lump element at temperature T_0. However, this assumption is not always valid. A TES can be thought of instead as a series of discrete resistors. The resistors will remain in thermal equilibrium as long as the thermal conductance between the elements is large compared to the conductance to the bath. For a rectangular TES, this can be expressed quantitatively with the inequality condition from [81]

$$R_n < \pi^2 \frac{L_0 T_c n}{G\alpha} \tag{2.63}$$

where L_0 is the Lorenz number, which is the dimensionless number relating a metal's temperature, thermal conductivity, and electrical conductivity. This topic of phase separation will be expanded upon in the following chapter.

2.3 TES Noise Sources

We can now turn our focus to the intrinsic noise sources of the TES and readout circuitry. The noise can be thought of as intrinsic and extrinsic. The intrinsic noise can be broken into

three noise sources: the Johnson–Nyquist noise from the parasitic and shunt resistances, the Johnson–Nyquist noise from the TES itself, and the phonon shot noise across the thermal connection from the TES to the bath. The extrinsic noise is any contribution from the SQUID and electronics readout, and additional environmental noise sources, e.g. IR loading, EMI, etc. In principle, the extrinsic noise can always be made negligible, though in practice this is often a very challenging task.

In order to compare the effect of all the different noise sources, it is necessary to reference them to a common point. Naturally, the most logical place to do this is the current through the TES. However, since ultimately we are measuring a power source, referencing the noise to the input power is the most physically meaningful. It is common to present noise at both of these reference points.

2.3.1 Passive Johnson Noise

Recall that the voltage variance per frequency in a given bandwidth, or the one-sided power spectral density (PSD), of a resistor is given by

$$S_V(\omega) = 4k_B T R. \tag{2.64}$$

We wish to quantify the noise contribution of the passive components in the TES bias circuit. Referring to Fig. 2.2, this would be the Johnson noise from R_ℓ or rather, R_{sh} and R_p. Note that in order to create the current source in the left diagram of Fig. 2.2 there is a sizable resistor R_B at room temperature. It turns out that the noise contribution from this resistor is suppressed by multiple orders of magnitude at the TES since most of it is shunted to the R_{sh} leg of the circuit and is thus negligible [76].

There is some subtlety in the calculation of the noise from the load resistance, since physically the components of this resistance are at different thermal stages. In the Pyle lab at UC Berkeley, the shunt resistor is thermalized at the 100 mK stage. The parasitic resistance in the wiring is primarily due to the contact resistance of the connectors in the wiring, one end at the 100 mK stage and the other on the mixing chamber plate (< 10 mK)[5]. Since the exact temperature of these resistances is difficult to quantify, it is easiest to lump all of the resistances together at an effective temperature T_ℓ and define the noise as

$$S_{V_\ell}(\omega) = 4k_B \left(T_{sh} R_{sh} + \sum_i T_{p_i} R_{p_i} \right) \equiv 4k_B T_\ell R_\ell. \tag{2.65}$$

This effective temperature can be estimated experimentally from the superconducting state noise, which is discussed in chapter 6. To reference this to the TES input current, we can scale by our current-to-voltage transfer function, or complex admittance.

[5]See Appendix D for details of this design.

$$S_{I_\ell}(\omega) = 4k_B T_\ell R_\ell \left|Y(\omega)\right|^2 \tag{2.66}$$

$$S_{I_\ell}(\omega) = 4k_B T_\ell R_\ell \left| R_\ell + R_0(1+\beta) + i\omega L + \frac{\mathscr{L} R_0(2+\beta)}{(1-\mathscr{L})} \frac{1}{1+i\omega\tau_I} \right|^{-2} \tag{2.67}$$

It is hard to gain much intuition from looking at this expression. Recall that we know the general form complex admittance from Fig. 2.3, so the passive Johnson noise is simply the square of this, scaled by $4k_B T_\ell R_\ell$.

More relevant to us is this noise referenced to input power. This is found quite simply by applying the current responsivity (Eq. 2.50) to Eq. 2.67.

$$S_{P_\ell} = S_{I_\ell} \left| \frac{\partial I}{\partial P}(\omega) \right|^{-2}, \tag{2.68}$$

$$S_{P_\ell} = 4k_B T_\ell R_\ell \left|Z(\omega)\right|^{-2} \left| I_0 \left(1 - \frac{1}{\mathscr{L}}\right) \left(1 + j\omega \frac{\tau}{1-\mathscr{L}}\right) Z(\omega) \right|^{-2}, \tag{2.69}$$

Simplifying, we get the nice compact form of

$$S_{P_\ell} = 4k_B T_\ell R_\ell I_0^2 \frac{(\mathscr{L}-1)^2}{\mathscr{L}^2} (1 + \omega^2 \tau_I^2). \tag{2.70}$$

2.3.2 TES Johnson Noise

The Johnson noise from the TES itself is slightly more complex due to the fact that the TES is a non-linear element. The voltage noise can be written as

$$S_{V_{\mathrm{TES}}} = 4k_B T_0 R_0 \xi(I_0) \tag{2.71}$$

where $\xi(I_0)$ accounts for the non-linearity of the TES. Irwin and Hilton in [81] treated the TES as a quadratic resistor and used a first order Taylor expansion to get $\xi(I_0) \approx (1+2\beta)$. However, for devices with large α, and devices operated very low in the superconducting transition, this expression tents to greatly under predict the Johnson noise [86, 87]. Further attempts to better model the TES Jonhson noise required an understanding of the $I-V$ characteristics in the superconducting transition region. Two common models are discussed in the literature, the resistively shunted junction (RSJ) model [88, 89], and the two-fluid model [90, 91]. The models predict the correction factor to be

$$\xi(I_0) = \begin{cases} 1 + \frac{5}{2}\beta + \frac{3}{2}\beta^2 & \text{RSJ} \\ 1 + 2\beta + \beta^2 & \text{Two-fluid} \end{cases} \tag{2.72}$$

For the time being, we will use the definition derived by Irwin and Hilton for the Johnson noise, but give the others as reference for when measured excess Johnson noise is discussed later. We thus write the TES voltage Johnson noise as

$$S_{V_{\rm TES}} = 4k_B T_0 R_0(1+2\beta). \tag{2.73}$$

To reference this to the TES current is not as simple as the case for the load resistance. This is due to the fact that the voltage-to-current transfer function was derived for an extrinsic source. We now need to re-derive the the transfer function for a noise source originating from the TES. We again follow a similar derivation as done by Irwin. Recall that the Joule power is given by $P_J = IV_{\rm TES}$. From Fig. 2.2, we can use Kirchhoff's voltage law to re-express this as

$$P_J = IV_{\rm TES} = I\left(V_B - IR_\ell - L\frac{dI}{dT}\right). \tag{2.74}$$

For the Johnson noise from the TES, let us consider a small perturbation to the current such that $I- \rightarrow I_0 + \delta I$.

$$P_J \approx (I_0+\delta I)\left(V_B - (I_0+\delta I)R_\ell - L\frac{d(I_0+\delta I)}{dT}\right) \tag{2.75}$$

Note that since this δI term is originating internally, the zero frequency bias voltage is simply $V_B = I_0(R_0+R_\ell)$

$$P_J \approx (I_0+\delta I)\left(I_0(R_0+R_\ell) - (I_0+\delta I)R_\ell - L\frac{d(I_0+\delta I)}{dT}\right) \tag{2.76}$$

$$P_J \approx I_0^2 R_0 + I_0(R_0-R_\ell)\delta I - I_0 L\frac{d\delta I}{dt}. \tag{2.77}$$

Plugging this back into the electrothermal ODE's in Eq. 2.35 and taking the Fourier transform, we get that the inverse of the generalized responsivity matrix becomes

$$\mathbf{M}_{\rm internal} = \begin{pmatrix} \dfrac{1}{\tau_{el}} + i\omega & \dfrac{\mathscr{L}G}{I_0 L} \\ [I_0(R_\ell - R_0) + i\omega L I_0)\,\dfrac{1}{C} & \dfrac{1}{\tau_I} + i\omega \end{pmatrix}. \tag{2.78}$$

Following the same process of before, we can use this to calculate the *internal* complex impedance. After some algebra, we get

$$Y_{\rm internal}(\omega) \equiv [Z_{\rm internal}(\omega)]^{-1} = -\frac{\partial I}{\partial P}(\omega)\, I_0 \frac{1}{\mathscr{L}}(1+i\omega\tau). \tag{2.79}$$

This differs from the external complex impedance derived before by a factor of $(\mathscr{L}-1)$

$$Y_{\text{external}}(\omega) \equiv [Z_{\text{external}}(\omega)]^{-1} = -\frac{\partial I}{\partial P}(\omega)\, I_0 \frac{\mathscr{L}-1}{\mathscr{L}}(1+i\omega\tau). \tag{2.80}$$

We can now express Eq. 2.73 in terms of current using Eq. 2.79

$$S_{I_{\text{TES}}} = 4k_B T_0 R_0 (1+2\beta)\left|Y_{\text{internal}}(\omega)\right|^2 \tag{2.81}$$

$$S_{I_{\text{TES}}} = 4k_B T_0 R_0 (1+2\beta)\frac{I_0^2}{\mathscr{L}^2}(1+\omega^2\tau^2)\left|\frac{\partial I}{\partial P}(\omega)\right|^{-2}. \tag{2.82}$$

Finally, referencing this to input power we get

$$S_{P_{\text{TES}}} = 4k_B T_0 R_0 (1+2\beta)\frac{I_0^2}{\mathscr{L}^2}(1+\omega^2\tau^2). \tag{2.83}$$

2.3.3 Thermal Fluctuation Noise

Our last intrinsic noise source to consider arises from the phonon shot noise across the thermal link between the TES and the thermal bath. This is sometimes also called 'G' noise or thermal fluctuation noise (TFN). We can quickly calculate the power spectral density for the shot noise with a simple back of the envelope estimate. We can write the power spectral density for a shot noise of quantum charge q and average current $\left\langle \dot{Q} \right\rangle$ with[6]

$$J(\omega) = 2q\left\langle \dot{Q} \right\rangle. \tag{2.84}$$

For the case of a micro-calorimeter connected to a thermal bath, the average thermal energy of a phonon will be $k_B T$, and there will be a power flow of $P = GT$ from both the bath to the calorimeter, and the calorimeter to the bath. Thus the power noise will be

$$J(\omega)_{\text{phonon}} = 2k_B T\,(GT + GT) = 4k_B T^2 G. \tag{2.85}$$

There is a key assumption in the above expression, which is that the TES and the thermal bath are at the same temperature. In an ETF TES (as well as many other calorimeters) this is not the case. The non-equilibrium nature of the thermal link connecting the TES to the bath is dependent on the nature of the thermal transport, and is derived in [78, 80] to be

$$F(T_0, T_{\text{bath}}) = \begin{cases} \dfrac{(T_{\text{bath}}/T_0)^{n+1}+1}{2} & \text{Ballistic limit} \\ \dfrac{n}{2n+1}\dfrac{(T_{\text{bath}}/T_0)^{2n+1}-1}{(T_{\text{bath}}/T_0)^{n}-1} & \text{Diffusive limit} \end{cases} \tag{2.86}$$

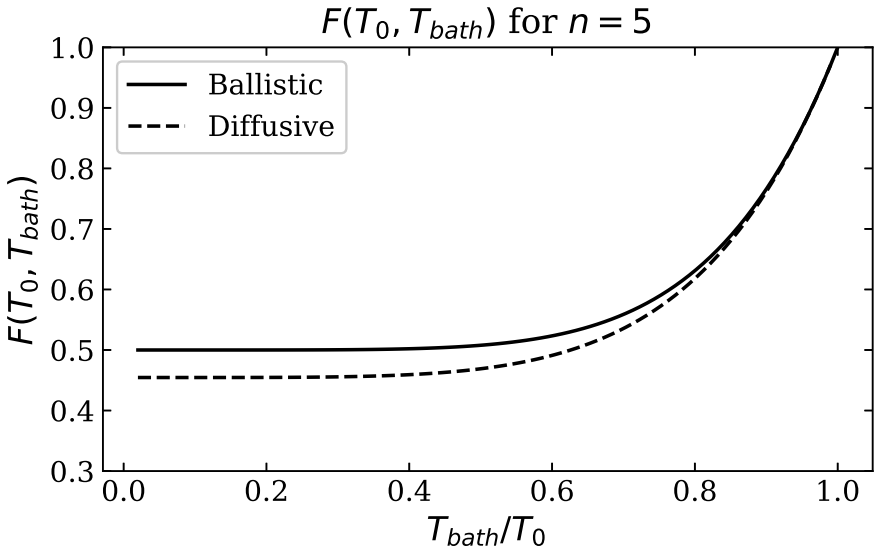

Figure 2.4: Plot of the factor $F(T_0, T_{\text{bath}})$ with $n = 5$, which accounts for the fact that the TES and thermal bath are at different temperatures.

As will be discussed later, for our devices the thermal conductance is limited by electron-phonon coupling and thus $n = 5$. As shown in Fig. 2.4, for both the ballistic and diffusive limits, $F(T_0, T_{\text{bath}}) \approx 0.5$ as long as T_{bath} is less than about $0.75 \times T_0$.

Combining this together we get that the TFN power spectrum is given by

$$S_{P_{\text{TFN}}} = 4k_B T_0^2 G F(T_0, T_{\text{bath}}). \tag{2.87}$$

This can be also be referenced to TES current in the usual way,

$$S_{I_{\text{TFN}}} = 4k_B T_0^2 G F(T_0, T_{\text{bath}}) \left|Y(\omega)\right|^2. \tag{2.88}$$

2.3.4 Electronics Noise

The contributions to the total noise spectrum from the electronics will generally be dependent on the experimental setup. For a well designed system, the noise of the SQUID itself will be the limiting factor in the electronics noise, and thus the electronics noise is often just referred to as the 'SQUID noise'. The noise of a SQUID array can be modeled as the combination of a white component ($S^{\text{white}}_{\text{SQUID}}$) and a $1/f$-like component. This is written as

$$S_{I_{\text{SQUID}}} = \left(S^{\text{white}}_{\text{SQUID}} \left[1 + \left(\frac{\omega_{\text{cut-off}}}{\omega}\right)^{n_{\text{SQUID}}}\right]\right)^2, \tag{2.89}$$

[6]See Ref. [92] for more detail on the subject of shot noise

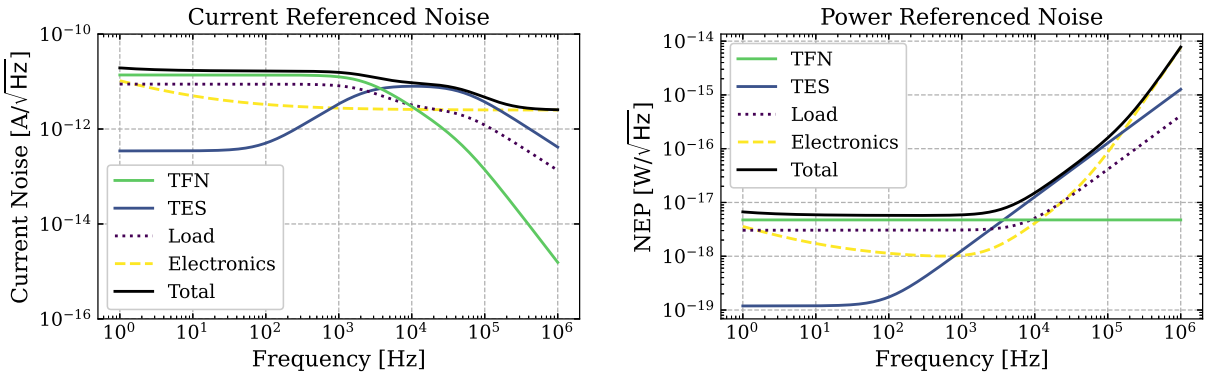

Figure 2.5: Left: Input referred current noise. Right: Input referred power noise, or NEP. Both plots generated using measured values from [84]

where $\omega_{\text{cut-off}}$ is the 'knee' of the $1/f$ component, and n_{SQUID} is the power of the $1/f$ noise and is less than one. As usual, this can be referenced to power space as

$$S_{P_{\text{SQUID}}} = S_{I_{\text{SQUID}}} \left|Z(\omega)\right|^{-2}. \tag{2.90}$$

2.3.5 Total Noise Contribution

Summing all noise sources together we get the expression for the total power referred noise spectrum

$$S_{P_{tot}}(\omega) = S_{P_{TFN}} + S_{V_{TES}} \frac{I_0^2}{\mathscr{L}^2}(1+\omega^2\tau^2) + S_{V_\ell} I_0^2 \frac{(\mathscr{L}-1)^2}{\mathscr{L}^2}\left(1+\omega^2\tau_I^2\right) + \frac{S_{I_{\text{SQUID}}}}{\left|\frac{\partial I}{\partial P}(\omega)\right|^2}. \tag{2.91}$$

It is common to report noise as the square root of the PSD, which would have units of current or power, per square root Hertz. In the case of power referred noise, this is known as the noise equivalent power, or NEP. Plotted in Fig. 2.5 are both current noise and NEP showing the total noise as well as the individual noise components, using measured TES parameters from [84].

2.4 TES based Micro-Calorimeter Energy Resolution

Given that we know the intrinsic noise sources of a TES and understand the dynamics, we can estimate the expected energy resolution. For a known noise and pulse template shape, the optimal resolution is achieved with the 'matched filter', also often called an 'optimum filter' [76, 93].

The expected power pulse shape $p(\omega)$ will depend on the type of detector. If the TES is directly measuring a photon, than the pulse shape will simply be a dirac-delta impulse of energy, with some efficiency factor for absorption. If operated as the sensor in a thermal (athermal) calorimeter, the the pulse shape can be approximated by

$$p(\omega) = \frac{\varepsilon}{1 + i\omega\tau_{ph}}, \tag{2.92}$$

where ε is an efficiency factor accounting for energy losses, and τ_{ph} is the time scale for collecting the thermal (athermal) phonons. The nature of the excitation for our purpose will be athermal phonons as will be discussed in later chapters, but the framework is the same regardless of thermal or athermal excitations.

Using an Optimum Filter with known pulse shape, the theoretical resolution of a TES is given by

$$\sigma^2 = \left[\int_0^\infty \frac{d\omega}{2\pi} \frac{4|p(\omega)|^2}{S_{P_{tot}}(\omega)}\right]^{-1} \tag{2.93}$$

In appendix B I derive that the energy variance for a TES in the presence of a DC parasitic power source is

$$\sigma^2 = \frac{1}{\varepsilon^2} S_{P_{tot}}(0)\left(\tau_{ph} + \tau_*\right) \tag{2.94}$$

where we obtain an effective noise time constant we call 'tau-star' given by

$$\tau_* \approx \tau_{\mathrm{ETF}} \sqrt{\frac{T_\ell}{T_0} \frac{\left(1 - \frac{T_{\mathrm{bath}}^n}{T_0^n}\right)}{nF(T_0, T_{\mathrm{bath}})\left[1 + \frac{S_{P_{\mathrm{par}}}}{S_{P_{TFN}}}\right]}}. \tag{2.95}$$

and the zero frequency noise power is given by where

$$S_{P_{tot}}(0) = S_{P_{\mathrm{TFN}}} + S_{P_{\mathrm{par}}} + \frac{I_0^2}{\mathscr{L}^2}\left(S_{V_{TES}} + S_{V_\ell}\left(\mathscr{L} - 1\right)^2\right). \tag{2.96}$$

It is interesting the note that the addition of an excess TFN-like power noise will actually slightly decrease the effective falltime (giving the appearance of an increased bandwidth). However, this effect on the overall baseline energy variance will be much smaller than the increase in $S_{P_{tot}}(0)$ that an excess TFN-like power noise would add. This false increase in bandwidth can also be used as a diagnostic tool when looking at excess noise.

For the time being, let us ignore τ_{ph}, letting it go to zero. The effects of τ_{ph} will be discussed in great detail in the next chapter. We wish to determine the resolution of energy

absorbed directly by the TES. For this limit we will label the variance as $\sigma^2_{\rm TES}$ to specify that we are not considering τ_{ph}. Let us also make a few further simplifications: We take the large loopgain limit, $\mathscr{L} \gg 1$, assume the parasitic power is negligible, $T_{\rm bath} \ll T_0$, and $R_\ell \ll R_0$, which also implies that the Johnson noise contribution from the load resistance is negligible. Lastly, we assume that the low frequency noise (noise below $1/\tau_{\rm ETF}$) is dominated by TFN. This last point is not only a reasonable assumption, but it is a design criteria in order to maximize the signal to noise for the TES.

In this limit, Eq. B.39 becomes

$$\sigma^2_{\rm TES} \approx \frac{1}{\varepsilon^2} 4 k_B T_0^2 G \tau_{ETF}. \tag{2.97}$$

The ETF time constant in this limit is approximately

$$\tau_{\rm ETF} \approx \frac{C}{G} \frac{\sqrt{n}}{\alpha}. \tag{2.98}$$

Combining these two expression, we get

$$\sigma^2_{\rm TES} \approx \frac{1}{\varepsilon^2} 4 k_B T_0^2 C \frac{\sqrt{n}}{\alpha}. \tag{2.99}$$

Recalling for a metal at cryogenic temperatures, the heat capacity scales as $C \propto V_{\rm TES} T$ Thus the fundamental energy variance of a TES scales like

$$\sigma^2 \propto \frac{V_{\rm TES} T_c^3}{\alpha}. \tag{2.100}$$

This suggests that optimum energy sensitivity is reached with small volume, low-T_c TESs with large α's. We have only considered this resolution from a noise perspective. However, ultimately it is the signal to noise ratio that is most important. We will discuss in the next chapter how to optimize the design for both signal efficiency and noise performance.

Chapter 3

Athermal-phonon Mediated Detector Design

The general detector concepts in this chapter are based on SuperCDMS technology. Much of this chapter can be thought of as an updated understanding of where Noah Kurinsky's thesis left off [77], which itself was a continuation of Matt Pyle's thesis [76]. This chapter will cover the differences between thermal and athermal calorimetry 3.1, quasiparticle trapping 3.2, QET Design 3.3, and optimizing the energy resolution of a QET based athermal phonon sensor 3.4. It is in this latter section that the concept of 'Bandwidth Matching' is discussed.

3.1 Thermal vs Athermal Calorimetry

Now that we have an understanding of the TES calorimeter, we turn our focus towards the design of a full detector using TES sensors. We concluded last chapter with the understanding that the energy variance of an impulse of energy into a TES scales as $\sigma^2_{\text{TES}} \propto V_{\text{TES}} T_c^3$, suggesting that optimal performance is a achieved with small volume TESs. However, the exposure of a rare event search scales with the target volume, meaning a small TES on its own makes a poor DM target.

3.1.1 Thermal Calorimeter

To increase the exposure of the TES calorimeter, it is common to connect the TES to a much larger volume heat capacity, and read out the change in temperature of the absorber, as shown in Fig. 3.1. This significantly increases the overall detector volume, but now presents new issues. If the the TES is reading out the change in equilibrium temperature (thermal phonons), then the energy variance of the detector is actually going to scale as

$$\sigma^2_{\text{det}} \propto C_{\text{absorber}} T_0^2. \tag{3.1}$$

Where C_{absorber} can often be larger than C_{TES}. Despite this setback in resolution, excellent performance can still be achieved due to the temperature dependence of C_{absorber}.

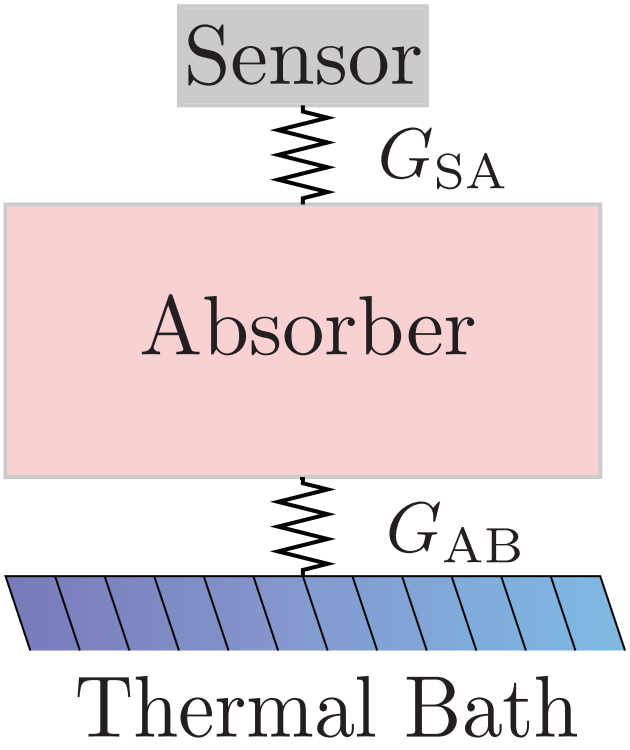

Figure 3.1: Thermal circuit for a thermal or athermal calorimeter

There is still one remaining problem faced by TES based thermal detectors. In a typical experimental setup, the absorber is thermally connected to the bath via an interface of a bulk material. This thermal conductance G_{AB} is referred to as a Kapitza boundary and is described by the acoustic mismatch model [94], thus the thermal conductance scales as $G_{AB} \propto T^3$. A TES is a thin metal film typically $\mathcal{O}(10-100)\,\mathrm{nm}$ thick, often much less than the wavelength of thermal phonons at mK temperatures. Consequently, phonons are being exchanged between the TES and the substrate, and thus the heat transfer is due to electron-phonon (*ep*) coupling [95]. For a thermal conductance described by *ep* coupling, the temperature dependence goes like $G_{SA} \propto T^4$. The problem should now be immediately clear: as the operating temperature is lowered to mK temperatures, the TES will begin to thermally decouple from the absorber.

3.1.2 Athermal Calorimeter

One solution to this thermal decoupling problem is simply to design a sensor that is primarily sensitive to the athermal phonons in the absorber before they thermalize. A cartoon schematic of this can be seen in Fig 3.2. A helpful way to think about this is that now the 'incident particle' we are detecting is no longer the particle interaction in the absorber, but rather the athermal phonon itself. The reason this is beneficial is that now the only heat

capacity to consider is the contribution from the TES, reducing the overall heat capacity by many orders of magnitude. Furthermore, the decrease in thermal conductance between the sensor and the bath G_{SA} with operating temperature is simply a non-issue as we are not concerned with thermal phonons.

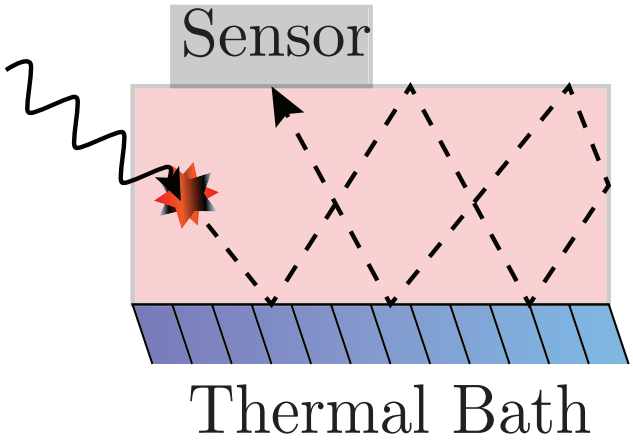

Figure 3.2: Schematic for athermal phonon sensitive calorimeter. The squiggly line represents some kind of incoming particle (photon, DM, etc) and the dashed line is an athermal phonon.

3.2 Quasiparticle Trapping

We now turn to the design of the sensors used in an athermal calorimeter. While a TES can be used, and indeed this is done, the heat capacity can be even further reduced through the use of quasiparticle-trap-assisted electrothermal-feedback TESs, or QETs. A schematic of a QET can be seen in Fig. 3.3. The general idea of quasiparticle (QP) trapping was originally suggested by Normal Booth for use with superconducting tunnel junctions (STJ) [96], and first implemented with TESs by the Cabrera group at Stanford [75, 97]. The process of QP trapping works as follows (refer to Fig. 3.3):

- Two SC materials are placed in contact with each other: one with a larger SC bandgap (Al in our case) and one with a smaller SC bandgap (W TES in our case).
- The large gap material is used to cover a large area of the surface of the absorber substrate, and is electrically connected to the small gap material.

- When an Athermal phonon in the absorber is incident on the large gap material, if it has greater than twice the superconducting bandgap (2Δ), then a cooper-pair is broken into two QPs.
- The QPs diffuse through the large gap material, down-converting into lower energy QPs and phonons.
- If the down-converted phonons have energy greater than 2Δ, more cooper pairs are broken, else they go back into the substrate.
- Eventually the QPs diffuse into the low-gap material, downconverting until they reach the edge of new bandgap and are collected.

Despite the term 'trap' being in the name, for the remainder of this thesis we will reserve the term 'trap' to refer to QPs that get trapped due to some impurity and are never measured, and the term 'collected' to refer to QPs that get trapped in the W/Al overlap region and are measured. As an aside, since we use Al for the high-T_c SC and W for the low-T_c SC (TES), I will henceforth refer to them as Al and W, rather than high-T_c and low-T_c for the remainder of this thesis.

For the case of the QET, the lower gap material is a TES which is biased at its superconducting transition temperature. Recall from BCS theory [98] that the ground state superconducting bandgap at zero temperature is

$$\Delta_0 = 1.76 k_B T_c. \tag{3.2}$$

For a SC at finite temperature, the bandgap has a temperature dependence that goes as

$$\frac{\Delta(T)}{\Delta_0} = 1.74\sqrt{1 - \frac{T}{T_c}}, \tag{3.3}$$

which says that as the operating temperature approaches T_c, the SC bandgap approaches zero (see Fig. 3.4). This reduction in bandgap is due to the fact that at finite temperatures there are thermally excited QPs present, which reduces the number of available states to electron pairs for phonon exchange. In this case, the TES behaves similar to a normal metal, since it will have many thermally excited states. Because of this, the 'collected' QPs strongly interact with the electron system in the TES and thermalize. This makes the final thermalization step in the TES very efficient compared to other technologies like the STJ.

Now that we understand the process of QP trapping, let us consider how this can improve the energy resolution of a TES. Broadly speaking, in order to efficiently absorb an athermal phonon signal from the absorber, a relatively large amount of the surface area of the absorber needs to be instrumented. (Later in this chapter we will discuss in detail exactly how much of the surface needs to be instrumented). From Eq. 2.100 we know the energy resolution depends on the total TES volume, therefor covering a large amount of surface area with TESs is detrimental to the energy resolution. Switching instead to QETs allows for the

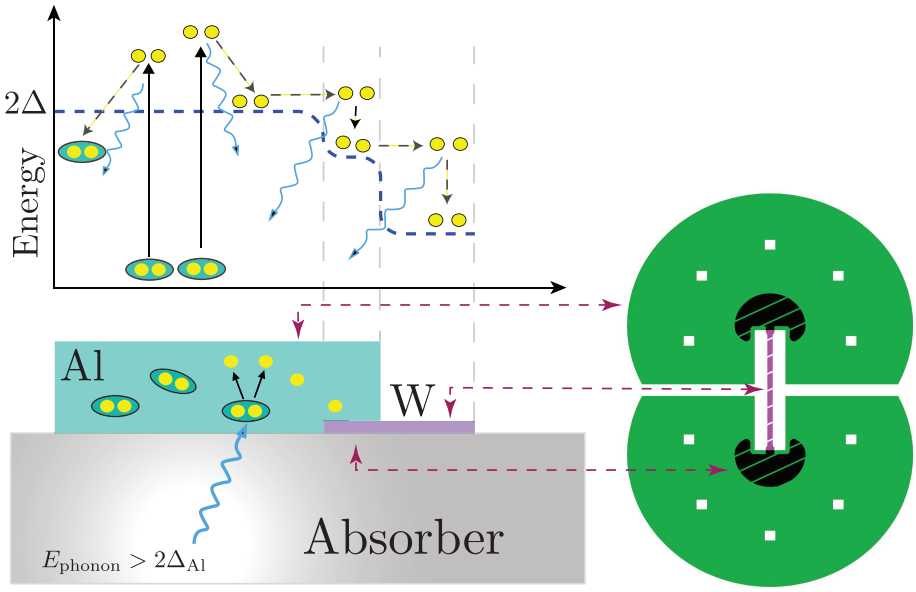

Figure 3.3: Schematic of a QET. The right side of the figure shows the top view (XY-plane) of a QET, and the bottom left shows the side view. The top shows how the band-gaps change for different parts of the QET. The yellow circles represent quasi-particles, while the grouped yellow circles represent cooper-pairs. The QP down-conversion process is shown by the arrows representing QP decay to lower energy and a wavy blue line as the phonon. The left most interaction represents QP down-conversion to sub-gap phonons. The next illustration shows the chain of QP down-conversions for a collected QP pair. Please note that these diagrams are not to scale.

same amount of instrumented surface coverage, but with substantially less amount of TES volume. The reason for this, is that since the high-T_c SC's bandgap is far above the average energy of thermal phonons in the absorber, the high-T_c material doesn't contribute to the overall heat capacity of the sensor. Thus, QETs keep the same sensor coverage, but make the effective TESs orders of magnitude smaller in volume.

3.2.1 Signal Efficiency Losses in QETs

It is clear that there are large reductions in fundamental noise by lowering the TES volume through the use of QETs. However, the QP collection process does introduce some inherent signal efficiency losses. It is now worth discussing the signal flow in a QET in more detail to allocate these sources of signal loss. For this section, we are only considering the QET, not the detector as a whole, i.e. we are starting from the step where a ballistic athermal phonon with energy $E_{phonon} > 2\Delta_{\text{Al}}$ has already broken a cooper-pair in the Al fin. From this point on, the following loss mechanisms occur:

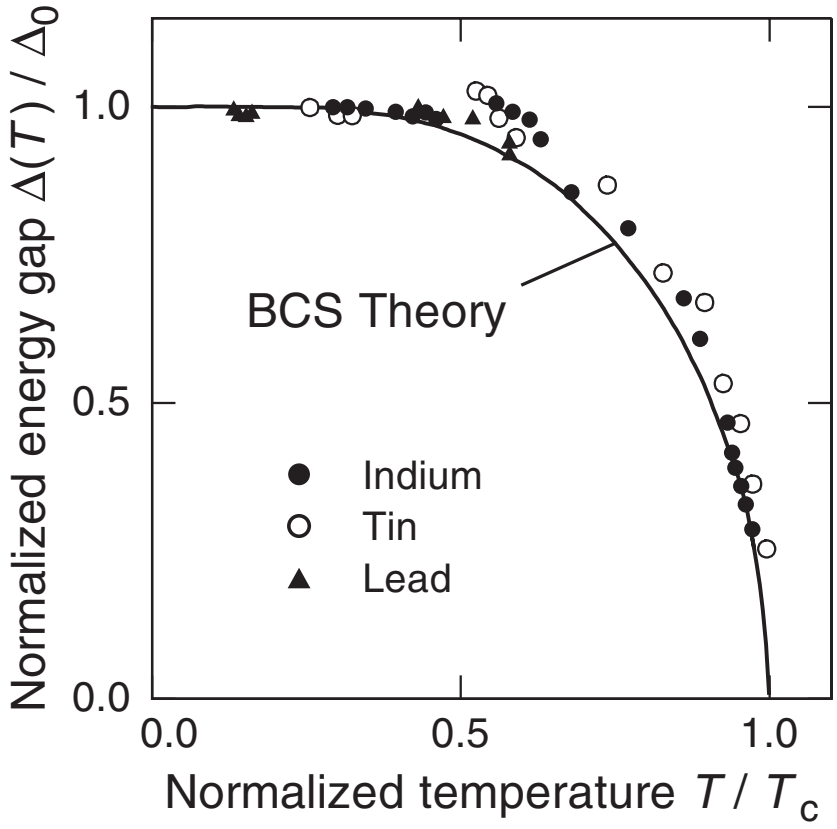

Figure 3.4: Plot of the measured superconducting bandgap Δ as a function of operating temperature T for various SC materials. Also shown is the prediction from BCS theory, given by Eq. 3.3. Figure adapted from Ref. [99]

1. **Phonon to QP population generation efficiency** ($\varepsilon_{\mathrm{QP}}$): An athermal phonon from the substrate enters the the SC fin with energy $\Omega_i \geq 2\Delta_{\mathrm{Al}}$ and breaks cooper-pairs, exciting QPs above the SC bandgap. These QPs then down-convert into lower energy QPs by releasing athermal phonons [100]. If this secondary phonon has energy $\Omega \geq 2\Delta_{\mathrm{Al}}$, another cooper-pair is broken, else the phonon is called a 'sub-gap phonon' and will go back into the substrate. This creates a QP cascade, until all the QPs have relaxed back to the SC bandgap edge. The QP down-conversion process is dependent on the energy of the incident pair-breaking particle (athermal phonon in our case).

   An important parameter to keep track of is the fraction of incident energy that remains in the QP system (rather than the phonon system) η_s as a function of Ω_i. If the initial athermal phonon has energy of $\Omega_i = 2\Delta_{\mathrm{Al}}$, then η_s is approximately unity. This is because the QP's created are already roughly at the band edge and will not undergo down-conversion. If the incident athermal phonon has energy $2\Delta_{\mathrm{Al}} \leq \Omega_i \leq 4\Delta_{\mathrm{Al}}$, η_s

decreases significantly. This happens because for this energy range, during the QP relaxation, the phonon released will have to be sub-gap, and thus not contribute to the QP population. For incident energies above this range, η_s tends to asymptote to a fixed value, this value depends in part on QP lifetimes and above-gap phonon loss mechanisms. A plot of η_s as a function of incident energy can be seen in Fig. 3.5. Since it would be near impossible to design an experiment in which all the athermal phonons were magically right at the SC band edge, we opt to design a detector in which the average athermal phonon energy is greater than at least $10\Delta_{\mathrm{Al}}$, and thus the down-conversion process limits this efficiency to $\varepsilon_{\mathrm{QP}} \approx 0.5 - 0.6$. This process has been modeled by a number of different authors, for more details on QP phonon down-conversion see Refs. [100–107].

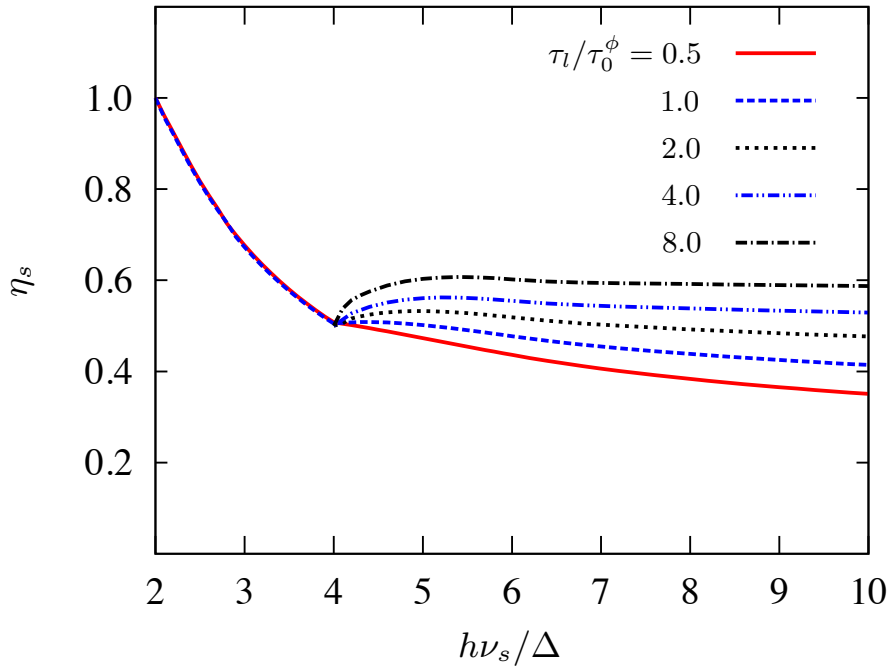

Figure 3.5: Simulated fraction of energy that remains in the QP system in a SC after the down-conversion process is complete as a function of initial energy of incident particle (Shown here as a photon of energy $h\nu_s$). Simulated curves are shown for various values of τ_ℓ/τ_0^ϕ, where τ_0^ϕ is the is the characteristic phonon lifetime and τ_ℓ is the characteristic phonon loss lifetime. Increasing the ratio τ_ℓ/τ_0^ϕ while keeping all other material parameters fixed is equivalent to increasing SC film thickness. Figure taken from [102].

2. **Efficiency of QP collection** (F_c): There is now a population of low energy QPs in the Al which will propagate diffusively through the fin until becoming trapped or

Table 3.1: Description of the tunable QET parameters.

Parameter	Description
ℓ_{TES}	Length of TES
w_{TES}	Width of TES
h_{TES}	Thickness of TES
h_{fin}	Thickness of the Al fin
ℓ_{fin}	Al fin length
ℓ_{overlap}	Length of W/Al overlap
n_{TES}	Total number of TESs/QETs
n_{Fin}	Number of fins in QET

collected. Ideally 100% of the QPs are collected at the W/Al overlap region, but a fraction of the QPs are lost before this is possible by trapping at the surfaces of the fin, QP recombining into cooper-pairs, or trapping in flux vertices. Estimations of these mechanisms must be done with empirically driven semi-analytic models. The precise model would need to depend on many aspects of a given film's quality and design, which would become exceedingly complex. This efficiency factor could really be broken up into two factors. One for the Al only, and one for the diffusion in the Al/W overlap. However no test devices have ever been fabricated to study this effect. Since we expect that the mechanisms are largely the same, it is easier to just lump them together for now.

3. **Thermalization of collected QPs in TES** ($\varepsilon_{\text{QP-TES}}$): Lastly, once the QPs are collected in the W/Al overlap region, they must thermalize in the TES. This process is currently not modeled and has only been back calculated from previous CDMS detector testing.

3.3 QET Design

3.3.1 Anatomy of a QET

The QETs designed for SuperCDMS and SPICE consists of long thin W TESs with an overall elliptical or circular shape [84, 108], divided into a number of fins. Rectangular QETs are also used in the case of the SuperCDMS HVeV detectors [109–111]. A schematic of a typical QET design from a SPICE detector can be seen in Fig. 3.6 (left) and the labeling/description of the various tunable parameters can be seen in Tab. 3.1. The thin purple line is the TES, the black semi-circles are the W/Al overlap regions, and the small purple connectors joining the W/Al overlap to the TES are called the 'fin connectors' (see the right schematic in Fig. 3.6).

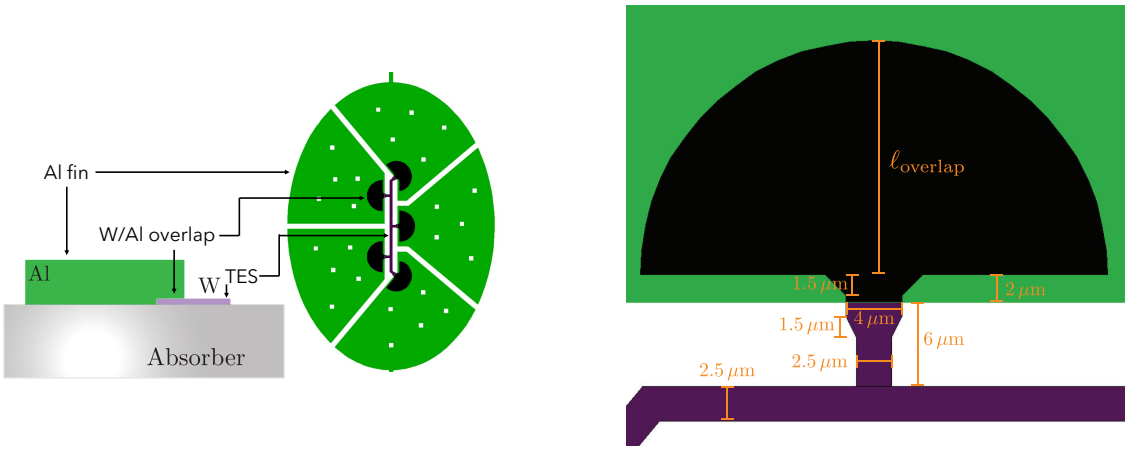

Figure 3.6: Left: Schematic of a typical QET. Right: Dimensions of typical TES fin connector region.

3.3.2 Heat Capacity Contributions of QET

Due to the overlapping W and Al regions of the QET, it is not clear a priori which parts of the W contribute to the overall TES heat capacity. This is due to the proximity effect from the nearby higher-T_c Al effectively raising the bandgap of parts of the W. We expect the TES to be far enough away that it should not be effected by the Al (see section 3.3.5 for more details on what sets this length). We also expect that the proximity effect on the fin connector regions and the W/Al overlap regions to be different. We can split all these terms up to quantify the total effective volume of the TES as

$$V_{eff} = V_{\text{TES}} + \zeta_{\text{W/Al}} V_{\text{W/Al}} + \zeta_{\text{connector}} V_{\text{connector}}, \tag{3.4}$$

where $V_{\text{W/Al}}$ and $V_{\text{connector}}$ are the true volume of the overlap region and the fin connector, and $\zeta_{\text{W/Al}}$ and $\zeta_{\text{connector}}$ are efficiency factors to account for the proximity effect from the Al.

We also introduce a unit-less volume parameter

$$\zeta_T = \frac{V_{\text{TES}}}{V_{eff}}, \tag{3.5}$$

where smaller number indicates that the fin connector and overlap volumes contribute significantly to the heat capacity, and a value of one indicates that only the TES itself contributes.

2017 QP Mask to Study Volume Efficiency Factors

A detector set was designed to measure the efficiency factors $\zeta_{\text{W/Al}}$ and $\zeta_{\text{connector}}$ by former UCB engineer Suhas Ganjam. The series of sensors consisted of an array of W TES lines,

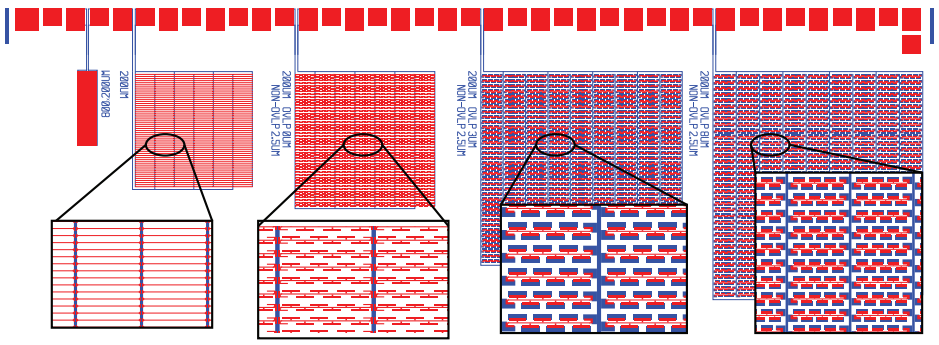

Figure 3.7: Photolithography mask for series of sensors designed to study the effective TES volume for various geometric designs. The red represents W and the blue represents Al. Zoomed in sections of each device are overlaid.

an array of W TES lines with fin connectors added but no Al, and an array of W TES lines with fin connectors and a W/Al overlap region, shown in Fig. 3.7.

By measuring equilibrium bias power as a function of bath temperature, Eq. 2.3 can be fit to extract the thermal conductance normalization factor K. Since the thermal conductance of these W films is dominated by electron-phonon coupling, K is given by

$$K = \Sigma_{ep}^{\mathrm{W}} V_{eff} \tag{3.6}$$

where Σ_{ep}^{W} is the electron-phonon coupling constant. This is a material property (for example it could change for different ratios of α-phase and β-phase W), and we would expect it to be constant for all the devices studied in Fig. 3.7. Measuring K for multiple devices, Eq. 3.4 can then be used to solve for Σ_{ep}^{W}, $\zeta_{\mathrm{W/Al}}$ and $\zeta_{\mathrm{connector}}$. The study found that

$$\Sigma_{ep}^{\mathrm{W}} = 0.25 \times 10^9 \, \frac{\mathrm{W}}{K^5 \mathrm{m}^3} \tag{3.7}$$

$$\zeta_{\mathrm{connector}} = 0.9 \tag{3.8}$$

$$\zeta_{\mathrm{W/Al}} = 0.13. \tag{3.9}$$

Cryogenic PhotoDetector (CPD) Measurement

The Cryogenic PhotoDetector (CPD) described in section 6.2 was also used to bound the effective volume factors. In order to make the detector design simulations match the achieved performance, it was necessary to increase the effective volume factor for the overlap region in the models from 0.13 to 0.45. Combining these two different measurements, we get that

$$\zeta_{\mathrm{connector}} = 0.9 \tag{3.10}$$

$$\zeta_{\mathrm{W/Al}} = 0.13 - 0.45. \tag{3.11}$$

Historically SuperCDMS did not separate these parameters, and treated thier effective sum to be $\zeta = 0.7$ in their designs [76, 77]. It was not clear which part of the fin connector and overlap contribute the most, but it was assumed that the fin connector had a larger effect. However, this new measured non-zero value for $\zeta_{\mathrm{W/Al}}$ means that we pay a sizable heat capacity penalty for large W/Al overlap regions. In the next few subsections, the quasiparticle signal path from Al into the TES, and examples of how design criteria effect this signal flow, will be discussed.

3.3.3 Al Fin Design

The next important parameter to tune is the fin size. In the most simple terms, we will think of this as the length of the fin and the thickness of the fin, we will then add in the complexity of the overall shape of the fin and W/Al overlap region.

From the point of view of absorbing athermal phonons, larger fins make sense, as this would allow for the efficient collection of more signal. However, SC films have a finite diffusion length L_d (average distance QPs travel before recombination) for reasons not well understood. In order to maximize the signal efficiency in the Al fin, the QPs must be collected before they have time to recombine. For a perfect QP absorbing W/Al interface, this suggests that the characteristic length of the Al fins ℓ_{fin} should be roughly equal to the diffusion length. We will see however that in practice this is not necessarily true.

1-D QP Dynamics Study

The diffusion length in Al QET fins was studied by Jeff Yen and the Cabrera group at Stanford [112, 113] with a series of devices shown in Fig. 3.8. Measurements of these devices showed that the diffusion length scaled linearly with the Al film thickness, as shown in Fig. 3.9. The diffusion length was measured to be

$$L_d = 567\, h_{\mathrm{fin}}. \tag{3.12}$$

From this, we see that as a first approximation we should design fins that are

$$\ell_{\mathrm{fin}} \leq L_d \lesssim 567\, h_{\mathrm{fin}}. \tag{3.13}$$

We can think about the collection region, still in 1-D, with a simple diffusion equation

$$\frac{\partial n(x,t)}{\partial t} = D_{\mathrm{Al}} \frac{\partial^2 n(x,t)}{\partial x^2} - \frac{n(x,t)}{\tau_{\mathrm{Al}}} + q\delta(x - x_0)\delta(t - t_0), \tag{3.14}$$

where D_{Al} and τ_{Al} are the QP diffusivity and QP collection time, $q\delta(x - x_0)\delta(t - t_0)$ is a source term, and $n(x,t)$ is the number density of QPs. Using the derivation by Robert Moffatt (see appendix D of [114]), we get that the average collection fraction is given by

$$F_c = \frac{\lambda_d}{\lambda_a/\lambda_d + \coth\left(\frac{1}{\lambda_d}\right)}, \tag{3.15}$$

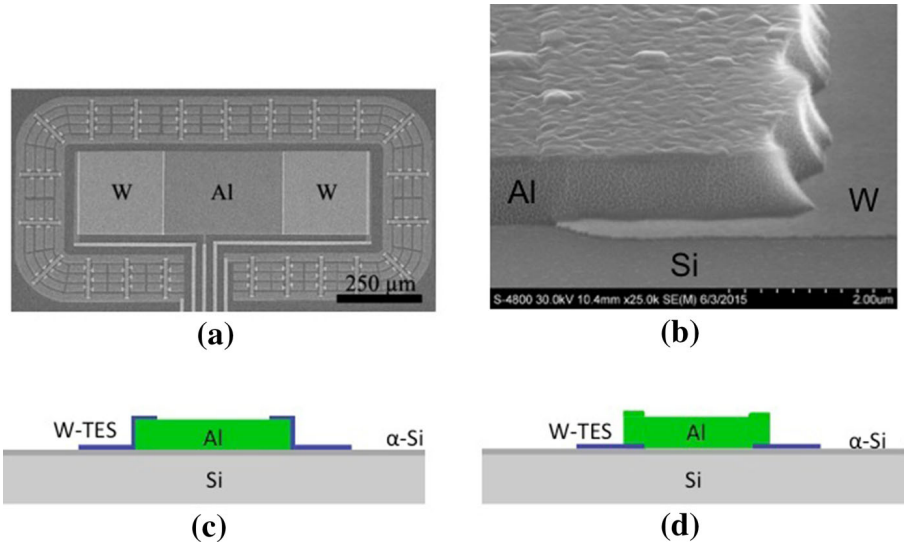

Figure 3.8: Image of device used to study QP transport and collection in W/Al QETs, from [113]. **(a)** A QET test device with W TESs at the ends of an Al film in the center of a ring of QETs used as a veto for substrate events. **(b)** SEM image of fabricated device. **(c)** 'Standard' device geometry. **(d)** 'Inverted' device geometry.

where

$$\lambda_d \equiv \frac{L_d}{\ell_{\text{fin}}} \tag{3.16}$$

$$\lambda_a \equiv \frac{L_a}{\ell_{\text{fin}}} = \frac{D_{\text{Al}}}{\nu_{abs}\ell_{\text{fin}}}, \tag{3.17}$$

and ν_{abs} can be thought of as an effective QP velocity.

We can now express this in terms of QET parameters. Since the study in [112, 113] showed that the diffusion length is limited by film thickness, we can write

$$\lambda_d \approx 567\frac{h_{\text{fin}}}{\ell_{\text{fin}}}. \tag{3.18}$$

We now need to express D_{Al} and ν_{abs} in terms of QET parameters. From the Einstein-Smoluchowski equation, we can express the diffusivity as

$$D_{\text{Al}} = \frac{1}{2}\frac{\lambda^2}{\tau_{QP}} = \frac{1}{2}\lambda v_{QP}, \tag{3.19}$$

where λ is the mean free path for a QP. For thickness limited films, the mean free path can be determined from geometrical constraints. This is a good point to pause and motivate why

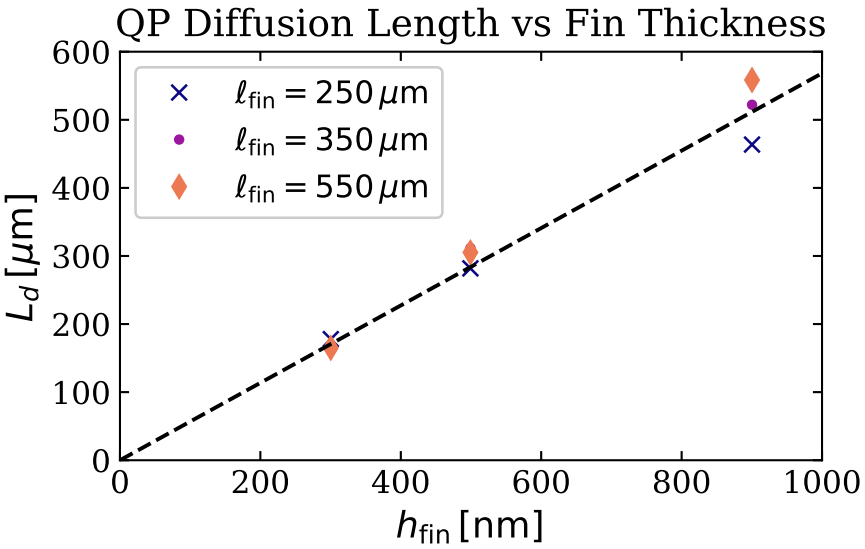

Figure 3.9: Measurement of diffusion Length L_d in Al films as a function of film thickness for 3 different fin lengths. The black dashed line is the linear fit to the data, with the intercept kept fixed at zero. Figure adapted from [113].

we are discussing a 1D (and next 2D) diffusion model for a 3D QET fin. From Ref. [115] the mean free path in a 3D box of length ℓ_{fin}, width w_{fin}, and height h_{fin} is given by

$$\lambda = 4\frac{\text{Volume}}{\text{Surface Area}}. \tag{3.20}$$

It turns out the the geometry in the XY plane is actually relatively unimportant for this parameter in the limit that the dimensions in this plane are much larger than the thickness, i.e. $\ell_{\text{fin}}, w_{\text{fin}} \gg h_{\text{fin}}$. That is to say that the surface area of the faces of the QET fin are much greater than the surface area of the sides of the fin. In this way, we can write

$$\text{Surface Area} = \text{SA}_{\text{sides}} + 2\text{SA}_{\text{single face}} \approx 2\text{SA}_{\text{single face}} \quad (\ell_{\text{fin}}, w_{\text{fin}} \gg h_{\text{fin}}). \tag{3.21}$$

Thus the mean free path is now

$$\lambda \approx 4\frac{h_{\text{fin}}\text{SA}_{\text{single face}}}{2\text{SA}_{\text{single face}}} \approx 2h_{\text{fin}}. \tag{3.22}$$

Plugging in this mean free path we get that

$$D_{\text{Al}} \approx h_{\text{fin}} v_{QP}. \tag{3.23}$$

Next we can characterize the effective QP absorption velocity as

$$\nu_{abs} = v_{QP}\frac{\ell_{\text{overlap}}}{h_{\text{fin}}}p_{abs}, \tag{3.24}$$

where p_{abs} is the probability of absorption happening at the overlap region once it is at the collection site. This probability has been measured to be approximately $p_{abs} \approx 1.22 \times 10^{-4}$. *This is a very small number.* This means that on average, a QP must interact with the W/Al region $\sim 10^4$ times before it will be collected! Finally, we can combine these relations to express λ_a as

$$\lambda_a = \frac{D_{\text{Al}}}{\nu_{abs}\ell_{\text{fin}}} = \frac{h_{\text{fin}}v_{QP}}{\nu_{abs}\ell_{\text{fin}}} = \frac{1}{p_{abs}}\frac{h_{\text{fin}}^2}{\ell_{\text{overlap}}\ell_{\text{fin}}}. \tag{3.25}$$

Lastly, the quantity λ_a/λ_d is

$$\frac{\lambda_a}{\lambda_d} = \frac{1}{567}\frac{1}{p_{abs}}\frac{h_{\text{fin}}}{\ell_{\text{overlap}}}. \tag{3.26}$$

Given the parameterization done in this section, the definitions of λ_a and λ_d also hold for the 2D diffusion model used in the next section! Using this new factorization, the average collection fraction in Eq. 3.15 becomes

$$F_c = \frac{567\frac{h_{\text{fin}}}{\ell_{\text{fin}}}}{\frac{1}{p_{abs}}\frac{1}{567}\frac{h_{\text{fin}}}{\ell_{\text{overlap}}} + \coth\left(\frac{1}{567}\frac{\ell_{\text{fin}}}{h_{\text{fin}}}\right)}. \tag{3.27}$$

A plot of this collection fraction as a function of fin length can be seen in Fig. 3.10 (left). Before moving on, it is useful to examine some limiting cases to gain some intuition. Using any reasonable design parameters for h_{fin} and ℓ_{fin}, our definition of Λ_d can be made much larger than one. As such, we can Taylor expand the $\coth\left(\lambda_d^{-1}\right)$ term in Eq. 3.15. Doing so, we get that

$$F_c \approx \frac{1}{\frac{\lambda_a}{\lambda_d^2} + 1} = \frac{1}{1 + \frac{\ell_{\text{fin}}}{\ell_{\text{overlap}}}\frac{1}{567^2 p_{abs}}}, \quad \lambda_d \gg 1. \tag{3.28}$$

This simplification is plotted against Eq. 3.27 for various fin thickness in Fig. 3.11. In the plot we can see that as long as we are in the thickness-limited QP diffusion limit, the the collection fraction gets asymptotically close to the large λ_d approximation. This implies, that the limiting factor in the QP collection fraction is actually the QP absorption probability p_{abs} at the W/Al interface. Increasing this value will be crucial in improving QET performance.

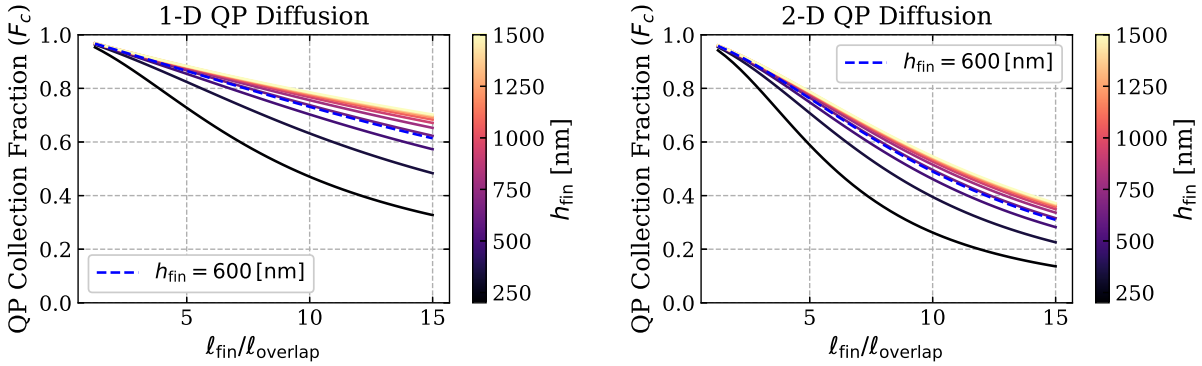

Figure 3.10: Left: QP collection fraction for a 1-D QET model as a function of $\ell_{\text{fin}}/\ell_{\text{overlap}}$ for various film thickness h_{fin} (Eq. 3.27). Right: QP collection fraction for a 2-D QET model as a function of $\ell_{\text{fin}}/\ell_{\text{overlap}}$ for various film thickness h_{fin} (Eq. 3.33). Shown on both figures in dashed blue, is $h_{\text{fin}} = 600\,\text{nm}$, the thickness commonly used on our current devices.

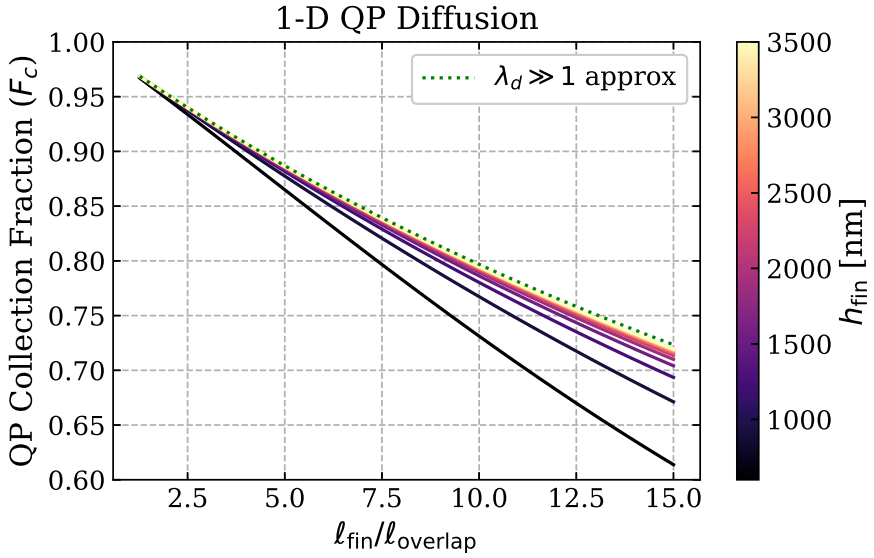

Figure 3.11: QP collection fraction for a 1-D QET model as a function of $\ell_{\text{fin}}/\ell_{\text{overlap}}$ for various film thickness h_{fin}. The green dotted line represents the large λ_d approximation in Eq.3.28.

Figure 3.12: Left: Example of an old CDMSII era QET that can be described by a 1D diffusion model. Figure from [76]. (Blue is Al, pink is W). Right: A more modern elliptical QET design from SPICE that is better modeled with a 2D diffusion model.(Green is Al, purple/black is W)

2-D QP Diffusion

The previous model describes the devices in Fig. 3.8 and Fig. 3.12 (left) very well. However, as can be seen by comparing the two QET's in Fig. 3.12, for a fixed TES length, the elliptical design can effectively instrument more surface area of a detector. This can be seen by noting that on the left and right edges of the CDMSII style QET, these fins will be very ineffective as they are not maximizing the amount of Al the TESs could be connected to.

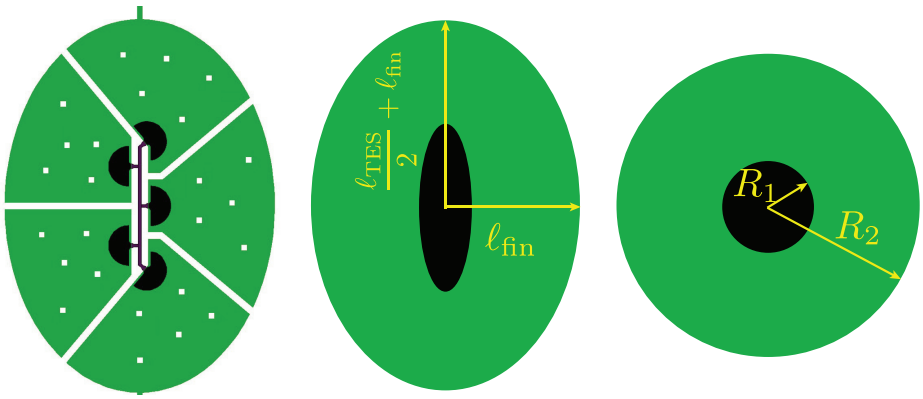

Figure 3.13: Transforming 'elliptical' QET design into two concentric circles to estimate QP collection fraction for elliptical QET design.

To model the QP diffusion in a device like Fig. 3.12 (right), we approximate the QET as two concentric circles as shown in Fig. 3.13. The exact transformation depends on the

details of the design of the QET, but to good approximation, we define the outer radius

$$R_2 = \frac{\text{circumference of ellipse}}{2\pi} \tag{3.29}$$

$$\text{Major Axis} \approx \frac{\ell_{\text{TES}}}{2} + \ell_{\text{fin}} \tag{3.30}$$

$$\text{Minor Axis} \approx \ell_{\text{fin}}. \tag{3.31}$$

The inner radius is more subtle, but for now, we approximate it as

$$R_1 \approx \sqrt{\frac{\text{Area of overlap}}{\pi}}. \tag{3.32}$$

Please note that this definitions of R_1 and R_2 are only shown here for scaling purposes, the actual definitions used in a real device are specific for each design.

As derived in [114], the average QP collection efficiency in a 2D annulus is given by

$$F_c^{2D} = \frac{2\rho_1}{\rho_2^2 - \rho_1^2} \frac{I_1(\rho_2)K_1(\rho_1) - I_1(\rho_1)K_1(\rho_2)}{I_1(\rho_2)\left[K_0(\rho_1) + \lambda_a K_1(\rho_1)\right] + K_1(\rho_2)\left[I_0(\rho_1) - \lambda_a I_1(\rho_1)\right]}. \tag{3.33}$$

where

$$\rho_1 \equiv \frac{R_1}{L_d} \tag{3.34}$$

$$\rho_2 \equiv \frac{R_2}{L_d} \tag{3.35}$$

$$\lambda_a \equiv \frac{L_a}{L_d}. \tag{3.36}$$

A plot of the 2D collection fraction as a function of QET fin length can be seen in Fig. 3.10. As is clear in the figure, the QP collection is worse for the 2D case. This is not surprising, since in the 2D case there is less inner area to collect QP's by a ratio of R_1/R_2. Then one might ask what is the point of going from a 1D design to a 2D design? The answer to this question can be understood by considering that the important design parameter is not the length of the fins, but the total area of the instrumented QET, A_{QET} (or equivalently the area of an individual fin). When the collection fraction for the 1D and 2D cases are plotted as a function of QET area in Fig. 3.14, we can see that the 2D QET design is actually more efficient.

Trapped Magnetic Flux

Although Al is a type 1 superconductor, thin Al films have been shown to transition to an intermediate type superconductor for characteristic sizes of roughly $40\,\mu$m [107]. This means that even though a type 1 SC should not allow magnetic flux, an intermediate type SC is able to develop magnetic flux vortices [98], which would act as a QP trap. This is not something that has been rigorously studied in SuperCDMS, but it is a hypothesis to explain measurements of lower than expected collection efficiencies. As a precaution, holes in the fins have been placed to try to break any continuous regions of the fin to be less than $40\,\mu$m.

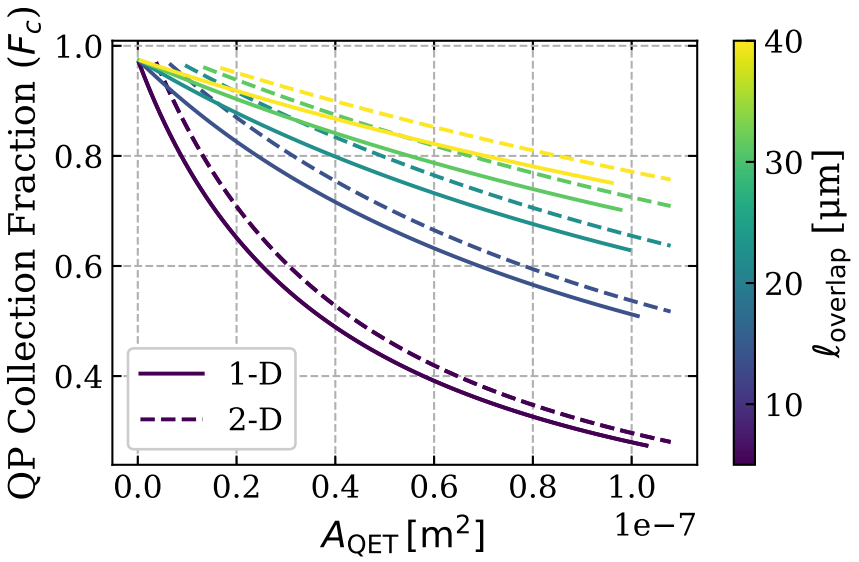

Figure 3.14: QP collection fractions for simplified 1d (solid) and 2d (dashed) QET designs as a function of QET area for various values of ℓ_{overlap}, using $\ell_{\mathrm{TES}} = 100\,\mu$m. The 1D area is estimated as $\sim 2\ell_{\mathrm{fin}}\ell_{\mathrm{TES}}$, and the 2D QET area is estimated as $\sim \pi\ell_{\mathrm{fin}}(\ell_{\mathrm{TES}}/2 + \ell_{\mathrm{fin}})$.

QP Recombination Time

There is one final check we must do regarding the length of the Al fins. In order to efficiently capture the QP's from the initial athermal phonon event, we need to wait for the prompt signal to create the QP cascade of low energy QP's at the band edge. This process typically takes about $\mathcal{O}(1)$ ns [106]. Next, we need to make sure the QP's are collected in the W/Al overlap before we begin losing signal efficiency due to quasiparticle recombination. This recombination time in SC Al films has been measured to be $\mathcal{O}(.1-1)$ ms [116, 117]. We can estimate the time it takes for the QP's to be collected by saying the average time it takes a QP to diffuse a distance ℓ_{fin} can be calculated as

$$\tau_{trap} \approx \frac{\ell_{\mathrm{fin}}^2}{2D_{\mathrm{Al}}}. \tag{3.37}$$

We know from the QP diffusion studies described above that the the diffusion of the Al films we use are limited by thickness, thus the diffusivity can be estimated with

$$D_{\mathrm{Al}} \approx \frac{v_{QP}^{\mathrm{Al}} h_{\mathrm{fin}}}{3}, \tag{3.38}$$

where from BCS theory the QP velocity can be estimated as [118]

$$v_{QP}^{\mathrm{Al}} \approx v_F^{\mathrm{Al}} \sqrt{1 - \left(\frac{\Delta}{\Delta + k_B T}\right)^2}, \tag{3.39}$$

where $v_F^{\mathrm{Al}} = 2.02 \times 10^6\,\mathrm{m/s}$ is the Fermi velocity of Al [119]. Using a fin thickness of $h_{\mathrm{fin}} = 600\,\mathrm{nm}$ and a fin length of $\ell_{\mathrm{fin}} = 100\,\mu\mathrm{m}$, we get that the QP collection should be $\tau_{\mathrm{Al}} \approx \mathcal{O}(100\,\mathrm{ns})$. Thus we are nowhere near the timescales of QP recombination. Also, since the this timescale is many orders of magnitude faster than the ETF-TES time constants that we are concerned with, for the time being we can ignore the QP collection time and simply consider the time between athermal phonon absorption to collected QPs to be instantaneous.

3.3.4 W/Al Overlap Design

In the previous section it was determined that for a given QET area, an elliptical or circular design was most efficient. We now turn to the question of the W/Al overlap design. As a reminder of the optimization trade-off we are trying to solve - we want to have the largest QP collection area possible with only adding minimal heat capacity. In older CDMSII era designs (see Fig. 3.12 left), the amount of overlapping and non-overlapping W was equal. In more modern designs, as seen in QET of the CPDv1 in Fig. 3.15 left, it was found that the important parameter was only the overlapping area. The reason for this is the QP absorption probability at the W/Al interface of $p \approx 10^{-4}$. Since the QP's will have to interact with the interface 10^4 times on average before absorption, the shape of this region is largely unimportant.

The overlap design used in the CPDv1 can be further optimized, as in the case of the SPICE MELANGE QETs in Fig. 3.15 (middle). These designs have pushed the W overlap further into the QET such that almost all of the W area is within the Al fin. Furthermore, as a second-order optimization the 'rectangular' shape of the overlap has shifted to a 'semi-circular' shape. This was done in an attempt to ensure that all trapped QP's had an equal path of travel into the TES, shown by the red arrows in the right side of the figure.

While this design criteria has not yet been systematically studied, the most efficient athermal phonon sensors designed by SuperCDMS have used a design similar to the one in Fig. 3.15 (right) with the HVeV devices [110, 111] achieving total efficiencies of $\gtrsim 29\%$. This measured efficiency is the total athermal phonon collection efficiency, so it is not conclusive that the efficiency gains are due to the overlap region, but it at least suggests the intuition in the design is correct.

Another change that has been implemented in the last few years is the addition of a $2\,\mu\mathrm{m}$ gap between the bottom of the W/Al overlap, and the edge of the Al fin (see right schematic in Fig. 3.15). This is done to account for alignment errors between the different layers in the photolithography processes. With our current fabrication at Texas A&M (TAMU), the alignment of the layers has a $1 - 2\,\mu\mathrm{m}$ uncertainty. This added $2\,\mu\mathrm{m}$ buffer in the design ensures that the overlap will be fully covered by Al. This helps guarantee equal QP collection

efficiency across all fins, but more importantly, if part of the overlap was not covered by Al it would contribute much more substantially to the overall heat capacity.

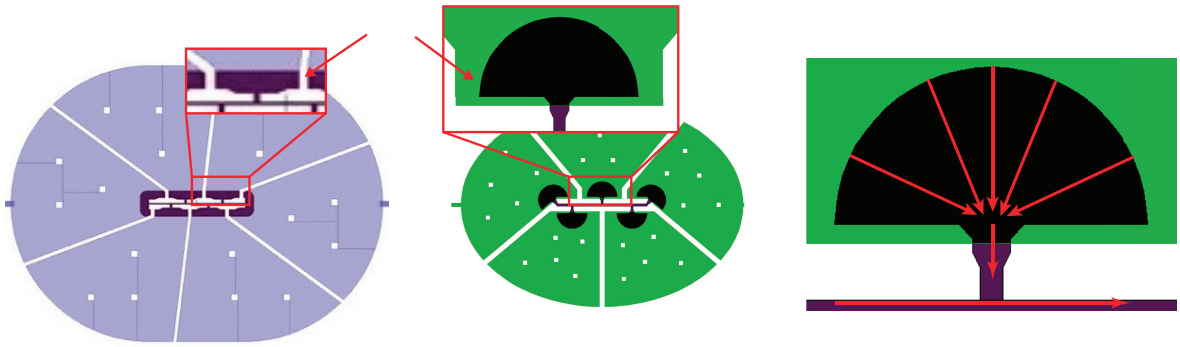

Figure 3.15: Comparison of CPD V1 QET Design (Left) from [84] with SPICE MELANGE 4% QET (Middle). The red arrows on the zoomed in portion of these two QETs points to 'excess' W on the CPD that will only serve to add more W volume to the system without gains in QP collection. Right: Zoomed in version of W/Al overlap of SPICE QET showing QP path to TES (red arrows). For the left figure, light blue is Al, dark blue is W. For middle and right figures, green is Al and back/purple is W.

3.3.5 Design of TES Fin Connector

With the QP's now collected in the W/Al overlap, they need to be efficiently transported into the the TES. Intuitively it would seem like the most efficient transport to the TES would be to have a wide fin connector, as shown in Fig. 3.16 (left). However, the heat capacity from even a single fin connector of this size would be larger than that of the whole TES. The next idea would be to 'funnel' the QP's into the TES with a design like Fig. 3.16 (middle). However, this design also adds a sizable amount of heat capacity. From historical CDMS QET R&D designs, it turns out that a fin connector of the same width of the TES, 2.5 μm is able to efficiently transport QP's while adding the least amount of heat capacity. This concept has been adopted in the design of Fig. 3.16 (right), where the majority of the fin connector is made the same width as the TES, but there has also been a gradual narrowing in two steps.

Another factor in the design of the fin connector is the overall length, separating the fin and the TES. Due to the presence of the high-T_c Al fin, the T_c of the W will be altered at some length scale due to the Longitudinal proximity effect (LoPE) [120], in much the same way that the bandgap of the collection region in the W/Al overlap region is in-between that of of Δ_W and Δ_{Al}[1]. We want to ensure that no part of the TES is proximitized as this will create inhomogeneities in the TES, potentially leading to poor performance and

[1]For a good summary of the proximity effect, see chapter 6 of Paul Brink's thesis [107]

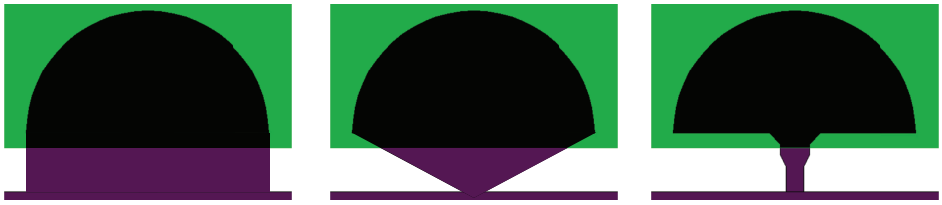

Figure 3.16: Schematic showing conceptual fin connector designs (the purple region connecting the black overlap region to the purple TES). Left: most efficient from QP transport perspective, but poor noise performance. Middle: Idea to 'funnel' QPs to TES, while reducing the W volume of the design on the left. Right: Actual fin connector design from a SPICE QET, where the bulk of the fin connector has been made as narrow as possible, but the funneling concept of the middle idea has been incorporated into the W/Al area part of the connector.

instabilities. The characteristic length scale at which the proximity effect becomes important is the temperature dependent coherence length $\xi(T)$.

A an important parameter for a SC is the ratio of the electron mean-free-path l and the zero temperature coherence length of a pure sample of the material ξ_0, classified as

$$\frac{l}{\xi_0} \gg 1 \quad \rightarrow \quad \text{'Clean Limit'} \tag{3.40}$$

$$\frac{l}{\xi_0} \ll 1 \quad \rightarrow \quad \text{'Dirty Limit'}. \tag{3.41}$$

We can calculate the electron mean-free-path for W from [121]

$$l = \frac{m_e v_F^{\mathrm{W}}}{n_{eff} e^2 \rho_{\mathrm{W}}}, \tag{3.42}$$

Where m_e is the electron mass, v_F^{W} is the Fermi velocity of electrons in W, e is the electron charge, n_{eff} is the effective density of electrons in W, and ρ_{W} is the resistivity of our W films, the values for which can be found in Tab. 3.2. The zero temperature coherence length is given by [98]

$$\xi_0 \approx 0.18 \frac{\hbar v_F}{k_B T_c}. \tag{3.43}$$

Assuming a $T_c \approx 40\,\mathrm{mK}$, we get that $l \approx 10\,\mathrm{nm}$ and $\xi_0 \approx 24\,\mu\mathrm{m}$, thus our films are clearly in the dirty limit. The relevant parameter to us is the temperature dependent coherence

length. In the dirty limit, for temperatures close to T_c, this is given by [122, 123]

$$\xi(T)_{T\to T_c} = 0.85\sqrt{\xi_0 l \left|\frac{T_c}{T_c - T}\right|}. \tag{3.44}$$

A plot of this temperature dependent coherence length can be seen in Fig. 3.17. Since the operating temperature is typically $0.5 - 1\,\mathrm{mK}$ of the transition temperature, this puts the coherence length at about $\xi \approx 3 - 4\,\mu\mathrm{m}$. This means that to ensure that the TES is not proximitized by the Al fin, the fin connectors should be at least $4\,\mu\mathrm{m}$ long. Accounting for up to $2\,\mu\mathrm{m}$ alignment errors, we choose to be conservative in the design, and use a fin connector length of $\ell_{\mathrm{connector}} = 6\,\mu\mathrm{m}$. A measurement of this parameter can be seen in chapter 7.

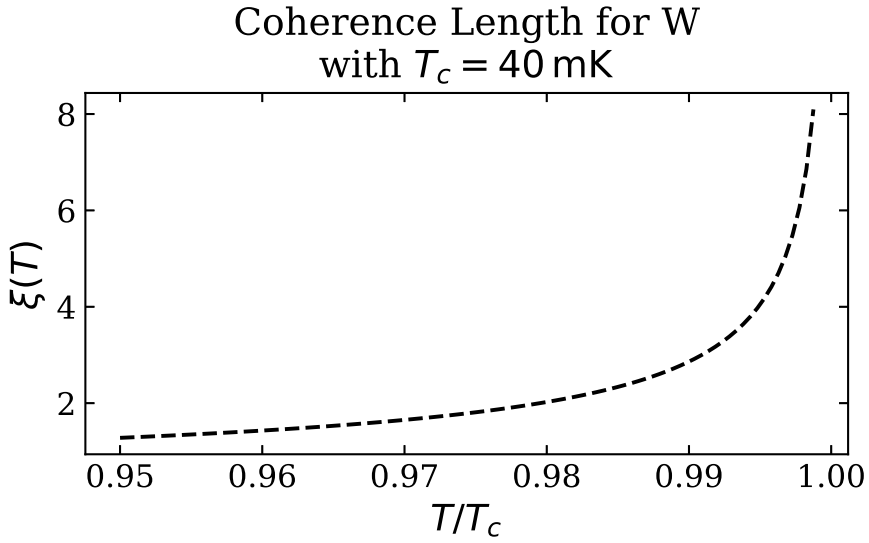

Figure 3.17: Plot of the temperature dependent coherence length near $T \approx T_c$ (Eq. 3.44) for a SC W film with $T_c = 40\,\mathrm{mK}$.

3.3.6 Number of QET Fins

The reader might have noticed that in almost every QET diagram shown thus far, there have been multiple Al Fins and collection areas leading into the TES. There are a number of reasons for doing this. The most simple of which is that in order to apply a voltage across the TES, there needs to be at least two fins. A more precise reasoning to set the number of fins is as follows: At this stage in the signal path, the the QP's have traveled down the fin connector, and need to thermalize in the TES. There are two potential problems here:

Table 3.2: Values for various physical constants there were used in calculations in this chapter.

Symbol	Description	Value
ρ_{W}	Tungsten Resistivity	$9.6 \times 10^{-8}\,[\Omega\mathrm{m}]$
L_0	Lorenz number	$2.44 \times 10^{-8}\,\left[\frac{\mathrm{W}\Omega}{\mathrm{K}^2}\right]$
Σ_{ep}^{W}	Electron-Phonon Coupling Constant	$0.22 \times 10^{9}\,\left[\frac{\mathrm{W}}{\mathrm{K}^5\mathrm{m}^3}\right]$
c_{W}	Specific Heat for Tungsten	$108\,\left[\frac{\mathrm{J}}{\mathrm{K}^2\mathrm{m}^3}\right]$
v_F^{W}	Fermi velocity of electrons in W	$1.35 \times 10^{6}\,[\mathrm{m/s}]$
v_F^{Al}	Fermi velocity of electrons in Al	$2.02 \times 10^{6}\,[\mathrm{m/s}]$
n_{eff}	effective density of electrons in W	$5.49 \times 10^{22}\,\mathrm{cm}^{-3}$
$\langle c_s \rangle_{\mathrm{Si}}$	Average sound speed in Si	$6546\,[\mathrm{m/s}]$
$f_{abs}^{\text{Si-Al}}$	Phonon absorption probability for Si/Al interface	0.9

1. If all the heat transfers into the TES at a single section of the TES, there runs the risk of exceeding the critical current of a small section of the TES, while the remainder of the TES stays in transition. This can cause the TES to become highly non-linear, and degrade performance.

2. There is also the issue that it takes a finite amount of time to thermalize in the TES. We can estimate this time in a similar fashion to the QP absorption time estimate. We already calculated the mean free path of electrons in W to be $l \approx 10\,\mathrm{nm}$, and thus the diffusivity for our W films is $D_{\mathrm{W}} \approx v_F^{\mathrm{W}} l/3 \approx 0.002\,\mathrm{m}^2/s$. This means the average time for QP to diffuse across a TES of length $\ell_{\mathrm{TES}} = 300\,\mu\mathrm{m}$ is $\tau_{\mathrm{thermalize}} = \ell_{\mathrm{TES}}^2/(2D_{\mathrm{W}}) \approx 20\,\mu\mathrm{s}$. As will be seen in the chapter 6, this is similar to the ETF time constant of the TES. This would significantly degrade performance by causing saturation effects at lower energy scales.

Both of these problems can be minimized in the QET design through the use of multiple fins/fin connectors. As can be seen in most of the QET diagrams in this chapter (e.g. Fig. 3.15), the fins are broken up into equal area segments, and the fin connectors are equally distributed across the length of the TES. This limits the possibility of creating 'hot spots' in the TES, and also vastly reduces the thermalization time constant $\tau_{\mathrm{thermalize}}$. As a rule of thumb, we set the number of fins such that the length of TES between QP injection points is $25 - 50\,\mu\mathrm{m}$, which corresponds to $\tau_{\mathrm{thermalize}} \approx 0.1 - 0.5\,\mu\mathrm{s}$, meaning this time constant can effectively be ignored.

There is one final benefit to subdividing the elliptical QET into wedges. The thinner the slices, the more 'one-dimensional' the QP diffusion behaves in the fin. As we saw in Fig. 3.10, all else being equal, for a given fin length, the 1-D diffusion is more efficient.

It is also worth noting that there are downsides to adding more fins. For example, for every 'slice' the QET is divided into, empty area is introduced by separating the Al. This means that QETs with more fins have less active sensor area than equivalent footprint QETs

with less fins. Also, each fin requires a W/Al overlap region as well as a fin connector. Both of these increase the heat capacity of the TES which can limit the baseline energy performance. This implies that smaller QETs will actually benefit from having less fins.

3.3.7 TES Dimensions

After the long journey from athermal phonon to QP's in the Al fin, through the collection region, down the fin connector, we can finally consider the TES! It is now time to decide on the total number of QETs (n_{TES}). There are a number of design criteria that go into this decision, but for now we will simply look at how this parameter depends on the TES properties. For a W TES film, the normal state resistance is given by

$$R_{\mathrm{single}} = \rho_W \frac{\ell_{\mathrm{TES}}}{w_{\mathrm{TES}} h_{\mathrm{TES}}}, \tag{3.45}$$

Where ρ_W is the resistivity for Tungsten. As will soon become clear, we need more than a single TES/QET instrumenting the detector. We connect n_{TES} TESs in parallel, such that the normal state resistance of the full sensor array is given by

$$R_N = \frac{\rho_W}{n_{\mathrm{TES}}} \frac{\ell_{\mathrm{TES}}}{w_{\mathrm{TES}} h_{\mathrm{TES}}}. \tag{3.46}$$

We learned in the previous chapter that the energy resolution of a TES is improved as volume is decreased, thus we want to minimize the quantity $V_{\mathrm{TES}} = \ell_{\mathrm{TES}} w_{\mathrm{TES}} h_{\mathrm{TES}}$. From a signal efficiency perspective, for a fixed TES volume, a long-thin TES is much more efficient than a short-stubby TES. A long-thin TES allows for more Al fin area in contact with the TES for a given volume. As such, w_{TES} and h_{TES} are set to the smallest values that we can consistently fabricate, which are currently $w_{\mathrm{TES}} = 2.5\,\mu\mathrm{m}$ and $h_{\mathrm{TES}} = 40\,\mathrm{nm}$, for a photolithography process. Therefor the number of TESs is determined by

$$n_{\mathrm{TES}} = \frac{\rho_W}{w_{\mathrm{TES}} h_{\mathrm{TES}}} \frac{\ell_{\mathrm{TES}}}{R_N}, \tag{3.47}$$

Where it is really only the ℓ_{TES} and R_N parameters that are practically tunable. Additionally, the normal state resistance has the following constraints:

- ETF criteria: Recall from chapter 2 that for the TESs to be in the extreme negative electrothermal feedback regime, we need $\mathscr{L} \gg 1$ and $R_0 \gg R_\ell$. The loopgain tends to be highest very low in the transition, so we want to operate the TES as low as possible. However, to meet the second requirement, we need to have the operating resistance be much larger than R_ℓ. This ETF condition would suggest large resistances operated very low in their transition are best.

- SQUID Amp Bandwidth: As discussed earlier, the bandwidth of our SQUID feedback amplifier is limited by the 'L/R' time constant. Thus the effective bandwidth of the SQUID amplifier can be increased with a larger R_0.

- TES Johnson Noise: As discussed in section 2.3, the input-power-referred noise PSD of the TES Johnson noise scales as R_0, thus from a noise perspective we want the resistance to be as small as possible.

As will be seen in chapter 6, the optimum TES operating resistance is typically in the range $R_0 \approx 0.2 - 0.5\,R_N$. This means that $0.2R_N \gg R_\ell$, which for the SPICE and SuperCDMS electronics, R_ℓ is about $7 - 15\,\mathrm{m\Omega}$. On the high side, we want to maximize the signal to noise of the readout system, which means we want as low an operating resistance as possible. We will find in the next section on low-surface coverage designs that this upper bound can become problematic for designs with very few TESs. Combining all of these criteria together, we find that the optimum normal resistance for our system should be roughly around $R_n \approx 300 - 400\,\mathrm{m\Omega}$.

The length of the TES has an upper bound set by thermal phase separation. This was introduced in the previous chapter with Eq. 2.63. In light of the QET parameters introduced in this chapter, we can re-express this in more useful terms. As derived in [76], this can be written as

$$\ell_{\max} = \sqrt{\frac{\pi^2 L_0 \zeta_T}{n\Sigma_{ep}^{\mathrm{W}} T_c^{n-2} \rho_{\mathrm{W}} \left[\frac{\alpha}{n}\left(1 - \frac{T_{\mathrm{bath}}^n}{T_c^n}\right) - 1\right]}}, \tag{3.48}$$

Interestingly, this tells us that as we lower T_c, phase separation becomes less of a concern.

3.3.8 QET Summary

Perhaps the most powerful implication of the results of the past few sections, is that since all the QP dynamics are orders of magnitude faster than the characteristic time scales of the ETF-TES, the dynamics of the QET are effectively just that of the bare TES. This is huge, as it allows us to separate the R&D into multiple parallel paths

1. TES dynamics - Sets the bandwidth and and fundamental noise resolution
2. QP dynamics - Controls the signal efficiency

3.4 Optimization of QET based detector

In the last section, we discussed the factors that go into the design of a QET from the perspective of optimizing QP collection within the QET itself. We now discuss the design considerations for a QET based athermal detector as a whole. A schematic of the detection process can be seen in Fig. 3.18. In the previous sections we discussed in detail what happens when an athermal phonon interacts with our QET sensor. We will take a step back and discuss what happens to the phonons in a target after a particle has deposited some energy in it.

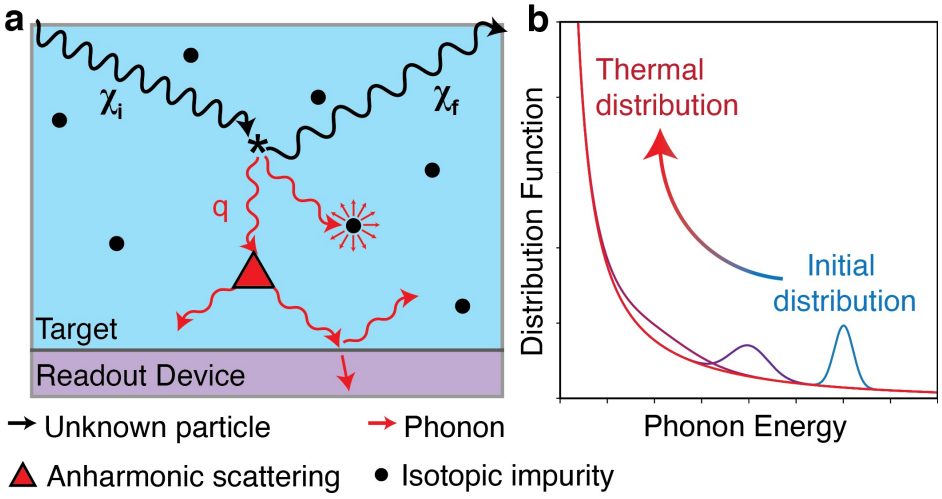

Figure 3.18: Left: Dark matter scattering event in solid state crystal creating an athermal phonon (red arrow) The different decay modes and energy loss mechanisms are shown. Right: Schematic of the phonon distribution as a function of phonon energy. Figure from Ref. [124].

3.4.1 Phonon Lifecycle in Substrate

When an incident particle (DM, photons, etc.) hits the absorber (e.g. Si wafer), depending on the mediating force of the particle, either optical phonons or energetic acoustic phonons are created. These optical phonons quickly decay into the acoustic branch on the order of $10 - 100\,\text{ps}$ [124], which creates a high energy population of acoustic athermal phonons. These phonons propagate quasidiffusively due to their very short mean free path. During this time the phonons are down-converting to lower energy states. As the energy of the phonons lowers, the mean free path increases. Eventually the mean free path of the phonons will be on the order of the size of the detector target, at which point the phonons are considered ballistic, as they will bounce around the detector much like pool balls. These processes continue until the phonons are collected by the instrumented area. There are a few fundamental phonon scattering mechanisms to consider [125]:

1. **Isotopic scattering:** a phonon will scatter when it encounters an impurity in the lattice. This is common even in single species crystals from the different isotopes present. Even relatively pure Si will still contain ^{28}Si, ^{29}Si, and ^{30}Si. This scattering rate is energy dependent,

$$\Gamma_I = R_I \nu^4, \tag{3.49}$$

where ν is the phonon frequency, and R_I is material dependent decay rate constant. For Si, this value has been calculated in terms of the second and third order elastic constants in the isotropic model to be 2.43×10^{-42} [126]. Note that no energy is lost in this process, only the direction of the phonon is changed.

2. **Anharmonic decay:** A phonon will decay into multiple lower energy phonons due to nonlinear terms in the elastic coupling between adjacent lattice ions. This interaction scales as

$$\Gamma_A = R_A \nu^5, \tag{3.50}$$

where R_A is again a material dependent decay rate constant, equal to 7.41×10^{-56} for Si [127].

3. **Surface Effects:** Once the phonons have decayed to low enough energies that isotopic scattering and anharmonic decay rates are negligible, the phonons are fully ballistic and bouncing back and forth from the surfaces of the detector. In an ideal scenario, these surfaces would be perfectly reflective, but in reality this can become a significant loss of energy.

The phonon lifetimes due to each of these processes has been simulated in [124] for GaAs and Si, shown in Fig. 3.19. *Note that these simulations represent a lower bound for the lifetimes due to surface scattering, as they treat surface anharmonic decay and diffusive scattering as the same. In reality, only the surface anharmonic decay would result in a loss of phonon signal.* We can see in the simulation that even for relatively pure targets, at optical phonon energies the phonon scattering is completely dominated by bulk effects (isotopic and anharmonic processes). It is not until the phonons are below 20 meV for Si, that the surface scattering begins to be the limiting process. However, from Ref. [128], the inelastic scattering probability at the edges for Si was measured (see Fig. 3.20) to be roughly 10^{-3}. For a 1 cm cube Si crystal this corresponds to inelastic scattering lifetimes of approximately $\mathcal{O}(10\,\text{ms})$.

The phonons that we are interested in measuring must be ballistic, and above twice the Al superconducting bandgap. We can however still technically detect these subgap phonons by direct absorption into the W TES (as it essentially has a no gap when biased at T_c). However, due to the incredibly low amount of TES-only coverage on the detectors, this timescale will be very long, and thus it is highly unlikely to be able to efficiently collect all this subgap energy. We can estimate how much of the energy will be ballistic and above $2\Delta_{\text{Al}}$ with a back of the envelope calculation done by Matt Pyle [76], and will call this efficiency factor $\varepsilon_{\text{ballistic}}$. Ignoring effects from surfaces, we get

$$\varepsilon_{\text{ballistic}} \approx 1 - \frac{(2\Delta_{\text{Al}})^4}{E_{\text{ballistic}}^4}. \tag{3.51}$$

$E_{\text{ballistic}}$ is the ballistic energy cutoff, which is approximately 3 meV for Si [129], meaning that for Si $\varepsilon_{\text{ballistic}} \gtrsim 99\%$ of the ballistic phonons will be above gap.

One thing worth nothing, once the phonons have gone ballistic, essentially all position information from the original event will be lost. For past SuperCDMS devices, position reconstruction was important to them. For us, we are primarily concerned with energy sensitivity and thus losing position information is fine.

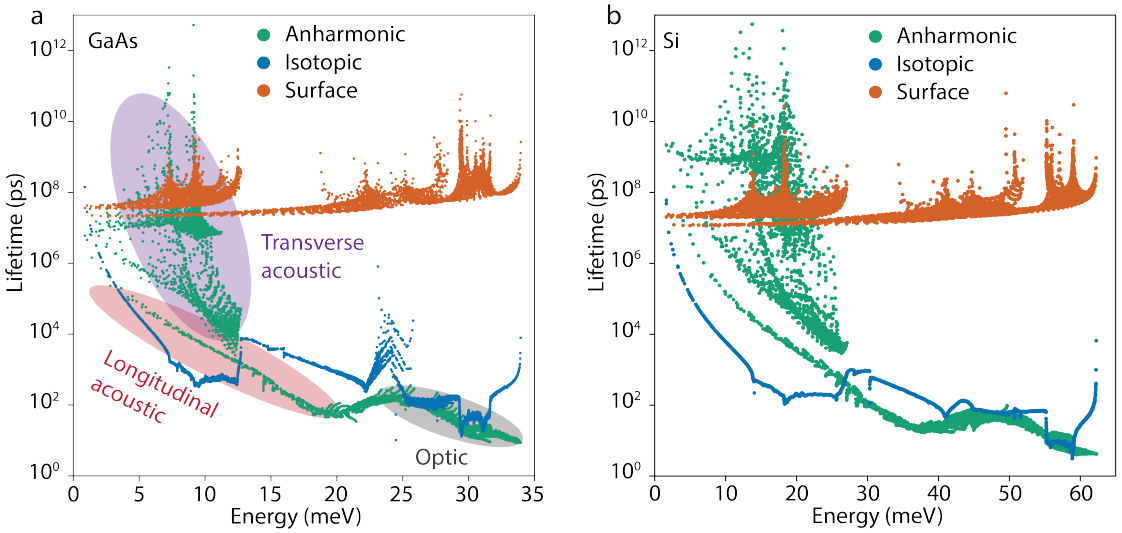

Figure 3.19: Simulations of Isotopic, Anharmonic, and Surface scattering for 1 cm cubic GaAs (left) and Si (right) crystals. The isotopic makeup of the substrates for the simulation was (92.2% ^{28}Si, 4.7% ^{29}Si, 3.1% ^{30}Si, and 60.1% ^{60}Ga, 39.9% ^{71}Ga). Note that these simulations represent a lower bound for the lifetimes due to surface scattering, as they treat surface anharmonic decay and diffusive scattering as the same. Figure from [124].

3.4.2 Athermal Phonon Absorption

Once the phonons are fully ballistic in the target, we need to absorb them in an instrumented part of the detector (active). Unfortunately there are surfaces on the detector that can also absorb phonons that are not able to measure the energy (passive) e.g. bias rails, wirebonding pads, etc. This efficiency penalty is easily calculated as

$$\varepsilon_{\text{passive}} = \frac{A_{\text{active}}}{A_{\text{active}} + A_{\text{passive}}}, \tag{3.52}$$

where A_{active} and A_{passive} are the areas of the QET fins and area of all non-instrumented phonon absorptive surfaces in contact with the substrate.

Athermal Phonon Collection Time

To get an estimate of the characteristic timescale that athermal phonons are collected by our sensors, we can use similar logic to sound waves in a large room. We can use a simple derivation first done by W. Sabine to understand reverberation times in lecture halls [130, 131]. At the core of Sabine's model is the *diffuse field approximation*, which assumes that the sound energy density is spatially uniform and there is isotropic distribution of its flow in all directions. We can ask how valid is this for our phonon model? For even a low energy

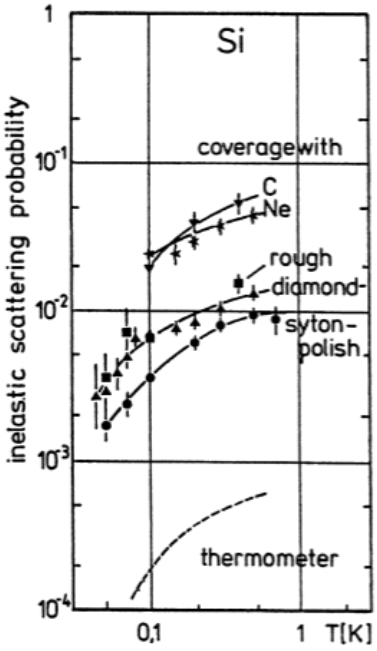

Figure 3.20: Measurement of inelastic scattering probability at Si crystal surfaces for various surface treatments. Figure from Ref. [128].

event that excites an optical-phonon in Si, this will downconvert within pico-seconds to $\mathcal{O}(10-100)$ of acoustic phonons that will travel isotropically in the crystal. By the time these acoustic phonons have bounced off the edges of the detector a few times, their energy can be approximated as uniform throughout the volume.

Let us assume that this energy density U_a is uniform in a volume V with a total surface area of S. From conservation of energy, we can write

$$\frac{\partial}{\partial t}\int_V U_a dV + \int_S \vec{I}\cdot\vec{n}dS = P \tag{3.53}$$

where P is the power of the localized source, $\vec{I}$ is the intensity, and $\vec{n}$ is the normal vector from surface S. At some arbitrary time, we let $P = 0$, and since U_a is spatially uniform, the equation becomes

$$\frac{\partial U_a}{\partial t}V = -\int_S \vec{I}\cdot\vec{n}dS \tag{3.54}$$

$$\frac{\partial U_a}{\partial t}V = -\int_S |I|\cos(\theta)dS \tag{3.55}$$

$$\frac{\partial U_a}{\partial t}V = -\int_S U_a c_s\cos(\theta)dS \tag{3.56}$$

$$\tag{3.57}$$

where c_s is the speed of sound, and θ is the angle between the normal vector $\hat{n}$ and the surface S. Averaging the intensity integral over the full solid angle 4π

$$\int_S U_a c_s\cos(\theta)dS = \frac{U_a c_s}{4\pi}\int_0^{\frac{\pi}{2}} d\phi\int_0^{2\pi}\cos(\theta)\sin(\theta)d\theta \tag{3.58}$$

$$= \frac{U_a c_s}{2}\left.\frac{\sin^2(\theta)}{2}\right|_0^{\frac{\pi}{2}} \tag{3.59}$$

$$= \frac{U_a c_s}{4}. \tag{3.60}$$

Plugging this back into Eq. 3.57, we get

$$\frac{\partial U_a(t)}{\partial t}V = -\frac{U_a(t)c_s}{4}. \tag{3.61}$$

This is a separable ODE with the solution

$$U_a(t) = U_i e^{-\frac{t}{\tau_a}} \tag{3.62}$$

where $\tau_a = 4V/Sc_s$. In a physical room, only a certain fraction of the surfaces will absorb sound. S must be replaced by the total area of absorptive surfaces, A_{absorb}. In the field of acoustics, this is quantified as $A_{\text{absorb}} = \sum_i \alpha_i A_i$, where α_i is the coefficient of absorption of a material i, and A_i is the corresponding area. In our model of athermal phonon absorption, we assume that all bare surfaces are perfectly reflective and only the W and Al surfaces absorb phonons. Our absorptive area is thus

$$A_{\text{absorb}} = f_{abs}^{\text{Al}}A_{\text{Al}} + f_{abs}^{\text{W}}A_{\text{W}}, \tag{3.63}$$

where f_{abs} accounts for the probability of reflection due to the acoustic mismatch between the Al (or W) and the substrate [132]. Putting this all together, we get that the characteristic timescale for athermal phonon absorption is

$$\tau_{\text{collect}} = \frac{4V_{\text{absorber}}}{\langle c_s\rangle\left(f_{abs}^{\text{Al}}A_{\text{Al}} + f_{abs}^{\text{W}}A_{\text{W}}\right)} \approx \frac{4V_{\text{absorber}}}{\langle c_s\rangle f_{abs}^{\text{Al}}A_{\text{Al}}}, \tag{3.64}$$

where we now use $\langle c_s \rangle$ rather than c_s because the the sound speed in crystal will be directional, unlike in air. We also note that since $A_{\mathrm{Al}} \gg A_{\mathrm{W}}$, we can largely ignore this term.

It is also worth noting that in this derivation, we assumed that all the energy in the diffuse field was above twice the Al SC bandgap. There however will be some component of the energy that is below this bandgap, yet still above the W bandgap (which is effectively zero since it is biased at T_c). A more accurate solution to Eq. 3.57 would be

$$U_a(t) = U_i e^{-\frac{t}{\tau_a}} + U_i^{\text{sub-gap}} e^{-\frac{t}{\tau_{\text{sub-gap}}}}. \tag{3.65}$$

where $\tau_{\text{sub-gap}}$ is the time-scale of absorption of only the acoustic energy below that of Δ_{Al}.

$$\tau_{\text{sub-gap}} = \frac{4V_{\text{absorber}}}{\langle c_s \rangle f_{abs}^{\mathrm{W}} A_{\mathrm{W}}}. \tag{3.66}$$

This second time constant is sometimes seen in our detectors, specifically in the CPDv1, which is discussed in section 6.2.5. However since typically such little amounts of energy are in this population of phonons, for design purposes we consider only the primary athermal phonon collection time constant given by Eq. 3.64.

The above derivation assumes that the boundaries of the crystal are perfectly reflective and the crystals are pure. However, this neglects the fact that the ballistic phonon lifetime due to bare-surface down-conversion (τ_{BS}) is finite. The true phonon collection time is thus

$$\frac{1}{\tau_{ph}} = \frac{1}{\tau_{\mathrm{BS}}} + \frac{1}{\tau_{\text{collect}}}. \tag{3.67}$$

In the limit that the lifetime of the ballistic phonons was much shorter than the designed collection time (due to surface losses), there should also be a decrease in the signal strength. This efficiency factor can be estimated as the ratio of the ballistic phonon lifetime vs the combined lifetime and collection time

$$f_c^{\text{phonon}} = \frac{\tau_{\mathrm{BS}}}{\tau_{\mathrm{BS}} + \tau_{\text{collect}}}. \tag{3.68}$$

In the limit that the phonon lifetime is infinitely long lived, then we collect all the phonons in τ_{collect} and the collection fraction is 1.

Finally, considering the phonon pulse in the frequency domain, the normalized athermal phonon signal can be approximated as

$$p(\omega) = \frac{1}{1 + i\omega\tau_{ph}}. \tag{3.69}$$

As will be discussed in the next chapter, by designing multiple detectors with varying τ_{collect}'s, one can measure τ_{BS}.

Table 3.3: Description of the various efficiency losses in a QET based athermal sensitive particle detector.

Symbol	Description	Definition/Value
$\varepsilon_{\text{ballistic}}$	Population of ballistic phonons with energy above $2\Delta_{\text{Al}}$	Eq. 3.51
f_c^{phonon}	Fraction of ballistic phonons collected before ballistic phonon lifetime	Eq. 3.68
$\varepsilon_{\text{passive}}$	Fraction of phonons absorbed by active instrumented surfaces	Eq. 3.52
ε_{QP}	Percentage of athermal energy in Al fins that remains in the low-energy QP system	$\sim 62\%$
F_c	Fraction of QP's in the Al fin collected at the W/Al overlap	Eq. 3.33
$\varepsilon_{\text{QP-TES}}$	Percentage of collected QP's thermalized in the TES	$\sim 60\%$
ε	Absolute athermal phonon collection efficiency	Eq. 3.70

3.4.3 Total Athermal phonon Collection Efficiency

All of these energy loss terms described in the last few section are combined into a single efficiency factor, referred to as the absolute athermal phonon collection efficiency

$$\varepsilon = \varepsilon_{\text{ballistic}} \times f_c^{\text{phonon}} \times \varepsilon_{\text{passive}} \times \varepsilon_{\text{QP}} \times F_c \times \varepsilon_{\text{QP-TES}}. \tag{3.70}$$

A summary of all the efficiency factors can be found in Tab. 3.3. As discussed in the relevant above sections, some of these individual efficiencies can be measured with specific R&D sensors, however for a full DM detector, only the total absolute athermal phonon collection efficiency is measurable. This efficiency is trivially measured by calculating the energy removed by the TESs via ETF with Eq. 2.62 for events with a known energy (e.g. from a radioactive calibration source), and dividing this by the known energy of the events. See section 6.2.5 for an example of this.

3.4.4 QET Layout

In general, in order to minimize the effects of local QET saturation and positional dependence, the QETs are laid out homogeneously on either one or two surfaces of the substrate as shown in Fig. 3.21. In an effort to reduce some of the passive Al that this layout scheme adds, different layouts are explored in chapter 4.

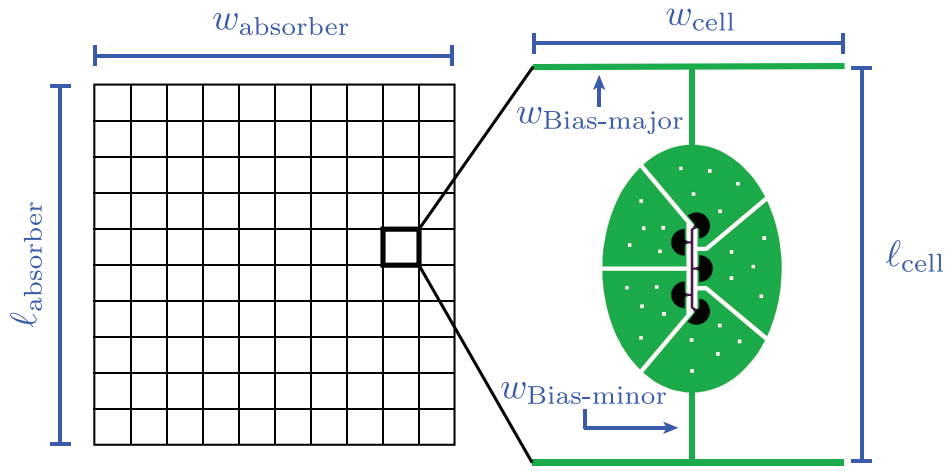

Figure 3.21: Left: Schematic of division of surface of detector of dimension ℓ_{absorber} by w_{absorber} into cells. Right: Zoom in on QET unit cell of dimension ℓ_{cell} by w_{cell}, showing the major and minor bias rails.

3.4.5 Bandwidth Matching

With and understanding of how the TES and QET parameters correspond to physical design parameters, we can now return to Eq. 2.94 to understand how the energy resolution of a full athermal phonon detector scales. This section will be making approximations for the reader to gain intuition. Note that none of these approximations are made in the design of the detectors in the next chapter.

Low Frequency Noise

We first consider the low frequency noise in the absence of parasitic power noise.

$$S_{P_{\text{tot}}}(0) = S_{P_{\text{TFN}}} + \frac{I_0^2}{\mathscr{L}^2} S_{V_{TES}} + S_{V_\ell} \frac{I_0^2}{\mathscr{L}^2} \left(\mathscr{L} - 1\right)^2 + S_{P_{\text{SQUID}}}. \tag{3.71}$$

For good performance, we require a device with large temperature sensitivity, or equivalently a large loopgain. This large loopgain will serve to suppress the low frequency TES Johnson noise. The Johnson noise from the load resistance can be neglected because in practice R_ℓ can always be designed to be much less than R_0. The shunt resistance and the TES side parasitic resistance can be made incredibly small ($\sim$ a few mΩ each) and be cooled to temperatures of $\sim T_0$ if needed. Lastly, we can neglect the SQUID noise, because again, in practice, a modern SQUID amplifier can be made to have a lower input noise than our TES arrays. Combining all of these assumptions, we are left with the low frequency noise of an ideal device being limited only by the TFN,

$$S_{P_{\rm tot}}(0) \approx S_{P_{\rm TFN}} = 4k_B T_0^2 G F(T_0, T_{\rm bath}). \tag{3.72}$$

From here on out, let us simply write $F(T_0, T_{\rm bath})$ as F to save space. We can re-write the thermal conductance in Eq. 2.4 using the fact that this conductance will be limited by electron-phonon coupling as

$$G = nKT^{n-1} = n\Sigma_{ep}^{\rm W} V_{eff}^{\rm total} T^{n-1}. \tag{3.73}$$

Where $V_{eff}^{\rm total}$ is the total effective volume for TESs on the detector. Inserting this into our noise expression, we get

$$S_{P_{\rm tot}}(0) \approx 4nk_B F \Sigma_{ep}^{\rm W} V_{eff}^{\rm total} T^{n+1}. \tag{3.74}$$

Combining Eq. 3.4 with the knowledge gained in the last few sections, the volume of the TES can be written as

$$V_{eff}^{\rm total} = n_{\rm TES} V_{eff} = n_{\rm TES} h_{\rm TES} \left[\ell_{\rm TES} w_{\rm TES} + n_{\rm fin}\left(\zeta_{\rm W/Al} A_{\rm W/Al} + \zeta_{\rm connector} A_{\rm connector}\right)\right], \tag{3.75}$$

where $A_{\rm W/Al}/A_{\rm connector}$ is referring to the surface area of a single overlap/fin connector.

Finally, the NEP for a TFN limited TES based detector is

$$S_{P_{\rm tot}}(0) \approx n4Fk_B n_{\rm TES} \Sigma_{ep}^{\rm W} T^{n+1} h_{\rm TES} \left[\ell_{\rm TES} w_{\rm TES} + n_{\rm fin}\left(\zeta_{\rm W/Al} A_{\rm W/Al} + \zeta_{\rm connector} A_{\rm connector}\right)\right]. \tag{3.76}$$

Active and Passive Aluminum

Lets now turn to the time constant τ_{ph}. For the sake of argument, let us assume that we are using a target in which the phonon ballistic lifetime $\tau_{\rm BS}$ is infinite, or at least large compared with $\tau_{\rm collect}$ and thus $\tau_{ph} \approx \tau_{\rm collect}$. In theory, this condition can be made true with a pure crystal, well polished or cleaved edges [133–135], and a decreased characteristic size[2]. From Eq. 3.64,

$$\tau_{ph} \approx \tau_{\rm collect} = \frac{4V_{\rm absorber}}{\langle c_s \rangle A_{\rm Al} f_{abs}}. \tag{3.77}$$

We now need to quantify the area of phonon absorbing surfaces $A_{\rm Al}$. For simplicity we will approximate the area a single QET as

$$A_{\rm QET} \approx \pi \ell_{\rm fin}\left(\ell_{\rm fin} + \frac{\ell_{\rm TES}}{2}\right). \tag{3.78}$$

[2]We will discuss the practical validity of this assumption in the next chapter.

This is a slight overestimate of the QET area, as we are not subtracting out the empty spaces in the QET. To estimate the area of the passive Al, let us assume that the instrumented face of the absorber is a square with $w_{\text{absorber}} = \ell_{\text{absorber}}$. We also assume that we are only instrumenting a single face. Then divide the area of the instrumented face into n_{TES} cells, which we will call the 'QET unit cell' with area A_{cell} given by

$$A_{\text{cell}} = \frac{\ell_{\text{absorber}} w_{\text{absorber}}}{n_{\text{TES}}} = \frac{\ell^2_{\text{absorber}}}{n_{\text{TES}}}, \tag{3.79}$$

and the length is

$$\ell_{\text{cell}} = w_{\text{cell}} = \sqrt{A_{\text{cell}}} = \frac{\ell_{\text{absorber}}}{\sqrt{n_{\text{TES}}}}. \tag{3.80}$$

Each one of these unit cells is connected with a grid of bias rails. We define the inter-cell bias rails to be of thickness $w_{\text{Bias-major}}$, and the intra-cell rails that connect the QET to the major bias rails to be of thickness $w_{\text{Bias-minor}}$.

The area of Al due to the major rail is

$$\begin{aligned} A_{\text{Bais-major}} &= w_{\text{Bais-major}} w_{\text{cell}} n_{\text{rows}} n_{\text{columns}} && (3.81)\\ &= w_{\text{Bais-major}} w_{\text{cell}} n_{\text{TES}} && (3.82)\\ &= w_{\text{Bais-major}} \ell_{\text{absorber}} \sqrt{n_{\text{TES}}}. && (3.83) \end{aligned}$$

Noting the fact that $n_{\text{rows}} = n_{\text{columns}} = \sqrt{n_{\text{TES}}}$.

The Al area from the minor rails is given by

$$\begin{aligned} A_{\text{Bais-minor}} &= w_{\text{Bais-minor}} \left[\ell_{\text{cell}} - (2\ell_{\text{fin}} + \ell_{\text{TES}})\right] n_{\text{rows}} n_{\text{columns}} && (3.84)\\ &= w_{\text{Bais-minor}} \left[\ell_{\text{cell}} - (2\ell_{\text{fin}} + \ell_{\text{TES}})\right] n_{\text{TES}} && (3.85)\\ &= w_{\text{Bais-minor}} \left[\frac{\ell_{\text{absorber}}}{\sqrt{n_{\text{TES}}}} - (2\ell_{\text{fin}} + \ell_{\text{TES}})\right] n_{\text{TES}} && (3.86)\\ &= w_{\text{Bais-minor}} \left[\ell_{\text{absorber}} \sqrt{n_{\text{TES}}} - (2\ell_{\text{fin}} + \ell_{\text{TES}}) n_{\text{TES}}\right]. && (3.87) \end{aligned}$$

There are also contributions to the passive aluminum from the wirebonding pads, and phonon loss from physically holding the detector in place in the housing, but these effects can be made significantly small and thus we can neglect them for now. Combining all the areas, we have

$$A_{\text{Al}} = A_{\text{Active}} + A_{\text{Passive}} \tag{3.88}$$

where

$$\begin{aligned} A_{\text{Active}} &= n_{\text{TES}} A_{\text{QET}} && (3.89)\\ &= n_{\text{TES}} \pi \ell_{\text{fin}} \left(\ell_{\text{fin}} + \frac{\ell_{\text{TES}}}{2}\right), && (3.90) \end{aligned}$$

$$A_{\text{Passive}} = A_{\text{Bais-major}} + A_{\text{Bais-minor}} \tag{3.91}$$

$$A_{\text{Passive}} = \ell_{\text{absorber}}\sqrt{n_{\text{TES}}}\left(w_{\text{Bias-major}} + w_{\text{Bias-minor}}\right) - w_{\text{Bias-minor}}\left(2\ell_{\text{fin}} + \ell_{\text{TES}}\right)n_{\text{TES}} \tag{3.92}$$

$$= n_{\text{TES}}\frac{\ell_{\text{absorber}}}{\sqrt{n_{\text{TES}}}}\left(w_{\text{Bias-major}} + w_{\text{Bias-minor}}\left[1 - \left(2\ell_{\text{fin}} + \ell_{\text{TES}}\right)\frac{\sqrt{n_{\text{TES}}}}{\ell_{\text{absorber}}}\right]\right) \tag{3.93}$$

$$A_{\text{Al}} = n_{\text{TES}}\left[\frac{\ell_{\text{absorber}}}{\sqrt{n_{\text{TES}}}}\left(w_{\text{Bias-major}} + w_{\text{Bias-minor}}\right) - w_{\text{Bias-minor}}\left(2\ell_{\text{fin}} + \ell_{\text{TES}}\right)\right] + n_{\text{TES}}\pi\ell_{\text{fin}}\left(\ell_{\text{fin}} + \frac{\ell_{\text{TES}}}{2}\right). \tag{3.94}$$

We can see in this form, that the total aluminum area depends on the number of TESs, the area of a single QET, plus an additional component of passive Al per QET. Since the area of the QET depends much more strongly on the fin length than the TES length, lets make the assumption that $\ell_{\text{fin}} > \ell_{\text{TES}}$, making the area of a single QET $\sim \pi\ell_{\text{fin}}^2$, and the total aluminum area becomes

$$A_{\text{Al}} \approx n_{\text{TES}}\left(\pi\ell_{\text{fin}}^2 + A_{\text{passive}}^{\text{cell}}\right), \tag{3.95}$$

where we have defined

$$A_{\text{passive}}^{\text{cell}} = \frac{\ell_{\text{absorber}}}{\sqrt{n_{\text{TES}}}}\left(w_{\text{Bias-major}} + w_{\text{Bias-minor}}\right) - w_{\text{Bias-minor}}\left(2\ell_{\text{fin}} + \ell_{\text{TES}}\right). \tag{3.96}$$

Finally, we can express the phonon collection time as

$$\tau_{ph} \approx \frac{4V_{\text{absorber}}}{n_{\text{TES}}\left(\pi\ell_{\text{fin}}^2 + A_{\text{passive}}^{\text{cell}}\right)\langle c_s\rangle f_{abs}}. \tag{3.97}$$

To give an idea of the effects of these passive contributions, Fig. 3.22 (left) shows a plot of the fraction of phonons absorbed by the active aluminum given by Eq. 3.52 for $\ell_{\text{TES}} = 100\,\mu\text{m}$ and $\ell_{\text{fin}} = 150\,\mu\text{m}$. In Fig. 3.22 (right), the athermal phonon collection time is shown.

We can see that as the number of QETs gets small, the relative amount of passive Al becomes quite large compared to the active area, and the signal efficiency will drop dramatically. Inherent in this calculation of the passive area was the assumption that the QETs would be homogeneously distributed on the surface of the detector. For positional dependence reasons this is advantageous, but for detectors that rely on long phonon collection times (i.e. the phonons are bouncing around the detector many many times) this criteria becomes less important. We will see in the next chapter that when the number of TESs is reduced, this passive aluminum penalty can be negated by packing the QETs together in a smaller region of the detector surface.

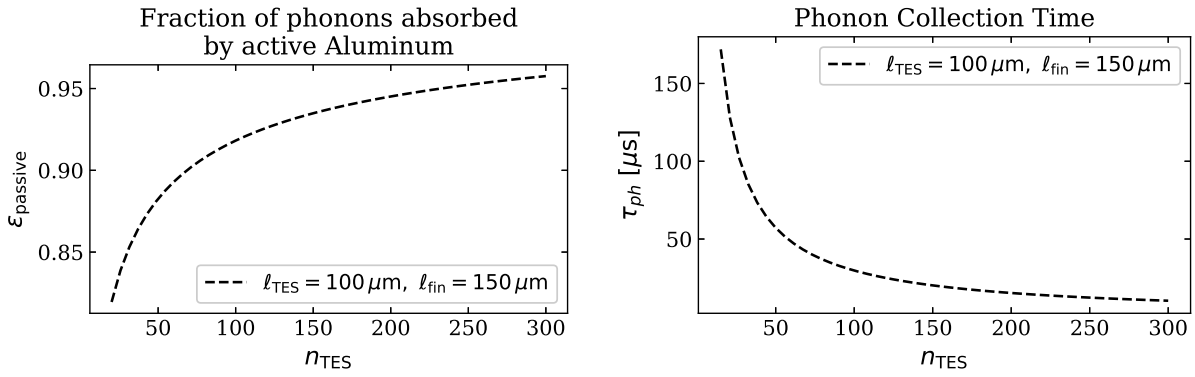

Figure 3.22: Left: Fraction of athermal phonon energy absorbed by active instrumented Aluminum in the QET vs total phonon absorbing surface area. Right: Athermal phonon collection time from the calculation in Eq. 3.97. The major bias rail thickness was 6 μm and the minor was 4 μm for this calculation.

Effective Sensor Bandwidth

The last part to consider is the effective sensor bandwidth τ_* derived in section 2.4. We copy Eq. B.38 here for convenience

$$\tau_* \approx \tau_{\text{ETF}} \sqrt{\frac{T_\ell}{T_0} \frac{\left(1 - \frac{T_{\text{bath}}^n}{T_0^n}\right)}{nF(T_0, T_{\text{bath}}) \left[1 + \frac{S_{P_{\text{par}}}}{S_{P_{TFN}}}\right]}}. \tag{3.98}$$

where τ_{ETF} is given by Eq. 2.53

$$\tau_{\text{ETF}} = \frac{C}{G} \frac{1 + \beta + R_\ell/R_0}{1 + \beta + R_\ell/R_0 + (1 - R_\ell/R_0)\mathscr{L}}. \tag{3.99}$$

We make the usual assumptions that $\mathscr{L} \gg 1$, $\beta, R_\ell/R_0 < 1$. We also make the assumption that the bath temperature is sufficiently low, $T_{\text{bath}} < T_0/2$ and that $T_\ell \sim T_0$. In this limit, we get,

$$\tau_* \approx \frac{C}{G} \frac{1}{\mathscr{L}\sqrt{nF}}. \tag{3.100}$$

The heat capacity for a superconducting W film in transition is given by [98]

$$C = f_{sc} c_W V_{eff}^{\text{total}} T_c, \tag{3.101}$$

where f_{sc} is a correction factor accounting for the additional energy required to break cooper pairs, which ranges from $1 - 2.4$ depending on where in the transition the film is biased, c_W

is the specific heat of W. Using this definition for C and our previous definition of G from Eq. 3.73, τ_* becomes

$$\tau_* \approx \frac{f_{sc} c_W V_{eff}^{\text{total}} T_0}{n \Sigma_{ep}^{\text{W}} V_{eff}^{\text{total}} T_0^{n-1}} \frac{1}{\mathscr{L}\sqrt{nF}}. \tag{3.102}$$

In the limit that $T_{\text{bath}} < T_0/2$, the loop gain is simply $\mathscr{L} \approx \alpha/n$, we finally arrive at

$$\tau_* \approx \frac{f_{sc} c_W}{\Sigma_{ep}^{\text{W}} \sqrt{nF}} \frac{1}{\alpha T_0^{n-2}}. \tag{3.103}$$

Worth noting is the the absence of the total TES volume. Since almost all of the parameters in the expression are simply material properties, the sensor bandwidth is largely set by the superconducting transition temperature. Obviously this assumes that α has no dependence on T_c, which may or may not be true. Both α and T_c have complex dependencies on film morphology, but in principle, there is no fundamental reason why α must decrease with T_c.

Energy Resolution

Finally, we can combine all three components of the energy resolution estimate,

$$\sigma_E^2 = \frac{1}{\varepsilon^2} S_{P_{tot}}(0) \left(\tau_{ph} + \tau_*\right) \tag{3.104}$$

$$\sigma_E^2 = \frac{1}{\varepsilon^2} n 4 F k_B n_{\text{TES}} \Sigma_{ep}^{\text{W}} T^{n+1} V_{eff} \left(\frac{4 V_{\text{absorber}}}{n_{\text{TES}} \left(\pi \ell_{\text{fin}}^2 + A_{\text{passive}}^{\text{cell}}\right) \langle c_s \rangle f_{abs}} + \frac{f_{sc} c_W}{\Sigma_{ep}^{\text{W}} \sqrt{nF}} \frac{1}{\alpha T_0^{n-2}} \right). \tag{3.105}$$

To gain intuition on the above expression, we re-write it in terms of constants:

$$K_1 = 4 n F k_B \Sigma_{ep}^{\text{W}} h_{\text{TES}} \left[w_{\text{TES}} + \frac{1}{\ell_{\text{TES}}} n_{\text{fin}} \left(\zeta_{\text{W/Al}} A_{\text{W/Al}} + \zeta_{\text{connector}} A_{\text{connector}} \right) \right] \tag{3.106}$$

$$K_2 = \frac{4}{\left(\pi + \frac{A_{\text{passive}}^{\text{cell}}}{\ell_{\text{fin}}^2}\right) \langle c_s \rangle f_{abs}} \tag{3.107}$$

$$K_3 = \frac{f_{sc} c_W}{\alpha \Sigma_{ep}^{\text{W}} \sqrt{nF}}. \tag{3.108}$$

The resolution then gets a little more digestible,

$$\sigma_E^2 = \frac{1}{\varepsilon^2} K_1 n_{\rm TES} \ell_{\rm TES} T_c^{n+1} \left(\frac{4V_{\rm absorber}}{n_{\rm TES}\ell_{\rm fin}} K_2 + \frac{K_3}{T_0^{n-2}} \right). \tag{3.109}$$

From this form, we can see that the resolution has strong dependence on T_c and $n_{\rm TES}$. From Fig. 3.23 (left) we can see that the optimum resolution is achieved by lowering both of these parameters together. Also noticeable is the fact that the energy resolution improves faster with T_c for fewer numbers of QETs, this is the ideal scenario to be in. The point at which this occurs is when the two time constants are $\tau_{ph} \approx 2\tau_*$. This condition will henceforth be referred to as **Bandwidth Matched** (BW)[3]. It is important to note that since the QP collection efficiency is strongly correlated with the length of the Al fins, the total instrumented Al area of a sensor is dependent on the number of TESs. As such, surface coverage is essentially synonymous with $n_{\rm TES}$. The BW matching condition implicitly has the assumption built in that $\ell_{\rm fin}$ is effectively constant. In a world where we could make arbitrarily large collection fins without QP loss, the optimum resolution would always tend towards a bigger collection fin. Thus, the BW matching argument can be thought of as the *fastest improvement in energy resolution with T_c for a roughly fixed size QET.*

This BW matching can be seen in the above equation by noting that when the second and third terms are equal, the energy variance will scale to leading order in T_c as

$$\sigma_E^2 = \frac{1}{\varepsilon^2} K_1 K_2 \frac{\ell_{\rm TES}}{\ell_{\rm fin}} V_{\rm absorber} T_c^{n+1} + \mathcal{O}\left(T_c^3\right) \qquad (\tau_{ph} \approx \tau_*). \tag{3.110}$$

This can be said more quantitatively as

$$n_{\rm TES}\left(A_{\rm QET} + A_{\rm passive}^{\rm cell}\right) = 2\frac{\Sigma_{ep}^{\rm W}\sqrt{nF}\alpha 4V_{\rm absorber}}{f_{sc}f_{abs}\langle c_s\rangle c_{\rm W}} T_c^{n-2} \quad \text{[BW matching condition]}. \tag{3.111}$$

In the limit that the passive aluminum can be made negligible (as we will see later, this condition can almost always be met), we can write this as

$$n_{\rm TES} \approx 2\frac{\Sigma_{ep}^{\rm W}\sqrt{nF}\alpha 4V_{\rm absorber}}{f_{sc}f_{abs}\langle c_s\rangle c_{\rm W}} \frac{T_c^{n-2}}{\pi\ell_{\rm fin}\left(\ell_{\rm fin} + \ell_{\rm TES}/2\right)}. \tag{3.112}$$

We thus now have an expression for determining the optimum number of QETs for a given T_c and QET size. This suggests that the best energy performance can be achieved by designing a detector with low-T_c and low overall instrumented surface coverage, or $n_{\rm TES}$.

Eq. 3.112 is plotted in Fig. 3.24 for a variety of QET dimensions. As can be seen in the figure, as we lower the T_c we must also decrease the length of the fins and the TES in order to maintain a reasonable number of QETs, where the number of QETs needed is determined

[3]The term bandwidth matched is a bit of a misnomer. It is not the matching of the time constants that improves the resolution, but rather the lowering of the number of TESs.

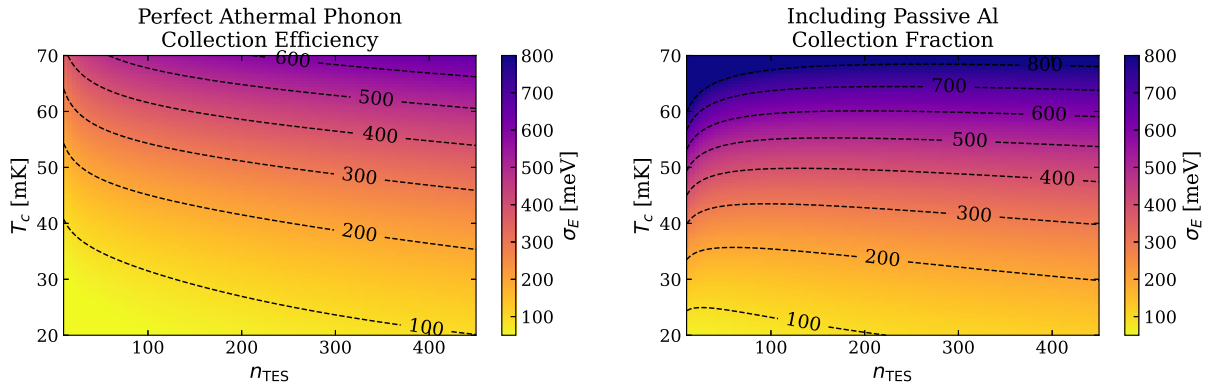

Figure 3.23: Plot of energy resolution as a function of T_c and n_{TES} for $\ell_{\mathrm{TES}} = 25\,\mu$m and $\ell_{\mathrm{fin}} = 70\,\mu$m from Eq. 3.108. Left: Assuming no sources of athermal phonon loss, i.e. $\varepsilon = 1$. Right: The effect of phonon loss due to passive aluminum is considered, i.e. $\varepsilon = \varepsilon_{\mathrm{passive}}$.

somewhat by the required R_n. Thus, to get the full advantage of very low T_c designs (sub 20 mK), the QET designs must deviate substantially from the designs previously shown in this chapter.

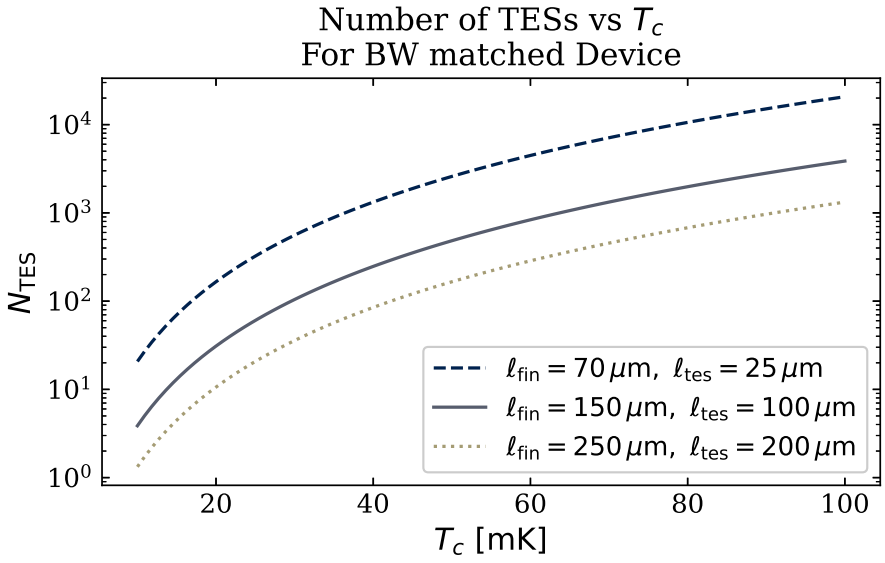

Figure 3.24: Number of TESs as a function of superconducting transition temperature for a bandwidth matched device, shown for multiple values of ℓ_{TES} and ℓ_{fin}.

Thus far in this discussion on energy resolution, we have neglected the total phonon

collection efficiency ε. Since we are talking about the overall detector, we can assume that all QET parameters are equivalent, and we are only tuning the number of TESs. In this case, most of the efficiency factors will be the same for all cases, and so it is fine to ignore them when comparing relative performance. There is however one factor we must consider, and that is the effect of the passive aluminum, $\varepsilon_{\text{passive}}$. As the total number of QETs decreases, the relative percentage of passive Al becomes substantial, and the energy resolution begins to suffer, as shown in Fig. 3.23 (right). This limitation can be overcome with design techniques that will be discussed in the next section.

3.5 Chapter Summary

In this chapter, we have discussed the benefits of athermal calorimetry, how the energy resolution of a TES based detector can be enhanced through the use of quasiparticle trapping, and the considerations that go into the design of a QET. This chapter also discussed at length how all of the tunable parameters of a QET factor into the overall design of an athermal detector, and most notably, showed how this energy resolution depends strongly on the superconducting transition temperature at the bandwidth matched point. The following chapter will take all of the design guidelines laid out in this chapter, and use them to discuss the design of the initial prototype dark matter detectors for the SPICE/HeRALD collaboration.

Chapter 4

Design of SPICE MELANGE and DEATH Detectors

The previous chapters detailed the considerations that go into the design of a QET and the overall principles of an athermal phonon sensor mediated particle detector. We will now apply these principles to a real detector, specifically the initial set of detectors I designed for the SPICE/HeRALD collaboration. I derived in the previous section that for a bandwidth matched device, the energy variance scales linearly with the number of QETs and T_c^{n+1} (Eq. 3.110). This suggests that the best energy sensitivity can be achieved with few QETs and low-T_c. However, to remain in the bandwidth matched limit ($\tau_{ph} \approx 2\tau_*$), the number of QETs must decrease rapidly with T_c as shown in Eq. 3.112. From the definition of τ_{ph} in Eq. 3.97, this means that for a bandwidth matched low-T_c device, the phonon collection times will get exceedingly slow. Said another way, the lower limit of the T_c of the TESs on a optimized detector will be determined by the ballistic phonon lifetime in the substrate for the detector target. Of course, there can still be improvements in energy sensitivity by lowering T_c beyond this threshold, but the gains will be less dramatic than in the BW matched case.

For small detector substrates with characteristic sizes of $\sim 1\,\mathrm{cm}$ or less, the low energy ballistic phonon lifetimes are limited by surface effects for sufficiently pure detector grate materials (Ge, Si, GaAs, Sapphire, etc). From Semi-analytic models for surface effects and measurements, we expect that the rough scale for or ballistic phonon lifetimes in Si, and GaAs is $\mathcal{O}(.1 - 10\,\mathrm{ms})$ for a $1\,\mathrm{cm}$ cube crystal [124, 128, 136]. The properties of surfaces are much too complex to accurately model, and ultimately the ballistic phonon lifetimes must be measured. We can however use the simulations as a rule of thumb in our designs.

The codes written for the following optimizations in this chapter were packaged into the open source python package DarkOpt to make QET based phonon sensor development by future grad students more streamlined!

4.1 Detector Goals and Overview

As motivated in previous chapters of this thesis, the overall goal of our group is to design detectors with $\mathcal{O}$(meV) energy resolutions. The bulk of the previous chapter(s) laid out how this can be achieved through low-T_c low-surface coverage QET based athermal phonon sensor mediated designs. In chapter 6 the characterization of low-T_c TESs will be discussed. There is thus the remaining question of 'how low in surface coverage can you go?'.

This set of detectors was designed to study this question with a series of detectors with varying total Al surface coverages. The devices were designed to be $1\,\text{cm} \times 1\,\text{cm}$ fabricated on a 4 mm thick wafer, with total instrumented surface coverages of 4%, 1%, and 0.25%. These devices are named the **SPICE MELANGE** detectors (Milli Electronvolt sensor with Low AlumiNum coveraGE). These values were chosen such that there would be at least an order of magnitude difference in the expected phonon collection times between the range of surface covereages, making it easy to study the phonon down-conversion probabilities at the surfaces.

There was an additional device designed and fabricated as a high surface coverage device to optimize for fast collection times for use with the HeRALD group, named the **DEATH** detector (Dark matter Excitation generated Athermal phonons for TESs in Helium).

4.2 Optimizing for R_N and n_{TES}

The overall amount of instrumented surface area was pre-determined for the reasons laid out in the previous section. However the overall design of each detector is still free to be chosen. As described in previous chapters, the number of TESs, length of the TESs, and the normal state resistance are all connected. Additionally, as shown for the BW matching condition in Eq. 3.111, the number of TESs and the length of the fins are also a function of T_c, but these parameters are somewhat less intertwined. Due to this complexity, an analytical optimization is not practical and a numerical technique must be used.

In the numerical optimization all noise sources in Eq. 2.91 were considered. As will be seen in later chapters, excess noise is often observed. However it is thought to be environmental in nature, so it was left out of the optimization under the assumption[1] that it can always be mitigated. In order to keep the total surface coverage fixed at a certain value, the following loss function was minimized

$$\mathcal{L} = \left[\varepsilon^2 \int_0^\infty \frac{d\omega}{2\pi} \frac{4|p(\omega)|^2}{S_{P_{tot}}(\omega)}\right]^{-1} \left[1 + |\text{SA} - \text{SA}_{\text{target}}|\right], \tag{4.1}$$

where ε is the the total athermal collection efficiency defined in Eq. 3.70 and is a function of $n_{\text{fin}}, \ell_{\text{TES}}, \ell_{\text{overlap}}$, and ℓ_{fin}. The noise $S(\omega)$ is a function of $n_{\text{TES}}, n_{\text{fin}}, \ell_{\text{TES}}$, and ℓ_{overlap}. The pulse shape is given by Eq. 3.69 and is a function of $n_{\text{TES}}, \ell_{\text{TES}}$, and ℓ_{fin}. SA is the percent

[1] hope

active and passive surface area and is a function of $n_{\text{TES}}, \ell_{\text{TES}}$, and ℓ_{fin}. $\text{SA}_{\text{target}}$ is the target percent surface area e.g $4\%, 1\%, 0.025\%$.

Note, while there is obviously strong dependence on T_c, this is not considered an optimization parameter. Since the energy resolution has monotonic dependence on T_c, the choice of T_c in the actual optimization is simply a scale factor. As such, each detector is optimized for it's bandwidth matched T_c as given by Eq. 3.111. Ultimately this detector set will be fabricated at a variety of T_c's to study the T_c dependence for BW matched devices.

Recall from Eq. 3.47 the relation between n_{TES}, ℓ_{TES}, and R_N. Since R_N is the parameter that is constrained by the ETF condition, we instead express n_{TES} in terms of R_N. Since n_{TES} and n_{fin} are discrete variables, and the rest are continuous, the optimization is done in two steps. For each surface coverage design, the following steps are done:

1. Fix n_{fin} and R_N
2. Minimize loss function in Eq. 4.1 by varying ℓ_{TES}, ℓ_{fin}, and ℓ_{overlap}.
3. Repeat grid search over n_{fin} and R_N.

Once this process is done, the R_N and n_{fin} corresponding to the minimum energy resolution are chosen. After this step, a second optimization is done. From section 3.3.2, we learned that the the W/Al overlap region contributes $13 - 45\%$ of its volume to the total heat capacity of the system. To account for this, a finer binned grid search in a small window around the optiumum R_N is performed, with a now fixed n_{fin}. This is done once using $\zeta_{\text{W/Al}} = 0.13$ and once using $\zeta_{\text{W/Al}} = 0.45$. The average of all the optimum parameters is then used for the final design.

4.3 Design of 4% Surface Coverage Device

For the 4% total coverage device, from Fig. 4.1 it can be seen that there is little difference in resolution between $R_n = 300 - 350\,\text{m}\Omega$ for most fin values. As such, a normal resistance of $R_N = 325\,\text{m}\Omega$ was chosen. It is also clear that the best resolution comes from a 3-fin device, however from Fig. 4.1 (right) we see that this would require an overlap length of greater than $18\,\mu\text{m}^2$. Since at the time of this design, SuperCDMS or SPICE has not fabricated overlaps of this length, the conservative choice was made to choose overlaps of less than $17\,\mu\text{m}$. With this limitation, the QET design was chosen to have 5 fins. A plot of how the various free parameters effect the energy resolution at the BW matched T_c of $\sim 67\,\text{mK}$ is shown in Fig. 4.2.

4.3.1 Design of Elliptical QET

This optimization sets the general design parameters for the number of QETs and the overall dimensions, which now must be translated into a QET design. As discussed in section 3.3.3,

[2]Note that $18\,\mu\text{m}$ was set as the upper limit in the optimization.

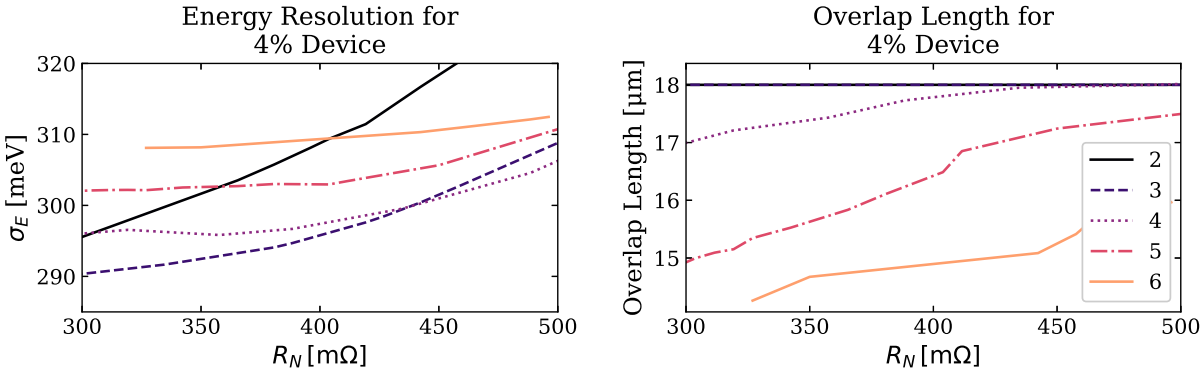

Figure 4.1: Optimum energy resolution (left) and corresponding ℓ_{overlap} (right) as a function of R_N for 2-6 fin QETs for 4% coverage device. Note that $\ell_{\text{TES}}, \ell_{\text{fin}}, \ell_{\text{overlap}}$ are all allowed to float in the optimization.

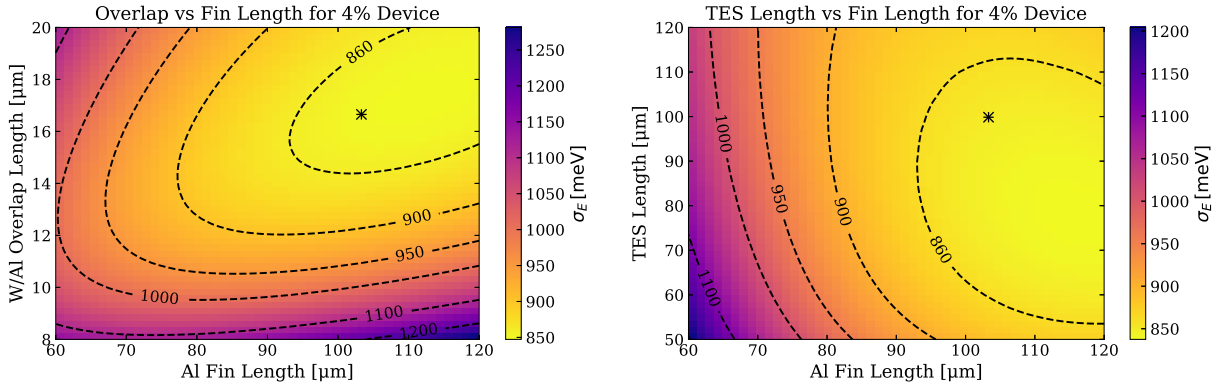

Figure 4.2: Energy resolution as a function of ℓ_{overlap} and ℓ_{fin} (left) and ℓ_{TES} and ℓ_{fin} (right). This plot was generated assuming $T_c = 67\,\text{mK}$, and $\zeta_{\text{W/Al}} = 0.29$, which is the average of the two measured values. Note that the devices are not at the exact minimum, which is mainly due in part by the fact that the optimum parameters were chosen from an average of two different optimizations with different values of $\zeta_{\text{W/Al}}$.

Table 4.1: General parameters of the SPICE MELANGE and HeRALD DEATH detectors. The detectors are 1 cm × 1 cm in size. The total surface coverage is calculated assuming a wafer height of 4 mm.

	Device Name			
	Death	Melange		
Parameter	27%	4%	1%	0.25%
Total Al Coverage [%]	27	4.06	1.006	0.253
Single Face Al Coverage [%]	97.2	14	3.6	0.9
Active Al [%]	> 27.5	3.705	0.956	0.239
Passive Al [%]	$< .5$	0.356	0.049	0.014
R_N mΩ]	230	325	320	450.0
n_{TES} (single channel)	N/A	293	177	51
n_{TES} (two channels)	254/215 (inner/outer)	147/146 (inner/outer)	53/124 (inner/outer)	25/26 (left/right)
n_{fin}	6	5	2	2
QET Type	Rectangular	Elliptical	Circular	Circular
ℓ_{TES} [μm]	120	99	59	24
w_{TES} [μm]	2.5	2.5	2.5	2.5
h_{TES} [nm]	40	40	40	40
ℓ_{overlap} [μm]	17	16.7	16.6	14.4
ℓ_{fin} [μm]	185	105	69	70
h_{fin} [nm]	600	600	600	600
Au pad size [μm × μm]	350 × 455	300 × 300	150 × 150	75 × 65
$\ell_{\mathrm{veto\ TES}}$ μm	N/A	30	30	30
$w_{\mathrm{veto\ TES}}$ μm	N/A	295	295	215
T_c [mK] BW Matched	N/A	67	43	33
τ [μs]	N/A	790	3000	6645
τ_{ETF} [μs]	N/A	11	44	97
τ_{ph} [μs]	< 3	24	97	385
Homogeneous Coverage	Yes	Yes	No	No
F_c		0.58	0.58	0.49
$\varepsilon_{\mathrm{passive}}$		0.91	0.95	0.94
ε		0.24	0.25	0.21
$\zeta_{\mathrm{connector}}$	0.9	0.9	0.9	0.9
$\zeta_{\mathrm{W/Al}}$	0.29	0.29	0.29	0.29
σ_{E}		850	222	100

a 2D fin design offers a higher QP collection fraction per area than a 1D design. From Tab. 4.1, we can see that for the 4% device, the TES is roughly the same size as the fin length, thus an elliptical shape is a logical choice for the overall QET design. The QET was designed by creating an ellipse with dimensions

$$R_{\text{major}} = \ell_{\text{fin}} + w_{\text{empty}} + \frac{\ell_{\text{TES}}}{2} \tag{4.2}$$

$$R_{\text{minor}} = \ell_{\text{fin}} + w_{\text{empty}} + \frac{w_{\text{TES}}}{2}, \tag{4.3}$$

where w_{empty} is the empty space between the the Al fin and the W TES as shown in Fig. 3.6. The ellipse was segmented into 5 equal area sections, and connected to the TES is a staggered fashion such that the length of TES between fin connectors was $\sim 25\,\mu$m. A schematic of this QET design can be seen in Fig. 4.3 (B). Additionally, 5 holes were placed in each fin, of size $5\,\mu\text{m} \times 5\,\mu$m, to mitigate trapped flux as described in section 3.3.3.

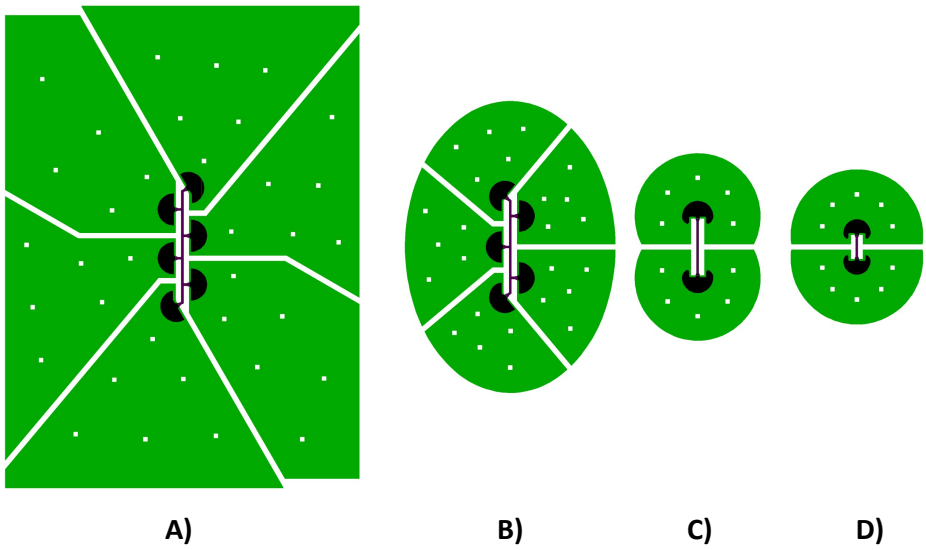

Figure 4.3: Comparison of DEATH (**A**) QET and MELANGE QETs: 4% (**B**), 1% (**C**), 0.25% (**D**). All QETs are to scale.

4.3.2 QET and Channel Layout

The 293 QETs were evenly distributed across one face of the 1 cm detector, with a $100\,\mu$m curb on each side, all connected in parallel. A single channel and two channel device were designed, as shown in Fig. 4.4. The two channel device consisted of an 'outer' and 'inner' channel, each with equal QET density and number. The two channel devices were designed to allow for more discrimination power during the analysis. Having multiple channels allows one to understand the positional dependence of where the event occurred in the detectors,

discrimination against signal-like events, and events originating in the TESs/QETs themselves (ie W film stress events). Lastly, having two channels allows for the measurement of the thermal conductance between the substrate and the thermal bath, as will be described in later chapters.

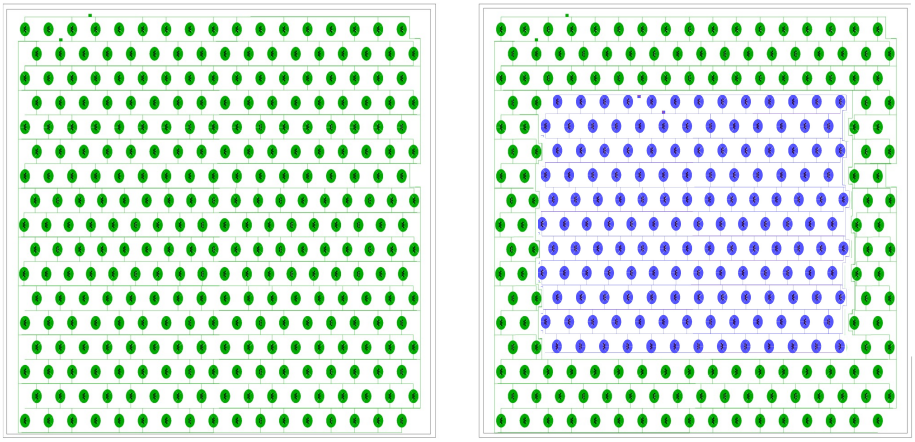

Figure 4.4: 4% total coverage device QET layout. Left: single channel device. Right: two channel device, with 'inner' and 'outer' channel with the inner channel Aluminum colored in blue. Note, this color change was made to highlight the channel location and is only for visual purposes, some of the connections were altered while making this diagram. This was not the actual final design file.

4.4 Design of Ultra-Low Coverage Devices

The same process as above was repeated for the lower coverage devices (i.e. the 1% and 0.25% coverage devices). However it was quickly noticed that for a homogeneous QET layout, the relative amount of passive aluminum began to dominate the total aluminum budget. This in turn drove the number of QETs down in the optimization (equivalently drove the normal resistance up), consequently degrading the energy resolution as shown in Fig. 4.5. This degradation in resolution is due mostly to the decrease in signal efficiency from $\varepsilon_{\text{passive}}$ from Eq. 3.52.

To reduce the percentage of passive aluminum, the QETs were placed in close contact with each other in a small region of the detector surface in what I will refer to as a 'close packed' design. An example of a close packed design can be seen for the 1% device layout in Fig. 4.6 and the 0.25% device in Fig. 4.7. By no longer having a homogeneous QET layout, there is a possibility of positional dependence: where events that occur further away from densely populated QET regions will have a different signal shape than events occurring closer

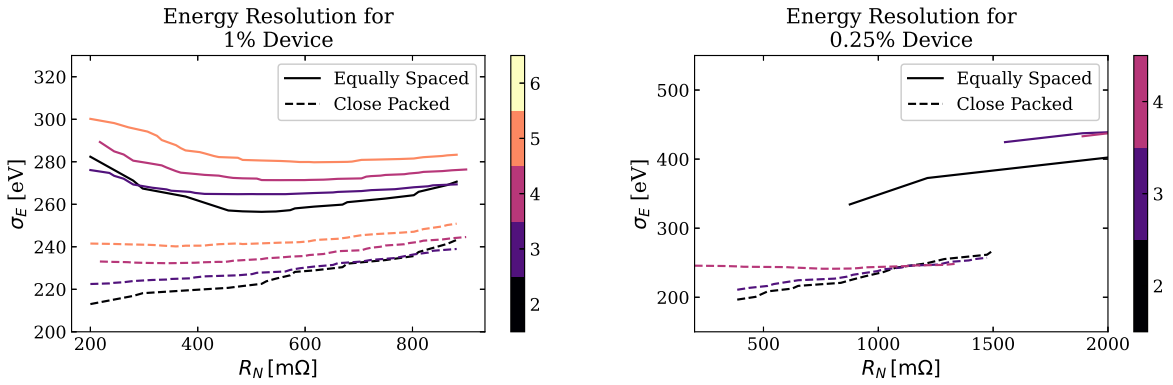

Figure 4.5: Optimum energy resolution as a function of R_N for 2-5 fin QETs for the 1% coverage device (left) and 0.25% coverage device (right) for both an equally spaced design (solid) and and tightly packed QET layout (dashed). Notice that for the 0.25% device, for the equally spaced layout, values are not shown below $R_N \approx 1\,\Omega$, this is because it was not possible to make a design within the given constraints that met the surface area requirement.

as the time to collect the phonon energy will differ. The spiral design attempts to mitigate this effect by placing QETs in roughly all quadrants of the surface of the device.

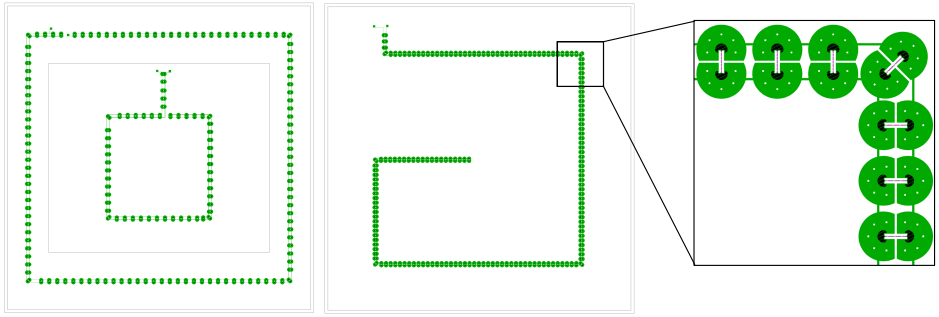

Figure 4.6: QET Layouts for the 1 percent device. The two channel version (left) is divided into an inner and outer channel, of equal QET density, which necessitated an unequal number distribution of QETs for the two channels. The single channel version (middle) was laid out in a spiral in order to minimize positional dependence. A zoomed in version of the QET spacing is shown on the right.

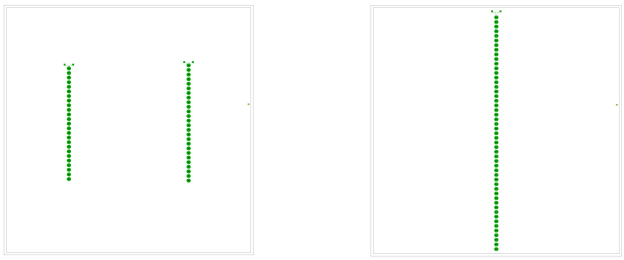

Figure 4.7: QET Layouts for the 0.25 percent device. The two channel version (left) is divided into a left and right channel. The single channel version (right) was laid out in a line to minimize positional dependence.

4.4.1 Design of 'Peanut' QET

From Fig. 4.5, the lowest energy resolution can be achieved with 2 fin devices. Only having two fins, with relatively short TESs ($25-50\,\mu$m) allows for more flex ability in the fin design itself. The design of the 1% and 0.25% QETs can be seen in Fig. 4.3, and have the slight resemblance of a peanut, hence the name 'peanut QET'. For this design, each fin and overlap combination were designed as full circles and then the divided apart to have two distinct fins. It is hoped that this design of the W/Al overlapping region allows for more efficient QP collection than for the more classic elliptical QET design.

4.5 DEATH Detector

For posterity, I'll include the rational for the deign of the high coverage device. The primary design driver for this device was fast athermal phonon collection time. Since the numerical optimization described in the previous sections was written with energy resolution in mind, the optimization for this device was more hand-tuned. For a fixed overlap length, the athermal phonon collection time and energy resolution were simulated as a function of TES length and Al fin length as shown in Fig. 4.8. As can be seen in the figure, these two parameters are somewhat at odds with each other. The optimum TES length and fin length were chosen to be a compromise of these two metrics.

4.5.1 Rectangular QET Design

To minimize the thermalization time for the chosen TES length of $\ell_{\mathrm{TES}} = 120$, the QET was divided into 6 fins[3]. It was also realized that a 'rectangular' shaped QET would offer a substantial boost in surface coverage over the elliptical or circular QET designs used in the other devices. Similar QETs have been used with great success in the SuperCDMS HVeV

[3]See section 3.3.6 for reasoning behind the choice of number of subdividing fins.

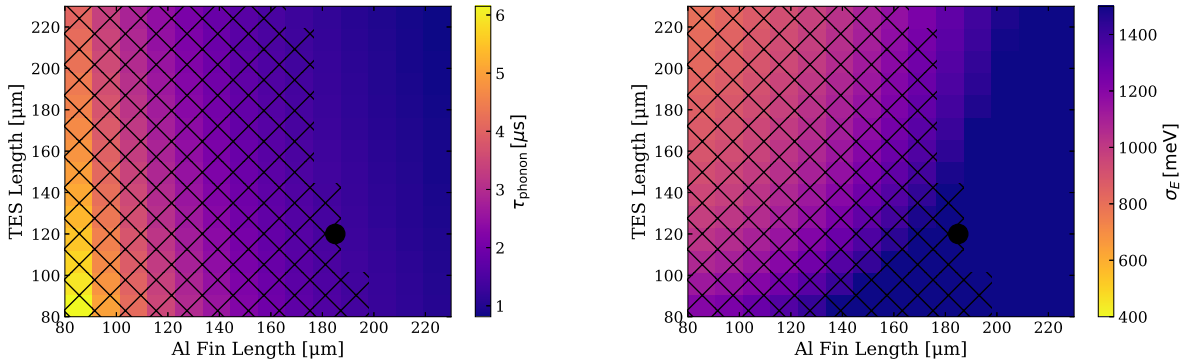

Figure 4.8: Athermal phonon collection time (left) and energy resolution (right) as a function of TES length and fin length. The black hatched area corresponds to the parameters that will physically fit on a single face of the detector. The black represents the chosen design parameters.

program [109–111]. For the choice of overlap, I chose the maximum conservative value of $\ell_{\text{overlap}} = 17\,\mu\text{m}$. The final QET can be seen in comparison to the other QETs in the detector set in Fig. 4.3.

4.5.2 QET Layout

Unlike for the previous devices, the number of QETs and fin dimensions were chosen based on the physical constraints of the overall layout. The optimization was answering the question 'what combination of ℓ_{fin} and n_{TES} maximally cover an area of $1\,\text{cm}^2$?' Rather than connecting devices with bias rails, the fins themselves were used to join neighboring QETs. Similar to the 4% device, the QETs were divided into and 'inner' and 'outer' channel, each with equal QET number and density. A graphic of the photolithography mask design, as well photo of the fabricated detector can be seen in Fig. 4.9.

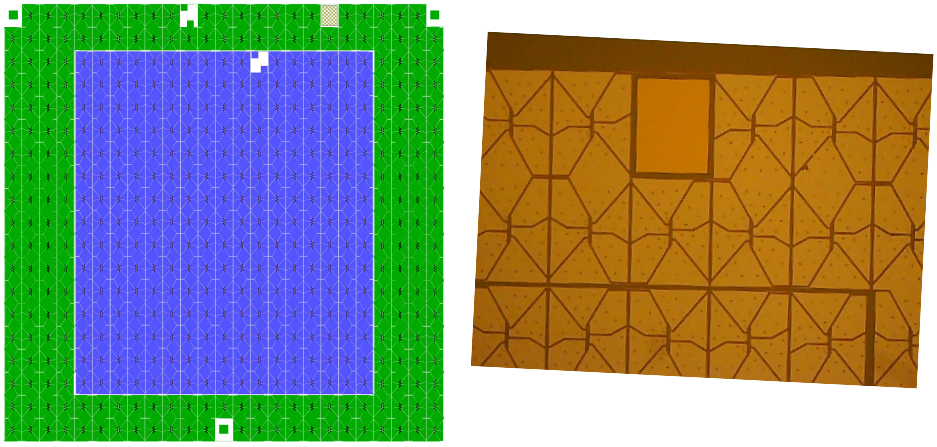

Figure 4.9: Left: Layout of QETs on the DEATH detector. The 'inner' channel is shown in blue and 'outer' channel is shown in green. Again, please note that this graphic is only to help aid in visualization. Right: Image of section of DEATH detector after fabrication.

4.6 Mask Layout and Fabrication

The MELANGE and DEATH devices were positioned together into a mask that could be fabricated on either a standard 3 inch or 4 inch wafer. The detectors were fabricated by Mark Platt at Texas A&M in an 'inverted style', fabricating the W below the Al layers. An amorphous Si etch mask was also made for future fabrication on non-Si substrates, to be used as well for post fabrication cleaning and etching. There was an additional Au mask designed for thermalization pads, which will be discussed in the following subsections. After fabrication, the wafer was diced into 57 1 cm^2 squares. The photolithography masks, full fabricated wafer, and example of single detector after dicing can be seen in Fig. 4.10.

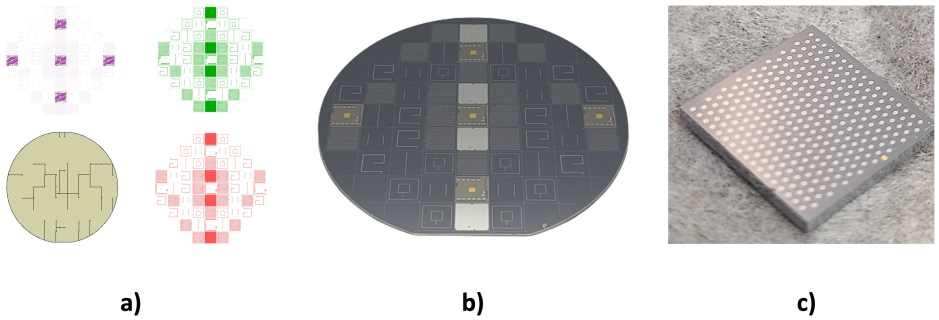

Figure 4.10: **a)** Photolithography masks for MELANGE and DEATH detector mask for fabrication on 4 inch wafer. clockwise from upper left: Tungsten, Aluminum, Inverted Gold, Amorphous Si. **b)** Image of the detectors fabricated on a 4 inch Si wafer before dicing. **c)** Image of single channel 4% MELANGE detector after dicing.

4.6.1 Wafer Characterization Device

Since the fabrication of low-T_c W films is more of a dark art than it is a science, a chip containing a set of test structures was included on this mask in order to characterize the W film. The device consisted of two sets of simple TES rectangles varying in size from $200\,\mu\text{m} \times 800\,\mu\text{m} \times 40\,\text{nm}$ down to $25\,\mu\text{m} \times 25\,\mu\text{m} \times 40\,\text{nm}$. For simplicity, this chip will be referred to as the TESTR device: TES Test Rectangles. These types of TES devices have been immensely helpful in understanding fundamental TES dynamics, as well as diagnosing EMI noise sources, as discussed in detail in chapter 6 (or equivalently see Ref. [137]). Measurements of these particular devices and how they allow us to understand basic properties of the W films will be discussed in chapter 7. Also included was a slightly modified version of the set of X-ray QET devices used in the Stanford QP dynamics study in Refs. [112, 113]. An image of the photolithography mask can be seen in Fig. 4.11.

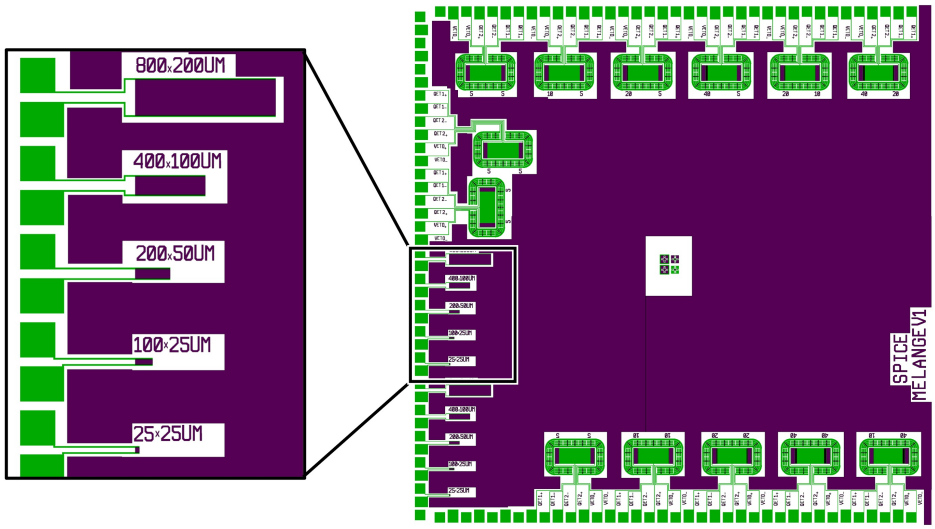

Figure 4.11: TESTR device (right) and zoomed in section of TES rectangles (left). Green is aluminum and purple is tungsten.

4.7 Mounting and Thermalization of Detectors

For any calorimeter, thermalization is important, but for the very low coverage MELANGE detectors this becomes a technical challenge. Historically in CDMS, detectors are securely held in place and thermalized by cirlex clamps on the edges of the detector. There are three reasons that we don't want to go this route for the MELANGE detectors:

1. Cirlex and FR-4 materials have been connected to an excess of low energy events in DM detectors via Cherenkov radiation [138].

2. CDMS has also had problems with the cirlex clamps getting stuck at temperatures above T_{bath}.

3. For the low coverage devices to realize their full potential we require long ballistic athermal phonon lifetimes. We therefor need a thermalization technique that minimizes the amount of passive phonon loss.

To solve problems one and two, we elected to get rid of the clamping scheme all together and minimize any insulating materials inside the optical cavity holding the detector[4]. To solve problem three, we decided to fabricate a gold pad on each device and connect that to the copper housing with a gold wirebond. The heat is removed via the electron-phonon coupling in the Au pad. As a back of the envelope calculation, we require than the thermal conductance from the substrate to bath G_{AB} be roughly $\times 50$ the thermal conductance

[4]This doesn't actually count as a solution, because we still aren't actually thermalizing anything yet...

between the TESs and the substrate G_{TA}. The electron phonon-coupling for Au has been measured to be $\sim 1\,[\mathrm{W/m^3/K^5}]$, which is roughly a factor 10 greater than for W [139, 140]. Recall from Eq. 3.73, the thermal conductance for an electron-phonon limited thermal impedance is given by

$$G = n\Sigma_{ep} V T^{n-1}, \tag{4.4}$$

where n equals 5 or 6 [139]. The ratio of thermal conductances for the Au and W films is

$$\frac{G_{\mathrm{AB}}}{G_{TA}} = \frac{\Sigma_{ep}^{\mathrm{Au}}}{\Sigma_{ep}^{\mathrm{W}}} \frac{A_{\mathrm{Au}}}{A_{\mathrm{TES}}} \frac{h_{\mathrm{Au}}}{h_{\mathrm{TES}}}. \tag{4.5}$$

If we assume that we can reliable fabricate 800 nm thick Au film, then we get that

$$\frac{G_{\mathrm{AB}}}{G_{TA}} = 200 \frac{A_{\mathrm{Au}}}{A_{\mathrm{TES}}}. \tag{4.6}$$

Thus we see that to get out desired ratio of 50, we require that

$$A_{\mathrm{Au}} \approx \frac{A_{\mathrm{TES}}}{4}. \tag{4.7}$$

Using values from Tab. 4.1, this means the Au pad is approximately 0.1% of the Al surface area, or said another way: The Au pads should be negligible as a source of athermal phonon loss. A close up view of a Au pad fabricated on a detector can be seen in Fig. 4.12.

4.7.1 Detector Mounting

While this is not the focus of this chapter, it is necessary to briefly discuss the planned detector mounting schemes as it pertains to the detector design. There are two proposed ideas:

1. 'Resting' - The detectors simply rest on a copper plate in little indents. They are clamped down during electrical and thermal bonding, but left free-floating during operation (see Fig.4.12 middle).

2. 'Hanging' - The detectors would be suspended by three 3 mil wirebonds. These would also have the same electrical and thermal bonds as the resting device as well.

Both of these ideas would effectively thermalize the detectors, while also minimizing any amount of insulating materials and sources of passive phonon loss. While the 'resting' idea is much simpler to implement, it will require some form of vibration isolation in order to achieve its optimum performance. The subject of passive vibration isolation will be discussed at length in Sam Watkins thesis.

The 'Hanging' concept will potentially alleviate the need to fully mechanically decouple the detector housing from the mixing chapter, at least in the short term. However implementing this plan does present some serious technical difficulties. The design and installation of the corresponding detector holder for this idea was done by our engineer Siddhant Mehrotra and fellow grad student Roger Romani. As far as the design of the detectors in concerned, three additional $300\,\mu\text{m} \times 300\,\mu\text{m}$ Al bonding pads were placed in a triangular pattern on the detector, as can be seen Fig. 4.13. A subset of all detectors was designed with and without this set of hanging bonding pads.

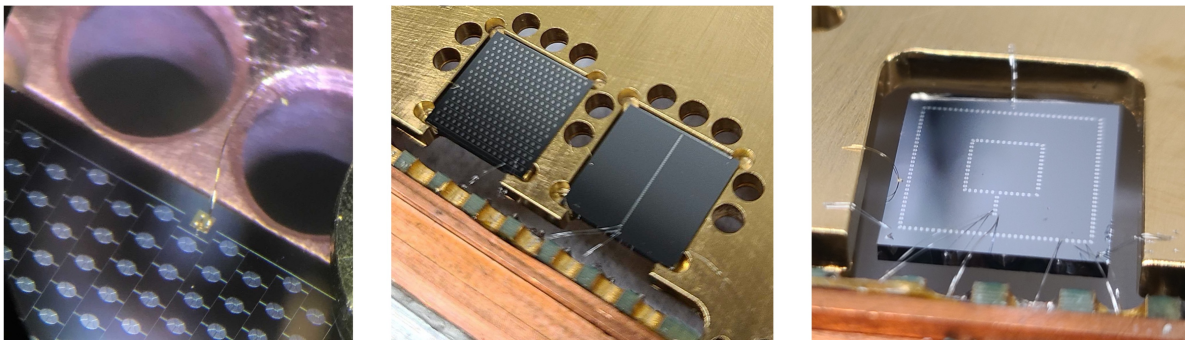

Figure 4.12: Left: Close up view of Gold pad on 4% MELANGE detector, wirbonded to copper housing. Middle: Two MELANGE detectors (4% and 0.25% left to right) in a resting configuration. Right: A two channel 1% MELANGE detector in the hanging configuration. The structural hanging bonds can be seen on the left, right, and far side of the image. The electrical readout bonds are in the front, and the gold thermalization bond is shown on the left.

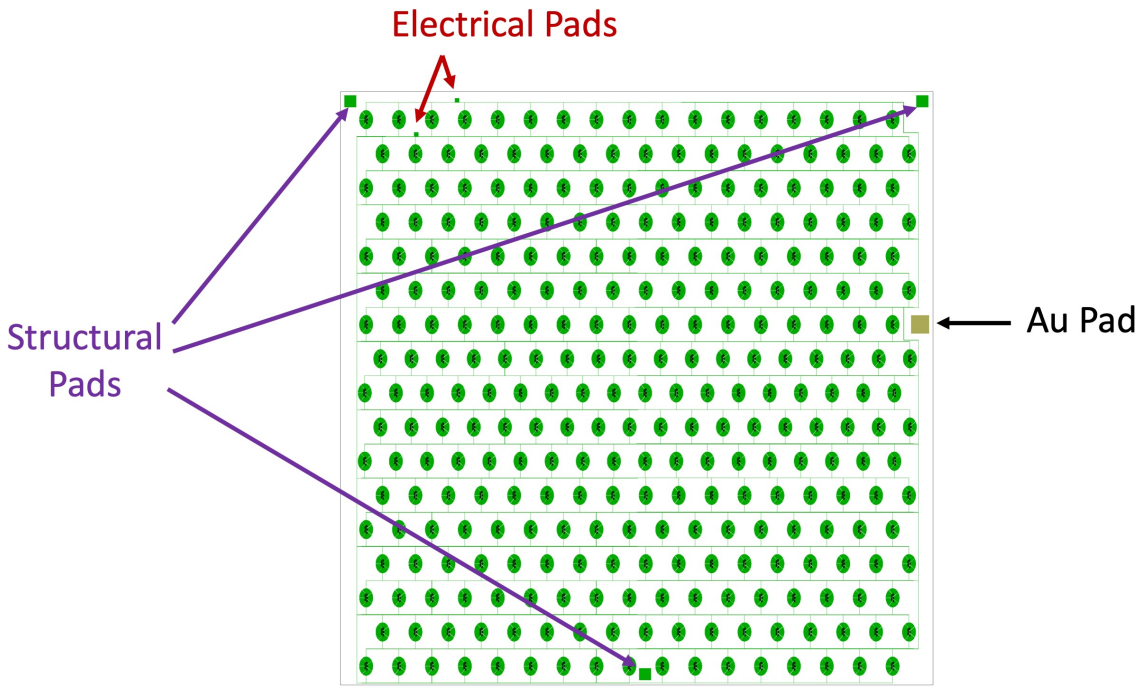

Figure 4.13: Schematic of 4% device with labels showing the electrical readout bonding pads, the gold thermalization bonding pads, and the structural bonding pads for hanging the device from.

4.8 Expected Performance

Finally we can simulate the performance of these detectors. In Fig. 4.14 we can see the expected energy resolution for the 0.25%, 1%, and 4% MELANGE devices as a function of T_c. Note that this energy resolution estimate assumes only intrinsic noise sources. As will be seen in the following chapters, these values are likely too low by a factor of $1.25 - 2$. We had a high-T_c version made at $T_c \approx 55\,\mathrm{mK}$ and a low-T_c version at $T_c \approx 19\,\mathrm{mK}$, shown by two dashed lines in the figure. We can see the effect of the bandwidth matching as described in section 3.4.5. Above the higher T_c line τ_{ETF} is much faster than τ_{ph}, to the point that the noise gains from reducing the number of QETs is cancelled by the decrease in effective bandwidth. In this limit, the expected energy resolution of all 3 designs is roughly the same. Looking at the lower T_c region around 19 mK we are now in the regime where the two time constants are roughly the same, and we get very large benefits by decreasing the the number of QETS (decrease surface coverage). Even the high-T_c version of these detectors should achieve roughly half eV resolution, while the lowest coverage low-T_c devices should achieve sub-50 eV baseline energy resolution!

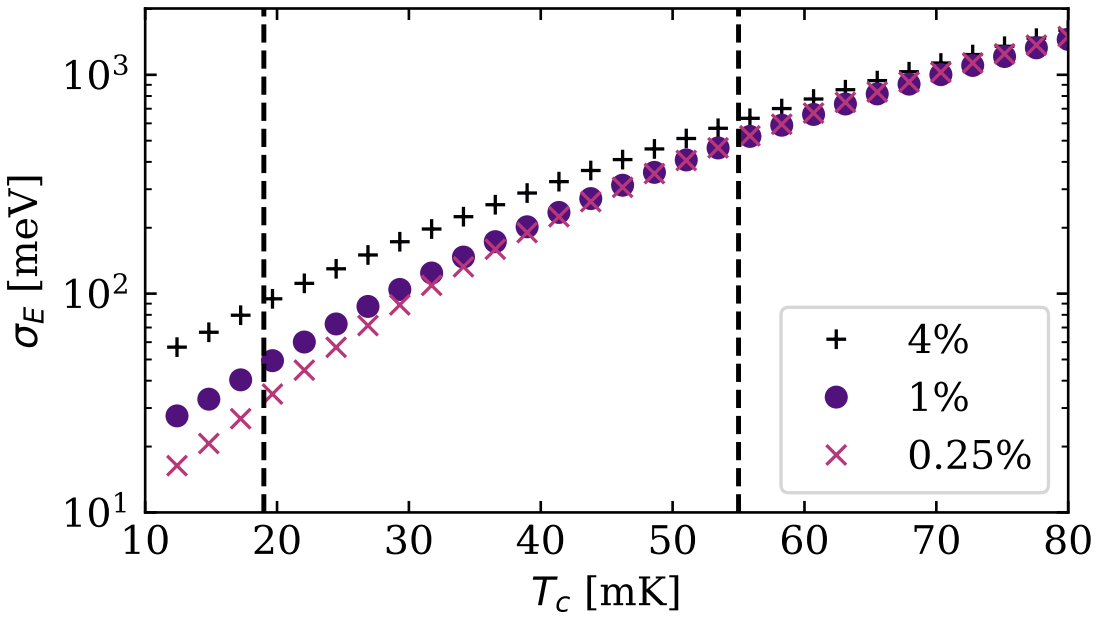

Figure 4.14: Simulated baseline energy resolution for the 0.25%, 1%, and 4% MELANGE devices as a function of T_c. The two dashed lines correspond to the expected T_c's from the first two fabrication runs of the mask.

We can now use these energy resolutions to get an idea of the DM reach that these detectors will have. In a previous dilution refrigerator in our lab with a lead shield placed around the detectors, we have observed a flat background rate above $\mathcal{O}(100\,\text{eV})$ of 10^4 events/keV/kg/day. In our new lab, we are currently working on a system to surround our detector package with this same lead shield, so we are confident we will achieve this same background rate. If we make the optimistic assumption that this background will remain flat down to our detector threshold, we can simulate the detectors sensitivity to Nuclear recoil DM in Fig. 4.15. We can see that even the high-T_c devices should be able to probe new NR DM parameter space. Clearly the there are many assumptions that go into this flat background model, namely the fact that many existing DM experiments have observed unexplained elevated low-energy excess background rates. The details of this are beyond the scope of this thesis, but fellow graduate student Samuel Watkins has a whole chapter on what we think these backgrounds might be, and how we can minimize them with our detectors.

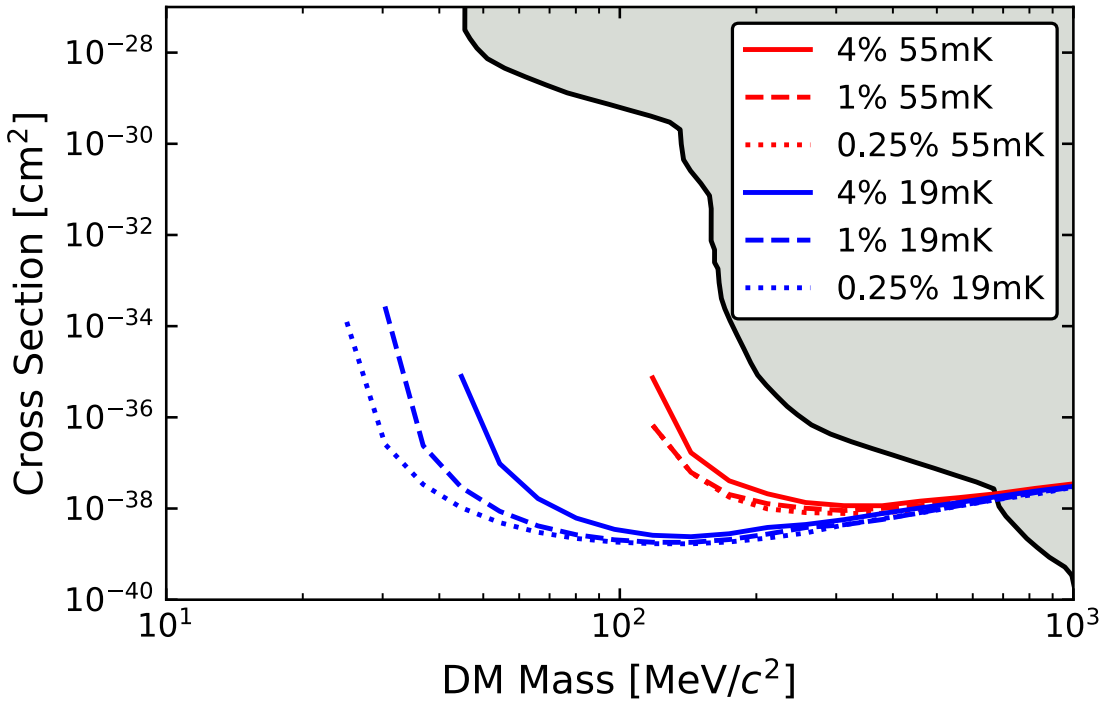

Figure 4.15: Nuclear recoil DM sensitivity projections for the 0.25%, 1%, and 4% MELANGE devices at $T_c = 19\,\text{mK}$ (blue) and $T_c = 55\,\text{mK}$ (red) assuming a flat background of 10^4 events/keV/kg/day. Shown in grey are the current NR DM limits from existing experiments.

4.9 Chapter Conclusion

This chapter presented an overview of the design of a full set of athermal phonon sensitive dark matter detectors. This chapter serves as a reference for both the optimization process, as well as a home for all the design parameters for initial prototype SPICE/HeRALD detector set. In the following chapters, we will switch gears to the study of detector performance. Chapter 5 will discuss the general techniques we used to study our detectors. Chapter 6 will detail the characterization of an older set of TES rectangles and the characterization of a photon detector used by SuperCDMS in a LDM search. Chapter 7 will discuss the initial performance of the SPICE MELANGE detector described in this chapter.

Part III

Detector Testing

Chapter 5

Experimental Techniques

After spending many chapters on detector design, the remainder of this thesis will focus on experimental techniques and results. This chapter is relatively short and mostly serves as an introduction to some of the analysis tools used in our group to characterize athermal phonon sensors. Most of the following analysis techniques and corresponding code were developed in collaboration with fellow grad student Samuel Watkins.

5.1 Overview of Experimental Setup

At the heart of our UCB lab is the CryoConcept 200 μW Ultra Quiet Dilution Refrigerator capable of achieving base temperatures of ~ 6 mK. The detectors are placed on the mixing chamber plate (MC) at base temp in an EMI tight copper housing. The current through the TESs is read out by repurposed CDMSII SQUIDs which are housed on the cold plate (CP) at ~ 100 mK. A picture of the various stages in the fridge can be seen in Fig. 5.1 and a wiring diagram of the cryogenic electronics can be see in Fig. 5.2. More details of the cryogenic electronics I played a large roll in designing can be found in Appendix D.

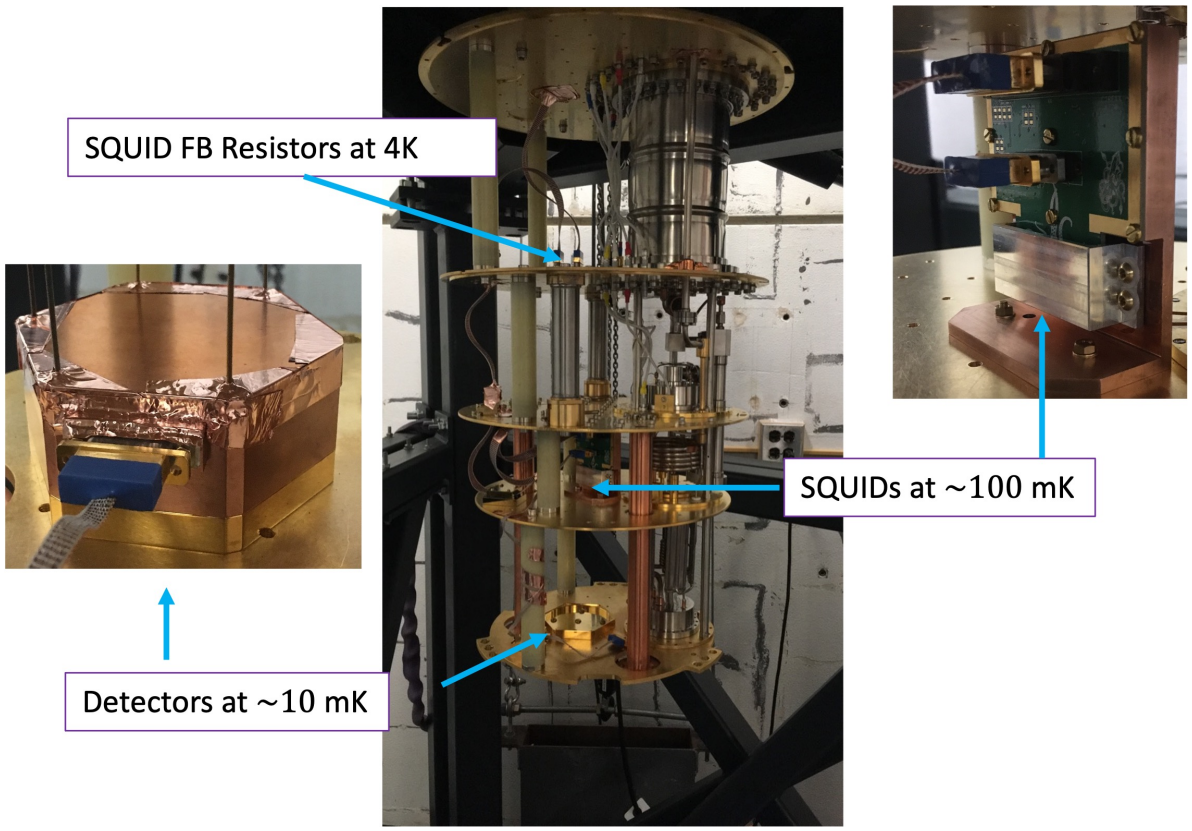

Figure 5.1: Picture of the dilution refrigerator used in the UCB Pyle Group lab with key electronics and detector stages highlighted.

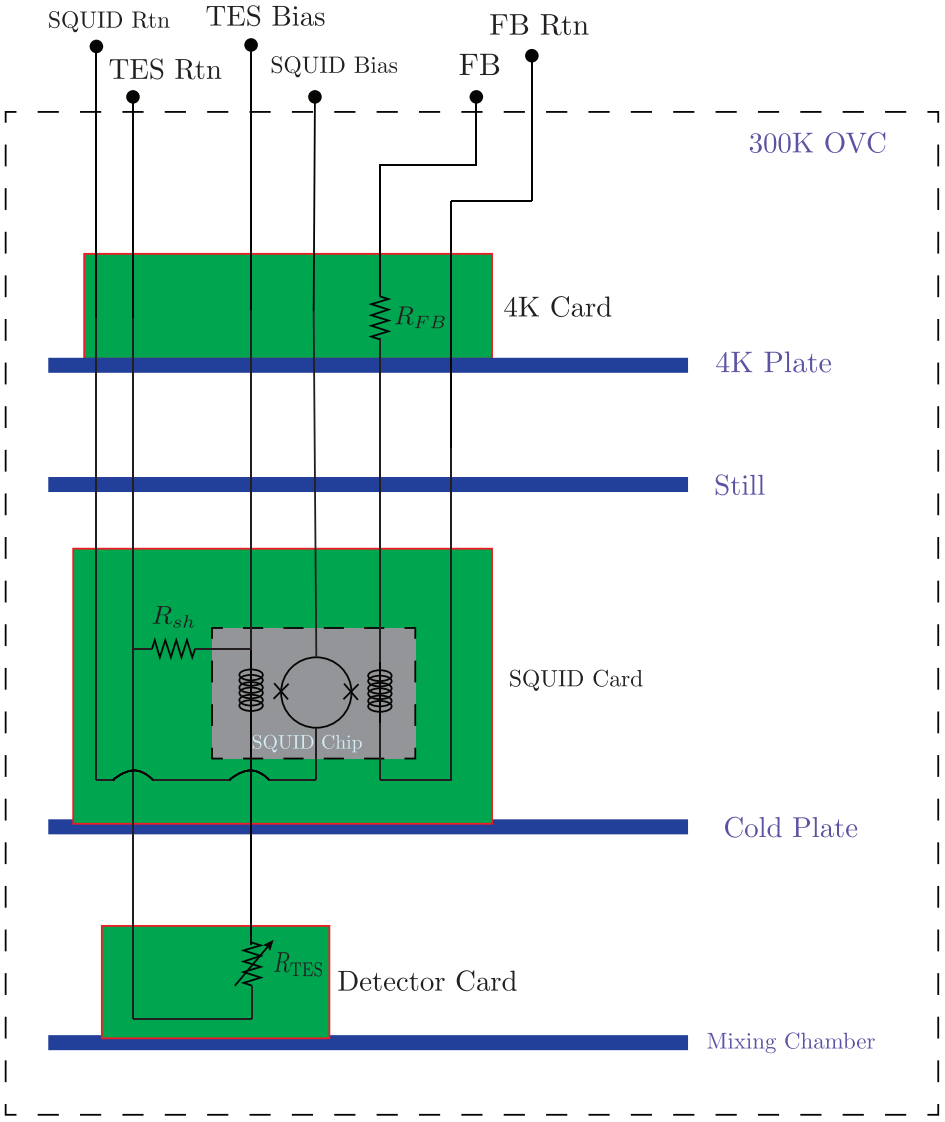

Figure 5.2: Schematic model of the cryogenic side wiring. This diagram represents a single channel of readout. Not pictures are ground lines and LED lines.

For the room temperature electronics outside the cryostat, the CDMSII front end boards (FEB) and RFT boards are used for the amplifiers and filters. After pre-amplification a National Instruments analog-to-Digital Converter is used to digitize the signal. For more details of the SQUID amp and FEBs in general, see any pre-SuperCDMS era CDMS thesis, specifically Appendix I of Kyle Sundqvist's thesis [141]. The DAQ system used in our lab is custom built, but essentially records a continuous data-stream at a digitization rate of 1.25 MHz. A schematic of this signal flow can be seen in Fig. 5.3.

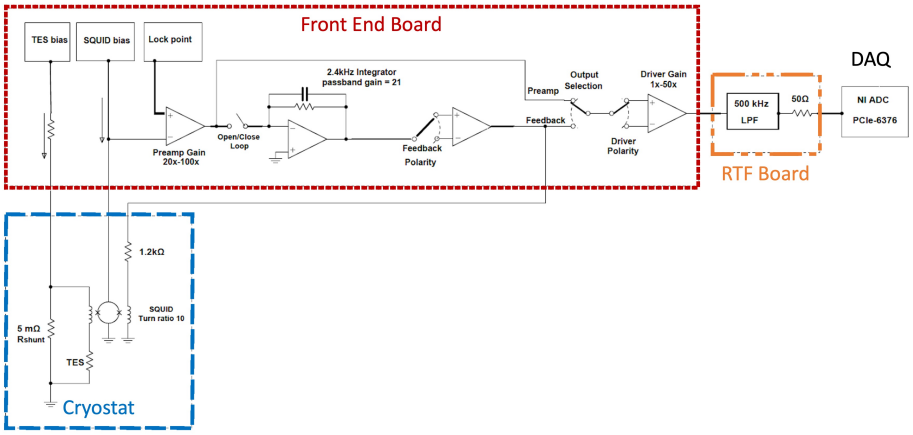

Figure 5.3: Schematic model of the detector readout chain.

5.2 Experimental Techniques

Before getting into the analysis of the detectors, I will talk in general about some of the techniques used by our group to characterize a device. As discussed in chapter 3, since the time scales of most physical processes of interest in a QET are much shorter than the relevant times scales of the TES, in most cases a QET based device can be treated as if it were simply made of TESs, with a penalty factor from the phonon collection efficiency.

It is helpful to define the goal of the analysis: measure the fundamental TES properties such that we can understand how to improve the baseline energy sensitivity. The details of the measurements are described in the following sections, but for now a list of the basic measurable parameters is shown in table 5.1. Additionally there are parameters that can be derived from these, with the addition of prior constraints. How these are derived and fit will be described next. In table 5.3 we can see typical electronic values for our experimental setup.

5.2.1 $I_B I_S$-Complex Admittance Sweeps

Perhaps one of the most common measurements of electronics components is a DC 'IV' sweep; how does the output current change as a function of applied voltage. In CDMS, we typically refer to this as an $I_B I_S$ measurement[1], but I will switch between both names throughout this chapter.

At every bais point in the IV sweep, two types of data are taken:

1. **Noise Data:** this is simply a few min of randomly sampled traces.

[1] I_B for applied QET bias and I_S for sensor current.

Table 5.1: List of basic measurable TES parameters

Parameter	Data type used to measure
$R_{\rm sh}$	Specified by manufacture (assumed 10% error)
R_p	$I_B I_S$
R_0	$I_B I_S$
P_0	$I_B I_S$
L	Bounded by SC dIdV data
β	dIdV
τ_I	dIdV
τ_+	dIdV
τ_-	dIdV
$G_{\rm TA}$	$I_B I_S$ vs T_B
n	$I_B I_S$ vs T_B
T_c	$I_B I_S$ vs T_B
T_ℓ	SC noise data
n_{SQ}	Normal noise data
f_{SQ}	Normal noise data

Table 5.2: List of derived TES parameters

Parameter	Required knowledge
τ	high T_B dIdV
$\mathscr{L}$	Needs good measure of τ and R_0
α	$\mathscr{L}$, P_0, and n
C	τ and $G_{\rm TA}$

Table 5.3: List of typical values used in our electronics.

Parameter	Typical Value
$R_{\rm sh}$	Specified by manufacture (assumed 10% error)
R_p	$2.5\,\mathrm{m\Omega}$
L	$250 - 450\,\mathrm{nH}$
T_ℓ	$65 - 75\,\mathrm{mK}$

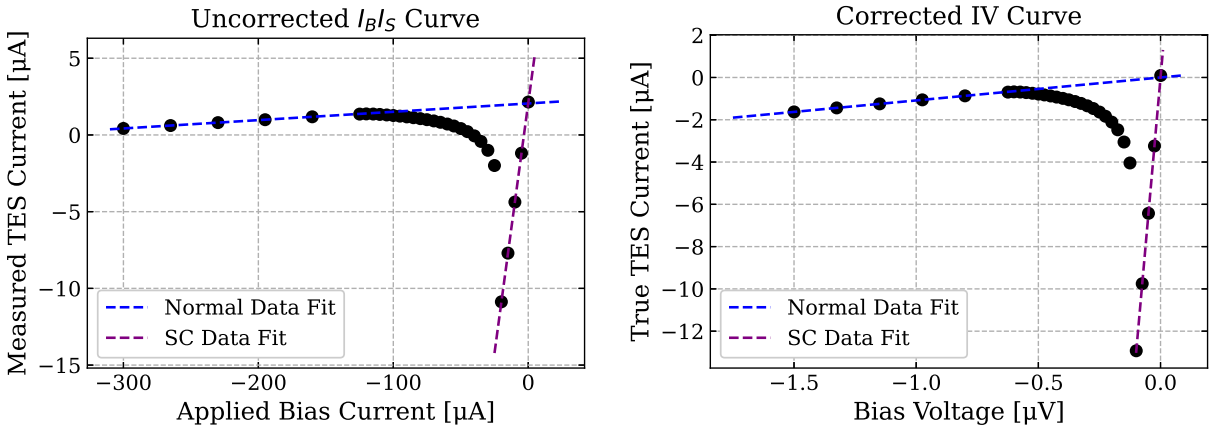

Figure 5.4: $I_B I_S$ or 'IV' curves before (left) and after (right) correction of SQUID and bias offsets.

2. **dIdV Data:** a small square wave is applied down the bias line when the data is taken. A derivation of the time-domain response of a TES to a small square wave excitation can be found in appendix C.

The first data type is typically what we refer to as the 'IV' data. Since the current through the TES is readout with a DC SQUID array, only a measurement of the relative current is possible. When we measure an IV sweep, we apply a bias of

$$I_{\text{Bias}}^{\text{Applied}} = I_{\text{Bias}}^{\text{True}} + I_{\text{Bias}}^{\text{offset}}, \tag{5.1}$$

and get a current response of

$$\Delta I_{\text{TES}} = I_{\text{TES}}^{\text{True}} + I_{\text{SQUID}}^{\text{offset}}. \tag{5.2}$$

Ultimately we wish to understand $I_{\text{TES}}^{\text{True}}$ as a function of $I_{\text{Bias}}^{\text{True}}$. The two offsets can be corrected for in the IV sweep so long as the SQUID stays locked in the same point throughout the duration of the sweep. From the left plot in Fig. 5.4, it is clear that there are two points in which the system behaves like simple resistors. Recall from the circuit in Fig. 2.2, when the TES is normal the IV characteristics should be that of a resistor of $R = R_N + R_\ell$, and when the TES is superconducting, the system will look like a resistor of $R = R_\ell$. By fitting the slopes and intercepts of these two regimes, the offsets can be corrected by the fact that we know the two lines must intersect each other at (0,0). The corrected IV curve, and fits of the SC and N regimes can be see in the right plot of Fig. 5.4.

Once the true bias and TES currents are known, they can be used to calculate the TES resistance (see left plot in Fig. 5.5). With the TES resistance now know, the bias power can be calculated (see right plot in Fig. 5.5). Notice how the plot of the bias power has again

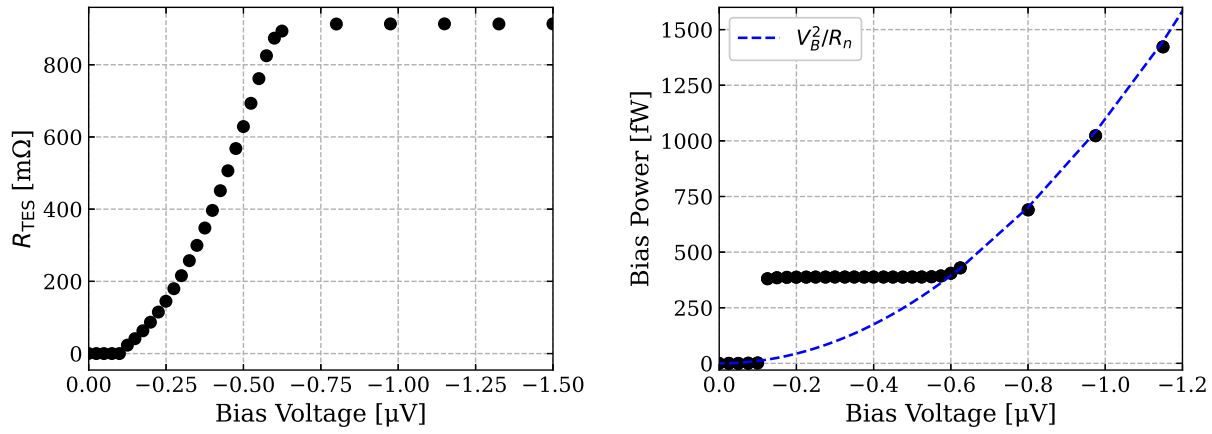

Figure 5.5: TES resistance (left) and Bias Power (right) as a function of TES bias voltage. Shown on the right is also the expected power from a pure resistor of resistance R_N.

two regions that match what would be expected from a normal resistor, shown as a dashed blue line. The region where the TES is in transition is the area where the power is constant, this is due to the fact that in the electrothermal feedback regime, the joule heating is in equilibrium with the cooling power of the bath.

5.2.2 Complex Admittance

Superconducting and Normal

With the complex admittance data taken at every bias point, the dynamic information of the TES can be extracted as a function of QET bias. For the regions where the TES is either superconducting or normal, the data can be fit to the complex admittance of the bias circuit given by

$$Z(\omega) = \frac{\partial V}{\partial I} = R_\ell + j\omega L \quad \text{(superconducting)} \tag{5.3}$$

$$Z(\omega) = \frac{\partial V}{\partial I} = R_\ell + R_N + j\omega L \quad \text{(normal)}. \tag{5.4}$$

We can see that these fits also give a cross check for the values of R_p and R_N found from the IV analysis, although their uncertainties are typically much larger than those found from the IV. The most valuable parameter obtained from these fits however is a robust measure of the TES inductance L from the SC data (the SQUID feedback amplifier typically limits one from seeing the inductance while in the normal state). Typical fits of both superconducting and normal state complex admittance data are shown in Figs. 5.6 and 5.7.

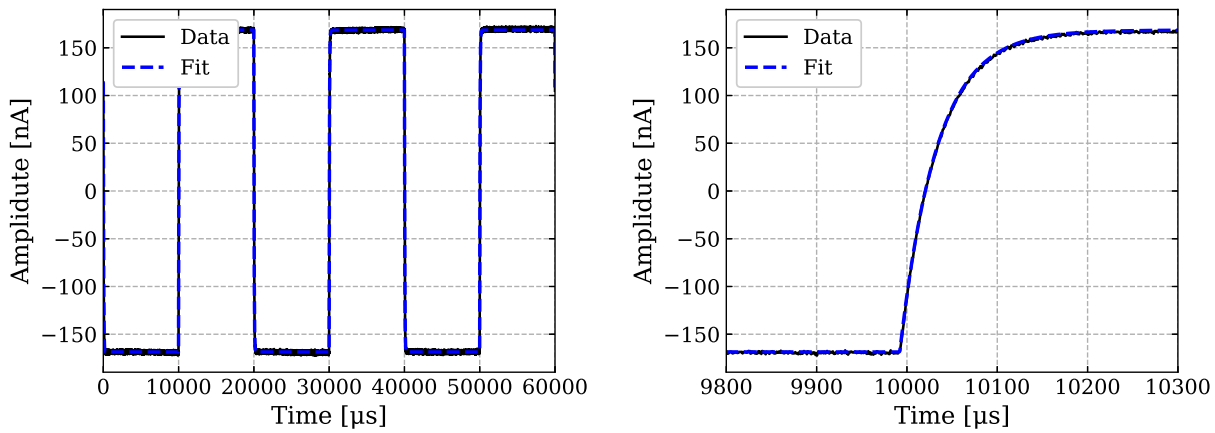

Figure 5.6: Left: Typical fit of superconducting complex admittance data shown in time domain. Right: zoomed in version of fit.

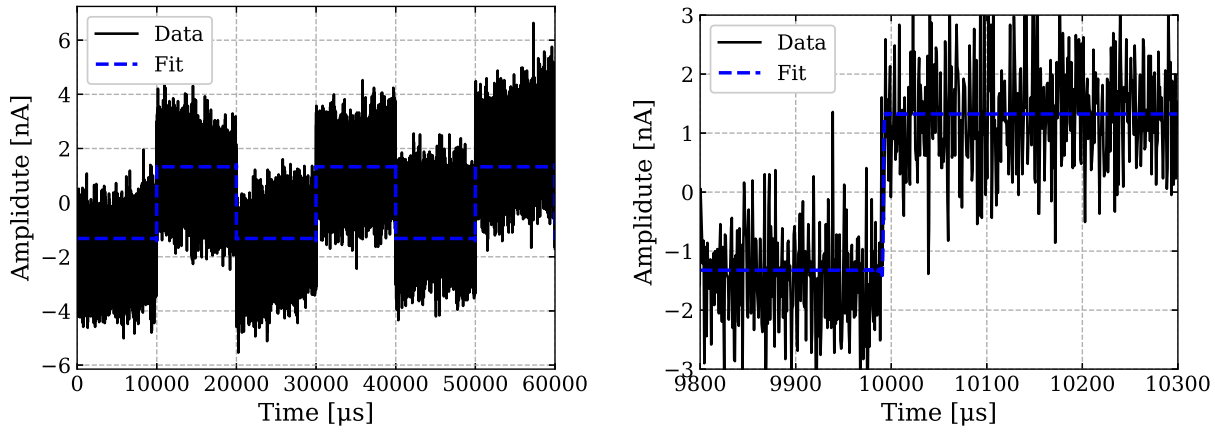

Figure 5.7: Left: Typical fit of normal state complex admittance data shown in time domain. Right: zoomed in version of fit.

Transition State

Recall from chapter 2, the complex impedance contains all the relevant information about the TES. The complex impedance is parameterized by

$$Z(\omega) = R_\ell + R_0(1+\beta) + i\omega L + \frac{\mathscr{L} R_0(2+\beta)}{(1-\mathscr{L})} \frac{1}{1+i\omega\tau_I}, \tag{5.5}$$

where again the loopgain is defined as

$$\mathscr{L} = \frac{P_{\rm bath}\alpha}{GT} = \frac{\alpha}{n}\left(1 - \frac{T^n_{\rm bath}}{T^n_0}\right). \tag{5.6}$$

We can see that Eq. 5.5 has many degeneracy's, thus the function must be re-parameterized before it can be fit. We re-define the equation to be

$$Z(\omega) = A(1 + j\omega\tau_{el}) + \frac{B}{1+j\omega\tau_I}, \tag{5.7}$$

where

$$A = R_\ell + R_0(1+\beta) \tag{5.8}$$

$$B = \frac{R_0\mathscr{L}}{1-\mathscr{L}}(2+\beta) \tag{5.9}$$

$$\tau_{el} = \frac{L}{R_\ell + R_0(1+\beta)} \tag{5.10}$$

$$\tau_I = \frac{\tau}{1-\mathscr{L}}. \tag{5.11}$$

The fit for these parameters can be done without any user input. With R_0 and R_ℓ previously known from the IV data, the small signal TES parameters can then be calculated from

$$\beta = \frac{A - R_\ell}{R_0 - 1} \tag{5.12}$$

$$\mathscr{L} = \frac{B}{A + B + R_0 - R_\ell} \tag{5.13}$$

$$L = \frac{A}{\tau_{el}} \tag{5.14}$$

$$\tau = \tau_I \frac{A + R_0 - R_\ell}{A + B + R_0 - R_\ell}. \tag{5.15}$$

Note that although we have an good estimate of L from the superconducting complex admittance data, the L is this case is actually an effective L due to the fact that this inductance does change slightly throughout the transition as a consequence of the mutual inductance between the input and feedback coils in the SQUID [142].

Table 5.4: Parameters used for generation of fake TES complex impedance data.

Parameter	Data type used to measure
R_{sh}	$5\,\mathrm{m}\Omega$
R_p	$5\,\mathrm{m}\Omega$
R_0	$100 - 250\,\mathrm{m}\Omega$,
L	$200\,\mathrm{nH}$
β	0.1
τ	$1.7\,\mathrm{ms}$
$\mathscr{L}$	100

Combining these with our definition of loopgain in Eq. 5.6, we can calculate the logarithmic temperature sensitivity α. Unfortunately, measuring α in practice is quite challenging. The way that the loopgain manifests in the complex impedance is non-linear and also causes A, B, and τ_I to be highly correlated. This causes the uncertainties in τ and $\mathscr{L}$ to be very large. To illustrate this, we can take a small aside to look at some fake complex impedance data. We generate fake complex admittance data with the parameters from table 5.4. Noise is added to this from a PSD generated from the same parameters. A plot of the average trace, as well as the TES response for the true parameters (TES response before addition of noise) can be seen in Fig. 5.8.

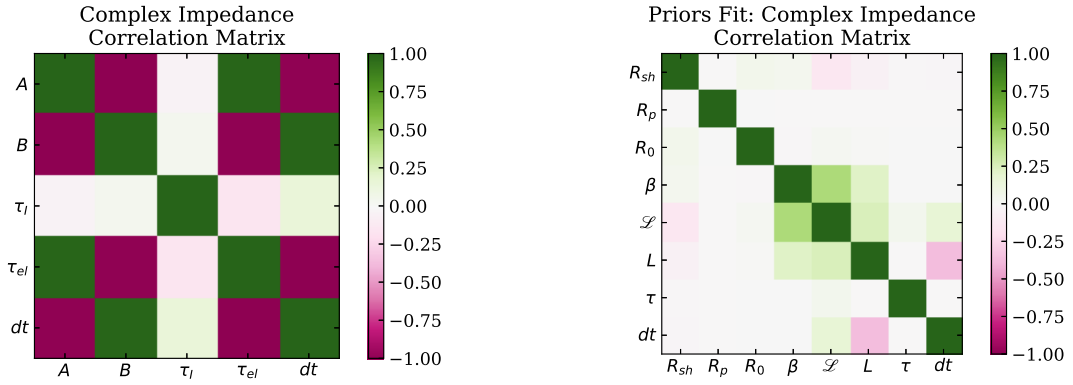

Figure 5.9: Left: correlation matrix for best fit parameters. Right: correlation matrix for the same data-set, but fit using prior constraints on the τ parameter.

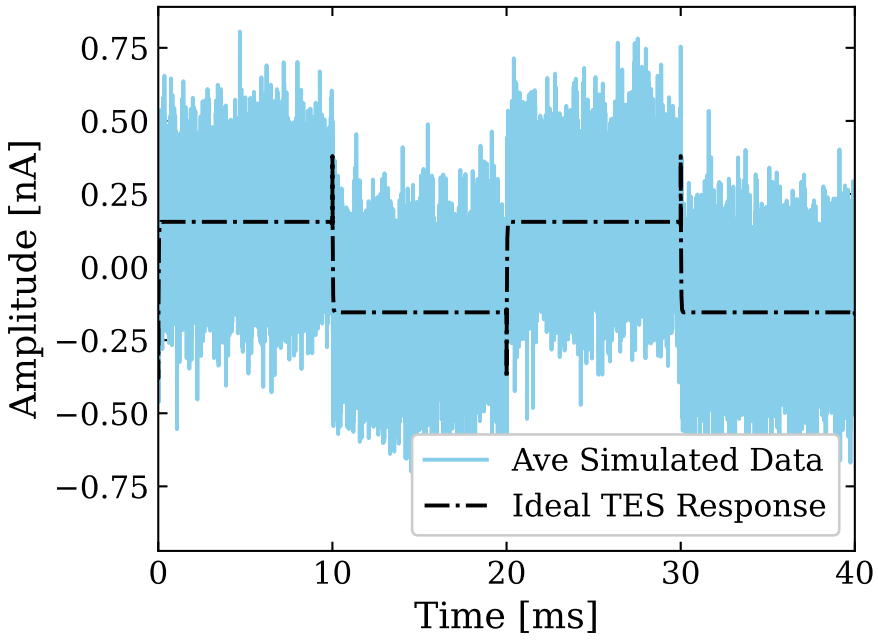

Figure 5.8: Fake complex impedance data

We fit the fake data-set generated over a range of R_0 values and convert the best fit parameters to the small signal TES parameters. The correlation matrix for a typical fit can be seen in Fig. 5.9 (left) which shows how most of the parameter are *strongly* correlated.

Improved Fitting with Priors

We can improve the situation if we have any prior knowledge of some of the calculated small signal parameters in the previous section. We can re-do the fit, but using a log-likelihood technique in which priors are included on all 'known' parameters. In this case, Eq. 5.5 is fit directly, where all parameters are considered 'free', including R_{sh}. This fit will only give sensible results when strong priors on the degenerate terms are given. The two parameters that are often the most difficult to disentangle are τ and $\mathscr{L}$, where the reason for this can easily be seen in the definition of τ_I.

In our fake dataset, let us repeat the fit from before, but using the 'priors fit' with only a strong prior on τ. Best fit values for τ and $\mathscr{L}$ before and after the 'priors fit' can be seen in Fig. 5.10 and Fig. 5.11 respectively. Unsurprisingly, the errors on τ are very small when given a prior constraint on τ. More importantly though, notice that the fitted values for $\mathscr{L}$ are much closer to the true value, and the errors have shrunken substantially. Finally, the correlation matrix for the priors fit can be seen in Fig. 5.9, where we can see that the off diagonal terms have been substantially reduced.

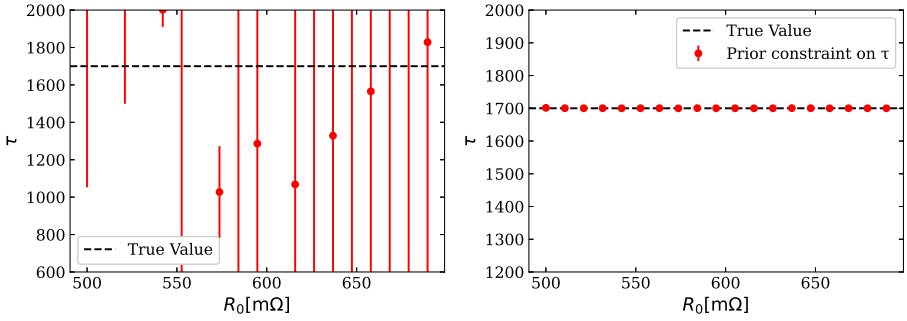

Figure 5.10: Left: Fits of τ for various simulated complex admittance data-sets. Right: Fits of τ for the same simulated data, but with a prior constraint placed on τ.

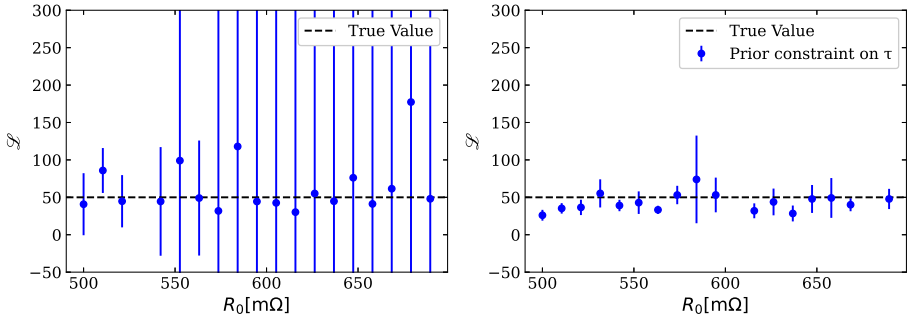

Figure 5.11: Left: Fits of $\mathscr{L}$ for various simulated complex admittance data-sets. Right: Fits of $\mathscr{L}$ for the same simulated data, but with a prior constraint placed on τ.

The question now becomes, how do we get the prior value of τ in the first place? Recall the from of the loopgain in Eq. 5.6 that there is a strong dependence on bias power, or rather T_B. The loopgain can be made arbitrarily small when the bath temperature approaches T_c. Thus fitting complex admittance data at $T_B \sim T_c$ can allow for more robust measurements of τ. Recall $\tau = C/G$, where the C and G are determined at the operating temperature T_c. This operating temperature is the same regardless of T_B, thus a measure of τ for high T_B should be invariant of temperature. This can now be used as a strong prior on τ for lower bath temperature IV sweeps to get better fits for $\mathscr{L}$. In practice however this sometimes proves to be challenging.

An alternative method that should be robust, but would require the modification of existing code, would be to chose complex admitance data from the same point in transition for a variety of bath temperatures. Then construct a loss function in which all of these data were fit simultaneously to Eq. 5.5 with the constraint that τ must be constant for all the fits. By doing this, the degeneracy between τ and $\mathscr{L}$ is broken.

For completeness, a typical fit to real complex admittance data is shown in Fig. 5.12.

5.2.3 Noise Modeling

Estimation of SQUID Noise Model

After the basic DC parameters are extracted from the IV data and the complex admittance is fit, we can begin to analyze the noise. Our system is designed such that when the TES is in its normal state, the Johnson noise from the TES and the load resistance will be subdominant to the SQUID and readout electronics noise. We can therefor fit the normal state noise PSD to the function

$$S_{I_{\text{Normal}}} \approx S^{\text{N}}_{I_{\text{TES}}} + S_{\text{SQUID}}, \tag{5.16}$$

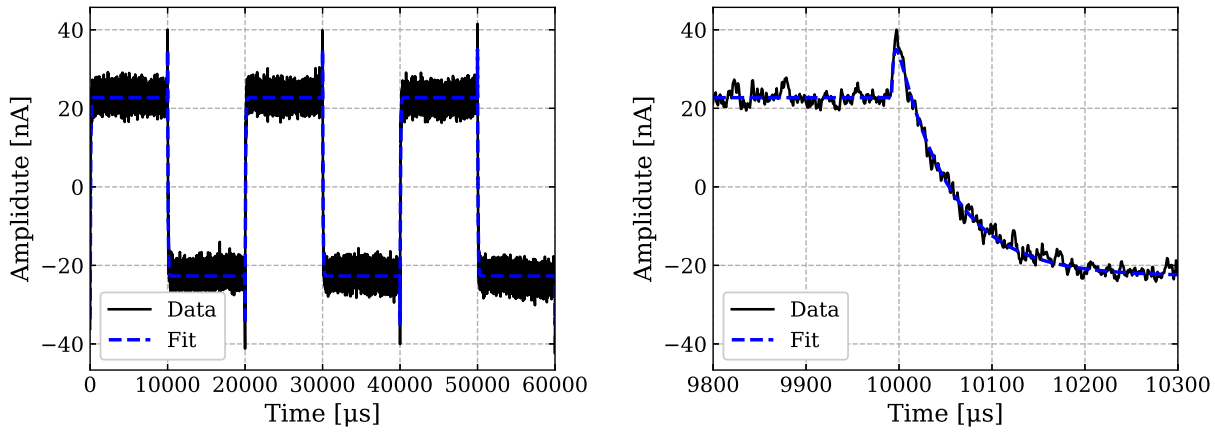

Figure 5.12: Left: Fit of transition state complex admittance data shown in time domain. Right: zoomed in version of fit.

where

$$S_{I_{\mathrm{TES}}}^{\mathrm{N}} = 4k_B T_0 R_N \left| \frac{1}{R_\ell + R_N + j\omega L} \right|^2 \tag{5.17}$$

and S_{SQUID} is given by Eq. 2.89, which is repeated below for convenience:

$$S_{I_{\mathrm{SQUID}}} = \left(S_{\mathrm{SQUID}}^{\mathrm{white}} \left[1 + \left(\frac{\omega_{\text{cut-off}}}{\omega} \right)^{n_{\mathrm{SQUID}}} \right] \right)^2 . \tag{5.18}$$

In this fit, only the SQUID parameters $S_{\mathrm{SQUID}}^{\mathrm{white}}$, $\omega_{\text{cut-off}}$, and n_{SQUID} are free. We can neglect the contribution from the load resistance at this point, as it will be significantly less than the Johnson noise from the TES. An example of this fit can be seen in Fig. 5.13.

Estimation of Load Resistance Temperature

Now that we have a handle on the SQUID plus any downstream electronics noise, we can use the superconducting state noise to estimate the temperature of the load resistance. When SC, the noise of the load resistance is no longer being heavily suppressed by R_N like it was when the TES was normal,

$$S_{I_\ell}^{\mathrm{SC}} = 4k_B T_\ell R_\ell \left| \frac{1}{R_\ell + j\omega L} \right|^2 . \tag{5.19}$$

Thus when the TES is SC, the load resistance is by far the dominant noise source, and we can fit the PSD to

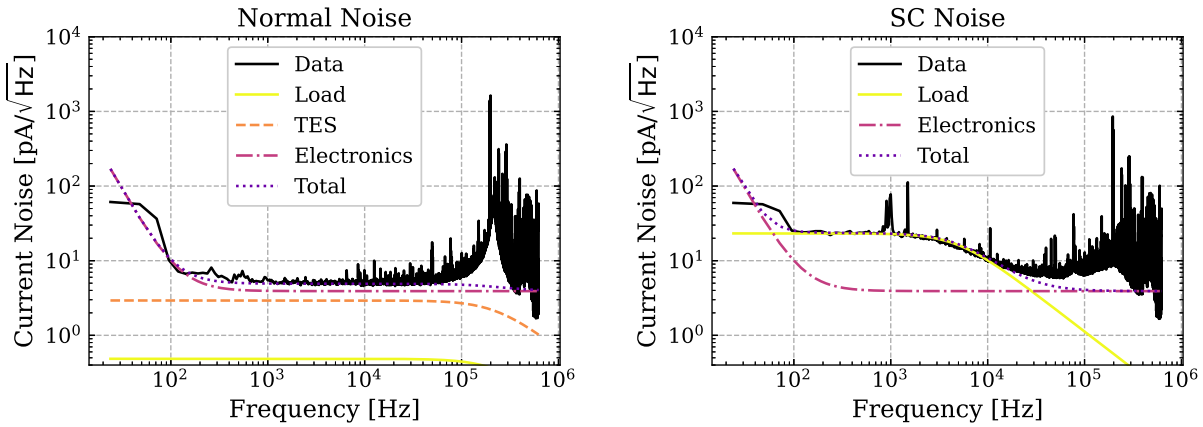

Figure 5.13: Left: Normal state noise referenced to TES current, shown with the best fit noise model parameters. Right: SC state noise referenced to TES current, shown with the best fit noise model parameters.

$$S_{I_{\rm SC}} = S_{I_\ell}^{\rm SC} + S_{\rm SQUID}, \tag{5.20}$$

where the SQUID noise is now fixed and we can extract T_ℓ. An example fit is shown in Fig. 5.13. From table 5.3, typical values for T_ℓ can be seen. We can check this value against our expectation. From Fig. 5.2, we know that R_{sh} is held at the temperature of the CP, which is typically $60 - 100\,\mathrm{mK}$, and we have $\sim 1\,\mathrm{m\Omega}$ of parasitic resistance from the contact resistance in the connector at the SQUID card and $\sim 1\,\mathrm{m\Omega}$ at the MC detector card. Summing up all these contributions, a fitted value of $60 - 75\,\mathrm{mK}$ seems right in line with expectations.

Estimation of Thermal Conductance

At this point, the SQUID/electronics noise has been measured, load resistance temperature measured, and dynamic TES characteristics measured from the complex admittance data. Before the noise in transition can be modeled[2], we need to first estimate the thermal conductance between the TES and the absorber $G_{\rm TA}$. This can be done in two different ways. From Eq. 2.4, in the limit that we have no parasitic power and that $T_B \ll T_0$, then the thermal conductance can be simply estimated as

$$G \approx \frac{nP_0}{T_0}. \tag{5.21}$$

[2]described in section 2.3.

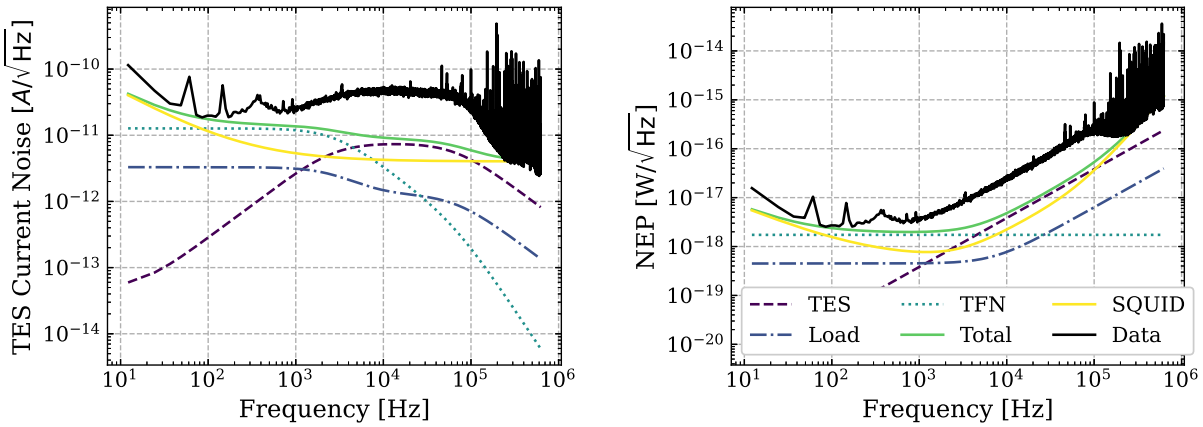

Figure 5.14: Left: Transition state noise model and data referenced to TES current. Right: Transition state noise model and data referenced to TES power.

The other, more robust, method is to fit Eq. 2.3 directly as a function of bath temperature. This can by done by taking multiple IV sweeps at various bath temperatures, selecting a point of constant R_0 across all temperatures, and fitting the corresponding bias powers as a function of T_B. See chapter 7 for an example of this. This method offers the advantage that it also gives you T_c and n as part of the fit. This method however is still not able to disentangle the issue of parasitic power, as this power would be removed with the same temperature scaling as the bias power. Since we are typically able to operate in the limit where $T_B \ll T_c$, we often use the former approximation, and assume $n = 5$.

With the thermal conductance in hand, we can now compare the modeled noise components with the measured noise power, example shown in Fig. 5.14 (left). The real figure of merit of a bolometer or calorimeter is the noise equivalent power (NEP). This is measured by referencing the current-noise PSD to TES power with the power-to-current-responsivity from Eq. 2.50 using measured values from the complex admittance data,

$$\mathrm{NEP}^2 \equiv S_p(\omega) = S_I(\omega) \left| \frac{\partial I}{\partial P}(\omega) \right|^{-2}. \tag{5.22}$$

An example NEP plot can be seen in Fig. 5.14 (right).

The final step in the analysis chain is to integrate the signal-to-noise ratio in power space using this NEP to calculate the expected energy resolution from Eq. B.2. This is done for all bias points in transition. If the athermal phonon collection efficiency has already been measured (see next section), this value should be included in this step.

5.3 Estimating Logarithmic Temperature Sensitivity

The above analysis tools are all packaged into an integrated suite in which multiple types of data are stitched together to estimate most of the TES parameters in an automated way. As was discussed, the estimate of $\mathscr{L}$ and thus α can be quite troublesome. Below is an alternative method to estimate this parameter from the same types of data.

While α can be somewhat measured from the complex admittance data, it is highly degenerate with other parameters, eg $\mathscr{L}$ and τ. We can however estimate it using a measured value for Σ_{ep}^{W} (see section 7.3.2 for a discussion of this measurement) and a measure of τ_{ETF}. Note that τ_{ETF} is a parameter that we can measure quite well. Recall from Eq. 2.53, the electrothermal time constant is given by

$$\tau_{\mathrm{ETF}} = \tau \frac{1+\beta+R_\ell/R_0}{1+\beta+R_\ell/R_0+(1-R_\ell/R_0)\mathscr{L}}. \tag{5.23}$$

From Eq. 3.101 we know the heat capacity is given by

$$C = f_{sc} c_W V_{eff}^{\mathrm{total}} T_c. \tag{5.24}$$

And as before, we know

$$G = n\Sigma_{ep}^{\mathrm{W}} V_{eff}^{\mathrm{total}} T^{n-1}, \tag{5.25}$$

Thus the natural time constant in the ETF time constant is

$$\tau = \frac{C}{G} = \frac{f_{sc} c_W}{n\Sigma_{ep}^{\mathrm{W}} T_c^{n-2}}. \tag{5.26}$$

Finally, recall the definition of the loopgain from Eq. 2.18,

$$\mathscr{L} = \frac{P_{J_0}\alpha}{GT_c}. \tag{5.27}$$

From Eqs. 5.23, 5.26, 5.27 we can see that we have everything measured (using the literature value for the W specific heat from table 3.2) except α. We can thus tune the value of α to match the measured electrothermal time constant. Note that in this estimate, there will be a systematic on the T_c due to any parasitic power.

5.4 Phonon Collection Efficiency

The total athermal phonon collection efficiency (ε) is one of the simplest measurements we do, and is somewhat a stand-alone measurement from the previous sections. It requires a calibration source with known energy, commonly an X-ray/gamma source, or in the future

a fiber optic setup. Recall from section 2.1.3 that the energy removed by the TES from electrothermal feedback can be written as

$$E_{\mathrm{ETF}} = \int \Delta P_J dt = \int_0^\infty \left[(V_B - 2I_0 R_\ell)\Delta I(t) - \Delta I^2(t) R_\ell\right] dt. \tag{5.28}$$

Where I_0 is the true baseline current, and $\Delta I(t)$ is the baseline subtracted TES current as a function of time.

To estimate ε, one selects a pulse (or preferably an average of pulses) with the known energy from the calibration source, numerically evaluates Eq. 5.28 for the pulse, and divides this energy by the known true energy of the pulse. It is as simple as that! For an example of how this is done in practice for the CPDv1 detector using an ^{55}Fe source, see section 6.2.5.

5.5 Future Updates to Characterization Analysis

The existing analysis suite described in this section allows for the characterization of a TES/QET sensor to be done in simply a few clicks of a mouse. As with any codebase, it can always be improved. There are a few specific improvements which should be implemented by future students.

Dynamic dV Excitation

In the current way the data is taken, a fixed square wave amplitude is used for all complex admittance data throughout the full IV sweep. Since this resistance of the TES is changing, the relative amplitude seen by the TES is changing as a function of bias point. This means that at some places in the transition the excitation is too large, and some places smaller than it needs to be. Ideally the excitation amplitude should be at a roughly constant relative level to the TES bias current.

Integration of High-T_{bath} Data

While we have discussed how the $\mathscr{L}$ parameter can be more precisely fit if prior knowledge of τ is known, it is a bit of a challenge to integrate this into the existing code. The tools are all in existance, but finding the correct high-T_{bath} dataset to use to get the priors and then plugged back into the base temperature IV sweep analysis must be done somewhat by hand. Figuring out a more automated way of first taking this high-T_{bath} data set and then integrating the results would be a huge improvement.

Estimation of Uncorrelated Noise Power

As will be discussed in the following chapters, one can use the time series data of multiple simultaneous channels to estimate the non-correlated components of the noise power for

each channel. While this is an analysis we commonly do, this is currently not automatically integrated into the IV sweep analysis.

This has by no means been an extensive list of everything done to characterize an athermal phonon detector, but hopefully provided enough of an overview to give a feel for the basic techniques used. The following chapters will take a deeper dive into the characterization of specific sensors and detectors.

Chapter 6

Characterization of TES and QET Based Detectors

The following chapter consists of two separate papers detailing the characterization of devices our group has designed and studied. The first section focuses on the characterization of low-T_c single TES test structures [137]. This paper is a direct application of the models introduced in the chapter 2 to simple TESs and describes the process of extracting TES parameters from data. The second section covers the characterization of a QET instrumented athermal phonon sensitive large area photon detector [84]. This section shows how the same models that describe single TESs can be applied to an aggregated array of TESs integrated with a larger detector target. Both of these devices were studied in the SuperCDMS test facility at the SLAC National Accelerator Laboratory. This data was collected during the period in time when our lab at UCB was not yet operational. The results of each of these papers were world leading at the time of publication (and possibly still so!)

6.1 Characterizing TES Power Noise for Future Single Optical-Phonon and Infrared-Photon Detectors

A version of this section was originally published as an Editor's Pick in *AIP Advances* as Ref. [137].

6.1.1 Abstract

In this letter, we present the performance of a $100\,\mu\text{m} \times 400\,\mu\text{m} \times 40\,\text{nm}$ W Transition-Edge Sensor (TES) with a critical temperature of 40 mK. This device has a noise equivalent power of $1.5 \times 10^{-18}\,\text{W}/\sqrt{\text{Hz}}$, in a bandwidth of 2.6 kHz, indicating a resolution for Dirac delta energy depositions of $40 \pm 5\,\text{meV}$ (rms). The performance demonstrated by this device

is a critical step towards developing a $\mathcal{O}(100)$ meV threshold athermal phonon detector for low-mass dark matter searches.

6.1.2 Introduction

As dark matter (DM) direct detection experiments probe lower masses, there is an increasing demand for sensors with excellent energy sensitivity. Several athermal phonon sensitive detector designs have been proposed using superconductors[143] or novel polar crystals[144–147] as the detection medium. Additionally, experiments that use single infrared (IR) sensitive photonic sensors to read out low band gap scintillators or multi-layer optical haloscopes for both axion and dark photon DM have also been proposed [148].

Each of these designs would ultimately require sensitivity to single optical-phonons or IR-photons, corresponding to energy thresholds of $\mathcal{O}(100)$ meV [143–145, 148]. Coherent neutrino scattering experiments have made recent progress using DM detector technology and are also interested in cryogenic detectors with very low thresholds [149]. Transition-Edge Sensor (TES) based detector concepts have been successfully applied in DM searches [150–152], as well as IR and optical photon sensors [153]. The same concepts can also be used in these new applications, as the necessary energy sensitivities can theoretically be achieved [143, 144].

The energy resolution of a calorimeter can be estimated with an optimum filter (OF) [76, 93] from

$$\sigma_E^2 = \left[\varepsilon^2 \int_0^\infty \frac{d\omega}{2\pi} \frac{4|p(\omega)|^2}{S_P(\omega)}\right]^{-1}, \tag{6.1}$$

where $S_P(\omega)$ is the total (one-sided) power-referred noise spectrum, ε is the total phonon collection efficiency, and $p(\omega)$ is power-referred pulse shape defined as $p(\omega) = 1/(1 + j\omega\tau_{ph})$, with τ_{ph} the athermal phonon collection time of the detector. The resolution for a TES-based calorimeter is minimized when the noise is dominated by the intrinsic thermal fluctuation noise (TFN) between the TES and the bath [81]. This noise can be written as

$$S_P(\omega) \approx 4k_B T_c^2 G F(T_c, T_B)(1 + \omega^2 \tau_{\mathrm{ETF}}^2), \tag{6.2}$$

where k_B is the Boltzmann constant, T_c is the superconducting (SC) critical temperature, T_B is the temperature of the bath, G is the dominant thermal conductivity between the TES and the bath, and $F(T_c, T_B) \approx 1/2$ is a scale factor accounting for the nonequilibrium nature of the thermal conductance. The effective time constant[1] in the strong electrothermal feedback zero inductance limit (also neglecting small effects from the resistance terms and the current sensitivity) can be approximated as $\tau_- \approx C\sqrt{2n}/(G\alpha)$, where α is the dimensionless temperature sensitivity, C is the heat capacity, and n is the thermal conduction power law

[1] This is also commonly referred to as τ_{eff}

exponent. Under this scenario, the integral in Eq. (6.1) becomes

$$\sigma_E^2 \approx \frac{1}{\varepsilon^2} 4 k_B T_c^2 G F(T_c, T_B)(\tau_{ph} + \tau_{\rm ETF}). \tag{6.3}$$

Note, as was derived in the previous chapter, this expression should actually have a τ_* instead of $\tau_{\rm ETF}$. However, in the limits this device is operating τ_* and $\tau_{\rm ETF}$ differ only by $\mathcal{O}(1)$ factors but contain the same fundamental scaling with volume and T_c, which is the only part important to the following arguments.

If the energy of an incident particle is absorbed directly by the TES, that is, $\tau_{ph} = 0$ and $\varepsilon = 1$, then the energy variance in Eq. (6.3) becomes

$$\sigma_E^2 \approx k_B T_c^2 \frac{C}{\alpha} \sqrt{\frac{n}{2}}\,. \tag{6.4}$$

For a metal in the low-temperature regime, the heat capacity scales with the volume of the TES ($\mathrm{V_{TES}}$) and the temperature as $C(T) \propto \mathrm{V_{TES}} T$, suggesting

$$\sigma_E^2 \propto \mathrm{V_{TES}} T_c^3. \tag{6.5}$$

However, if operated as an athermal phonon sensor, specifically a Quasiparticle-trap-assisted Electrothermal-feedback Transition-edge sensor (QET) [97], the energy sensitivity dependence on T_c becomes even more important. The energy resolution is minimized when athermal phonons bounce in the crystal for times long compared to the characteristic time scale of the TES sensor (i.e. $\tau_{\rm ETF} < \tau_{ph}$) [76, 143, 154], as long as the surface athermal phonon down-conversion rate is negligible [155]. In this case, the thermal conductance term is not cancelled from Eq. (6.3). For low-T_c W films, the thermal conductance is dominated by electron-phonon decoupling, thus scaling as $G \propto \mathrm{V_{TES}} T_c^{n-1}$ with $n = 5$, as confirmed by measurement described later in this letter. This implies that the baseline energy variance of the detector will scale with critical temperature as $\sigma_E^2 \propto T_c^6$, suggesting that a low-T_c device is ideal for single optical-phonon sensitivity.

6.1.3 Experimental Setup and Data

A set of 4 W TESs was fabricated on a 525 μm thick 1 cm × 1 cm Si substrate ("chip"). The smallest of the TESs was 25 μm × 100 μm × 40 nm. Each subsequent TES increased in area by a factor of four, keeping an aspect ratio of 1:4 (width : length), which implies all the TESs have the same normal resistance (R_N). The TES mask design can be seen in left panel Fig. 6.1. Two sets of these chips were made, one with TESs of $T_c = 40$ mK and the other with TESs of $T_c = 68$ mK. This letter focuses on the measurement and characterization of the low-T_c 100 μm × 400 μm × 40 nm TES (hereby referred to as simply "the TES"), but will also present characterization data from these other devices to elucidate scalings with T_c and volume. The utility of such devices for applications of photon detectors and athermal phonon sensors will also be discussed.

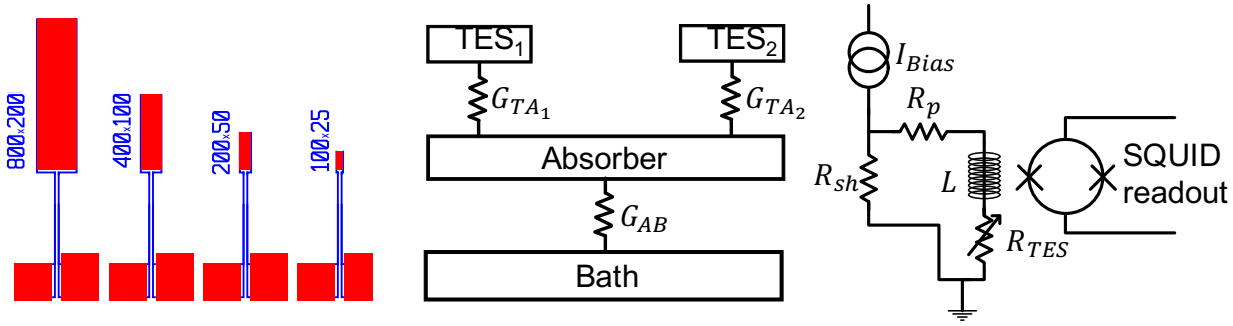

Figure 6.1: Left: TES mask design. The W is shown in red, while the blue represents Al bias rails. The Al connects to the left and right sides of the TES. Middle: Thermal model for experimental setup. For simplicity, only two TESs are shown in the model. Right: Electrical circuit. R_{sh} is a shunt resistor which turns the current source ($I_{\rm Bias}$) into a voltage bias. Any parasitic resistance on the shunt side of the bias circuit is absorbed into the value used for R_{sh} in this analysis. R_p is the parasitic resistance on the TES side of the bias circuit. L is the inductance in the TES line. $R_{\rm TES}$ is the TES resistance, which takes on a value of R_0 when in transition and takes on a value of R_N when its temperature is above T_c.

The voltage-biased TES was studied at the SLAC National Accelerator Laboratory in a dilution refrigerator at a bath temperature of 15 mK. The Si chip was mounted to a copper plate with GE varnish. The current through the TES was measured with a custom DC Superconducting Quantum Interference Device (SQUID) array system with a noise floor of $\sim$4 pA/$\sqrt{\rm Hz}$, fabricated for the SuperCDMS experiment, with a measured lower bound on the bandwidth of greater than 250 kHz. The SQUID array was read out by an amplifier similar to the one in Ref. [156].

Multiple measures were put in place to mitigate electromagnetic interference (EMI). Pi-filters with a cutoff frequency of 10 MHz were placed on all input and output lines to the refrigerator. Ferrite cable-chokes were placed around the signal readout cabling at 300 K, and the 4K and 1K cans were filled with broadband microwave-absorptive foam to suppress radio frequency (RF) radiation onto TESs. The outer vacuum chamber of the dilution refrigerator was surrounded by a high-permeability metal shield to suppress magnetic fields. These measures were the result of a systematic search of the system's susceptibility to environmental noise, and they lowered the measured electrical noise by roughly an order of magnitude. Despite these efforts, an unknown parasitic noise source remained, which inhibited the smallest two low-T_c TESs from going through their SC transition.

To characterize the TES, IV sweeps were taken at various bath temperatures by measuring TES quiescent current (I_0) as a function of bias current ($I_{\rm Bias}$)[2], with complex admittance

[2]We use the term "IV" even though we are applying a bias current, as the voltage and current are related by the shunt resistor: $V_{\rm Bias} = I_{\rm Bias} R_{sh}$

Table 6.1: Various calculated parameters of the TES.

R_{sh} [mΩ]	R_p [mΩ]	R_N [mΩ]	P_0 [fW]	G_{AB} [nW/K]	G_{TA} [pW/K]	T_c [mK]	T_B [mK]	T_ℓ [mK]	n
5.0 ± 0.5	5.8 ± 0.6	640 ± 65	31 ± 2	1.6 ± 0.1	4.0 ± 0.4	40 ± 1	15 ± 1	37 ± 2	5

data taken at each point in the IV curve [76, 77]. Data were also taken simultaneously with the largest low-T_c TES (TES2) on the same Si chip, biased at an operating resistance (R_0) of approximately 40% R_N, in order to attempt to quantify the amount of remaining excess noise that coupled coherently to both TES channels. From the IV sweep at each temperature, both the DC offset from the SQUID and any systematic offset in $I_{\rm Bias}$ were corrected for using the normal and SC regions of the data. After this correction, the parasitic resistance in the TES circuit (R_p), the normal state resistance, the TES resistance in transition, and the quiescent bias power (P_0) were calculated (see the right panel of Fig. 6.1 for circuit diagram).

Since the Si chip contained multiple TESs, the thermal conductance between the chip and the bath (G_{AB}) was measured by using one as a heater and one as a thermometer. Knowledge of G_{AB} allowed us to infer the temperature of the Si chip (T_A) from a measurement of T_B. See the middle panel of Fig. 6.1 for a thermal diagram of the setup. Measuring P_0 as a function of temperature from the IV sweeps, the thermal conductance between the TES and the Si substrate (G_{TA}), T_c, and n were fit to a power law [157], confirming our $n = 5$ assumption. We measured that G_{AB} was roughly 3 orders of magnitude larger than G_{TA}, meaning that T_A was effectively equal to T_B, and the system could be modeled as a single thermal conductance between the TES and the bath. The characteristics of the TES system from the IV data are shown in Table 6.5.

6.1.4 Parameter Estimation

For each point in transition, a maximum likelihood fit of the complex admittance was done, using the standard small-signal current response of a TES [81]:

$$\begin{aligned} Z(\omega) &\equiv R_{sh} + R_p + j\omega L + Z_{\rm TES}(\omega), \\ Z_{\rm TES}(\omega) &\equiv R_0(1+\beta) + \frac{R_0\mathscr{L}}{1-\mathscr{L}}\frac{2+\beta}{1+j\omega\frac{\tau}{1-\mathscr{L}}}. \end{aligned} \tag{6.6}$$

In this fit, L, R_0, R_p, R_{sh}[3], β, τ, and $\mathscr{L}$ are all free parameters. L is the inductance in the TES bias circuit, β is the dimensionless current sensitivity, τ is the natural thermal time constant, and $\mathscr{L}$ is the loop gain. We include the estimates from the IV data of R_0, R_p, and R_{sh} as priors in the fit. Additionally, we include a prior on L, measured from SC complex admittance data. The TES response times can also be measured from the

[3] R_{sh}, is a free parameter in the fit because we do not have a good measurement of it at cryogenic temperatures.

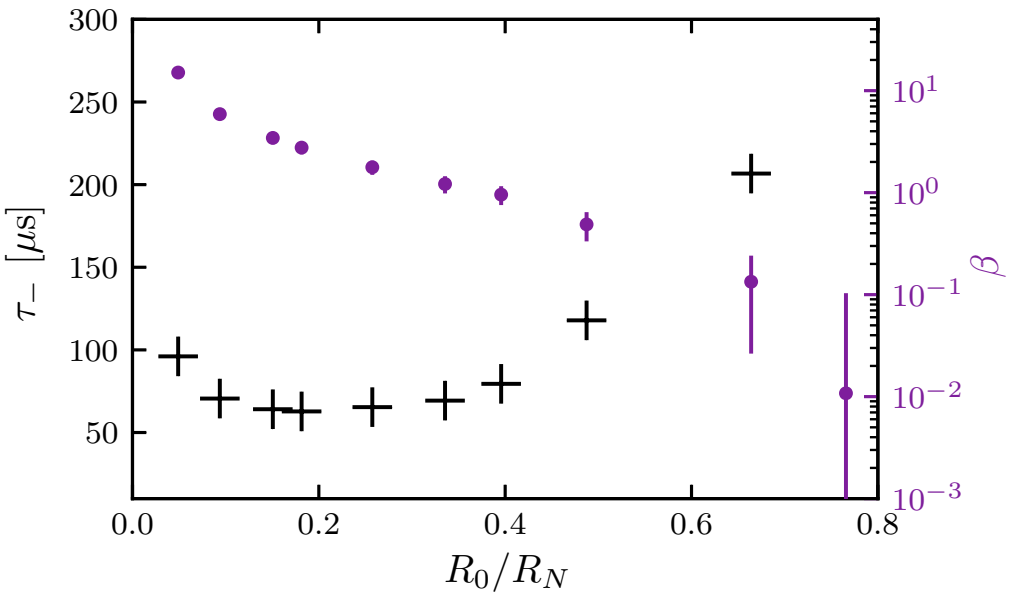

Figure 6.2: Fitted values for β (purple dots) and effective electrothermal TES response time τ_- (black crosses) as a function of TES resistance.

complex admittance data, defined as the rise and fall times of the TES response from a delta function impulse (τ_+ and τ_-, respectively) [81]. Best fit values of β and τ_- are shown in Fig. 6.2, while a typical complex impedance curve can be seen in Fig. 6.3.

6.1.5 Noise Modeling and Energy Resolution

The normal-state noise was used to estimate the SQUID and amplifier noise, once the Johnson noise component of the TES at R_N was subtracted out. The effective load resistance temperature[4] was estimated from the SC noise spectrum, resulting in $T_\ell \approx 37\,\mathrm{mK}$, which was used to estimate the Johnson noise from R_{sh} and R_p. The TFN and TES Johnson noise components of the system were calculated as defined in the standard small-signal noise model [81], using the complex admittance fit parameters. The measured power spectral density (PSD), referenced to TES current, of the device in transition was converted into the noise equivalent power (NEP) with the power-to-current transfer function [81]

$$\frac{\partial I}{\partial P}(\omega) = \left[I_0 \left(1 - \frac{1}{\mathscr{L}}\right) \left(1 + j\omega \frac{\tau}{1-\mathscr{L}}\right) Z(\omega) \right]^{-1}, \tag{6.7}$$

[4]The load resistance is $R_\ell = R_{sh} + R_p$. When the TES is SC, the noise spectrum is dominated by the Johnson noise of the R_ℓ, $S_{I_\ell} = 4k_B T_\ell R_\ell \left|1/(R_\ell + j\omega L)\right|^2$. With R_ℓ and L known, the measured noise can be used to estimate T_ℓ.

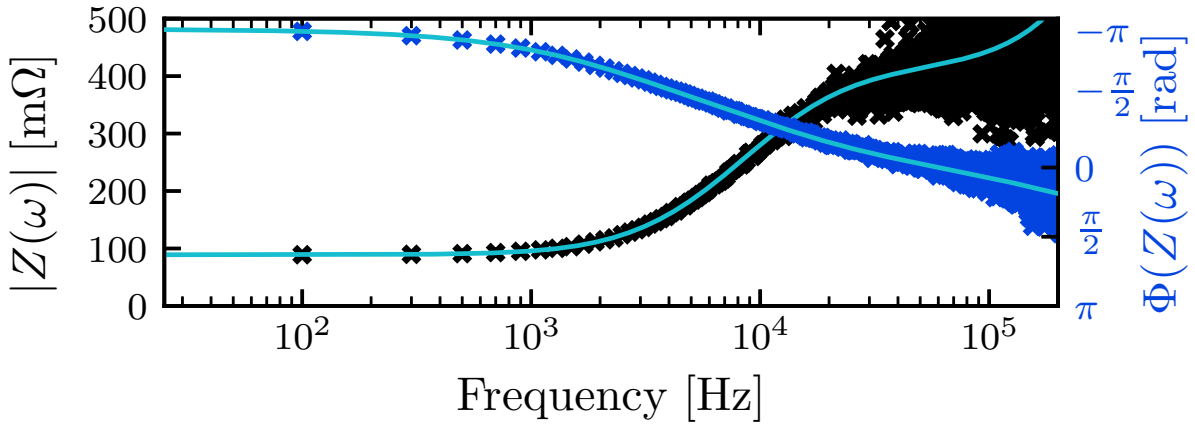

Figure 6.3: A typical complex impedance curve for the TES in transition for $R_0 \approx 15\% R_N$. The measured magnitude and phase of the complex impedance are shown in black and blue, respectively. In cyan, the complex impedance derived from the maximum likelihood fitting routine is shown.

where $Z(\omega)$ is defined in Eq. (6.6). A comparison of the noise model to the derived NEP for a typical operating point in transition is shown in Fig. 6.4.

From the derived NEP, the energy resolution of a Dirac delta impulse of energy directly into the TES was estimated using Eq. (6.1), with $\varepsilon = 1$ and $\tau_{ph} = 0$. It can be seen in the upper panel of Fig. 6.5 that when the TES is operated at less than $\sim$15% R_N, the estimated resolution of the collected energy is $\sigma_E = 40 \pm 5\,\text{meV}$. At this point in the transition, the sensor has an NEP of $1.5\times10^{-18}\,\text{W}/\sqrt{\text{Hz}}$ in a bandwidth of 2.6 kHz. This resolution represents the lower limit of the performance of this sensor given the measured noise, operated as either a photon or athermal phonon sensor. In the case of the athermal phonon sensor, there would be an additional efficiency factor based on the design of the detector.

It is evident from Fig. 6.4 that the NEP is elevated from the theoretical expectation across the full frequency spectrum. We split the excess noise into two categories. Noise that scales with the complex admittance and is present when the TES is biased in its normal or SC state, we call "voltage-coupled", e.g. inductively coupled EMF. Noise that is only seen when the TES is in transition is referred to as "power-coupled", e.g. IR photons radiating onto device. The excess voltage-coupled noise (S_{SC^*}) can be modeled by scaling the SC power spectral density (PSD) by the complex admittance transfer function when the TES is in transition via Eq. (6.8). This modeled noise can then be subtracted from the transition state PSD in quadrature.

$$S_{SC^*}(\omega) = S_{SC}(\omega)\frac{\left|[Z(\omega)]_{R_0}\right|^2}{\left|[Z(\omega)]_{R_0\to 0}\right|^2} \tag{6.8}$$

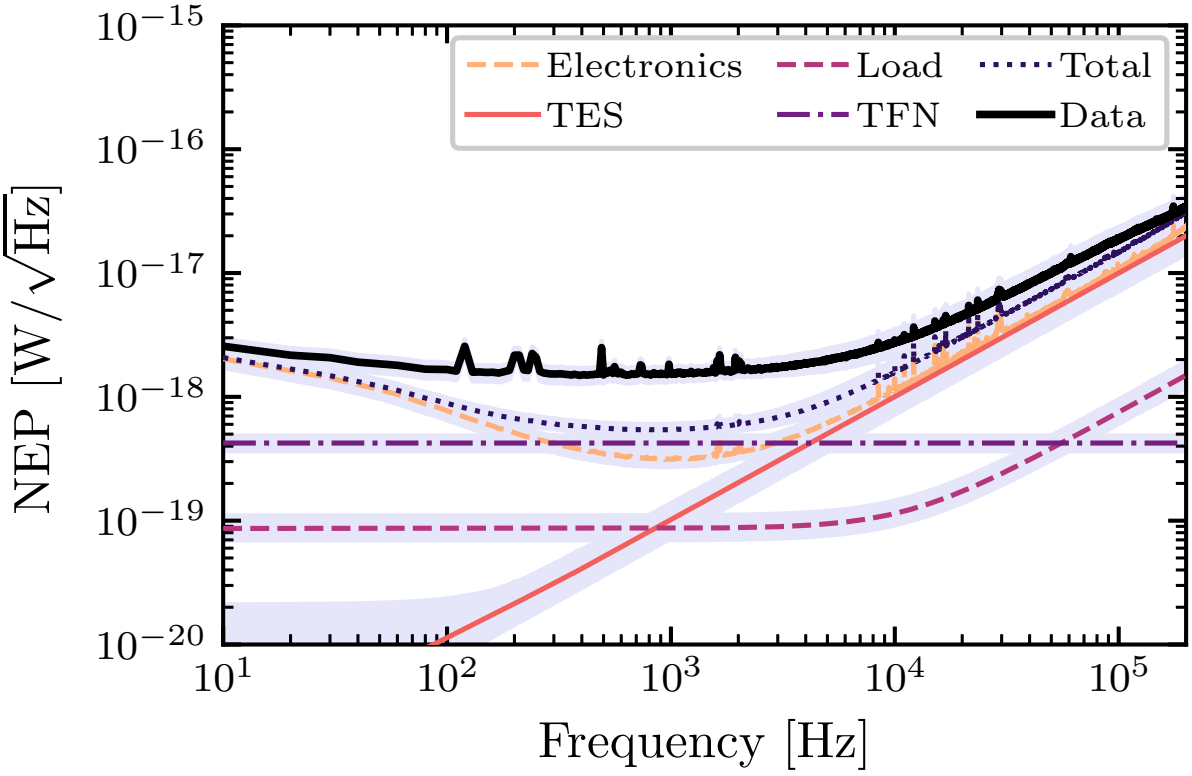

Figure 6.4: Modeled noise components: TES Johnson noise (orange solid), load resistor Johnson noise (red dashed), electronics noise (yellow dashed), thermal fluctuation noise (purple alternating dashes and dots), and total modeled noise (purple dots) compared with the derived NEP (black solid). The noise model and NEP are shown for $R_0 \approx 15\% R_N$. The shaded regions represent the 95% confidence intervals.

We expect power-coupled noise from an environmental origin to couple coherently to each TES on the same Si chip, though we have seen evidence of power-coupled noise generated by the Ethernet chip on our warm electronics to have significantly different couplings to different electronics channels. Because we acquired data simultaneously on TES2, we can determine the correlated and uncorrelated components of the noise by using the cross spectral density (CSD) [77, 158]. The scaled SC noise PSD and correlated part of the CSD are plotted with the measured PSD in Fig. 6.6 for $R_0 \approx 15\% R_N$. The two noise sources can explain the peaks in the noise spectrum, but cannot explain the overall elevated noise level.

To investigate the hypothesis of the excess noise being explained by IR photons radiating onto the TES structure, we modeled this system by multiplying the TFN by a scalar in order to make the total noise model match the NEP. This scale factor is shown in the lower panel of Fig. 6.5. The fact that this scale factor is monotonically increasing with R_0 implies that

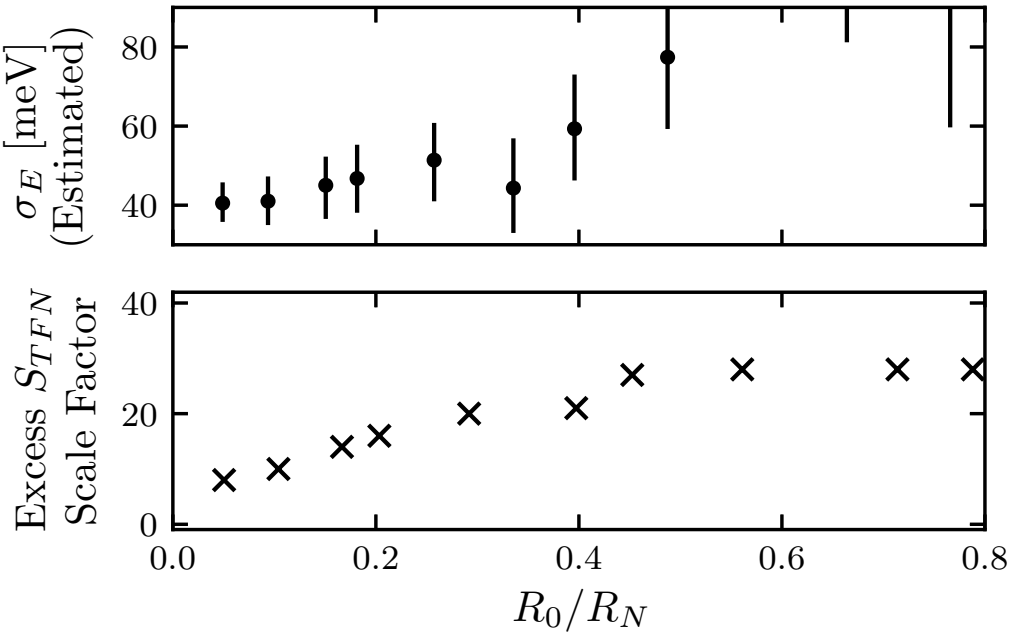

Figure 6.5: Upper: Estimated energy resolution (from data) throughout the SC transition. Lower: Scale factor needed to increase S_{TFN} to make the noise model match the measured PSD.

this mechanism is not a dominant source of excess noise, as it should be independent of the TES operational bias point.

We ruled out the possibility of the excess noise being due to multiple thermal poles [159, 160], as none of these models were able to explain the observed noise spectra. This is also evident by noting the lack of additional poles in the complex impedance in Fig. 6.3.

The fact that the two smallest low-T_c TESs (the most sensitive to parasitic power noise) were not able to go through their SC transition, suggests that a nonnegligible amount of the excess noise is environmental in origin. However, given the previous discussion, this leaves open the possibility that some of this excess noise is intrinsic to the TESs.

We compare the estimated energy resolution of the TES to the high-T_c TESs, using the same analysis techniques, in Table 6.2. The high-T_c TESs also observed a similar amount of excess noise. Despite the elevated noise seen on both sets of TESs, the resolution scaling with volume and T_c from Eq. (6.5) still approximately holds. We note that we do not compare the energy resolutions using the expected scaling relation for athermal phonon sensors because of its dependence on both substrate material and QET geometry.

With an estimated energy resolution of $40 \pm 5\,\mathrm{meV}$ (rms), this device has comparable energy sensitivity to world leading optical and near-IR TESs, but with a volume that is much larger, due to its low-T_c (see Table 6.3). It has immediate use as a photon detector in

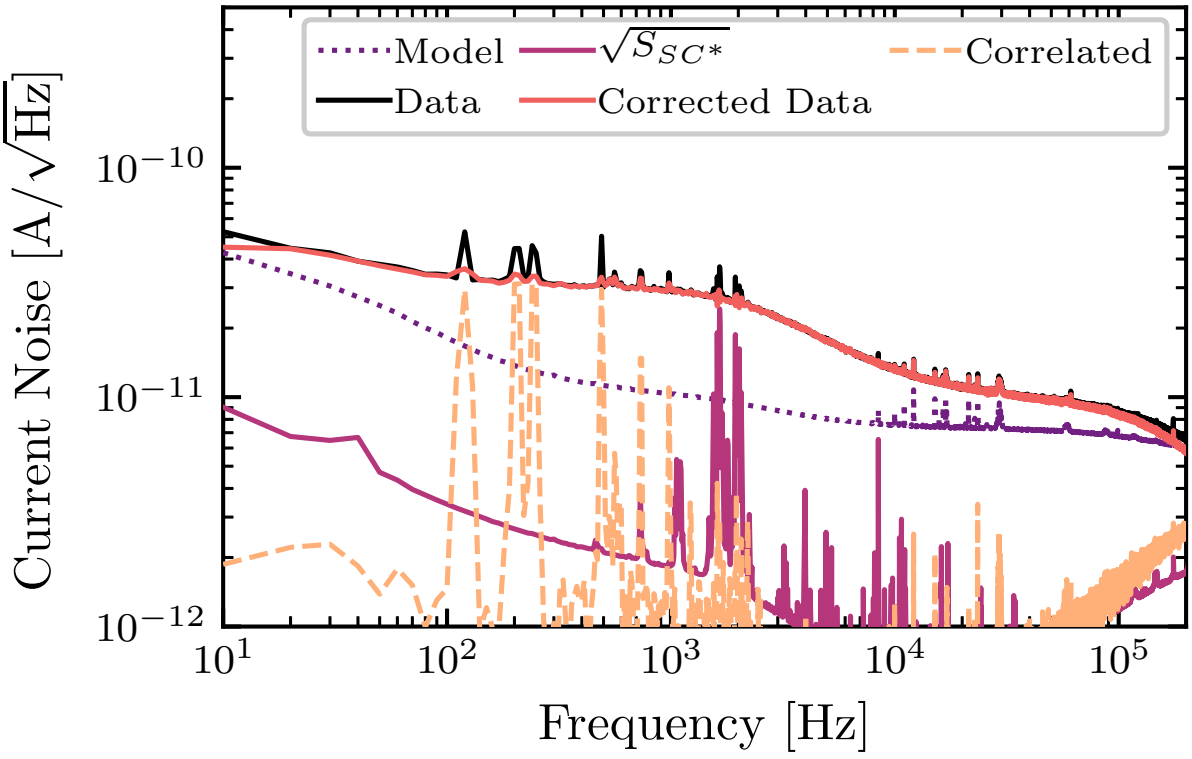

Figure 6.6: Measured noise (black solid), modeled voltage-coupled noise (purple solid), correlated noise (yellow dashed), measured noise with voltage-coupled and correlated components subtracted (orange solid), and theoretical noise model (purple dots) shown for $R_0 \approx 15\% R_N$. The environmental noise model explains the peaks in the measured spectrum, but there is still a discrepancy between the environmental-noise-corrected data and the noise model.

Table 6.2: Energy resolution estimates for 68 mK T_c TESs compared to the 40 mK T_c TES described in this work.

T_c [mK]	TES Dimensions [μm $\times$ μm $\times$ nm]	σ_E [meV] Estimated	σ_E[1] [meV] Predicted using Eq. (6.5)
40	$100 \times 400 \times 40$	40 ± 5	N/A
68	$50 \times 200 \times 40$	44 ± 5	44 ± 5
68	$100 \times 400 \times 40$	104 ± 10	89 ± 11

Table 6.3: Performance of state-of-the-art TES single photon calorimeters/bolometers.

TES	T_c [mK]	V_{TES} [μm^3]	σ_E [meV]	$\frac{\sigma_E}{\sqrt{V_{\mathrm{TES}}}}$ $\left[\frac{\mathrm{meV}}{\mu\mathrm{m}^{3/2}}\right]$	Method
W[161]	125	21.88	120	25.7	measured
Ti[162]	50	0.13	47	128.2	measured
MoCu[163]	110.6	2000	295.4	6.6	estimated[2]
TiAu[164]	106	90	48	16	measured
TiAu[165]	90	202.5	$\sim$23	1.6	estimated[2]
W (this)	40	1600	40	1	estimated

optical haloscope applications [148]. Furthermore, its large volume suggests that significant improvements in sensitivity can be made in short order; a $20\,\mu\mathrm{m} \times 20\,\mu\mathrm{m} \times 40\,\mathrm{nm}$ TES made from the same W film would be expected to have 4 meV (rms) sensitivity, provided that we can reduce observed excess noise and the volume scaling in Eq. (6.5) continues to hold.

6.1.6 Discussion

For athermal phonon sensor applications [143–147], the expected resolution is also impacted by the athermal phonon collection efficiency, which is typically $>$ 20% in modern designs [166]. Thus, small-volume crystal detectors ($\sim 1\,\mathrm{cm}^3$) should be able to achieve sub-eV triggered energy thresholds. Though such devices could not achieve the ultimate goal of single optical-phonon sensitivity, they could achieve the intermediate goal of sensitivity to single ionization excitations in semiconductors without E-field amplification mechanisms [151, 167], which have historically correlated with spurious dark counts. A decrease in TES volume and T_c, along with concomitant improvements in environmental noise mitigation and the use of crystals with very low athermal phonon surface down-conversion, would additionally be necessary to achieve optical phonon sensitivity. As we expect the energy variance to go as T_c^6 in this application, the benefit of lower T_c should be significant.

6.1.7 Acknowledgements

This work was supported by the U.S. Department of Energy under contract numbers KA-2401032, DE-SC0018981, DE-SC0017859, and DE-AC02-76SF00515, the National Science Foundation under grant numbers PHY-1415388 and PHY-1809769, and Michael M. Garland. The main findings of this letter can be replicated from the presented data, but the full data that support the findings of this study are available from the corresponding author upon reasonable request.

I would like to thank the full author list of the paper for letting this work be included in my thesis. The author list is as follows:

C.W. Fink, S.L. Watkins, T. Aramaki, P.L. Brink, S. Ganjam, B.A. Hines, M.E. Huber, N.A. Kurinsky, R. Mahapatra, N. Mirabolfathi, W.A. Page, R. Partridge, M. Platt, M. Pyle, B. Sadoulet, B. Serfass, and S. Zuber.

6.2 Performance of a Large Area Photon Detector for Rare Event Search Applications

A version of this section was originally published in *Applied Physics Letters* as Ref. [84]. The detector described in this paper was later used for a dark matter search in collaboration with SuperCMDS. That DM search was led by fellow UCB graduate student Sam Watkins, setting the most competitive limits of a cryogenic based detector for DM masses of $93-140\,\mathrm{MeV}$ [168]

6.2.1 Abstract

We present the design and characterization of a large-area Cryogenic PhotoDetector (CPD) designed for active particle identification in rare event searches, such as neutrinoless double beta decay and dark matter experiments. The detector consists of a $45.6\,\mathrm{cm}^2$ surface area by 1-mm-thick 10.6 g Si wafer. It is instrumented with a distributed network of Quasiparticle-trap-assisted Electrothermal feedback Transition-edge sensors (QETs) with superconducting critical temperature $T_c = 41.5\,\mathrm{mK}$ to measure athermal phonons released from interactions with photons. The detector is characterized and calibrated with a collimated ^{55}Fe X-ray source incident on the center of the detector. The noise equivalent power is measured to be $1 \times 10^{-17}\,\mathrm{W}/\sqrt{\mathrm{Hz}}$ in a bandwidth of 2.7 kHz. The baseline energy resolution is measured to be $\sigma_E = 3.86 \pm 0.04\,(\mathrm{stat.})^{+0.19}_{-0.00}\,(\mathrm{syst.})\,\mathrm{eV}$ (RMS). The detector also has an expected timing resolution of $\sigma_t = 2.3\,\mu\mathrm{s}$ for $5\,\sigma_E$ events.

6.2.2 Introduction

In rare event searches, experimental sensitivity is often limited by background signals [169–178]. Developing precision detectors to veto background and noise signals has been a high priority in these fields. Much interest in low temperature cryogenic detector technology has been shown by groups carrying out searches for neutrinoless double beta decay [179] ($0\nu\beta\beta$), such as the CUORE [169, 170], CUPID [180], and AMoRE [181] experiments. In these low-temperature calorimeters, the dominant source of background events consists of α decays from the surrounding environment [169, 170, 182]. It has been shown that Cherenkov emission or scintillation light can be used to positively identify the signal βs, allowing for background discrimination [183]. In order for these experiments to achieve a high level of rejection for these α backgrounds, photon detectors with large surface areas and baseline energy resolutions below 20 eV (RMS) for Cherenkov signals [184], or of $\mathcal{O}(100)\,\mathrm{eV}$ for scintillation signals [180], are required. To reject the pileup background from multiple ordinary

(two neutrino) double beta decay ($2\nu\beta\beta$) events, experiments need timing resolutions down to 10 μs (for the ^{100}Mo isotope) [180].

There has also been theoretical and experimental motivation to search for dark matter (DM) in the mass range of keV/c^2 to GeV/c^2 [185–188]. However, current experiments have been limited by unknown background signals in the energy range of $\mathcal{O}$(1-100) eV [172–178, 189]. If the source of such backgrounds are high energy photons that deposit only an extremely small fraction of their energy in the target [190], then a nearly 4π active shield composed of high-Z scintillating crystals read out by these large area photon detectors could be highly efficient at suppressing these backgrounds. Additionally, a sensitive large area cryogenic detector could be useful for discriminating small energy depositions due to radiogenic surface backgrounds. Other potential DM applications for this detector technology include searches for inelastic electronic recoils off scintillating crystals and searches for interactions with superfluid He [191–193].

We present the characterization of a large area Cryogenic PhotoDetector (CPD) with a measured baseline energy resolution of $3.86 \pm 0.04\,(\text{stat.})^{+0.19}_{-0.00}\,(\text{syst.})$ eV (RMS) and a timing resolution of 2.3 μs for 20 eV events that meets or exceeds the technical requirements for the currently proposed $0\nu\beta\beta$ experiments and DM searches. This is the first demonstration of the capabilities of such detectors, and further development may open opportunities for more novel applications.

6.2.3 Experimental Setup and Data Acquisition

The (100)-oriented substrate of the CPD is a 10.6 g Si wafer of thickness 1 mm and a surface area of 45.6 cm^2. A parallel network of 1031 Quasiparticle-trap-assisted Electrothermal feedback Transition-edge sensors (QETs) [82, 97] with $T_c = 41.5$ mK was deposited on one side of the wafer. The QETs are uniformly distributed over the wafer's surface and connected to a single readout channel. The uniform and distributed nature of the channel allows for the fast collection of athermal phonons with minimal positional dependence, reducing efficiency penalties from effects such as athermal phonon down-conversion [128, 194]. The opposite side of the Si wafer is unpolished and noninstrumented. The detector and QET mask design can be seen in Fig. 6.7. In Table 6.4, the QET design specifications for the CPD are listed.

The detector was studied at the SLAC National Accelerator Laboratory in a cryogen-free dilution refrigerator at a bath temperature (T_B) of 8 mK. The detector was placed in a copper housing and was held mechanically with the use of six cirlex clamps. The cirlex clamps also provided the thermal link between the detector and the copper housing. The QET arrays were voltage biased and the current through the TES was measured with a DC superconducting quantum interference device (SQUID) array with a measured noise floor of $\sim$4 pA/$\sqrt{\text{Hz}}$.

A collimated ^{55}Fe X-ray source was placed inside the cryostat and was incident upon the noninstrumented side of the CPD in the center of the detector. A layer of Al foil was placed inside the collimator to provide a calibration line from fluorescence at 1.5 keV [195, 196]. The collimator was tuned such that there was $\sim$5 Hz of the ^{55}Fe K$_\alpha$ and K$_\beta$ decays incident

Table 6.4: QET design specifications for the CPD describing the W TESs and the Al fins that each QET consists of. The active surface area refers to the amount of substrate that is covered by the Al fins of the QETs, while the passive surface area is that which is not covered by the Al fins, but by the Al bias rails, bonding pads, and other structures that absorb athermal phonons, but do not add to the signal.

Specification	Value
TES Length [μm]	140
TES Thickness [nm]	40
TES Width [μm]	3.5
Number of Al Fins	6
Al Fin Length [μm]	200
Al Fin Thickness [nm]	600
Al-W Overlap [μm]	10
Number of QETs	1031
Active Surface Area [%]	1.9
Passive Surface Area [%]	0.2

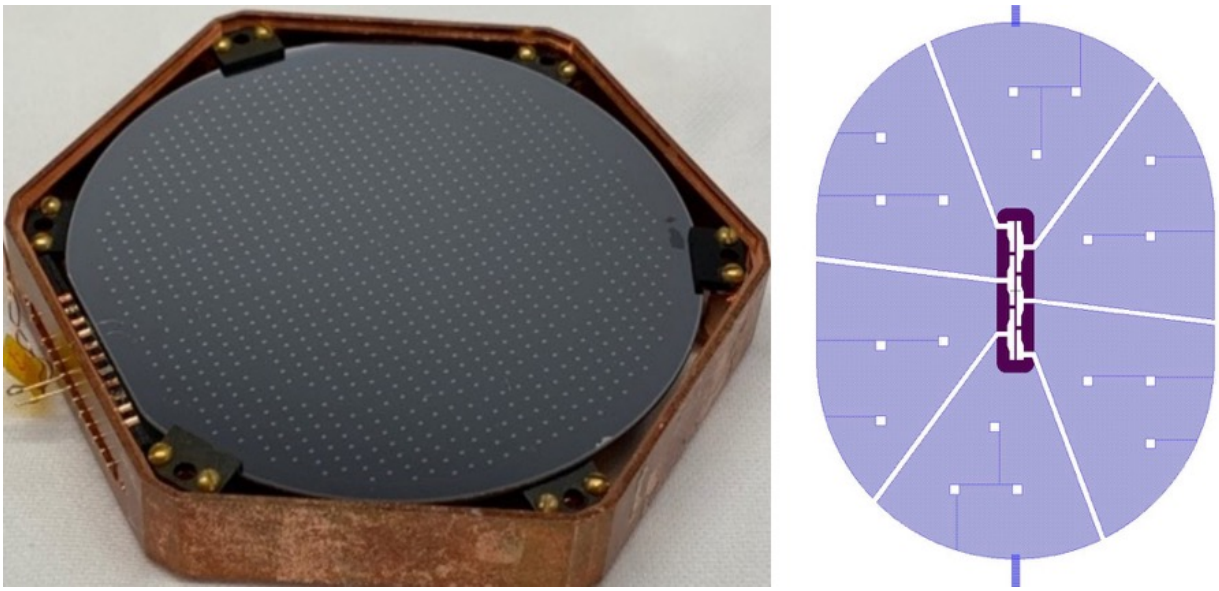

Figure 6.7: Left: A picture of the CPD installed in a copper housing. The instrumented side is shown facing up. Right: The design of the QETs used for the detector. (Blue: Al fins, Purple: W TES.)

Table 6.5: Fitted and calculated parameters of the TES from IV curves and complex impedance data. The complex impedance data are given for the bias point of $R_0 \approx 35\%\, R_N$ (see Ref. [197] for definitions of parameters). The systematic errors on G_{TA} and T_c represent the upper bounds on these values, using the hypothesis that the observed excess noise in the sensor bandwidth is entirely due to parasitic bias power.

Parameter	Value
R_{sh} [mΩ]	5 ± 0.5
R_p [mΩ]	8.7 ± 0.8
R_N [mΩ]	88 ± 10
P_0 [pW]	3.85 ± 0.45
G_{TA} [nW/K]	$0.48 \pm 0.04\,(\text{stat.})^{+0.49}_{-0.00}\,(\text{syst.})$
T_c [mK]	$41.5 \pm 1.0\,(\text{stat.})^{+10}_{-0}\,(\text{syst.})$
R_0 [mΩ]	31 ± 3
τ_0 [μs]	1700 ± 200
L [nH]	190 ± 10
β	1.1 ± 0.1
$\mathscr{L}$	80 ± 15

on the detector. The detector was held at a bath temperature $T_B \ll T_c$ for approximately two weeks to allow any parasitic heat added by the cirlex clamps to dissipate. During this time, we attempted to neutralize potential charged impurities within the Si wafer as much as possible with ionization produced by a 9.13 μCi ^{137}Cs source placed outside of the cryostat.

6.2.4 Detector Characterization

To characterize the QETs, IV sweeps were taken at various bath temperatures by measuring TES quiescent current as a function of bias current[5], with superimposed small square pulses providing complex admittance [82] at each point in the IV curve [76, 77, 197]. Since all the QETs are connected in parallel in a single channel, the channel was treated as if it were a single QET, describing the average characteristics of the total array. The IV data allowed for the estimation of the parasitic resistance in the TES line (R_p), the normal state resistance (R_N), and the nominal bias power (P_0). The effective thermal conductance between the QETs to the Si wafer (G_{TA}) and T_c were measured by fitting a power law to the measured bias power as a function of bath temperature [197]. This measurement is a lower bound of these values, as it assumes no parasitic bias power in the system. We summarize these characteristics of the detector in Table 6.5.

[5]Although we are applying a bias current, we use the term "IV" because the voltage and current are related by the shunt resistor: $V_{bias} = I_{\text{bias}} R_{sh}$

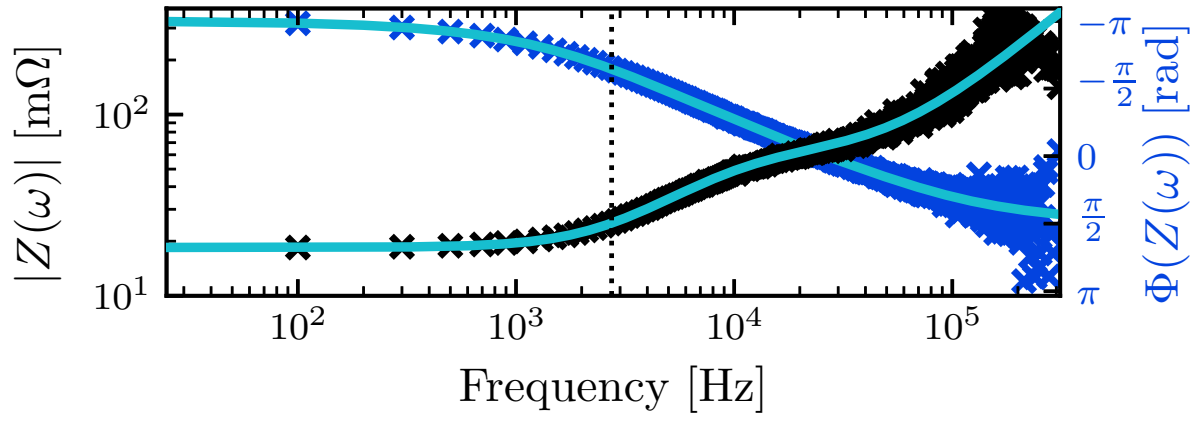

Figure 6.8: The magnitude and phase of the measured complex impedance are shown as the black and blue markers, respectively. The modeled complex impedance is shown as the cyan solid line. The black dotted line denotes the corresponding bandwidth of 2.7 kHz for the thermal time constant $\tau_- = 58\,\mu$s.

The complex admittance data allows us to estimate the dynamic properties of the sensors. Throughout the superconducting transition, primary and secondary thermal fall times were observed, e.g. 58 μs and 370 μs, respectively, at $R_0 \approx 35\%\,R_N$. The origin of this additional time constant is under investigation. Its appearance suggests that we have a more complex thermal or electrical system, e.g. phase separation [76, 198] or an extra heat capacity connected to the TES heat capacity [199]. A characteristic plot of complex impedance of the TES circuit can be seen in Fig. 6.8.

Knowledge of the TES parameters, given in Table 6.5, allowed for the calculation of the power-to-current responsivity, which was used to convert the measured current-referred power spectral density (PSD) to the noise equivalent power (NEP). These parameters were used to predict the expected noise spectrum using the single-heat-capacity thermal model [82]. A comparison of the NEP to the model at $R_0 \approx 35\%R_N$ can be seen in Fig 6.9. The excess noise spikes above approximately 500 Hz have been experimentally confirmed to be largely caused by vibrations from the operation of the pulse tube cryocooler. The observed noise is also elevated above our model at frequencies in the effective sensor bandwidth interval (approximately the inverse of the thermal time constant τ_- [82]) by a factor of $\sim$2, as compared to the prediction. This "in-band" excess noise is consistent with two different hypotheses: a white power noise spectrum incident on the detector of $8 \times 10^{-18}\,\mathrm{W}/\sqrt{\mathrm{Hz}}$ (e.g. a light leak) or a parasitic DC power in the bias circuit of approximately 6 pW. If we assume the latter is the source, this allows us to calculate the upper bounds on our estimates of G_{TA} and T_c, as reported in Table 6.5. There remains bias-dependent excess noise above the sensor bandwidth. We parameterize the excess TES Johnson–like noise with the commonly used

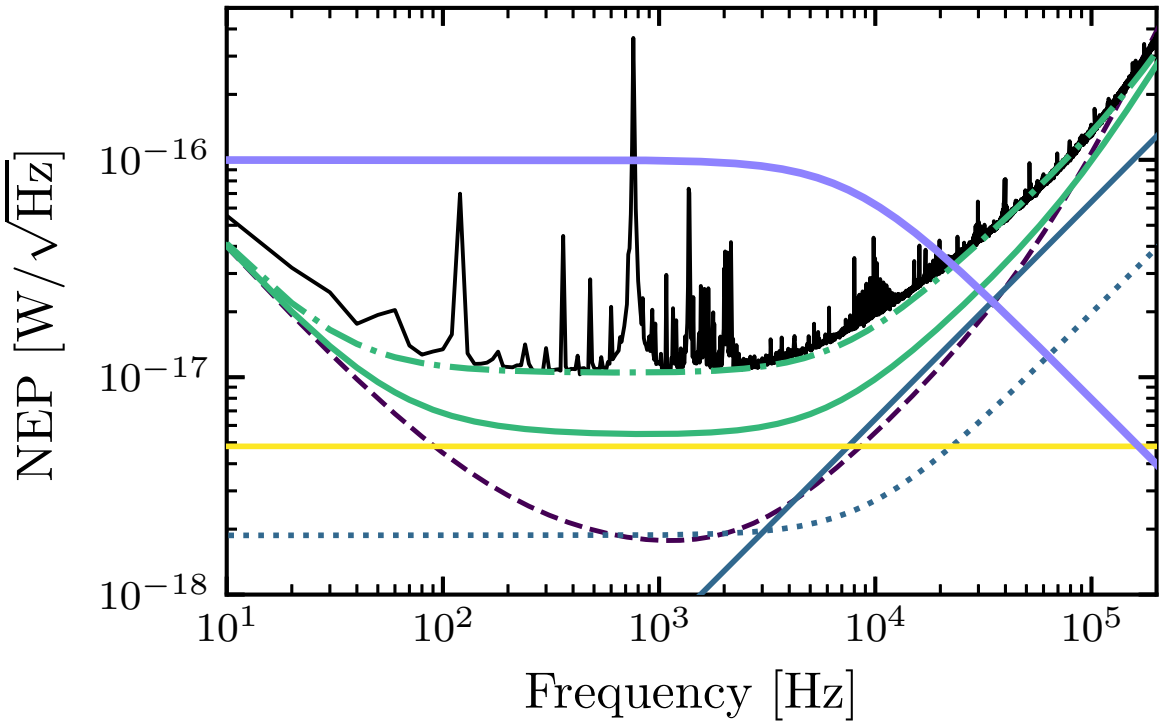

Figure 6.9: Modeled noise components: TES Johnson noise (blue solid), load resistor Johnson noise (blue dots), electronics noise (purple dashed), thermal fluctuation noise (TFN) between the TES and the bath (yellow solid), and total modeled noise (green solid) compared with the measured NEP (black solid) for $R_0 \approx 35\%R_N$. We additionally show the total noise model (green alternating dashes and dots), which includes a hypothetical environmental noise source of $8 \times 10^{-18}\,\mathrm{W}/\sqrt{\mathrm{Hz}}$ and excess TES Johnson noise with $M = 1.8$. The light-purple line in upper portion of the figure denotes the power-pulse shape (arbitrarily scaled), which consists of a single pole at the observed rise time of $1/\left(2\pi\tau_{\mathrm{ph}}\right) = 8\,\mathrm{kHz}$.

M factor [82, 86]. Using values of M up to 1.8, depending on bias point, can account for the discrepancy between observation and prediction at these frequencies. We note that this "excess" noise could possibly also be explained with a more complex thermal model.

The lowest integrated NEP was achieved at an optimum bias point of $R_0 = 31\,\mathrm{m}\Omega \approx 35\%R_N$. In addition to the characterization data, approximately 500,000 threshold triggered events and 80,000 randomly triggered events were recorded at this bias.

For the measured phonon-pulse shape, there are multiple characteristic time constants. The pulse rise time was measured as $\tau_{ph} = 20\,\mu\mathrm{s}$, which is the expected characteristic time scale for athermal phonons being absorbed by the Al collection fins of the QETs for this

design. The dominant pulse fall time is consistent with the expectation from the complex impedance as we approach zero-energy, where we confirmed the expected thermal time constant $\tau_- = 58\,\mu$s via a fit of the rise and fall times of the pulses. The secondary time constant from the complex impedance of $370\,\mu$s was also seen in these low-energy pulses. The secondary time constant from the complex impedance of $370\,\mu$s was also seen in these low-energy pulses, with an amplitude ratio of less than 2% to the dominant decay exponential.

We observed an additional long-lived behavior in the pulses, which can be estimated as a low-amplitude $\sim$3 ms exponential tail whose magnitude scales linearly with the event energy. As this tail is not seen in the complex impedance data, it might be due to direct absorption of phonons with energy smaller than the Al superconducting band gap into the TES [97].

For energies above 300 eV, we observed a local saturation effect that manifests as the dominant fall time lengthening with increased energy. In Fig. 6.10, we show averaged pulses for various event amplitudes, showing the dependence of the pulse fall time on energy. We associate this effect with high-energy, single-particle events pushing nearby QETs into the normal resistance regime, slowing down the response of the total single-channel device. We also note that there is a position-dependent effect for a subset of high-energy events, notable by a varying fall time for events with the same amplitude. Our hypothesis for this phenomenon is that events close to the edge of the detector have less solid angle to deposit the energy, which leads to longer recovery times as opposed to events in the center of the detector (e.g. the calibration events). These effects are specific to the single-particle nature of the measured events. For scintillation events, the isotropic nature of the photons would spread out the event energy across the entire detector channel, avoiding these local saturation and position-dependent effects.

6.2.5 Energy Calibration and Resolution

To reconstruct event energies, two energy estimators were used in this analysis: the optimum filter (OF) amplitude [93, 200] and the energy removed by electrothermal feedback (E_{ETF}) [82]. For the OF, we used an offline algorithm to reconstruct energies. A single noise spectrum was used, which was computed from the randomly triggered events. The phonon-pulse template used was an analytic template that matches the measured low-energy pulse shape, neglecting the 3 ms low-amplitude tail. Because we could not directly measure the low-energy phonon-pulse shape with high statistics, we used a template without the long-lived behavior.

The integral estimator E_{ETF} was calculated for each triggered event by measuring the decrease in Joule heating via

$$E_{\mathrm{ETF}} = \int_0^T \left[(V_b - 2I_0R_\ell)\Delta I(t) - \Delta I(t)^2 R_\ell\right] \mathrm{d}t, \tag{6.9}$$

where T is the time at which the integral is truncated, $\Delta I(t)$ is the baseline-subtracted pulse in current, I_0 is the quiescent current through the TES, R_ℓ is the load resistance, and

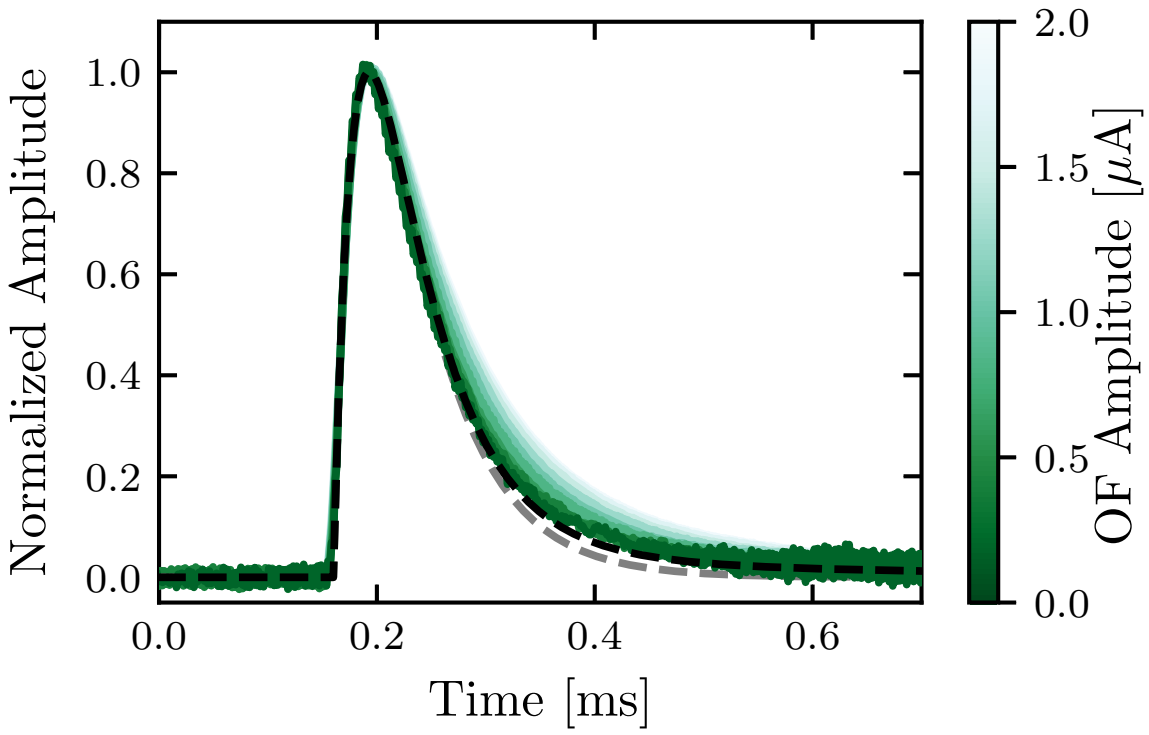

Figure 6.10: We show averaged pulse shapes (green solid) normalized by the peak current, for which the shade of green lightens with increased OF amplitude. For reference, 0.1 μA corresponds to about 0.1 keV, 1.1 μA corresponds to about 1.5 keV, and 2.0 μA corresponds to about 3.4 keV. Each averaged pulse consists of about 100 events averaged in 0.04 μA bin-widths. The lengthened fall time of the averaged pulse with increased OF amplitude (an energy estimator) is evident. The phonon-pulse template used in this analysis (black dashed) shows good agreement with the low energy (dark green) pulses. We also show an analytic phonon-pulse with only the first sensor fall time (gray dashed). Comparing to the phonon-pulse template, we see that the second sensor fall time has a small effect in this limited time interval.

V_b is the voltage bias of the TES circuit [82]. In comparison to the OF amplitude, this integral estimator was less sensitive to saturation effects, but had a worse baseline energy resolution. When characterizing this device, we used the integral truncation of $T \approx 7\tau_-$ for E_{ETF}. This was done to preserve good baseline energy sensitivity in this integral estimator when calibrating the OF amplitude energy estimator at low energies.

For pulse-shape saturation at high energies, we use the following empirical model:

$$E_{\mathrm{ETF}} = a\left(1 - \exp\left(-\frac{E_{\mathrm{true}}}{b}\right)\right). \tag{6.10}$$

This functional form has the expected behavior: it intercepts zero, approaches an asymptotic value at high energies, and becomes linear for small values of E_{true}. In Fig. 6.11, the fitted saturation model, as well as the calibrated and uncalibrated E_{ETF} spectra, are shown, as compared to the energies of various spectral peaks in both energy scales. For the event spectra, we observed an unknown background at low energies. As other surface experiments have seen excess backgrounds at similar energies [172, 173], we do not expect this to be detector-dependent. We are actively studying this detector at an underground facility, for which the results will be published in a future work.

The absolute phonon collection efficiency (ε_{ph}) of the detector was estimated by measuring E_{ETF} at the lowest energy calibration line (Al fluorescence) and dividing by the known energy of that line. Because of the long-lived behavior in the phonon-pulse shapes, the measured collection efficiency of this detector depends on the integration truncation time T. If it is chosen to only include energy collected by the first sensor fall time τ_- (e.g. $T \approx 7\tau_-$), then we find that $\varepsilon_{ph} = 13 \pm 1\%$. Alternatively, if we integrate to effectively infinity, this includes the low-amplitude long-lived behavior of the phonon pulses. In this case, the collection efficiency increases to $\varepsilon_{ph}^{\infty} = 17 \pm 1\%$, which implies that about 30% of the collected energy for a given event is associated with the low-amplitude tail of the phonon-pulse shape (about 8% and 22% from the 370 μs and 3 ms components, respectively).

To calibrate the OF amplitude to units of energy, we fit the relationship between the calibrated E_{ETF} and the OF amplitude to a linear slope at low energies (below approximately 300 eV). This method does not provide a calibration of the OF amplitude at high energies, but allows for the calculation of the baseline energy resolution.

For the calibration method used, the main source of systematic error is the saturation model in Eq. (6.10). Since it is empirical, its use introduces uncertainty in its applicability. We can estimate the upper bound of the effect of this systematic on the baseline energy resolution as the value that would be reached if we instead calibrated E_{ETF} linearly using the Al fluorescence line. In this case, this worsens the baseline energy resolution, as we are not taking into account the expected response (see Fig. 6.11).

The baseline energy resolution was calculated as the RMS of 46,000 randomly triggered events, after removing data contaminated by pileup events, electronic glitches, or thermal tails. This gave a resolution of $\sigma_E = 3.86 \pm 0.04\,(\mathrm{stat.})^{+0.19}_{-0.00}\,(\mathrm{syst.})\,\mathrm{eV}$ (RMS) for the OF energy estimator, where these data are consistent with a normal distribution. This is in agreement with our estimation from the observed NEP and the power-referred phonon-pulse

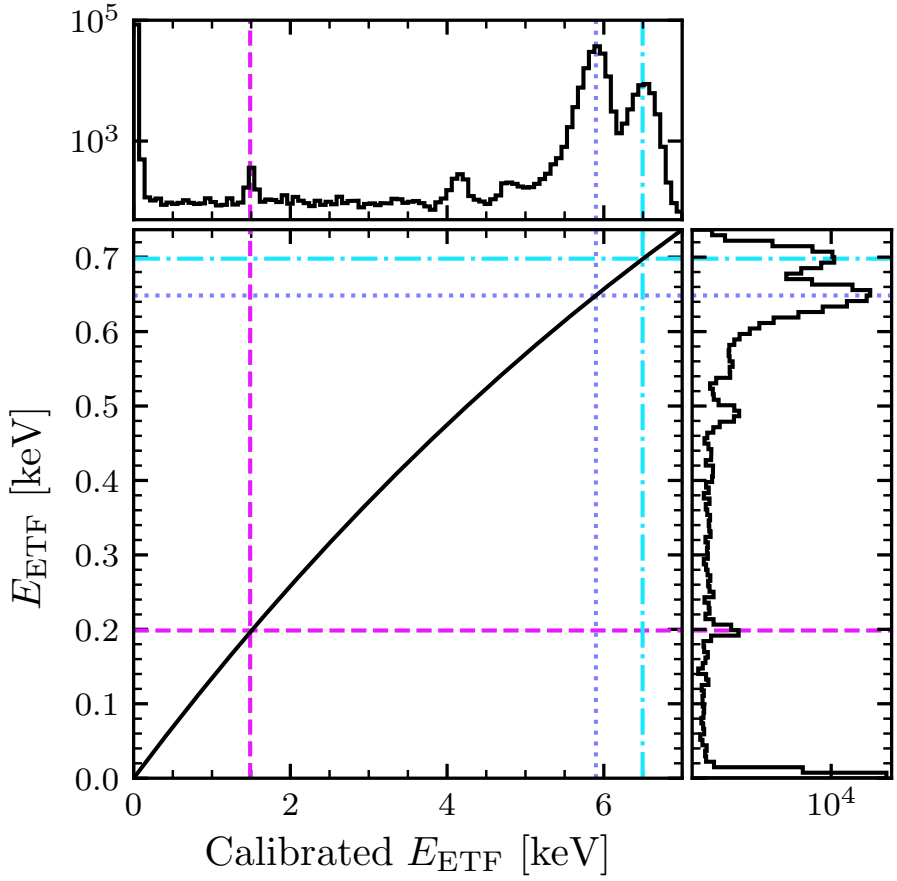

Figure 6.11: Upper: The calibrated $E_{\rm ETF}$ (which estimates $E_{\rm true}$) spectrum for the CPD (solid black) grouped in bins of width 70 eV. Right: The energy spectrum in $E_{\rm ETF}$ (solid black) grouped in bins of width 7.4 eV. Lower left: The fitted saturation model using Eq. (6.10) (solid black). In each of these panels, we have shown, for both the calibrated and uncalibrated $E_{\rm ETF}$ energy scales, the location of the K_α, K_β, and Al fluorescence calibration peaks (pink dashed, blue dotted, and cyan alternating dashes and dots, respectively). In the lower left panel, the intersections of the lines corresponding to each spectral peak represent the points used for calibration of $E_{\rm ETF}$ via Eq. (6.10). The unmarked peaks at 4.2 keV and 4.8 keV in calibrated $E_{\rm ETF}$ are the Si escape peaks [201].

shape (a single-exponential with fall time τ_{ph} and collection efficiency ε_{ph}), which gave an expected baseline energy resolution of $\sigma_E^{th} = 3.9 \pm 0.4\,\text{eV}$ (RMS), as was similarly done in Ref. [197].

Using the OF formalism, we can also calculate the expected timing resolution [200] of the CPD, which provides an estimate of the minimum resolving time for two pileup events. For a 5σ event, the corresponding timing resolution of this detector is $2.3\,\mu$s. For many $0\nu\beta\beta$ experiments, the minimum resolving time requirement to make pileup of multiple $2\nu\beta\beta$ events a negligible background is on the order of 1 ms [154, 202–204]. For the CUPID and CUPID-1T experiments, this requirement is about $300\,\mu$s and $10\,\mu$s, respectively [180]. An initial study of pileup events was carried out by adding two simulated 100 eV pulses of randomized time separation to the in-run randomly triggered events from the CPD dataset. In this simulation, we observed that minimum resolving times below $10\,\mu$s are achievable with an OF-based pileup detection algorithm. In the future, we will study the minimum resolving time with a more detailed simulation based on the expected $2\nu\beta\beta$ spectrum for ^{100}Mo. Given these initial studies, we expect the CPD to fulfill these requirements.

When comparing the baseline energy resolution of the CPD to the requirements of the CUPID experiment, the value surpasses the requirement of less than 20 eV (RMS) by a factor of five. While the CPD is a TES-based detector, it has been shown that Microwave Kinetic Inductance Detectors (MKIDs) and Neutron-Transmutation-Doped (NTD) Ge detectors are also promising avenues for achieving the sub-20 eV baseline goal. In Table 6.6, we report this result alongside those of other detectors for this application. In comparison to the devices that have met or exceeded the requirement, the CPD does not require Neganov-Trofimov-Luke (NTL) amplification [205, 206] (which often results in excess dark counts) and has the best baseline energy sensitivity for its size.

6.2.6 Discussion

The measured baseline energy resolution of $3.86 \pm 0.04\,(\text{stat.})^{+0.19}_{-0.00}\,(\text{syst.})$ eV and the expected timing resolution of $2.3\,\mu$s (at $5\sigma_E$), combined with its large surface area, makes this detector an excellent candidate for background rejection in both $0\nu\beta\beta$ and DM experiments. Because of the energy sensitivity, this device can be used as a dark matter detector itself, as we have done in collaboration with SuperCDMS to set limits on spin-independent dark matter-nucleon interactions for sub-GeV/c^2 dark matter particle masses [215]. Similarly, this gram-scale device could be applied to coherent elastic neutrino-nucleus scattering experiments [149]. The performance of the CPD can be further optimized through adjustment of characteristics such as the Al-W overlap and overall Al coverage. From these considerations, we anticipate up to a factor of two improvement in baseline energy resolution for a future iteration of the CPD, which is currently being designed.

Table 6.6: Comparison of this work to various state-of-the-art devices for degraded α rejection in $0\nu\beta\beta$ experiments. The table is sorted by decreasing $\frac{\sigma_E}{\sqrt{\text{Area}}}$, a common figure-of-merit of devices for this application. The column labeled "NTL?" denotes whether or not each detector relies on NTL amplification to achieve the corresponding result.

Device	Area [cm^2]	σ_E [eV]	$\frac{\sigma_E}{\sqrt{\text{Area}}}$ $\left[\frac{\text{eV}}{\text{cm}}\right]$	NTL?
MKID [207]	4.0	26	13	No
W-TES [208]	12.6	23	6.5	No
Ge-NTD [209]	15.6	20	5.1	No
Ge-NTD [210]	19.6	19	4.3	Yes
IrAu-TES [211]	4.0	7.8	3.9	Yes
Ge-NTD [38]	4.9	7.6	3.5	Yes
Ge-NTD [212]	15.2	10	2.6	Yes
Ge-NTD [213]	15.2	8	2.1	Yes
W-TES [214]	12.6	4.1	1.2	No
W-TES (this)	45.6	3.9	0.6	No

6.2.7 Acknowledgments

Authors C.W.F. and S.L.W. contributed equally to this work. This material is based upon work supported by the US Department of Energy (DOE) Office of Science under Contract Nos. DE-AC02-05CH11231 and DE-AC02-76SF00515, by the DOE Office of Science, Office of High Energy Physics under Contract Nos. KA-2401032, DE-SC0018981, and DE-SC0017859, by the National Science Foundation (NSF) under Grant Nos. PHY-1314881, PHY-1415388, and PHY-1809769, and by Michael M. Garland.

I would like to thank the full author list of the paper for letting this work be included in my thesis. The author list is as follows:

C.W. Fink, S.L. Watkins, T. Aramaki, P.L. Brink, J. Camilleri, X. Defay, S. Ganjam, Yu.G. Kolomensky, R. Mahapatra, N. Mirabolfathi, W.A. Page, R. Partridge, M. Platt, M. Pyle, B. Sadoulet, B. Serfass, and S. Zuber.

6.2.8 Data Availability

The data that support the findings of this study are available upon reasonable request to the corresponding authors.

Chapter 7

SPICE MELANGE Performance

This chapter details the characterization of the first set of fabricated detectors from the SPICE MELANGE photolithography mask described in chapter 4. At the time of this writing, our lab did not have a low energy calibration source, making it impossible to measure the total phonon collection efficiency. As such, this chapter represents a work in progress. It is hoped that the analysis of the detector characterization is at least helpful to new researchers doing similar studies.

7.1 Description of Devices

For the first fabrication run of the MELANGE detector set, two different versions were made. Both versions were fabricated on standard 4 inch, 1 mm thick Si wafers with the follow processes:

1. Wafer 1 (W1)
    - Used a Xe etching process for TES deposition
    - Had a target T_c of 28 mK $\implies$ measured to be $\sim$ 19 mK
2. Wafer 2 (W2)
    - Used a Ar etching process for TES deposition
    - Had a target T_c of 45 mK $\implies$ measured to be $\sim$ 55 mK

After dicing of both wafers, a subset of the devices from each wafer were put through an electro-chemical etching process, set aside for edge polishing, or left un-altered.

7.2 Description of Data Sets

Since our readout electronics currently only have 4 channels, only 2-4 devices could be studied at a time. Below is an overview of which devices have been studied:

7.2.1 Run 11

This was the first run with the MELANGE devices, and was primarily used to study the qualities of the W films. One TESTR chip from each wafer was glued with rubber cement onto a copper plate for thermalization, and two TESs from each chip were wirebonded to the DIB. Both devices were placed in the same housing, as seen in Fig. 7.1.

Devices Used:

- TESTR chip W1:
  - 100 μm $\times$ 400 μm TES
  - 200 μm $\times$ 800 μm TES
- TESTR chip W2:
  - 100 μm $\times$ 400 μm TES
  - 200 μm $\times$ 800 μm TES

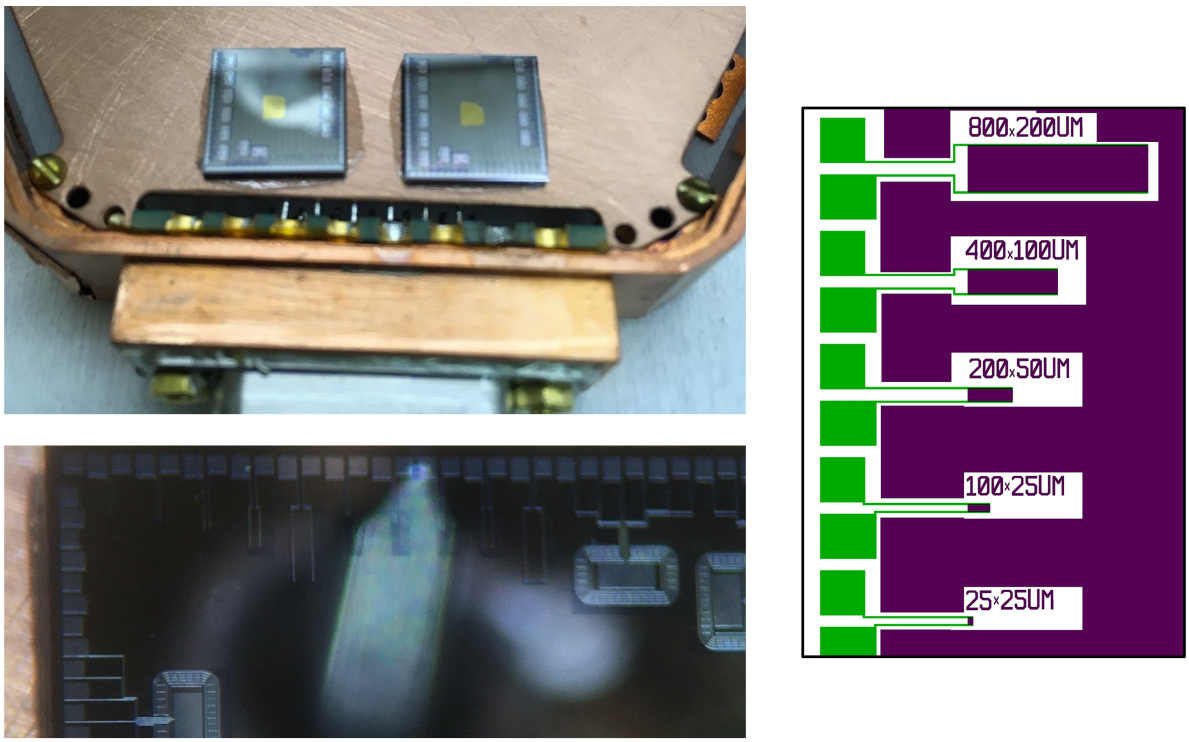

Figure 7.1: Upper Left: picture of detectors in their housing in Run 11. Lower Left: zoomed in view of TESs on the TES rectangles chip. Right: zoomed in section of TESs on the mask of the TESTR chip.

7.2.2 Run 14

This was the first run using the actual MELANGE athermal phonon detectors. A 0.25% and 4% single channel were each run in a resting configuration in one housing, and a 1% two channel device was run in a hanging configuration in a separate housing, all devices from the W2 wafer. The devices used a Au wirebond from the Au pad to the Cu plate for thermalization. See Fig. 7.2 for an image of the setup.

Devices Used:

- W2 Melange 4% Single channel, resting
- W2 Melange 0.25% Single channel, resting
- W2 Melange 1% Two channel, hanging

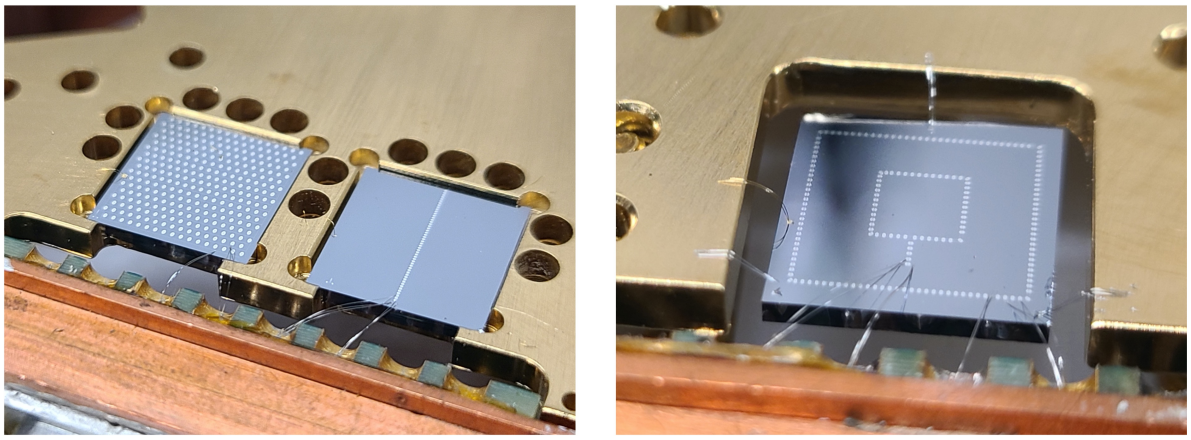

Figure 7.2: Left: Left to right, single channel 4% coverage MELANGE detector and single channel 0.25% coverage MELANGE detector in the resting configuration. Right: Two channel 1% coverage MELANGE detector in the hanging configuration.

7.2.3 Run 15

This run took a deeper dive into the study of excess phonon/photon noise by studying the the 4% 'no fin' vs regular fin devices side by side (see Fig. 7.3). Both devices were again from W2, in the resting position, and thermalized with Au wirebonds. Each device also had the EMI veto TES channel, which was readout on both detectors.

Devices Used:

- W2 Melange 4% Single channel, resting
  - QET channel

  - 40 μm $\times$ 295 μm TES

- W2 Melange 4% NO FIN Single channel, resting
  - QET channel
  - 40 μm $\times$ 295 μm TES (channel open after cooldown)

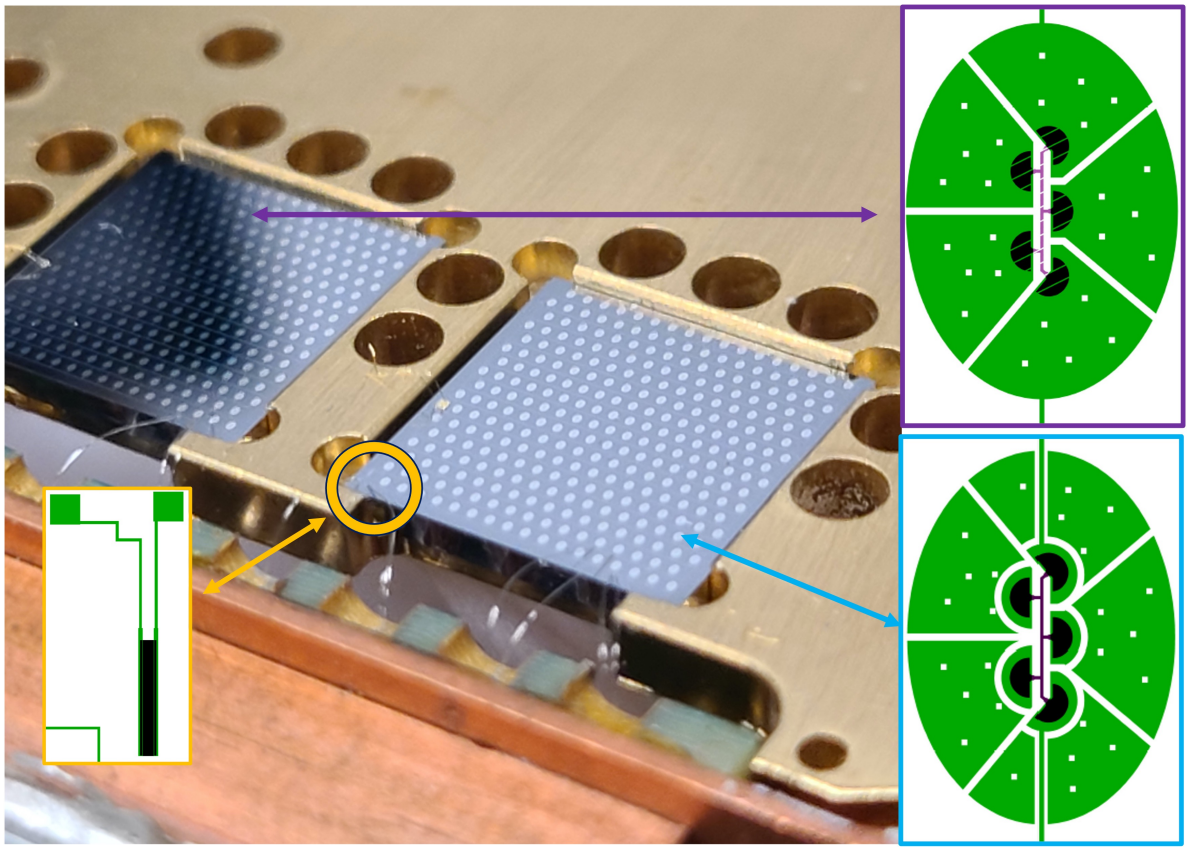

Figure 7.3: Run 15 setup, showing both 4% MELANGE devices, one standard, and one with 'no fins'. The design masks of the corresponding QETs are shown on the right. Each detector also had an additional single TES channel, highlighted with the orange circle.

7.2.4 Run 16

This run used the exact same setup and devices as Run 15, but using chips from W1. (Unfortunately add devices were unable to go superconducting after cooldown.)

Devices Used:

- W1 Melange 4% Single channel, resting

  - QET channel
  - $40\,\mu$m $\times$ $295\,\mu$m TES

- W1 Melange 4% NO FIN Single channel, resting
  - QET channel
  - $40\,\mu$m $\times$ $295\,\mu$m TES

7.3 Measurement of Basic Film Properties

An IV sweep analysis, as described in chapter 6, was performed on all TESTR devices in Run 11. The relevant IV and complex admittance characteristics from the analysis are shown in table 7.1. One huge advantage of the TES rectangles on this chip is that they are incredibly simple. This allows us to disentangle many of the parameters that are convoluted in a full QET. As such, we can use the measurements in table 7.1 to infer more fundamental properties of the W film itself.

7.3.1 Resistivity

Recall from chapter 3 that the normal resistance of a TES is given by

$$R_N = \rho_W \frac{\ell_{\text{TES}}}{w_{\text{TES}} h_{\text{TES}}}. \tag{7.1}$$

We have a very robust measure of h_{TES} using Atomic Force Microscopy (AFM) after fabrication. While there are uncertainties in ℓ_{TES} and w_{TES}, these are on the order of $< 1\,\mu$m. Since these TES rectangles are very long, these uncertainties are all sub 1%. This means that using the normal resistance measurement for these rectangles provides a robust measure of the resistivity of the W film. One does need to be careful in this calculation to account for the proximitation of the W from the Al bias rails (see Fig. 7.1). We thus need to subtract off the coherence length ξ from the TES length when calculating the resistivity as this section of W will still be SC,

$$\rho_W = R_N \frac{w_{\text{TES}} h_{\text{TES}}}{\ell_{\text{TES}} - 2\xi}. \tag{7.2}$$

Unfortunately this coherence length correction breaks the aspect ratio symmetry across the series of TES rectangles. However, looking at the asymmetry of multiple devices allows us to tune the value of the coherence length as well as the resistivity since the R_N's across all the devices should all be slightly different. Recall from Eq. 3.44, the coherence length near T_c in W is roughly $\xi \approx 4\,\mu$m. We find that reducing the effective length of the TES rectangles by approximately $8\,\mu$m is able to explain the differences in R_N in table 7.1.

Table 7.1: Table of basic measured parameters from the Run 11 TES chip study. The 100×400 W1 device never went superconducting, so it's parasitic resistance was assumed based on past measurements of that channel. It also has no measured bias power for the same reason. The first row contains the unmeasured shunt resistance, the second section of parameters (R_p through $\tau_{\rm ETF}$) are measured parameters, and the last 4 rows below the dividing line parameters calculated using the above measurements.

Device [μm $\times$ μm]	100x400 W2	200x800 W2	100x400 W1	200x800 W1
R_{sh} [mΩ]	5 ± 0.5	5 ± 0.5	5 ± 0.5	5 ± 0.5
R_p [mΩ]	2.4 ± 0.2	2.6 ± 0.2	2.4 ± 0.2	2.4 ± 0.2
R_N [mΩ]	873 ± 45	913 ± 45	1150 ± 120	1216 ± 65
$h_{\rm TES}$ [nm]	45.849	45.849	42.984	42.984
P_0 [fW]	103 ± 8	388 ± 20	Not Measured	3.9 ± 0.2
T_c [mK]	56.5 ± 1	56 ± 1	19 ± 1	19 ± 1
$\tau_{\rm ETF}$ [μs]	28 ± 5	30 ± 5	Not Measured	1300 ± 150
β	~ 3	~ 10	Not Measured	0.5
ξ [μm]	4 ± 1	4 ± 1	4 ± 1	4 ± 1
α	430 ± 50	430 ± 50	Not Measured	125 ± 20
$\rho_{\rm W}$ [Ωm]	1.745×10^{-7}	1.745×10^{-7}	2.155×10^{-7}	2.155×10^{-7}
$\Sigma_{ep}^{\rm W}$ $\left[\times 10^8 \frac{\rm W}{\rm K^5 m^3}\right]$	1.025 ± 0.125	1.025 ± 0.125	Not Measured	2.5 ± 0.2

7.3.2 Electron-Phonon Coupling

With the resistivity now calculated, we can shift to the measurement of bias power. Recall from Eq. 2.3 that the bias power is given by

$$P_{\rm bath} = K(T_c^n - T_B^n), \tag{7.3}$$

where from Eq. 3.73

$$K = \Sigma_{ep}^{\rm W} V_{eff}^{\rm total}. \tag{7.4}$$

Thus,

$$P_{\rm bath} = \Sigma_{ep}^{\rm W} V_{eff}^{\rm total} T_c^n \left(1 - \frac{T_B^n}{T_c^n}\right). \tag{7.5}$$

This cooling power is equal to the joule heating applied from the biasing circuit, as well as any zero frequency parasitic power coupling into the TES,

$$P_{\rm bath} = P_0 + P_{\rm par}. \tag{7.6}$$

In the limit that that the bath temperature is much less that the sensor temperature (which by design it is), we can drop the temperature ratio term. The effective volume of the

TES is known well, as per the same arguments in the previous section.

$$\Sigma_{ep}^{\mathrm{W}} \approx \frac{P_0 + P_{\mathrm{par}}}{V_{eff}^{\mathrm{total}} T_c^n}. \tag{7.7}$$

What is needed now is a measure of the true bias power P_0 and the superconducting critical temperature T_c. Typically in this situation, we make the claim that $P_0 \gg P_{par}$ and thus $P_{\mathrm{measured}} \approx P_0$. We additionally can measure the superconducting transition temperature by manually sweeping the bath temperature until the TES goes through transition.

However, interestingly the systematic from P_{par} on our estimate of P_0 shows up in exactly the same way as for our measurement for T_C. this means that we can get a very systematically robust estimate of Σ_{ep}^{W} from two measurements that themselves are both very sensitive to parasitic power! And thus we can use the following to calculate the coupling, regardless of the magnitude of P_{par}

$$\Sigma_{ep}^{\mathrm{W}} \approx \frac{P_{\mathrm{measured}}}{V_{eff}^{\mathrm{total}} (T_c^{\mathrm{measured}})^n}. \tag{7.8}$$

7.3.3 Estimating Logarithmic Temperature Sensitivity α

Using the method described in section 5.3, we estimate the α parameter for these devices, the results are shown in table 7.2.

7.3.4 Effective Volume of W/Al Overlap

Looking now at data from the QET based devices in Run 14, we can use the resistivity measured from the TES rectangles to cross check that other devices scale as expected. we can see in table 7.2 that the measured and predicted R_N values agree with each other, requiring only small tweaks to the designed TES line width (well within the expected fabrication uncertainty).

The prediction of bias power becomes more convoluted since we now have to worry about the contribution of the partially proximitized fin connectors and W/Al overlap regions. Recall from Eq. 3.4, the total effective volume of the QET is given by

$$V_{eff} = V_{\mathrm{TES}} + \zeta_{\mathrm{W/Al}} V_{\mathrm{W/Al}} + \zeta_{\mathrm{connector}} V_{\mathrm{connector}}. \tag{7.9}$$

However, since we measured Σ_{ep}^{W} from the TES rectangles, we can use the measured bias powers of the QETs as a measure of $\zeta_{\mathrm{W/Al}}$ and $\zeta_{\mathrm{connector}}$. Unfortunately there was an issue with the fridge during Run 14 that caused an early warm up and we did not get a T_c measurement. We did however re-run the same 4% devices in Run 15 and at least measured T_c for that device.

Table 7.2: Table of basic measured parameters from the Run 14 devices. Due to a problem with the fridge, this run ended early and the T_c was not measured. The T_c of the 4% device was measured when the device was run again in Run 15. The $*$ on the 0.25% predicted parameters comes from the assumption that the T_c of this devices is the same as the 4% device. This is a reasonable assumption since the fall times between the two devices are the same.

Device	4% Single channel	0.25% Single channel	1% Inner channel
R_{sh} [mΩ]	5 ± 0.5	5 ± 0.5	5 ± 0.5
Measurements			
R_p [mΩ]	4.4 ± 0.4	4.3 ± 0.4	2.9 ± 0.3
R_N [mΩ]	465 ± 45	492 ± 45	1227 ± 100
h_{TES} [nm]	45.849	45.849	45.849
P_0 [fW]	350 ± 20	11 ± 2	9.5 ± 1
T_c [mK]	53 ± 1	-	-
τ_{ETF} [μs]	34 ± 5	35 ± 5	59 ± 10
Predicted using Run 11 TES measurements			
R_N [mΩ]	467 ± 50	493 ± 50	1300 ± 150
τ_{ETF} [μs]	40 ± 5	36^*	-
P_0 [fW]	350 ± 20	12^*	-
w_{TES} [mΩ]	2.8	2.7	2.9
$\zeta_{\mathrm{connector}}$	0.9	0.9	-
$\zeta_{\mathrm{W/Al}}$	0.1	0.1	-

Using the 4% devices with fins and without fins from Run 14 and Run 15, we find that the W/Al overlap regions only contribute $\sim 10\%$ of their volume to the heat capacity, compared to the 45% value that was assumed in the design. This implies that for a version 2 design of the MELANGE detectors, the W/Al overlaps could be significantly enlarged - potentially resulting in a large QP collection efficiency with minimal noise increase. It is however unclear if making them too long would result in QP efficiency loss from QPs in the W/Al overlap down-converting before being thermalized in the TES. This would need to be systematically studied in further R&D devices. See tables 7.2 and 7.3 for the other parameter comparisons.

7.3.5 T_c Gradient Across Wafer

From the devices on the wafer that have had the T_c measured, there is seemingly a T_c gradient of at least $\Delta T_c = 5\,\mathrm{mK}$. The wafer location of the devices studied so far can be seen in Fig. 7.4.

Table 7.3: Table of basic measured parameters from the Run 15 devices.The measured values are on the top, and the predicted values based on Run 11 measurements is below, assuming $\epsilon_{\text{connector}}$ and $\epsilon_{\text{W/Al}}$ of 0.9 and 0.1 respectively. Highlighted in red are the values that are in disagreement with the measurement.

Device	4% Single channel	4% Single channel No Fins	TES on No Fin Device
R_{sh} [mΩ]	5 ± 0.5	5 ± 0.5	5 ± 0.5
Measurements			
R_p [mΩ]	2.5 ± 0.2	2.5 ± 0.2	2.6 ± 0.2
R_N [mΩ]	459 ± 50	375 ± 50	344 ± 50
h_{TES} [nm]	45.849	45.849	45.849
P_0 [fW]	355 ± 20	247 ± 15	11.3 ± 1
T_c [mK]	53 ± 1	49.5 ± 1	49.5 ± 1
τ_{ETF} [μs]	35 ± 10	55 ± 10	194 ± 10
Predicted using Run 11 TES measurements			
R_N [mΩ]	467 ± 50	467 ± 50	385 ± 50
τ_{ETF} [μs]	40 ± 5	53 ± 5	50
P_0 [fW]	350 ± 20	250 ± 20	13 ± 3
w_{TES} [mΩ]	2.8	2.8	-
$\zeta_{\text{connector}}$	0.9	0.9	-
$\zeta_{\text{W/Al}}$	0.1	0.1	-

7.3.6 Measurements of Thermal Conductances

The last fundamental film parameter of interest is the thermal conductance of the W to Si substrate G_{TA}, and the conductance from the substrate to the bath G_{AB}. While in the above section, we simply estimated G_{TA} under the assumption of $T_B \ll T_c$, for completeness we also performed a more robust measure. This was done in Run 11 by 9 IV sweeps of the 100x400 W2 device as a function of bath temperature, varying from base to expected T_c, as shown in Fig. 7.5 (left). A point of constant R_0 is selected, and the bias power calculated at this R_0 value at each bath temperature (middle plot of Fig. 7.5). Finally, this bias power vs bath temperature can be fit directly to Eq. 2.3 while keeping the thermal conductance exponent fixed to $n = 5$.

G_{TA}

This fit gives $G_{\text{TA}} = 9.26\,\text{pW/K}$ for the 100x400 W2 TES. Converting this to the volume invariant electron phonon coupling we get

$$\Sigma_{ep}^{\text{W}} = 1.1 \times 10^8 \, \frac{\text{W}}{\text{K}^5\text{m}^3}, \tag{7.10}$$

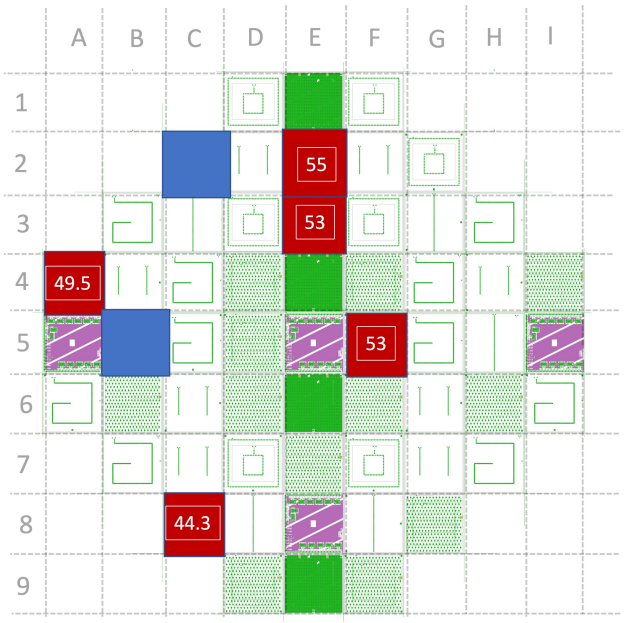

Figure 7.4: Wafer location of studied devices. The red squares represent the location of devices where the T_c was measured (T_c shown in white text in mK). The blue squares show devices that we've studied, but were unable to get a T_c measurement. E2:TESTR, E3: 4%, B5: 0.25%, A4: 4% No Fin, C2: 1%.

which is in perfect agreement with the value needed to make the bias powers for the TES and MELANGE devices match the measured values.

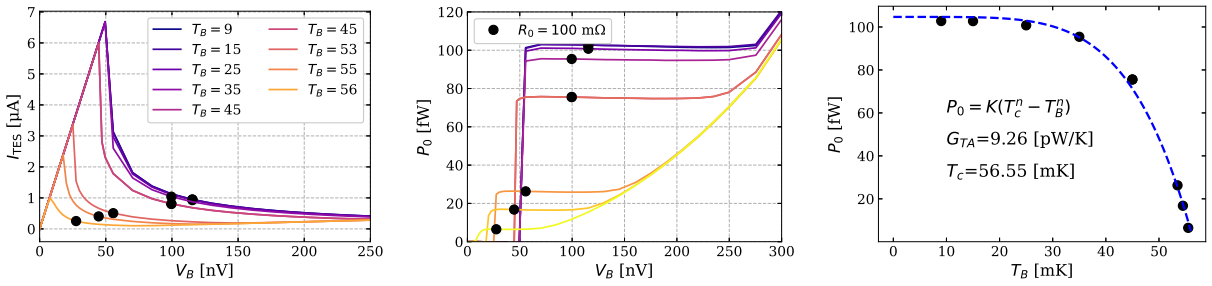

Figure 7.5: Calculation of the thermal conductance from TES to bath for the 100×400_W2 TES. Left: IV sweeps for various bath temperatures, the black dots represent the data points selected to calculate the bias power. Middle: IV curves from the left plot converted to bias power. Right: Bias power at $R_0 = 100\,\mathrm{m}\Omega$ as a function of bath temperature. The blue dashed line shows the fit to Eq. 2.3.

Thermal Conductance of Au pad

Measuring the thermal conductance to bath requires two channels on the same device. One channel acts and a 'heater' and the other a 'thermometer'. The heater applies a power to the substrate, warming it up enough that in equilibrium the thermometer TES is put into transition. This process is repeated as a function of bath temperature, adjusting the heater power at each point such that the thermometer remains at the same point in transition throughout the whole process. The power of the heater as a function of T_B is then fit to Eq. 2.3 in the same way that was done above.

This was done in Run 15 with the 4% no fin devices, using the single TES channel as the heater, and the QET array as the thermometer. The fit was done was done for both the case of letting n be a free fit parameter, as well as keeping it fixed at $n = 5$. The fits can be seen in Fig. 7.6 and the corresponding results are shown in table 7.4. Interestingly, when n is left free, the fit tends towards $n = 6$. Indeed, this is theoretically predicted for disordered normal metals such as Au and Cu, and this T^6 scaling has previously been observed for Au films [140].

Comparing this to the measured electron-phonon coupling for the W film in table 7.1, we see that the electron-phonon coupling for the Au is roughly 5-70 times larger. Using the effective volume of the 4% device and the measured Σ_{ep}^{W} to estimate its G_{TA}, we find that G_{AB} is exactly 50 times larger! So these pads were sized perfectly (at least for the 4% device).

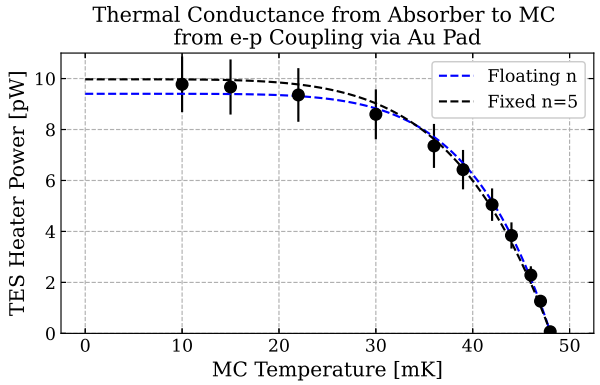

Figure 7.6: Fit of the heater power vs T_B to Eq. 2.3. The fit is done both with keeping the thermal conductance exponent fixed at $n = 5$ (black) or letting n be a free parameter in the fit. When n is left free the best fit tents towards $n = 6$.

Table 7.4: Results of the thermal conductance measurement of the Au pad. Results are shown for both the case of fixing n in the fit to $n = 5$, and letting n be a free fit parameter. *Notice the different units for the electron-phonon coupling constant between the two different cases*

Fit Parameter	Fixed $n = 5$	Free n
n	n=5	$n = 5.95$
T_a	48.1 mK	48.1 mK
G_{AB}	1.04 $\frac{\mathrm{nW}}{\mathrm{K}}$	1.16 $\frac{\mathrm{nW}}{\mathrm{K}}$
$\Sigma_{ep}^{\mathrm{Au}}$	9.34×10^9 $\frac{\mathrm{W}}{\mathrm{K}^6\mathrm{m}^3}$	0.58×10^9 $\frac{\mathrm{W}}{\mathrm{K}^5\mathrm{m}^3}$

7.4 Noise Analysis

It is now beneficial to take a slight aside to discuss unwanted excess noise sources. For the following discussion, the term noise is typically referring to unwanted excess above the fundamental intrinsic noise. Also, as a note to the reader, pay attention to the units used in various noise plots. Noise will often be presented as referenced to input current, or input power (NEP). The NEP is ultimately the most relevant, but for simplicity, sometimes the current noise is used as it requires no conversion with TESs parameters.

It is easiest to break the noise into three different categories:

1. **Structure:** theoretically we would expect the NEP to be a nice smooth curve, like the green line in Fig. 7.8. We see lots of peaks at various frequencies, as well as $1/f$ noise, that we refer to as 'structure'.

2. **Excess TFN-like noise:** White noise that is in our signal band, $\sim 2\pi/\tau_{\mathrm{ETF}}$, above the level of the TFN.

3. **Excess Johnson-like noise:** Excess noise that is above the ETF pole and resembles the TES Johnson noise.

4. **Out of band noise:** Any excess noise that is well above our sensor bandwidth. For example, all the excess above 100 kHz.

For the most part, it is the first two categories that we care about about most, specifically the second. The energy resolution of the detector is limited by the TFN-like component of the noise. Depending on the severity of the $1/f$, extra noise peaks, and excess Johnson-like noise, these will degrade the performance, but these are higher order effects. The out of band noise is typically inconsequential, unless it is of a large magnitude and is aliasing into our signal band somehow and becoming TFN-like.

7.4.1 Noise Coupling Sources

The first thing that should be checked when looking at excess noise structure, is to track down where it is coupling in. By putting the system in different states and seeing how the noise changes can give insights into its origin. One powerful tool we have at our disposal is the fact that we can drastically change the total resistance of the TES, changing the inductive properties of the TES circuit loop.

Voltage Noise in the TES Loop

As an example, for an unknown voltage noise source ($\tilde{v}_{\rm noise}$) coupling into the TES bias loop, from Fig. 7.7, the current noise on the TES goes like

$$\tilde{i}_{\rm noise} = \frac{\tilde{v}_{\rm noise}}{R_\ell + R_{\rm TES} + j\omega L}. \tag{7.11}$$

For frequencies below the L/R pole, when the TES is normal this voltage noise source should be suppressed by roughly a factor of $1/R_N$ relative to when the TES is superconducting. Thus if the magnitude of the excess noise peaks scales with $R_{\rm TES}$ and is dominant when SC, then it is likely that the excess noise is coupling into the TES bias circuit.

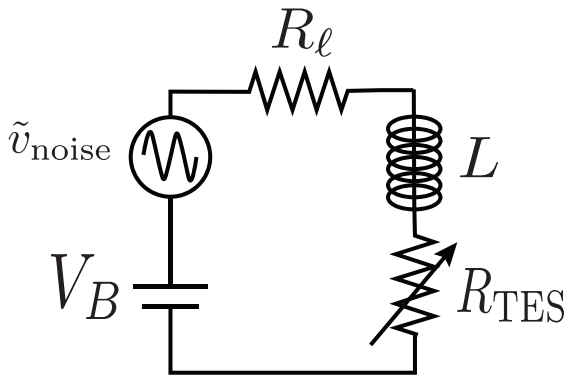

Figure 7.7: Thevenin equivalent circuit for the TES biasing circuit with added unknown voltage noise source $\tilde{v}_{\rm noise}$.

Current Noise in the Readout Electronics

An alternative scenario is the case of some current or voltage noise source coupling into either the SQUID or electronics in the amplifier/readout chain. In this case, changing the TES resistance should have no effect on the magnitude of the noise coupling. For our purposes here, this is the end of this story. However, these noise sources are typically quite 'easy' to find and 'solve'. You can typically vary all the different gain settings in the amplifiers and change the SQUID bias point to see which setting effected the input referenced noise. This

usually tells you unambiguously where in the readout chain the noise is coupling in and can typically be filtered e.g. if the noise occurs at a particular op-amp, some simple RC filtering on the bias rails can often solve this. For an example of diagnosing excess noise sources in a room temperature amplifier, see appendix E for a study I did for the SuperCDMS DCRC electronics.

Power Coupled Noise

So far, if noise occurs in all three states (SC, T, and N), then the noise source is one of the two options above. However, as is often the case, there are many unwanted noise sources that *only* couple into the system when the TES is in transition. Since TESs are ultimately sensitive to power fluctuations, we refer to any noise source in this category as 'power coupled'. The origins of these noise sources can be vast and exotic in nature, and these are by far the most difficult problems to remedy. Some of the more well known power coupled noise sources are:

1. **Vibrations:**
   - TESs vibrating in B-field: The TES resistance can also have a dependence on a changing magnetic field. If the TES is sitting in a static B-field, the vibrating TES will see this as an oscillating B-field which can induce noise. This is not something that we currently model in our TESs. Building a set of coils to create variable B-fields around the TES would be a very useful project to further optimize our TESs.
   - Phonon noise from frictional rubbing: Almost any type of holding mechanism relies on some form of frictional contact between the detector and the housing. When the housing is vibrating, this frictional rubbing will release athermal phonons. Methods for reducing this have been discussed in the previous chapters, and well as later in this chapter.
2. **Photon shot noise:** Shot noise is the irreducible Poissonian noise which is a consequences of the discrete nature of the particle in question, in this case a photon. For cryogenic experiments, photons from black body radiation from higher temperature stages in the cryostat, or from electronic components, can manifest as shot noise on the detector.
3. **Out of band EMI:** EMI sources well above the bandwidth of our sensors will effectively be aliased down into the signal band, or show up as a DC power source.

7.4.2 TESTR Devices in Run 11

With a fairly good understanding of the fundamental properties of the W films, and a crash course in noise analysis out of the way, we can now turn to modeling the noise. Just as the simple nature of the TES rectangles allowed us to study basic film properties without

unnecessary complications of the Al fins, they are also a powerful diagnostic tool in diagnosing noise problems. Thus we will start the analysis first with the TESTR devices from Run 11. We plot the NEPs for the three TESs in Fig. 7.8 along with the estimated noise model. From these plots, it is immediately obvious that the noise model differs from the measured NEP.

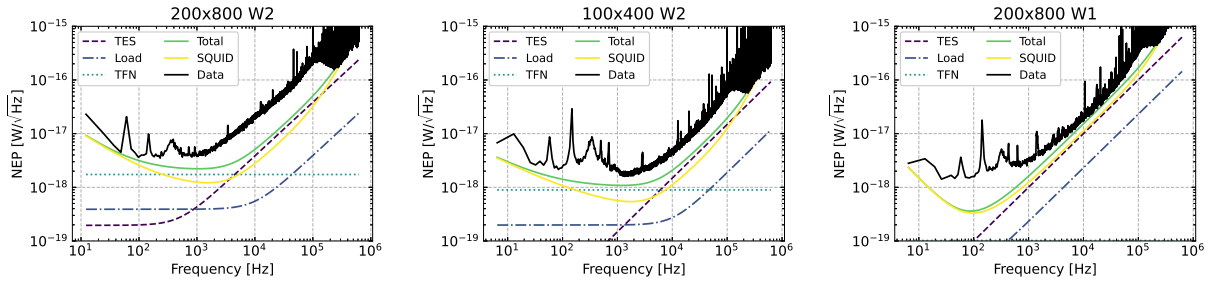

Figure 7.8: Noise Equivalent power for the three TES devices from Run 11 at $R_0 \approx 10\%R_N$.

In Fig. 7.9 we plot the normal, SC, and transition state noise. There are features at 10 Hz and 60 Hz and a few lines above 5 kHz that all have constant magnitude in all three states, suggesting this is due to downstream electronics. Additionally there is maybe one or two peaks that are largest in the SC state, suggesting these is a voltage noise coupling into the TES loop. However, there is quite a bit of structure that is only seen in transition.

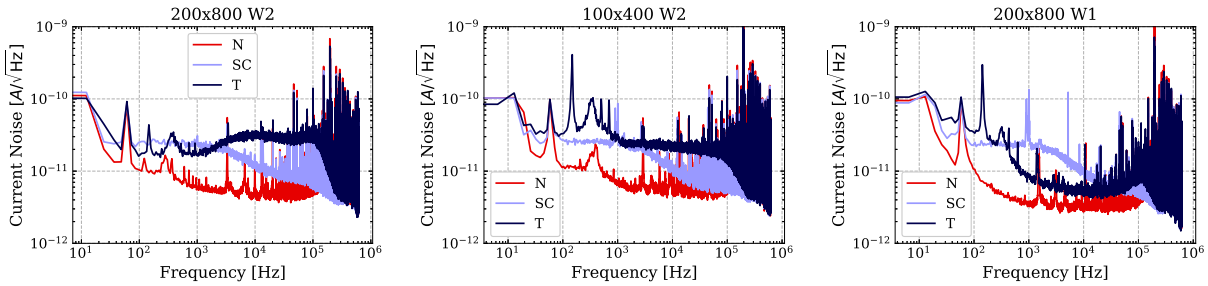

Figure 7.9: Comparison of superconducting, normal, and transition state at $R_0 \approx 10\%R_N$ for the Run 11 devices.

Since the TESTR chip that these TESs are on is covered with more than 95% of the instrumented surface with passive W, there should be effectively no phonon signal readout by the TES. Thus excess power coupled noise for the TESs should be a source that interacts with the TESs directly. We can look into the power coupled noise further to test the idea of excess vibration noise by temporarily turning off the pulse tube cryocooler (PT) in the DR, which is known to cause significant low frequency vibrations. A plot of the noise for PT on vs PT off for all Run 11 devices can be seen in Fig. 7.10. There is no significant difference in

the noise with the PT-off, suggesting any excess PT-on noise seen on other devices (which we will get to soon) is indeed caused by vibrations from the PT (as opposed to EMI from from the PT itself).

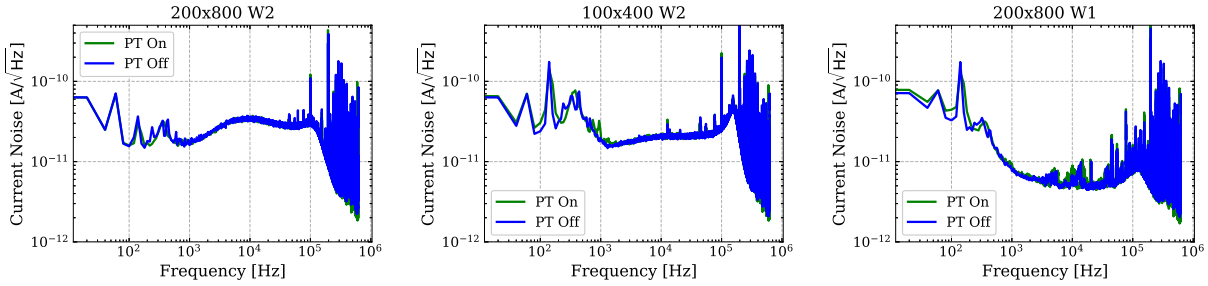

Figure 7.10: Comparison to the current reference TES noise with pulse tube on vs pulse pulse off for the three TESs in Run 11.

We will get more into the noise shortly when discussing other devices, but for now we can ask one more question about the excess noise: is the noise seen on different channels the same? This can be answered by looking at the cross spectral density between the channels, and specifically by inverting this matrix one can estimate the 'correlated' and 'un-correlated' components of the noise[1]. What is the utility in doing this? At the end of the day we wish to have an understanding of the the fundamental noise limitations of our devices. By definition, intrinsic noise should be random. The presence of noise correlated across devices suggests that its origin *must* be environmental in nature. The estimate of the un-correlated noise gives a better idea of what the intrinsic noise is for each device. From Fig. 7.11 we can see that almost all of the structure in the noise is correlated between the different devices and the resulting un-correlated PSDs are relatively flat as we would expect.

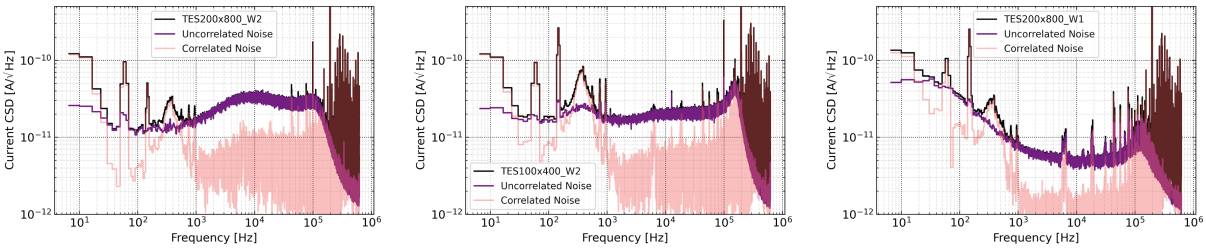

Figure 7.11: Estimation of the correlated and non-correlated components of the noise between the three TESs in Run 11.

[1]For a detailed derivation of why this is true, see section 5.3.5 of Noah Kurinsky's thesis [77]

It is clear that the total noise level of the excess noise spikes below $\sim$ 1 kHz is well above the un-correlated component of the noise for each channel. This implies that the magnitude of the noise of these spikes of the total noise is a good proxy for the correlated component throughout the transition[2]. In Fig. 7.12 we plot the magnitude of the noise peaks at approximately 150 Hz, 360 Hz, 720 Hz, and 900 Hz as a function of R_{TES} throughout the transition region. We can see that this noise is roughly flat as we change the TES bias point. This is indicative of a purely power coupled noise source - there is no sensitivity to R_0, only power.

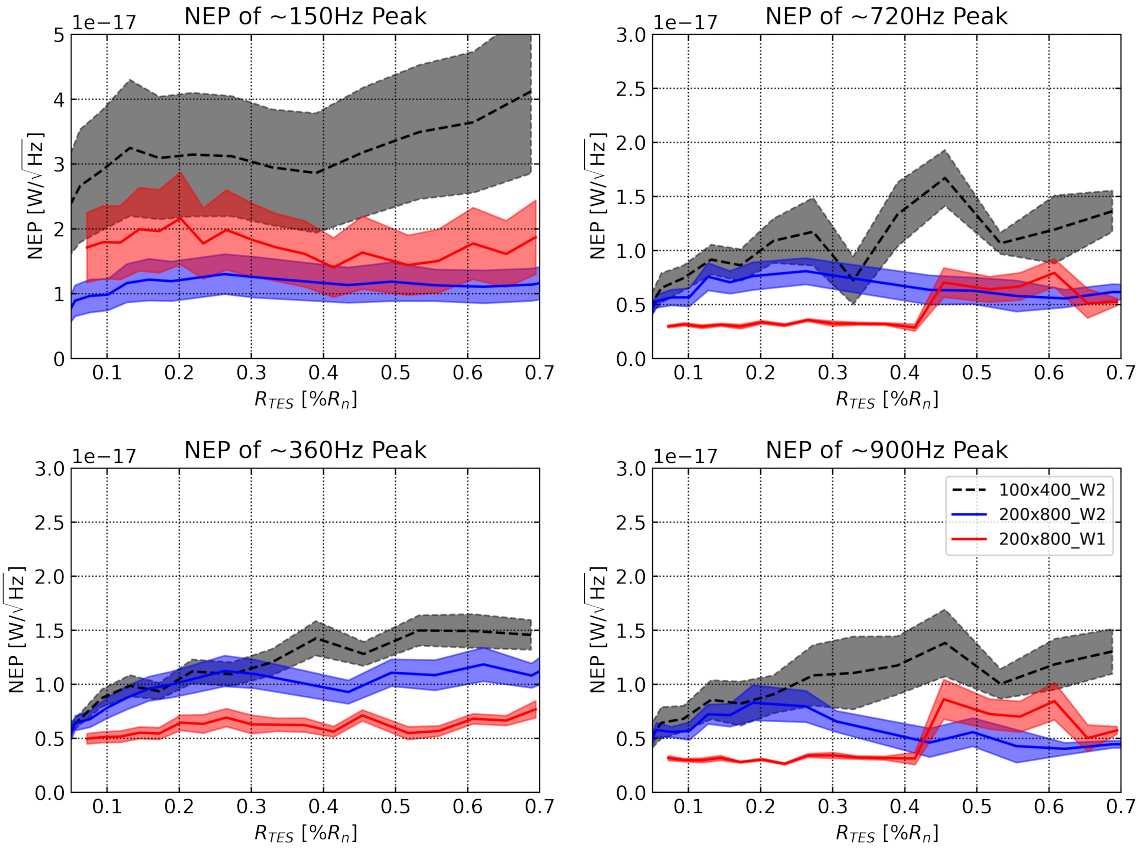

Figure 7.12: NEP of the 4 most prominent excess noise 'spikes' as a function of TES resistance

Lastly, it is interesting to look at the excess Johnson noise component. We can see from Fig. 7.8 that the Johnson noise model comes much closer to matching the measured NEP for the $W1$ TES than for the other TESs. This can also be seen in Fig. 7.13 with the $\sqrt{1+m^2}$ factor, which is roughly the ratio of excess Johnson noise to expected Johnson

[2]Since we only took this correlation data at one bias point, we were not able to measure the correlated/uncorrelated components throughout the full IV sweep.

noise. Although we cannot explain the excess noise using any known model of TES Johnson noise, we note that the trends seen in Fig. 7.13 do closely match the the way that β scales for these devices throughout the transition, as shown in Fig. 7.14.

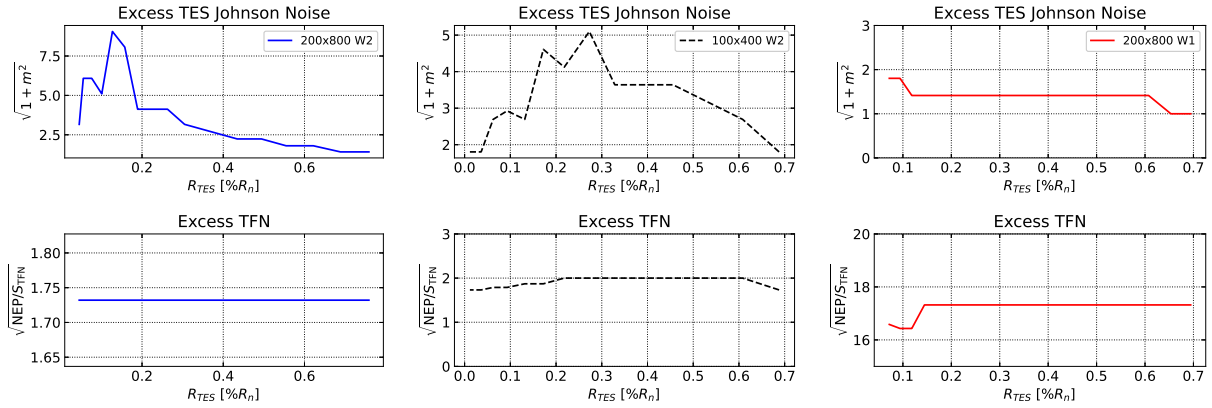

Figure 7.13: Measure of the excess white broad-band noise sources as a function of R_{TES}. The lower plot shows the square root of the ratio of the measured NEP to the expected TFN to quantify the excess 'in-band' noise. The top plot quantifies the ratio of excess TES Johnson-like noise with the m factor.

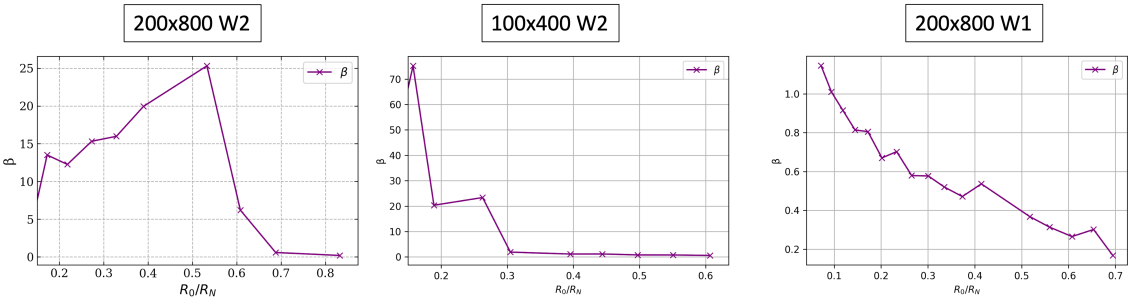

Figure 7.14: Logarithmic current sensitivity β as a function of R_0 for the TESTR devices from Run11.

Energy Resolution of TESTR TESs

Finally, we can use the measured noise to estimate the expected energy resolution to a Dirac delta impulse of energy. The reason that we are interested in this metric, is this is the minimum resolvable energy that could be delivered to the TES by a QET fin (after the efficiency losses in the phonon collection are already accounted for). This is an important

distinction from saying that this TESs would be sensitive to say a direct absorption of a photon of that energy. The photon case is more complex as there are many loss mechanisms, specifically phonon down conversion into the substrate.

We calculate the resolution using Eq. B.2, shown again below

$$\sigma^2 = \left[\int_0^\infty \frac{d\omega}{2\pi} \frac{4|p(\omega)|^2}{S_{P_{tot}}(\omega)}\right]^{-1} \tag{7.12}$$

with $p(\omega) = 1$. The resolutions estimates can be seen in table 7.5. Even though the un-correlated noise has a much cleaner spectrum, there is not actually very much energy contained in spikes when the noise power is integrated. Removal of the correlated components only gives a roughly 10% improvement in expected energy resolution, where we are really hoping for factors of more than $\times 2$ improvement in noise power. It is still the in-band TFN-like excess noise that is degrading the sensor performance the most.

It is worth checking if these results are consistent with our past devices. Recall that the energy resolution of a TES should scale as

$$\sigma_E \propto \sqrt{VT_c^3}. \tag{7.13}$$

Using the devices in table 6.2, we can confirm that the W2 TESTR TESs perform exactly as expected. However, the W1 device with a T_c of 19 mK should have performed about 6 times better than we measured. This should come as no surprise from the incredibly large deviation from the expected NEP in Fig. 7.8. In the next sections we will investigate the excess noise story further.

Table 7.5: Expected energy resolution of a Dirac delta impulse of energy into the TES. *the bias point of the 200x800 W2 that was used for the correlation study was not the optimum. The energy resolution was calculated with the NEP from a different data set, the 'un-correlated' resolution was estimated by scaling the ratio of the full PSD vs un-correlated PSD to get the percent change.

Device	σ_E [meV] (total noise)	σ_E [meV] (un-correlated noise)
100x400 W2	75	65
200x800 W2	145	125*
200x800 W1	174	145

7.4.3 Athermal Phonon Devices

We now add back in the complexity of the athermal phonon sensors with the MELANGE detectors. We can introduce the fins in a controlled way by studying the 4% single channel

MELANGE device, and the exact same device but with nearly all of the fin area decoupled, as was done in Run 15 (see Fig. 7.3. We learned in the last section that the the TES rectangles have practical zero sensitivity to vibration noise from the pulse tube, suggesting that PT induced noise is vibrational in nature. Under this hypothesis we would expect that the 4% melange device should be *significantly* more sensitive to vibrations than it's twin with the fins mostly removed. As shown in Fig. 7.15, this is exactly what we see. The low frequency noise of the regular 4% device is incredibly elevated compared with the the no fin device with the PT on, and the two devices have almost equivalent noise with the PT off. This now fully proves that the PT related noise is indeed phonon related and not due to any kind of electromagnetic coupling.

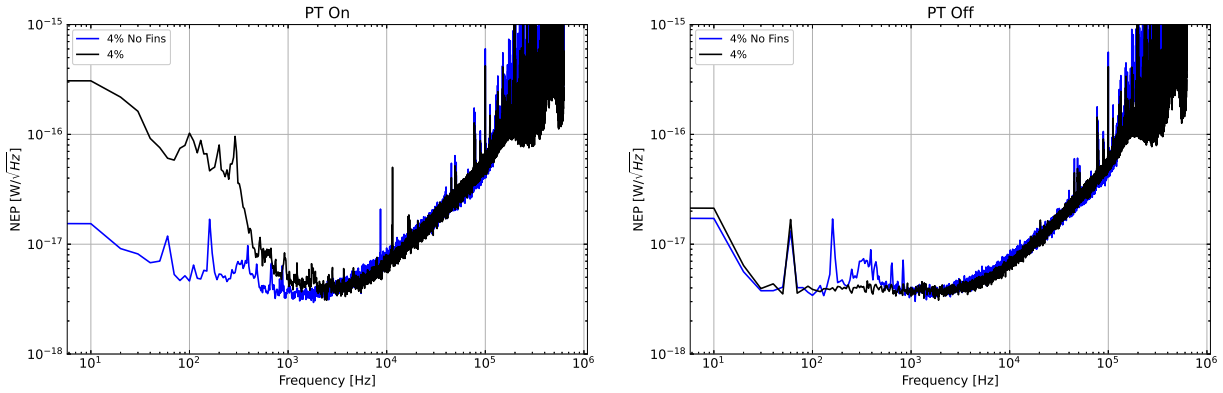

Figure 7.15: Comparison of the regular W2 4% devices and the W2 4% no fin device NEP with the PT on (left) and the PT off (right) from Run 15.

We do still notice that there is some unwanted structure to this noise: the $1/f$ and 60 Hz spike that is related to the readout electronics, and the spikes centered around 150 Hz and 360 Hz that were seen on the Run 11 TESTR devices. Since we learned before that this is all correlated, we can go look at the uncorrelated component of the PT off data for the most accurate estimate of the true intrinsic noise, which is plotted in Fig. 7.16 for the fin and no fin device. We notice that in this scenario, for the in-band NEP, we measure roughly twice what is predicted from the model. However there is very little TES Johnson-like excess noise. Interestingly the noise model of the single TES channel on the 4% no fin device comes quite close to the measured NEP spectrum. Looking at the values for β for this device, we see that it has a similar trend to that of the 200x800 W1 devices from Run 11 shown in Fig. 7.14.

7.4.4 Estimated Energy Resolution for MELANGE Devices

Lastly, we can use the measured NEPs to estimate the expected energy resolution for the SPICE MELANGE devices. We do this for for the both the case of dirac delta impulses of

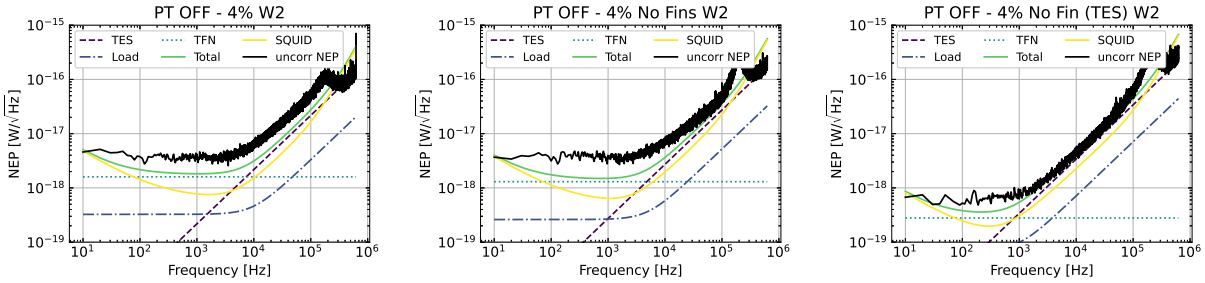

Figure 7.16: Un-correlated component of the NEP with the Pulse Tube turned off for all devices in Run 15. The figure on the right is the single TES channel that was on the 4% no fin device.

energy into the TESs, and using the expected athermal phonon collection times and total athermal phonon collection efficiencies from table 4.1. The energy resolutions are calculated for the devices ran in Run 14 and Run 15 in table 7.6.

Table 7.6: Expected energy resolution of a Dirac delta impulse of energy into the TES, as well as including the expected athermal phonon time constants and efficiencies for some of the MELANGE devices.

Device	Setup	Data Type	σ_E [meV] (Including τ_{ph} and ε)	σ_E [meV] (δ)
4% W2	Run 14, Resting	PT Off	513	110
4% W2	Run 15, Resting	PT Off, De-correlated	495	105
0.25% W2	Run 14, Resting	PT Off	460	22
1% W2 (Inner Channel)	Run 14, Hanging	PT Off	610	30

7.4.5 Infra-Red Loading

DC Parasitic Power Loading

We've established that the pulse tube adds lots of noise, why not just run without it? Well besides the obvious answer that the fridge will start warming up after about 20 min without the PT, there is a more surprising answer. With the PT off, the MC begins to cool slightly, however the temperature of the 4K stage begins to rise. We actually see this rise when measuring the shift in bias power and TES resistance as a function of time since the PT was turned off in Fig. 7.17. We see that the TES resistance *increases* and the bias power *decreases* as the 4K plate temperature increases. This seems to suggest that some amount

of bias power is being supplied via black-body radiation from the 4K plate. We see a similar effect when we change the temperature of the still stage as shown in Fig. 7.18.

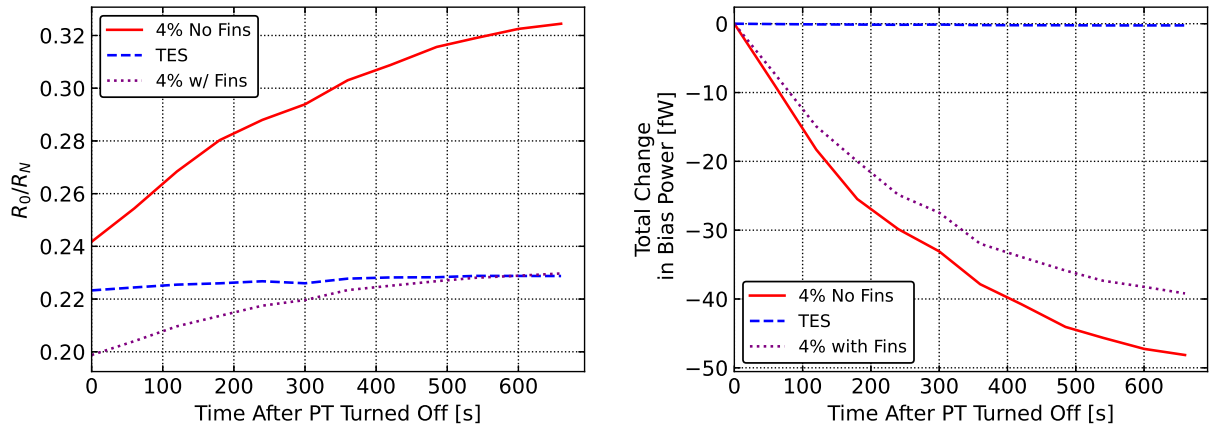

Figure 7.17: Change is relative TES resistance (left) and total shift in bias power (right) as a function of time since turning the pulse tube off. Since the 4K plate is warming up while the PT is off, the time axis is a qualitative proxy for the change in temperature.

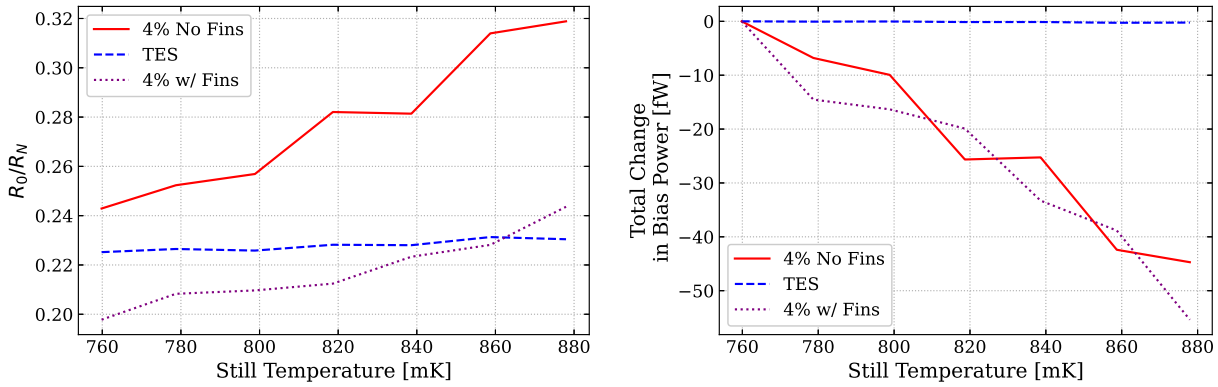

Figure 7.18: Change is relative TES resistance (left) and total shift in bias power (right) as a function the temperature of the still stage.

Recall from Wien's displacement law, the peak wavelength from a black-body (BB) at temperature T is given by

$$\lambda_{\text{peak}} = \frac{2.8977 \times 10^{-3}\,\text{K}}{T}. \tag{7.14}$$

Thus for the 4K plate and Still temperature sweep we would expect the BB spectrum to peak around 1700 μeV and 350 μeV respectively. These energy scales give us a clue into the coupling mechanism. Since these are all well below the Si electronic bandgap, we know they are not coupling in via the Si absorber. These are both above the 2Δ threshold to break cooper-pairs in the Al fins, and certainly the W.

Since for most of these devices, the Al surface area is 50-100 times larger than the W only area, we would expect that the dominant source of coupling would be into the Al fins. At first glance, the results Fig. 7.17 and Fig. 7.18 in are quite non-intuitive. The two 4% devices have the exact same W and W/Al overlap areas, the same amount of Al area, but with the important distinction that the 'no fin' device has over 90% of the Al electrically disconnected. Why then do the devices see the same shift in bias power in these two scenarios? This could imply that the dominant IR coupling is into the W or W/Al overlap. This was a very surprising result to our group! We were so confident that the IR was coupling into the Al fins, that we almost didn't do this study!

IR Shot Noise

The previous section hypothesized a DC heat loading from IR. One would also think that the presence of IR could contribute shot noise to the system. This was studied in a similar way to the DC heat loading, by looking at the NEP as a function of time while the 4K plate warmed up with the PT off. From Fig. 7.19 we see that there is no noticeable difference in the NEPs between any of the Run 15 devices across the full period of time with the PT off. This is again surprising, as we naively would have expected the 'with-fins' device to be orders of magnitude more susceptible to IR shot noise than its 'no fin' counterpart. However, upon second look, there is another explanation. From Fig. 7.16, we saw that for these devices, with the PT off, they were already operating near their intrinsic noise limit. This means that IR shot noise might very well be a problem, but it is at a level that is below the sensitivity of the sensors. To attempt test this hypothesis, we repeated the 'fins vs no fins' test with the lower T_c wafer (W1) in Run 16. Unfortunately neither detector was able to go through its super conducting transition. Scaling from the 200x800 W1 TESTR devices, we would have expected a bias power of about 4 pW for these detectors. The fact that they remained normal could be due to a T_c gradient on the wafer, resulting in a much lower T_c than expected, or simply a worse noise environment this run.

7.4.6 Getting Rid of Pulse Tube Noise

Since we've now discovered that the operating point of the TESs is highly variable when the PT is off, we need another method to get rid of the vibrational noise it induces. As a long term solution, much effort by Sam Watkins has been put into the design of a two stage passive vibration isolation system which will essentially mechanically decouple the mixing chamber plate from the rest of the fridge. This however is still in the design phase at the time of this writing, see his thesis for details.

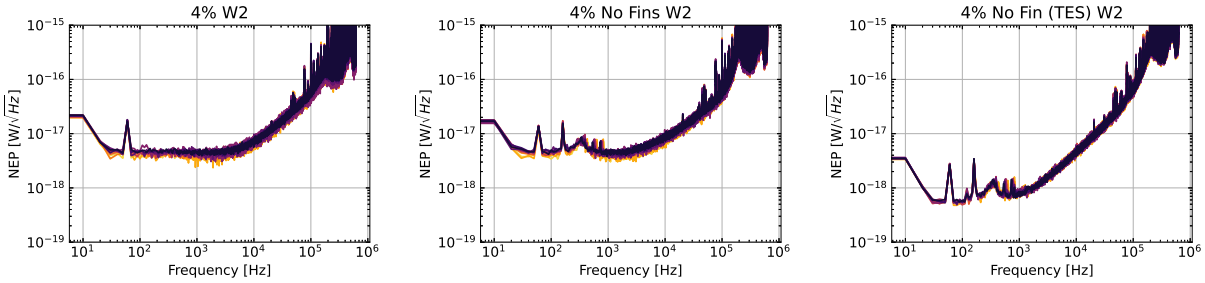

Figure 7.19: Variation of NEP across a 10 min period of the PT off. Lighter yellow colors indicate earlier times and darker colors indicate later times.

As a short term solution, we have studied the idea of mechanically decoupling detectors from the housing itself by suspending them from wirebonds as discussed in section 4.7.1. In Run 14 (see Fig. 7.2) we ran two devices in the 'resting' configuration and one device in the 'hanging' configuration. Looking at the NEP with the pulse tube on vs off in Fig. 7.20, we notice a large improvement in the NEP at low frequencies with the PT off for the resting devices, while there is essentially no change for the hanging device. It is also necessary to point out that we observe no elevated low frequency noise for the hanging device like we do for the two resting devices for PT on, suggesting that hanging the detector from wirebonds is seemingly incredibly effective at reducing vibration noise.

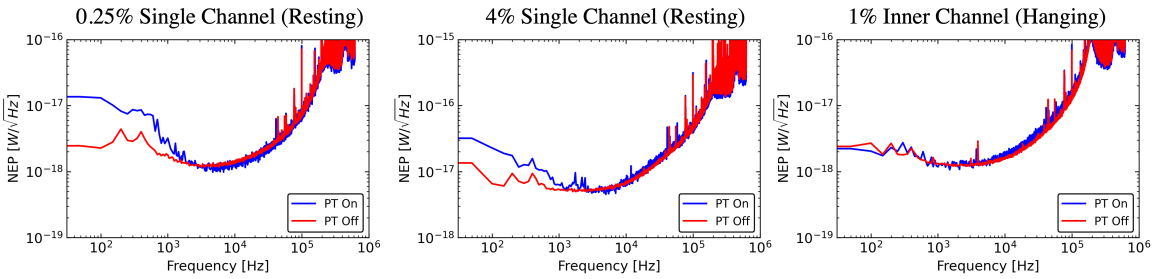

Figure 7.20: NEP for PT on and PT off for the 0.25% single channel device in the resting configuration (left), the 4% single channel device in the resting configuration (middle), and the inner channel of the 1% two channel device in the hanging configuration (right) from Run 14. Notice how the PT on vs off NEP for the device that is hanging is virtually the same, while there is a large different in low frequency NEP for both resting devices. Figure made by Samuel Watkins.

7.5 Future Studies

7.5.1 Ballistic Athermal Phonon Lifetime Study

A major goal of the design of the SPICE MELANGE detector set was to measure the ballistic athermal phonon lifetime for various detector materials to understand how far we could push the 'low coverage' design philosophy. In principle, this study should not be difficult, In practice, it turns out to be so.

Recall from Eq. 3.69 that the athermal phonon power pulse shape is approximated by

$$p_P(\omega) = \frac{1}{1 + i\omega\tau_{ph}}. \tag{7.15}$$

However, what we measure is actually the convolution of this pulse shape with the TES power-to-current response function given by Eq. 2.50. In the case where τ_{ph} and $\tau_{\rm ETF}$ are well separated from each other and both much larger than τ_{el}, the resulting measured current pulse is of the form

$$I_{\rm TES}(\omega) = A\left(\frac{\tau_f}{(1 + \omega j\tau_f)} - \frac{\tau_r}{(1 + \omega j\tau_r)}\right), \tag{7.16}$$

where the rise time (fall time) τ_r (τ_f) is whichever is the faster (slower) of τ_{ph} and $\tau_{\rm ETF}$, and A is simply an amplitude scale factor. In this case, using a non-linear fitting routine (described in Appendix F) to fit the rise and fall times easily gives you τ_{ph} and $\tau_{\rm ETF}$. In the case that the time constants are not well separated, comparable to τ_{el} or if the transfer function given by Eq. 2.50 is too simplistic for the thermal setup (e.g. if you have extra thermal bodies), this method fails.

However all is not lost. We have learned in this thesis that the components that go into the current-to-power responsivity are very well known from our measurements of the complex admittance (see chapters 2 and 6). These values can be used to remove the TES dynamics from the fitting itself. Since we know the responsivity, we can deconvolve the TES response from measured pulses and recover the original power pulse (with sizable amounts of noise added). This method I developed is described in detail Appendix F, and an example fit to fake data is shown in Fig. 7.21.

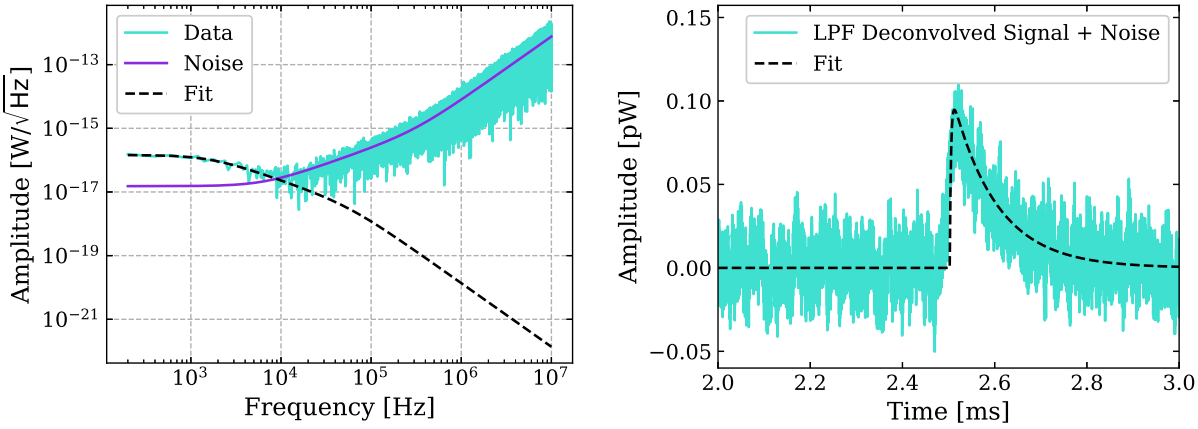

Figure 7.21: Example of pulse fitting routine using fake data. Left: Fit to the deconvolved signal plus noise in power done in the frequency domain. Right: the best fit parameters from the frequency domain fit shown in time domain with the low pass filtered noisy signal.

Finally, once a measurement of τ_{ph} has been made, we can use it as a measure of the ballistic athermal phonon lifetime. Recall that the the phonon time constant being measured is actually a combination of the lifetime and the estimated collection time based on the geometry of the device,

$$\frac{1}{\tau_{ph}} = \frac{1}{\tau_{\text{life}}} + \frac{1}{\tau_{\text{collect}}}. \tag{7.17}$$

Thus, for a measured phonon collection time we can make the statement,

$$\tau_{\text{life}} \geq \tau_{ph}. \tag{7.18}$$

Saturation vs Positional Dependence

Unfortunately for the case of the MELANGE devices studied so far, we have been unable to get clean data-sets to make this measurement. The pulse fitting algorithm has worked quite well, but the variation seen in pulse shapes cannot be explained with out limited data. For the 0.25% and 4% devices, we only have data with the devices in the resting configuration, which means they are dominated by low frequency vibration noise up to 10+ σ. This is potentially into the regime where events will begin to saturate some of the QETs. As shown in appendix F, this manifests as a lengthening of τ_{ETF}, which when deconvolved from the measured pulse, will falsely lengthen τ_{ph}. However, we are also worried about an energy independent positional dependence due to the fact that the ultra-low coverage devices (0.25% and 1%) didn't have homogeneous QET coverage of the detector surface. This type of positional dependence would show up as events occurring far from the QETs having longer

time constants than events originating closer to the QETs, and should be invariant to event energy. The latter of these two effects is a *real* change in τ_{ph} where as the former is artificial. Thus by only having relatively high energy events to fit, we are not able to disentangle these two effects.

For the 1% we were able to take data with it hanging to limit the vibrational noise, but unfortunately one of the channels had an 'open' electrical connection after the fridge cooled down. This also makes the positional dependence problem difficult to answer, as 60% of the phonon absorbing surfaces are not being read out.

Ideally, this study needs to be done with either single channel devices, or two functioning channels, mounted in the hanging configuration. By the time this thesis is published that will likely be the case, but as of the time of this writing that data has yet to be taken.

7.5.2 Relative Energy Calibration

As has been discussed at length in this thesis, one of the primary figures of merit of a low-temperature micro-calorimeter is its energy resolution. And while I have discussed many ways this can be estimated from the noise and complex admittance measurements, a direct energy calibration is needed in order to fully understand the detector.

A standard method of calibration is to place a source of events with a well known energy incident on your detector. This calibration 'line' is then used to scale your energy estimator for all the events relative to this value. With the energy of this line now known, one can look at the ratio of the energy removed from the TES via electro-thermal feedback, given by Eq. 2.62, with the known source energy to calculate the total athermal phonon collection efficiency.

For the CPDv1 detector described in section 6.2, the energy scale was barely high enough that a low energy nuclear source could be used for a calibration line, albeit with some saturation. For the SPICE MELANGE detectors, nuclear sources are simply too energetic and a fiber optic photon source is needed. At the time of this writing, a design for this calibration system has been finalized and parts ordered, but it will be some time before it is commissioned in the fridge.

7.6 Conclusions

While I had originally hoped for this thesis to include more results, it has still shown the indented goal that the energy resolution improves rapidly with T_c and TES Volume. I think some very interesting results from this chapter are the fact that the effective volume contributions to the TES heat capacity from the W/Al overlap are much smaller than we had originally assumed based on past measurements. This suggests that we could increase the size of the overlap region to hopefully improve QP collection efficiency, without paying much of a penalty in the NEP of the TES. This result will greatly influence the next iteration of SPICE detectors.

Another important take away from this work is the benefit of including the TES rectangle devices in every detector mask set (when making lots of devices on a single wafer). By studying those devices on this wafer first, I was able to show that there was a decent about of variability across the film in terms of resistivity and T_c. It was also only possible to calculate the effective volume contributions of the overlap regions by first studying the TES rectangles without the complications of the Al overlap.

Lastly, the 'IR test' device with the fins cut off was instrumental in breaking the degeneracy between Infra-Red and EMI backgrounds in the fridge. While it is not evident after the fact, the results of Run 15 were completely against everyone in our lab's intuition at the time.

Chapter 8

Conclusions and Looking Forward

After finishing this thesis, the detector physics minded reader might have noticed an asymmetry between the amount of spaced dedicated the theory and measurement of noise, vs the theory and measurement of athermal phonon/QP collection efficiency. Understanding the phonon dynamics is something that is being pursued by many condensed matter theory groups, with measurements that will follow using the devices designed in this thesis (as well as other groups). However, the effort to understand and improve, the quasiparticle collection process in the QETs has somewhat stagnated. This is not from sheer laziness, this is an incredibly challenging problem that requires an entire dedicated R&D work program. However in order to reach the stretch goals of the SPICE/HeRALD project, there is no way around the fact that athermal phonon collection efficiencies must be increased.

8.1 Increasing Athermal Phonon Collection Efficiency

A major focus of the designs in this thesis has been pushing down the intrinsic noise of the sensors, both by lowering the TES T_c and the total TES volume. While this is an absolutely necessary path to go down, the ultimate goals for $\mathcal{O}(1\,\mathrm{meV})$ detector thresholds cannot be realized without also increasing the signal efficiency. As discussed in section 3.2, current designs have measured athermal phonon collection efficiencies of $\varepsilon \approx 15-25\%$. Theoretically this could be increased to roughly $50-60\%$, limited primarily by the down-conversion to sub-gap phonons in the Al film. While a gain in signal efficiency of say 3-5 doesn't sound that impressive, the implications for the design could be substantial.

Increased QET Fin Thickness

As previously discussed, the diffusion length of QPs in the Al fins used in our QETs is limited by the thickness of the film used. This has been measured for up to 900 nm thick films. Fabricating thicker Al fins wouldn't necessarily increase the QP collection efficiency, but would allow us to make *longer* fins with the *same* efficiency. The benefit of doing this is

that it would allow you to reduce the total number of TESs while keeping the surface area fixed - ie reduce the intrinsic noise while keeping the signal efficiency the same.

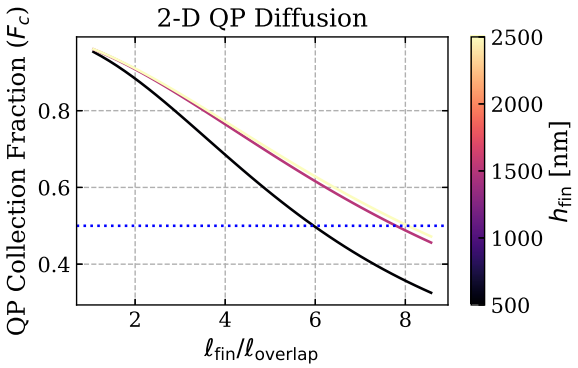

Figure 8.1: QP Collection fraction in 2D Al fin model as a function of $\ell_{\text{fin}}/\ell_{\text{overlap}}$ for $h_{\text{fin}} = 600\,\text{nm}$ (black) and $h_{\text{fin}} = 2500\,\text{nm}$ (orange). The blue dotted line shows a line of constant QP collection fraction.

To get an idea for the improvement we could get, we can go through the following example. In Fig. 8.1 the QP collection fraction is shown for $h_{\text{fin}} = 600\,\text{nm}$ and $h_{\text{fin}} = 2500\,\text{nm}$ as a function of fin length using typical values from the devices in this thesis. We can see that for a collection fraction of about 50% (roughly what is expected for the MELANGE designs), by increasing the fin thickness up to 2500 nm would allow us to increase the fin length by $\sim 33\%$ with the same overlap size. Let us make the assumption that the fin length is much larger than the TES length, and thus

$$A_{\text{QET}} \approx \pi \ell_{\text{fin}}^2, \quad \ell_{\text{fin}} \gg \ell_{\text{TES}}. \tag{8.1}$$

In this case, the new QETs would be

$$A_{QET}^{2.5\,\mu\text{m}} \approx \left(\frac{4}{3}\right)^2 A_{QET}^{0.9\,\mu\text{m}}. \tag{8.2}$$

Assuming all the surface coverage is active (only counting the area of the QETs), we can calculate the reduction in number of QETs needed for the same amount of surface coverage.

$$SA \equiv N_{\text{TES}}^{2.5\,\mu\text{m}} A_{\text{QET}}^{2.5\,\mu\text{m}} = N_{\text{TES}}^{0.9\,\mu\text{m}} A_{\text{QET}}^{0.9\,\mu\text{m}} \tag{8.3}$$

$$N_{\text{TES}}^{2.5\,\mu\text{m}} \left(\frac{4}{3}\right)^2 A_{\text{QET}}^{0.9\,\mu\text{m}} = N_{\text{TES}}^{0.9\,\mu\text{m}} A_{\text{QET}}^{0.9\,\mu\text{m}} \tag{8.4}$$

$$N_{\text{TES}}^{2.5\,\mu\text{m}} = \left(\frac{3}{4}\right)^2 N_{\text{TES}}^{0.9\,\mu\text{m}} \tag{8.5}$$

we can can reduce the total number of QETs by almost 50%. Finally, recall that the baseline energy resolution scales with the square-root of the total number of TESs, thus

$$\sigma^{2.5\,\mu\mathrm{m}} \approx \sqrt{\frac{N_{\mathrm{TES}}^{2.5\,\mu\mathrm{m}}}{N_{\mathrm{TES}}^{0.9\,\mu\mathrm{m}}}}\sigma^{0.9\,\mu\mathrm{m}} \tag{8.6}$$

$$\sigma^{2.5\,\mu\mathrm{m}} \approx \frac{3}{4}\sigma^{0.9\,\mu\mathrm{m}}. \tag{8.7}$$

By increasing the fin thickness from 600 nm to 2.5 μm, we can get a 25% improvement in baseline energy sensitivity with the same phonon collection efficiency! While making thicker Al films is not on it own a difficult task, it will begin to put constraints on the complexity of the 2D geometries of the QET designs. The thicker the film, the more problems you get with over/under etching. This would require a bit of fabrication R&D to understand how problematic this would be, but in terms of R&D costs, this should be minimal.

Increased W/Al Overlap

To maximize the Al QP collection fraction, the design should have short fins and large overlap regions. We've now discussed a way in which the Al fins could be lengthened without penalty of the QP collection. As I've shown from the results of the SPICE MELANGE detectors in chapter 7, the contribution of the overlapping region volume to the total TES heat capacity is seemingly sub-10%. This means that we can increase the overlapping region and improve the collected QP collection fraction with minimal noise costs.

From and R&D perspective, this should be incredibly easy to study. One needs to design a mask set of detectors all of the same design, but with systematically increasing overlaps. As we also learned, there can be lots of variation in the film properties across a full wafer, so care should be taken when doing the layout of the devices to ensure that devices to be compared are physically close to each other on the wafer.

Increase W/Al QP Transmission Probability

As was discussed in section 3.3.3, the limiting factor in the QP collection efficiency of the QET is the transmission probability at the W/Al interface p_{abs}. While the above two changes could allow us to further optimize our designs, the low value of p_{abs} is fundamentally limiting our current performance.

This area of the QET is not well understood. It has been shown that this transmission probability depends greatly on the fabrication process, eg oxidation formation between W and Al depositions, or poor connectivity between the two layers, will reduce p_{abs} [216]. Switching to a fabrication process where the W is deposited before the Al has greatly increased the reliability of this transmission probability.

At the end of the day, there will always be some probability of reflection of the QP at the interface due to the impedance mismatch between the two materials. This naturally

suggests that other materials should be studied for either the TES or fins, or both. Some of these studies are indeed being done by the group at Argonne National Laboratory using IrPt TESs.

Multi-Step QP Trapping

As a final thought on improving the QP collection, this idea is much more of a conceptual musing than a finalized design. I feel that it is perhaps more effort than it might be worth, and I am not 100% sure the concept would work. I feel that it is at least an interesting thought and is possibly worth consideration by a future student interested in a gaining a deeper understanding of SC QP dynamics.

As a somewhat stand alone idea for improving the QP collection fraction, one could re-imagine how the QP collection process is used in the QET. The current designs use a 'two-stage' QP trap. We could instead use a continually varying trapping region, or 'multi-step' trap. This could be implemented by radially varying the T_c of the fin during fabrication. Practically this could be achieved with a series of photolithography masks of consecutively smaller dimension, depositing either additional Al to increase total thickness in a region, or another metal to create bi-layer fins. Both of these methods would alter the T_c which in turn changes the superconducting bandgap. A schematic of how this might look is shown in Fig. 8.2.

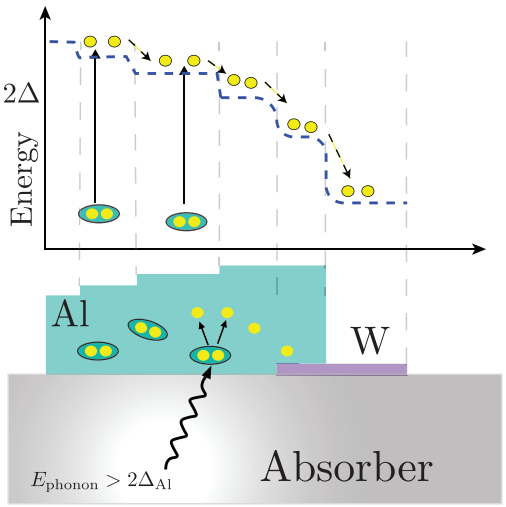

Figure 8.2: Schematic toy model of a multi-step QP trap QET design.

The natural question is now: why would we want to do this? The idea would be that this acts as a QP guide to funnel the QPs to the TES. As a QP down-converts to the band-edge in a lower gap section of the fin, it is now 'stuck' in the parts of the fin with even lower bandgaps. Thus, for each down-conversion, the effective fin size seen by the QP is smaller. The hope would be, that the majority of QPs interacting with the W part of the trap would

be limited to a quite small area of fin, and thus the low probability of transmission between the Al and W of $p_{abs} \approx 1.2 \times 10^{-4}$ becomes less important.

In terms of R&D costs, this would be quite challenging. The fabrication of such a device could be very difficult and costly. Also, there are many subtleties in the assumptions of how such a device would work. One would need to do further study to figure out the ideal ΔT_c size for the fins. One could imagine that the wrong choice of step could result in a larger population of subgap phonons at each step. Someone would need to work out the ideal design such that the maximum population of QPs relaxed at the band edge in each step.

8.2 Final Thoughts

As is likely the case for many PhD theses, I had originally hoped to get more results from the detectors I spend so long designing. While I was not able to use them for a dark matter search, this body of work as a whole has still shown the intended goal: that incredible energy sensitivities from low-temperature athermal phonon based calorimeters can be achieved through the use of Low-T_c low-surface coverage TES based sensors. While I hope to remain connected to this work in some respect in the future, I am incredibly excited to see where future grad students in this group take it, good luck!

Bibliography

[1] S. Perlmutter et al. "Measurements of Ω and Λ from 42 High-Redshift Supernovae". In: *The Astrophysical Journal* 517.2 (1999), pp. 565–586. DOI: 10.1086/307221. URL: https://doi.org/10.1086/307221.

[2] H. Andernach and F. Zwicky. *English and Spanish Translation of Zwicky's (1933) The Redshift of Extragalactic Nebulae*. 2017. arXiv: 1711.01693 [astro-ph.IM].

[3] H. Andernach, M. Plionis, O. López-Cruz, E. Tago, and S. Basilakos. "The Cluster M/L Ratio and the Value of Ω_m". In: *Nearby Large-Scale Structures and the Zone of Avoidance*. Ed. by A. P. Fairall and P. A. Woudt. Vol. 329. Astronomical Society of the Pacific Conference Series. 2005, pp. 289–293. arXiv: astro-ph/0407098 [astro-ph].

[4] V. C. Rubin, J. Ford W. K., and N. Thonnard. "Extended rotation curves of high-luminosity spiral galaxies. IV. Systematic dynamical properties, Sa -¿ Sc." In: *apjl* 225 (1978), pp. L107–L111. DOI: 10.1086/182804.

[5] S. Dodelson. *Modern Cosmology*. Amsterdam: Academic Press, 2003. ISBN: 978-0-12-219141-1.

[6] A. V. Zasov, A. S. Saburova, A. V. Khoperskov, and S. A. Khoperskov. "Dark matter in galaxies". In: *Physics-Uspekhi* 60.1 (2017), pp. 3–39. ISSN: 1468-4780. DOI: 10.3367/ufne.2016.03.037751. URL: http://dx.doi.org/10.3367/UFNe.2016.03.037751.

[7] Y. Sofue and V. Rubin. "Rotation Curves of Spiral Galaxies". In: *Annual Review of Astronomy and Astrophysics* 39.1 (2001), pp. 137–174. DOI: 10.1146/annurev.astro.39.1.137. eprint: https://doi.org/10.1146/annurev.astro.39.1.137. URL: https://doi.org/10.1146/annurev.astro.39.1.137.

[8] T. Treu. "Strong Lensing by Galaxies". In: *Annual Review of Astronomy and Astrophysics* 48.1 (2010), pp. 87–125. DOI: 10.1146/annurev-astro-081309-130924. eprint: https://doi.org/10.1146/annurev-astro-081309-130924. URL: https://doi.org/10.1146/annurev-astro-081309-130924.

[9] L. Jenner. *Hubble views a Faraway Galaxy through a cosmic lens*. 2021. URL: https://www.nasa.gov/image-feature/goddard/2021/hubble-views-a-faraway-galaxy-through-a-cosmic-lens.

[10] P. D. Group et al. "Review of Particle Physics". In: *Progress of Theoretical and Experimental Physics* 2020.8 (2020). 083C01. ISSN: 2050-3911. DOI: 10.1093/ptep/ptaa104. eprint: https://academic.oup.com/ptep/article-pdf/2020/8/083C01/34673722/ptaa104.pdf. URL: https://doi.org/10.1093/ptep/ptaa104.

[11] P. D. Serpico, S. Esposito, F. Iocco, G. Mangano, G. Miele, and O. Pisanti. "Nuclear reaction network for primordial nucleosynthesis: a detailed analysis of rates, uncertainties and light nuclei yields". In: *Journal of Cosmology and Astroparticle Physics* 2004.12 (2004), pp. 010–010. DOI: 10.1088/1475-7516/2004/12/010. URL: https://doi.org/10.1088/1475-7516/2004/12/010.

[12] F. Iocco, G. Mangano, G. Miele, O. Pisanti, and P. D. Serpico. "Primordial nucleosynthesis: From precision cosmology to fundamental physics". In: *Physics Reports* 472.1 (2009), pp. 1–76. ISSN: 0370-1573. DOI: https://doi.org/10.1016/j.physrep.2009.02.002. URL: https://www.sciencedirect.com/science/article/pii/S0370157309000374.

[13] B. D. Fields, K. A. Olive, T.-H. Yeh, and C. Young. "Big-Bang Nucleosynthesis after Planck". In: *Journal of Cosmology and Astroparticle Physics* 2020.03 (2020), pp. 010–010. DOI: 10.1088/1475-7516/2020/03/010. URL: https://doi.org/10.1088/1475-7516/2020/03/010.

[14] *Planck's view of the cosmic microwave background*. URL: https://www.esa.int/ESA_Multimedia/Missions/Planck/(sortBy)/view_count/(result_type)/images.

[15] N. Aghanim, Y. Akrami, M. Ashdown, J. Aumont, C. Baccigalupi, M. Ballardini, A. J. Banday, R. B. Barreiro, N. Bartolo, and et al. "Planck 2018 results". In: *Astronomy and Astrophysics* 641 (2020), A6. ISSN: 1432-0746. DOI: 10.1051/0004-6361/201833910. URL: http://dx.doi.org/10.1051/0004-6361/201833910.

[16] N. Aghanim, Y. Akrami, F. Arroja, M. Ashdown, J. Aumont, C. Baccigalupi, M. Ballardini, A. J. Banday, R. B. Barreiro, and et al. "Planck2018 results". In: *Astronomy and Astrophysics* 641 (2020), A1. ISSN: 1432-0746. DOI: 10.1051/0004-6361/201833880. URL: http://dx.doi.org/10.1051/0004-6361/201833880.

[17] G. F. Smoot, M. V. Gorenstein, and R. A. Muller. "Detection of Anisotropy in the Cosmic Blackbody Radiation". In: *Phys. Rev. Lett.* 39 (14 1977), pp. 898–901. DOI: 10.1103/PhysRevLett.39.898. URL: https://link.aps.org/doi/10.1103/PhysRevLett.39.898.

[18] R. A. Sunyaev and Y. B. Zeldovich. "The Observations of Relic Radiation as a Test of the Nature of X-Ray Radiation from the Clusters of Galaxies". In: *Comments on Astrophysics and Space Physics* 4 (1972), p. 173.

[19] J. Silk. "Cosmic Black-Body Radiation and Galaxy Formation". In: *apj* 151 (1968), p. 459. DOI: 10.1086/149449.

[20] G. Hinshaw et al. "NINE-YEAR WILKINSON MICROWAVE ANISOTROPY PROBE (WMAP) OBSERVATIONS: COSMOLOGICAL PARAMETER RESULTS". In: *The Astrophysical Journal Supplement Series* 208.2 (2013), p. 19. ISSN: 1538-4365. DOI: 10.1088/0067-0049/208/2/19. URL: http://dx.doi.org/10.1088/0067-0049/208/2/19.

[21] S. Das et al. "The Atacama Cosmology Telescope: temperature and gravitational lensing power spectrum measurements from three seasons of data". In: *Journal of Cosmology and Astroparticle Physics* 2014.04 (2014), pp. 014–014. ISSN: 1475-7516. DOI: 10.1088/1475-7516/2014/04/014. URL: http://dx.doi.org/10.1088/1475-7516/2014/04/014.

[22] K. T. Story et al. "A MEASUREMENT OF THE COSMIC MICROWAVE BACKGROUND DAMPING TAIL FROM THE 2500-SQUARE-DEGREE SPT-SZ SURVEY". In: *The Astrophysical Journal* 779.1 (2013), p. 86. ISSN: 1538-4357. DOI: 10.1088/0004-637x/779/1/86. URL: http://dx.doi.org/10.1088/0004-637X/779/1/86.

[23] W. Hu and S. Dodelson. "Cosmic Microwave Background Anisotropies". In: *Annual Review of Astronomy and Astrophysics* 40.1 (2002), pp. 171–216. ISSN: 1545-4282. DOI: 10.1146/annurev.astro.40.060401.093926. URL: http://dx.doi.org/10.1146/annurev.astro.40.060401.093926.

[24] J. Zavala and C. S. Frenk. *Dark matter haloes and subhaloes*. 2019. arXiv: 1907.11775 [astro-ph.CO].

[25] M. Boylan-Kolchin, V. Springel, S. D. M. White, A. Jenkins, and G. Lemson. "Resolving cosmic structure formation with the Millennium-II Simulation". In: *Monthly Notices of the Royal Astronomical Society* 398.3 (2009), pp. 1150–1164. ISSN: 1365-2966. DOI: 10.1111/j.1365-2966.2009.15191.x. URL: http://dx.doi.org/10.1111/j.1365-2966.2009.15191.x.

[26] J. Zavala, M. R. Lovell, M. Vogelsberger, and J. D. Burger. "Diverse dark matter density at sub-kiloparsec scales in Milky Way satellites: Implications for the nature of dark matter". In: *Physical Review D* 100.6 (2019). ISSN: 2470-0029. DOI: 10.1103/physrevd.100.063007. URL: http://dx.doi.org/10.1103/PhysRevD.100.063007.

[27] J. D. Bekenstein. "Relativistic MOND as an alternative to the dark matter paradigm". In: *Nuclear Physics A* 827.1 (2009). PANIC08, pp. 555c–560c. ISSN: 0375-9474. DOI: https://doi.org/10.1016/j.nuclphysa.2009.05.122. URL: https://www.sciencedirect.com/science/article/pii/S0375947409003881.

[28] S. D. McDermott, H.-B. Yu, and K. M. Zurek. "Turning off the lights: How dark is dark matter?" In: *Physical Review D* 83.6 (2011). ISSN: 1550-2368. DOI: 10.1103/physrevd.83.063509. URL: http://dx.doi.org/10.1103/PhysRevD.83.063509.

[29] D. Clowe, M. Bradac, A. H. Gonzalez, M. Markevitch, S. W. Randall, C. Jones, and D. Zaritsky. "A Direct Empirical Proof of the Existence of Dark Matter". In: *The Astrophysical Journal* 648.2 (2006), pp. L109–L113. ISSN: 1538-4357. DOI: 10.1086/508162. URL: http://dx.doi.org/10.1086/508162.

[30] S. W. Randall, M. Markevitch, D. Clowe, A. H. Gonzalez, and M. Bradač. "Constraints on the Self-Interaction Cross Section of Dark Matter from Numerical Simulations of the Merging Galaxy Cluster 1E 0657-56". In: *The Astrophysical Journal* 679.2 (2008), pp. 1173–1180. ISSN: 1538-4357. DOI: 10.1086/587859. URL: http://dx.doi.org/10.1086/587859.

[31] D. Harvey, R. Massey, T. Kitching, A. Taylor, and E. Tittley. "The nongravitational interactions of dark matter in colliding galaxy clusters". In: *Science* 347.6229 (2015), pp. 1462–1465. ISSN: 1095-9203. DOI: 10.1126/science.1261381. URL: http://dx.doi.org/10.1126/science.1261381.

[32] D. A. Buote, T. E. Jeltema, C. R. Canizares, and G. P. Garmire. "ChandraEvidence of a Flattened, Triaxial Dark Matter Halo in the Elliptical Galaxy NGC 720". In: *The Astrophysical Journal* 577.1 (2002), pp. 183–196. ISSN: 1538-4357. DOI: 10.1086/342158. URL: http://dx.doi.org/10.1086/342158.

[33] A. Boyarsky, O. Ruchayskiy, and D. Iakubovskyi. "A lower bound on the mass of dark matter particles". In: *Journal of Cosmology and Astroparticle Physics* 2009.03 (2009), pp. 005–005. ISSN: 1475-7516. DOI: 10.1088/1475-7516/2009/03/005. URL: http://dx.doi.org/10.1088/1475-7516/2009/03/005.

[34] S. Tremaine and J. E. Gunn. "Dynamical Role of Light Neutral Leptons in Cosmology". In: *Phys. Rev. Lett.* 42 (6 1979), pp. 407–410. DOI: 10.1103/PhysRevLett.42.407. URL: https://link.aps.org/doi/10.1103/PhysRevLett.42.407.

[35] L. Randall, J. Scholtz, and J. Unwin. "Cores in Dwarf Galaxies from Fermi Repulsion". In: *Monthly Notices of the Royal Astronomical Society* (2017), stx161. ISSN: 1365-2966. DOI: 10.1093/mnras/stx161. URL: http://dx.doi.org/10.1093/mnras/stx161.

[36] M. Aker et al. "Improved Upper Limit on the Neutrino Mass from a Direct Kinematic Method by KATRIN". In: *Physical Review Letters* 123.22 (2019). ISSN: 1079-7114. DOI: 10.1103/physrevlett.123.221802. URL: http://dx.doi.org/10.1103/PhysRevLett.123.221802.

[37] R. Hlozek, D. Grin, D. J. E. Marsh, and P. G. Ferreira. "A search for ultralight axions using precision cosmological data". In: *Physical Review D* 91.10 (2015). ISSN: 1550-2368. DOI: 10.1103/physrevd.91.103512. URL: http://dx.doi.org/10.1103/PhysRevD.91.103512.

[38] E. Armengaud, N. Palanque-Delabrouille, C. Yèche, D. J. E. Marsh, and J. Baur. "Constraining the mass of light bosonic dark matter using SDSS Lyman-alpha forest". In: *Monthly Notices of the Royal Astronomical Society* 471.4 (2017), pp. 4606–4614. ISSN: 1365-2966. DOI: 10.1093/mnras/stx1870. URL: http://dx.doi.org/10.1093/mnras/stx1870.

[39] E. O. Nadler, V. Gluscevic, K. K. Boddy, and R. H. Wechsler. "Constraints on Dark Matter Microphysics from the Milky Way Satellite Population". In: *The Astrophysical Journal* 878.2 (2019), p. L32. ISSN: 2041-8213. DOI: 10.3847/2041-8213/ab1eb2. URL: http://dx.doi.org/10.3847/2041-8213/ab1eb2.

[40] T. D. Brandt. "CONSTRAINTS ON MACHO DARK MATTER FROM COMPACT STELLAR SYSTEMS IN ULTRA-FAINT DWARF GALAXIES". In: *The Astrophysical Journal* 824.2 (2016), p. L31. ISSN: 2041-8213. DOI: 10.3847/2041-8205/824/2/l31. URL: http://dx.doi.org/10.3847/2041-8205/824/2/L31.

[41] M. A. Monroy-Rodríguez and C. Allen. "THE END OF THE MACHO ERA, REVISITED: NEW LIMITS ON MACHO MASSES FROM HALO WIDE BINARIES". In: *The Astrophysical Journal* 790.2 (2014), p. 159. ISSN: 1538-4357. DOI: 10.1088/0004-637x/790/2/159. URL: http://dx.doi.org/10.1088/0004-637X/790/2/159.

[42] B. Audren, J. Lesgourgues, G. Mangano, P. D. Serpico, and T. Tram. "Strongest model-independent bound on the lifetime of Dark Matter". In: *Journal of Cosmology and Astroparticle Physics* 2014.12 (2014), pp. 028–028. ISSN: 1475-7516. DOI: 10.1088/1475-7516/2014/12/028. URL: http://dx.doi.org/10.1088/1475-7516/2014/12/028.

[43] J. L. Feng. "Dark Matter Candidates from Particle Physics and Methods of Detection". In: *Annual Review of Astronomy and Astrophysics* 48.1 (2010), pp. 495–545. ISSN: 1545-4282. DOI: 10.1146/annurev-astro-082708-101659. URL: http://dx.doi.org/10.1146/annurev-astro-082708-101659.

[44] G. Jungman, M. Kamionkowski, and K. Griest. "Supersymmetric dark matter". In: *Physics Reports* 267.5 (1996), pp. 195–373. ISSN: 0370-1573. DOI: https://doi.org/10.1016/0370-1573(95)00058-5. URL: https://www.sciencedirect.com/science/article/pii/0370157395000585.

[45] S. Profumo, L. Giani, and O. F. Piattella. "An Introduction to Particle Dark Matter". In: *Universe* 5.10 (2019). ISSN: 2218-1997. DOI: 10.3390/universe5100213. URL: https://www.mdpi.com/2218-1997/5/10/213.

[46] O. Piattella. "Lecture Notes in Cosmology". In: *UNITEXT for Physics* (2018). ISSN: 2198-7890. DOI: 10.1007/978-3-319-95570-4. URL: http://dx.doi.org/10.1007/978-3-319-95570-4.

[47] D. B. Chitwood et al. "Improved Measurement of the Positive-Muon Lifetime and Determination of the Fermi Constant". In: *Physical Review Letters* 99.3 (2007). ISSN: 1079-7114. DOI: 10.1103/physrevlett.99.032001. URL: http://dx.doi.org/10.1103/PhysRevLett.99.032001.

[48] A. Goobar, S. Hannestad, E. Mörtsell, and H. Tu. "The neutrino mass bound from WMAP 3 year data, the baryon acoustic peak, the SNLS supernovae and the Lyman-α forest". In: *Journal of Cosmology and Astroparticle Physics* 2006.06 (2006), pp. 019–019. ISSN: 1475-7516. DOI: 10.1088/1475-7516/2006/06/019. URL: http://dx.doi.org/10.1088/1475-7516/2006/06/019.

[49] B. W. Lee and S. Weinberg. "Cosmological Lower Bound on Heavy-Neutrino Masses". In: *Phys. Rev. Lett.* 39 (4 1977), pp. 165–168. DOI: 10.1103/PhysRevLett.39.165. URL: https://link.aps.org/doi/10.1103/PhysRevLett.39.165.

[50] K. Griest and M. Kamionkowski. "Unitarity limits on the mass and radius of dark-matter particles". In: *Phys. Rev. Lett.* 64 (6 1990), pp. 615–618. DOI: 10.1103/PhysRevLett.64.615. URL: https://link.aps.org/doi/10.1103/PhysRevLett.64.615.

[51] L. J. Hall, K. Jedamzik, J. March-Russell, and S. M. West. "Freeze-in production of FIMP dark matter". In: *Journal of High Energy Physics* 2010.3 (2010). ISSN: 1029-8479. DOI: 10.1007/jhep03(2010)080. URL: http://dx.doi.org/10.1007/JHEP03(2010)080.

[52] K. M. Zurek. "Asymmetric Dark Matter: Theories, signatures, and constraints". In: *Physics Reports* 537.3 (2014), pp. 91–121. ISSN: 0370-1573. DOI: 10.1016/j.physrep.2013.12.001. URL: http://dx.doi.org/10.1016/j.physrep.2013.12.001.

[53] Y. B. Zel'dovich and I. D. Novikov. "The Hypothesis of Cores Retarded during Expansion and the Hot Cosmological Model". In: *sovast* 10 (1967), p. 602.

[54] S. Hawking. "Gravitationally collapsed objects of very low mass". In: *Mon. Not. Roy. Astron. Soc.* 152 (1971), p. 75.

[55] M. A. Buen-Abad, R. Emami, and M. Schmaltz. "Cannibal dark matter and large scale structure". In: *Physical Review D* 98.8 (2018). ISSN: 2470-0029. DOI: 10.1103/physrevd.98.083517. URL: http://dx.doi.org/10.1103/PhysRevD.98.083517.

[56] Y. Hochberg, E. Kuflik, T. Volansky, and J. G. Wacker. "Mechanism for Thermal Relic Dark Matter of Strongly Interacting Massive Particles". In: *Physical Review Letters* 113.17 (2014). ISSN: 1079-7114. DOI: 10.1103/physrevlett.113.171301. URL: http://dx.doi.org/10.1103/PhysRevLett.113.171301.

[57] M. Battaglieri et al. *US Cosmic Visions: New Ideas in Dark Matter 2017: Community Report*. 2017. arXiv: 1707.04591 [hep-ph].

[58] H. Haber and G. Kane. "The search for supersymmetry: Probing physics beyond the standard model". In: *Physics Reports* 117.2 (1985), pp. 75–263. ISSN: 0370-1573. DOI: https://doi.org/10.1016/0370-1573(85)90051-1. URL: https://www.sciencedirect.com/science/article/pii/0370157385900511.

[59] R. D. Peccei and H. R. Quinn. "CP Conservation in the Presence of Pseudoparticles". In: *Phys. Rev. Lett.* 38 (25 1977), pp. 1440–1443. DOI: 10.1103/PhysRevLett.38.1440. URL: https://link.aps.org/doi/10.1103/PhysRevLett.38.1440.

[60] D. J. Marsh. "Axion cosmology". In: *Physics Reports* 643 (2016), pp. 1–79. ISSN: 0370-1573. DOI: 10.1016/j.physrep.2016.06.005. URL: http://dx.doi.org/10.1016/j.physrep.2016.06.005.

[61] P. Sikivie. "Experimental Tests of the "Invisible" Axion". In: *Phys. Rev. Lett.* 51 (16 1983), pp. 1415–1417. DOI: 10.1103/PhysRevLett.51.1415. URL: https://link.aps.org/doi/10.1103/PhysRevLett.51.1415.

[62] A. Boyarsky, M. Drewes, T. Lasserre, S. Mertens, and O. Ruchayskiy. "Sterile neutrino Dark Matter". In: *Progress in Particle and Nuclear Physics* 104 (2019), pp. 1–45. ISSN: 0146-6410. DOI: 10.1016/j.ppnp.2018.07.004. URL: http://dx.doi.org/10.1016/j.ppnp.2018.07.004.

[63] E. Bulbul, M. Markevitch, A. Foster, R. K. Smith, M. Loewenstein, and S. W. Randall. "DETECTION OF AN UNIDENTIFIED EMISSION LINE IN THE STACKED X-RAY SPECTRUM OF GALAXY CLUSTERS". In: *The Astrophysical Journal* 789.1 (2014), p. 13. ISSN: 1538-4357. DOI: 10.1088/0004-637x/789/1/13. URL: http://dx.doi.org/10.1088/0004-637X/789/1/13.

[64] A. Boyarsky, O. Ruchayskiy, D. Iakubovskyi, and J. Franse. "Unidentified Line in X-Ray Spectra of the Andromeda Galaxy and Perseus Galaxy Cluster". In: *Physical Review Letters* 113.25 (2014). ISSN: 1079-7114. DOI: 10.1103/physrevlett.113.251301. URL: http://dx.doi.org/10.1103/PhysRevLett.113.251301.

[65] T. Jeltema and S. Profumo. "Discovery of a 3.5 keV line in the Galactic Centre and a critical look at the origin of the line across astronomical targets". In: *Monthly Notices of the Royal Astronomical Society* 450.2 (2015), pp. 2143–2152. ISSN: 0035-8711. DOI: 10.1093/mnras/stv768. URL: http://dx.doi.org/10.1093/mnras/stv768.

[66] M. E. Anderson, E. Churazov, and J. N. Bregman. "Non-detection of X-ray emission from sterile neutrinos in stacked galaxy spectra". In: *Monthly Notices of the Royal Astronomical Society* 452.4 (2015), pp. 3905–3923. ISSN: 1365-2966. DOI: 10.1093/mnras/stv1559. URL: http://dx.doi.org/10.1093/mnras/stv1559.

[67] D. Malyshev, A. Neronov, and D. Eckert. "Constraints on 3.55 keV line emission from stacked observations of dwarf spheroidal galaxies". In: *Physical Review D* 90.10 (2014). ISSN: 1550-2368. DOI: 10.1103/physrevd.90.103506. URL: http://dx.doi.org/10.1103/PhysRevD.90.103506.

[68] T. Jeltema and S. Profumo. "DeepXMMobservations of Draco rule out at the 99 per cent confidence level a dark matter decay origin for the 3.5 keV line". In: *Monthly Notices of the Royal Astronomical Society* 458.4 (2016), pp. 3592–3596. ISSN: 1365-2966. DOI: 10.1093/mnras/stw578. URL: http://dx.doi.org/10.1093/mnras/stw578.

[69] Planck Collaboration et al. "Planck 2018 results - VI. Cosmological parameters". In: *A&A* 641 (2020), A6. DOI: 10.1051/0004-6361/201833910. URL: https://doi.org/10.1051/0004-6361/201833910.

[70] T. Trickle, Z. Zhang, K. M. Zurek, K. Inzani, and S. M. Griffin. "Multi-channel direct detection of light dark matter: theoretical framework". In: *Journal of High Energy Physics* 2020.3 (2020). DOI: 10.1007/jhep03(2020)036. URL: https://doi.org/10.1007%5C%2Fjhep03%5C%282020%5C%29036.

[71] Y. Kahn and T. Lin. *Searches for light dark matter using condensed matter systems*. 2021. DOI: 10.48550/ARXIV.2108.03239. URL: https://arxiv.org/abs/2108.03239.

[72] "Snowmass2021-Letter of Interest The TESSERACT Dark Matter Project". In: 2020.

[73] S. M. Griffin, K. Inzani, T. Trickle, Z. Zhang, and K. M. Zurek. "Multichannel direct detection of light dark matter: Target comparison". In: *Physical Review D* 101.5 (2020). DOI: 10.1103/physrevd.101.055004. URL: https://doi.org/10.1103%2Fphysrevd.101.055004.

[74] M. A. Lindeman. "Microcalorimetry and the transition-edge sensor". In: (2000). DOI: 10.2172/15009469. URL: https://www.osti.gov/biblio/15009469.

[75] K. D. Irwin. "Phonon-Mediated Particle Detection Using Superconducting Tungsten Transition-Edge Sensors." PhD thesis. STANFORD UNIVERSITY., 1995.

[76] M. Pyle. "Optimizing the design and analysis of cryogenic semiconductor dark matter detectors for maximum sensitivity". PhD thesis. Stanford University, 2012. DOI: 10.2172/1127926.

[77] N. Kurinsky. "The Low-Mass Limit: Dark Matter Detectors with eV-Scale Energy Resolution". PhD thesis. Stanford University, 2018. DOI: 10.2172/1472104.

[78] J. C. Mather. "Bolometer noise: nonequilibrium theory". In: *Appl. Opt.* 21.6 (1982), pp. 1125–1129. DOI: 10.1364/AO.21.001125. URL: http://www.osapublishing.org/ao/abstract.cfm?URI=ao-21-6-1125.

[79] S. H. Moseley, J. C. Mather, and D. McCammon. "Thermal detectors as x-ray spectrometers". In: *Journal of Applied Physics* 56.5 (1984), pp. 1257–1262. DOI: 10.1063/1.334129. eprint: https://doi.org/10.1063/1.334129. URL: https://doi.org/10.1063/1.334129.

[80] D. McCammon. "Thermal Equilibrium Calorimeters – An Introduction". In: *Cryogenic Particle Detection*. Ed. by C. Enss. Berlin, Heidelberg: Springer Berlin Heidelberg, 2005, pp. 1–34. ISBN: 978-3-540-31478-3. DOI: 10.1007/10933596_1. URL: https://doi.org/10.1007/10933596_1.

[81] K. D. Irwin and G. C. Hilton. "Transition-Edge Sensors". In: *Cryogenic Particle Detection*. Ed. by C. Enss. Berlin, Heidelberg: Springer Berlin Heidelberg, 2005, pp. 63–150. ISBN: 978-3-540-31478-3. DOI: 10.1007/10933596_3.

[82] K. D. Irwin and G. C. Hilton. "Transition-Edge Sensors". In: *Cryogenic Particle Detection*. Ed. by C. Enss. Berlin, Heidelberg: Springer Berlin Heidelberg, 2005, pp. 63–150. ISBN: 978-3-540-31478-3. DOI: 10.1007/10933596_3.

[83] M. A. Lindeman, S. Bandler, R. P. Brekosky, J. A. Chervenak, E. Figueroa-Feliciano, F. M. Finkbeiner, M. J. Li, and C. A. Kilbourne. "Impedance measurements and modeling of a transition-edge-sensor calorimeter". In: *Review of Scientific Instruments* 75.5 (2004), pp. 1283–1289. DOI: 10.1063/1.1711144. eprint: https://doi.org/10.1063/1.1711144. URL: https://doi.org/10.1063/1.1711144.

[84] C. W. Fink et al. "Performance of a large area photon detector for rare event search applications". In: *Applied Physics Letters* 118.2 (2021), p. 022601. DOI: 10.1063/5.0032372. eprint: https://doi.org/10.1063/5.0032372. URL: https://doi.org/10.1063/5.0032372.

[85] K. D. Irwin, S. W. Nam, B. Cabrera, B. Chugg, and B. A. Young. "A quasiparticle-trap-assisted transition-edge sensor for phonon-mediated particle detection". In: *Review of Scientific Instruments* 66.11 (1995), pp. 5322–5326. DOI: 10.1063/1.1146105. eprint: https://doi.org/10.1063/1.1146105. URL: https://doi.org/10.1063/1.1146105.

[86] N. Jethava, J. N. Ullom, K. D. Irwin, W. B. Doriese, J. A. Beall, G. C. Hilton, L. R. Vale, and B. Zink. "Dependence of Excess Noise on the Partial Derivatives of Resistance in Superconducting Transition Edge Sensors". In: *AIP Conference Proceedings* 1185.1 (2009), pp. 31–33. DOI: 10.1063/1.3292343. eprint: https://aip.scitation.org/doi/pdf/10.1063/1.3292343. URL: https://aip.scitation.org/doi/abs/10.1063/1.3292343.

[87] A. Wessels et al. "A model for excess Johnson noise in superconducting transition-edge sensors". In: *Applied Physics Letters* 118.20 (2021), p. 202601. DOI: 10.1063/5.0043369. eprint: https://doi.org/10.1063/5.0043369. URL: https://doi.org/10.1063/5.0043369.

[88] J. E. Sadleir, S. J. Smith, S. R. Bandler, J. A. Chervenak, and J. R. Clem. "Longitudinal Proximity Effects in Superconducting Transition-Edge Sensors". In: *Phys. Rev. Lett.* 104 (4 2010), p. 047003. DOI: 10.1103/PhysRevLett.104.047003. URL: https://link.aps.org/doi/10.1103/PhysRevLett.104.047003.

[89] A. Kozorezov et al. "Modelling the resistive state in a transition edge sensor". In: *Applied Physics Letters* 99.6 (2011), p. 063503. DOI: 10.1063/1.3621829. eprint: https://doi.org/10.1063/1.3621829. URL: https://doi.org/10.1063/1.3621829.

[90] D. Bennett, D. Swetz, R. Horansky, D. Schmidt, and J. Ullom. "A Two-Fluid Model for the Transition Shape in Transition-Edge Sensors". In: *Journal of Low Temperature Physics* 167 (2011). DOI: 10.1007/s10909-011-0431-4.

[91] K. D. Irwin, G. C. Hilton, D. A. Wollman, and J. M. Martinis. "Thermal-response time of superconducting transition-edge microcalorimeters". In: *Journal of Applied Physics* 83.8 (1998), pp. 3978–3985. DOI: 10.1063/1.367153. eprint: https://doi.org/10.1063/1.367153. URL: https://doi.org/10.1063/1.367153.

[92] F. Rice. "A frequency-domain derivation of shot-noise". In: *American Journal of Physics* 84.1 (2016), pp. 44–51. DOI: 10.1119/1.4934706. eprint: https://doi.org/10.1119/1.4934706. URL: https://doi.org/10.1119/1.4934706.

[93] L. A. Zadeh and J. R. Ragazzini. "Optimum Filters for the Detection of Signals in Noise". In: *Proc. IRE* 40.10 (1952), pp. 1223–1231. DOI: 10.1109/JRPROC.1952.274117.

[94] L. De Bellis, P. E. Phelan, and R. S. Prasher. "Variations of Acoustic and Diffuse Mismatch Models in Predicting Thermal-Boundary Resistance". In: *Journal of Thermophysics and Heat Transfer* 14.2 (2000), pp. 144–150. DOI: 10.2514/2.6525. eprint: https://doi.org/10.2514/2.6525. URL: https://doi.org/10.2514/2.6525.

[95] F. C. Wellstood, C. Urbina, and J. Clarke. "Hot-electron effects in metals". In: *Phys. Rev. B* 49 (9 1994), pp. 5942–5955. DOI: 10.1103/PhysRevB.49.5942. URL: https://link.aps.org/doi/10.1103/PhysRevB.49.5942.

[96] N. E. Booth. "Quasiparticle trapping and the quasiparticle multiplier". In: *Applied Physics Letters* 50.5 (1987), pp. 293–295. DOI: 10.1063/1.98229. eprint: https://doi.org/10.1063/1.98229. URL: https://doi.org/10.1063/1.98229.

[97] K. D. Irwin, S. W. Nam, B. Cabrera, B. Chugg, and B. A. Young. "A quasiparticle-trap-assisted transition-edge sensor for phonon-mediated particle detection". In: *Rev. Sci. Instrum.* 66.11 (1995), pp. 5322–5326. DOI: 10.1063/1.1146105.

[98] A. Goldman. "Low-Temperature Physics". In: *Physics Today* 59.7 (2006), pp. 50–51. DOI: 10.1063/1.2337830. eprint: https://doi.org/10.1063/1.2337830. URL: https://doi.org/10.1063/1.2337830.

[99] I. Giaever and K. Megerle. "Study of Superconductors by Electron Tunneling". In: *Phys. Rev.* 122 (4 1961), pp. 1101–1111. DOI: 10.1103/PhysRev.122.1101. URL: https://link.aps.org/doi/10.1103/PhysRev.122.1101.

[100] S. B. Kaplan, C. C. Chi, D. N. Langenberg, J. J. Chang, S. Jafarey, and D. J. Scalapino. "Quasiparticle and phonon lifetimes in superconductors". In: *Phys. Rev. B* 14 (11 1976), pp. 4854–4873. DOI: 10.1103/PhysRevB.14.4854. URL: https://link.aps.org/doi/10.1103/PhysRevB.14.4854.

[101] Y. Hochberg, E. D. Kramer, N. Kurinsky, and B. V. Lehmann. *Directional Detection of Light Dark Matter in Superconductors*. 2021. arXiv: 2109.04473 [hep-ph].

[102] T. Guruswamy, D. J. Goldie, and S. Withington. "Quasiparticle generation efficiency in superconducting thin films". In: *Superconductor Science and Technology* 27.5 (2014), p. 055012. DOI: 10.1088/0953-2048/27/5/055012. URL: https://doi.org/10.1088/0953-2048/27/5/055012.

[103] W. D. Gregory. "Boundary Scattering in Superconductors". In: *Phys. Rev. Lett.* 20 (2 1968), pp. 53–56. DOI: 10.1103/PhysRevLett.20.53. URL: https://link.aps.org/doi/10.1103/PhysRevLett.20.53.

[104] J.-J. Chang and D. J. Scalapino. "Kinetic-equation approach to nonequilibrium superconductivity". In: *Phys. Rev. B* 15 (5 1977), pp. 2651–2670. DOI: 10.1103/PhysRevB.15.2651. URL: https://link.aps.org/doi/10.1103/PhysRevB.15.2651.

[105] J. Bardeen, G. Rickayzen, and L. Tewordt. "Theory of the Thermal Conductivity of Superconductors". In: *Phys. Rev.* 113 (4 1959), pp. 982–994. DOI: 10.1103/PhysRev.113.982. URL: https://link.aps.org/doi/10.1103/PhysRev.113.982.

[106] A. G. Kozorezov, A. F. Volkov, J. K. Wigmore, A. Peacock, A. Poelaert, and R. den Hartog. "Quasiparticle-phonon downconversion in nonequilibrium superconductors". In: *Phys. Rev. B* 61 (17 2000), pp. 11807–11819. DOI: 10.1103/PhysRevB.61.11807. URL: https://link.aps.org/doi/10.1103/PhysRevB.61.11807.

[107] P. L. Brink. "Non-Equilibrium Superconductivity induced by X-ray Photons". PhD thesis. Magdalen College, Oxford University, 1995.

[108] N. Kurinsky, P. Brink, R. Partridge, B. Cabrera, and M. Pyle. *SuperCDMS SNOLAB Low-Mass Detectors: Ultra-Sensitive Phonon Calorimeters for a Sub-GeV Dark Matter Search*. 2016. arXiv: 1611.04083 [physics.ins-det].

[109] R. K. Romani et al. "Thermal detection of single e-h pairs in a biased silicon crystal detector". In: *Applied Physics Letters* 112.4 (2018), p. 043501. DOI: 10.1063/1.5010699. eprint: https://doi.org/10.1063/1.5010699. URL: https://doi.org/10.1063/1.5010699.

[110] Z. Hong et al. "Single electron–hole pair sensitive silicon detector with surface event discrimination". In: *Nuclear Instruments and Methods in Physics Research Section A: Accelerators, Spectrometers, Detectors and Associated Equipment* 963 (2020), p. 163757. ISSN: 0168-9002. DOI: https://doi.org/10.1016/j.nima.2020.163757. URL: https://www.sciencedirect.com/science/article/pii/S0168900220302989.

[111] R. Ren et al. "Design and characterization of a phonon-mediated cryogenic particle detector with an eV-scale threshold and 100 keV-scale dynamic range". In: *Phys. Rev. D* 104 (3 2021), p. 032010. DOI: 10.1103/PhysRevD.104.032010. URL: https://link.aps.org/doi/10.1103/PhysRevD.104.032010.

[112] J. J. Yen et al. "Measurement of quasiparticle transport in aluminum films using tungsten transition-edge sensors". In: *Applied Physics Letters* 105.16 (2014), p. 163504. DOI: 10.1063/1.4899130. eprint: https://doi.org/10.1063/1.4899130. URL: https://doi.org/10.1063/1.4899130.

[113] J. Yen, J. M. Kreikebaum, B. Young, B. Cabrera, R. Moffatt, P. Redl, B. Shank, P. Brink, M. Cherry, and A. Tomada. "Quasiparticle Transport in Thick Aluminum Films Coupled to Tungsten Transition Edge Sensors". In: *Journal of Low Temperature Physics* 184 (2016). DOI: 10.1007/s10909-015-1406-7.

[114] R. Moffatt. "Two-Dimensional Spatial Imaging of Charge Transport in Germanium Crystals at Cryogenic Temperatures". In: (2016). DOI: 10.2172/1350526. URL: https://www.osti.gov/biblio/1350526.

[115] C. W. Kosten. "The mean free path in room acoustics". In: *Acta Acustica united with Acustica* 10.4 (1960), pp. 245–250. ISSN: 1610-1928. URL: https://www.ingentaconnect.com/content/dav/aaua/1960/00000010/00000004/art00008.

[116] K. E. Gray, A. R. Long, and C. J. Adkins. "Measurements of the lifetime of excitations in superconducting aluminium". In: *The Philosophical Magazine: A Journal of Theoretical Experimental and Applied Physics* 20.164 (1969), pp. 273–278. DOI: 10.1080/14786436908228699. eprint: https://doi.org/10.1080/14786436908228699. URL: https://doi.org/10.1080/14786436908228699.

[117] P. De Visser, D. Goldie, P. Diener, S. Withington, J. Baselmans, and T. Klapwijk. "Nonlinear electrodynamics of a superconductor due to the redistribution of quasiparticles". In: (2013).

[118] J. N. Ullom, P. A. Fisher, and M. Nahum. "Energy-dependent quasiparticle group velocity in a superconductor". In: *Phys. Rev. B* 58 (13 1998), pp. 8225–8228. DOI: 10.1103/PhysRevB.58.8225. URL: https://link.aps.org/doi/10.1103/PhysRevB.58.8225.

[119] W.J.O.-T. "Electronic structure and the properties of solids: the physics of the chemical bond: Walter A. Harrison, W.H. Freeman and Co., San Francisco, 1980, pp. xiv + 582, price £16.30". In: *Journal of Molecular Structure* 71 (1981), p. 355. ISSN: 0022-2860. DOI: https://doi.org/10.1016/0022-2860(81)85136-8. URL: https://www.sciencedirect.com/science/article/pii/0022286081851368.

[120] J. E. Sadleir, S. J. Smith, S. R. Bandler, J. A. Chervenak, and J. R. Clem. "Longitudinal Proximity Effects in Superconducting Transition-Edge Sensors". In: *Phys. Rev. Lett.* 104 (4 2010), p. 047003. DOI: 10.1103/PhysRevLett.104.047003. URL: https://link.aps.org/doi/10.1103/PhysRevLett.104.047003.

[121] E. Sondheimer. "The mean free path of electrons in metals". In: *Advances in Physics* 1.1 (1952), pp. 1–42. DOI: 10.1080/00018735200101151. eprint: https://doi.org/10.1080/00018735200101151. URL: https://doi.org/10.1080/00018735200101151.

[122] A. Lykov. "The superconducting mixed state of artificial microstructures". In: *Advances in Physics* 42.3 (1993), pp. 263–342. DOI: 10.1080/00018739300101494. eprint: https://doi.org/10.1080/00018739300101494. URL: https://doi.org/10.1080/00018739300101494.

[123] A. D. C. Grassie. *The superconducting state /*. London : 1975.

[124] T. F. Harrelson, I. Hajar, and S. M. Griffin. *Theoretical investigation of decoherence channels in athermal phonon sensors*. 2021. arXiv: 2109.10988 [cond-mat.mtrl-sci].

[125] M. Martinez, L. Cardani, N. Casali, A. Cruciani, G. Pettinari, and M. Vignati. "Measurements and Simulations of Athermal Phonon Transmission from Silicon Absorbers to Aluminum Sensors". In: *Phys. Rev. Applied* 11 (6 2019), p. 064025. DOI: 10.1103/PhysRevApplied.11.064025. URL: https://link.aps.org/doi/10.1103/PhysRevApplied.11.064025.

[126] S.-i. Tamura. "Spontaneous decay rates of LA phonons in quasi-isotropic solids". In: *Phys. Rev. B* 31 (4 1985), pp. 2574–2577. DOI: 10.1103/PhysRevB.31.2574. URL: https://link.aps.org/doi/10.1103/PhysRevB.31.2574.

[127] S.-i. Tamura. "Quasidiffusive propagation of phonons in silicon: Monte Carlo calculations". In: *Phys. Rev. B* 48 (18 1993), pp. 13502–13507. DOI: 10.1103/PhysRevB.48.13502. URL: https://link.aps.org/doi/10.1103/PhysRevB.48.13502.

[128] W. Knaak, T. Hauß, M. Kummrow, and M. Meißner. "Thermalization of Ballistic Phonon Pulses in Dielectric Crystals Below 1K Using Time-Resolved Thermometry". In: *Phonon Scattering in Condensed Matter V*. Ed. by A. C. Anderson and J. P. Wolfe. Berlin, Heidelberg: Springer Berlin Heidelberg, 1986, pp. 174–176. ISBN: 978-3-642-82912-3. DOI: 10.1007/978-3-642-82912-3_52.

[129] M. E. Msall and J. P. Wolfe. "Phonon production in weakly photoexcited semiconductors: Quasidiffusion in Ge, GaAs, and Si". In: *Phys. Rev. B* 56 (15 1997), pp. 9557–9564. DOI: 10.1103/PhysRevB.56.9557. URL: https://link.aps.org/doi/10.1103/PhysRevB.56.9557.

[130] W. Sabine. *Collected Papers on Acoustics*. Peninsula Publishing, 1993. ISBN: 9780932146601. URL: https://books.google.lu/books?id=3B8%5C_PQAACAAJ.

[131] R. W. Young. "Sabine Reverberation Equation and Sound Power Calculations". In: *The Journal of the Acoustical Society of America* 31.7 (1959), pp. 912–921. DOI: 10.1121/1.1907816. eprint: https://doi.org/10.1121/1.1907816. URL: https://doi.org/10.1121/1.1907816.

[132] S. B. Kaplan. "Acoustic matching of superconducting films to substrates". In: *Journal of Low Temperature Physics* 37.3-4 (1979), pp. 343–365. DOI: 10.1007/BF00119193.

[133] A. J. Blue. "Edgeless and Slim-edge Detectors". In: *PoS* Vertex2014 (2015), p. 042. DOI: 10.22323/1.227.0042.

[134] R. Bates et al. "Characterisation of edgeless technologies for pixellated and strip silicon detectors with a micro-focused X-ray beam". In: *Journal of Instrumentation* 8.01 (2013), P01018–P01018. DOI: 10.1088/1748-0221/8/01/p01018. URL: https://doi.org/10.1088/1748-0221/8/01/p01018.

[135] V. Fadeyev et al. "Update on scribe–cleave–passivate (SCP) slim edge technology for silicon sensors: Automated processing and radiation resistance". In: *Nuclear Instruments and Methods in Physics Research Section A: Accelerators, Spectrometers, Detectors and Associated Equipment* 765 (2014). HSTD-9 2013 - Proceedings of the 9th International "Hiroshima" Symposium on Development and Application of Semiconductor Tracking Detectors, pp. 59–63. ISSN: 0168-9002. DOI: https://doi.org/10.1016/j.nima.2014.05.032. URL: https://www.sciencedirect.com/science/article/pii/S0168900214005518.

[136] A. Malhotra and M. Maldovan. "Impact of Phonon Surface Scattering on Thermal Energy Distribution of Si and SiGe Nanowires". In: *Scientific reports* 6 (2016), p. 25818. DOI: 10.1038/srep25818.

[137] C. W. Fink et al. "Characterizing TES power noise for future single optical-phonon and infrared-photon detectors". In: *AIP Advances* 10.8 (2020), p. 085221. DOI: 10.1063/5.0011130. eprint: https://doi.org/10.1063/5.0011130. URL: https://doi.org/10.1063/5.0011130.

[138] P. Du, D. Egana-Ugrinovic, R. Essig, and M. Sholapurkar. "Sources of Low-Energy Events in Low-Threshold Dark-Matter and Neutrino Detectors". In: *Phys. Rev. X* 12 (1 2022), p. 011009. DOI: 10.1103/PhysRevX.12.011009. URL: https://link.aps.org/doi/10.1103/PhysRevX.12.011009.

[139] J. T. Karvonen, L. J. Taskinen, and I. J. Maasilta. "Electron–phonon interaction in thin copper and gold films". In: *physica status solidi (c)* 1.11 (2004), pp. 2799–2802. DOI: https://doi.org/10.1002/pssc.200405326. eprint: https://onlinelibrary.wiley.com/doi/pdf/10.1002/pssc.200405326. URL: https://onlinelibrary.wiley.com/doi/abs/10.1002/pssc.200405326.

[140] A. N. Mocharnuk-Macchia, Y. H. Kim, H. Eguchi, Y. H. Huang, R. E. Lanou, H. J. Maris, G. M. Seidel, B. Sethumadhavan, and W. Yao. "Measurement of Electron-Phonon Interactions in a Gold Film on a Quartz Substrate". In: *AIP Conference Proceedings* 850.1 (2006), pp. 1603–1604. DOI: 10.1063/1.2355320. eprint: https://aip.scitation.org/doi/pdf/10.1063/1.2355320. URL: https://aip.scitation.org/doi/abs/10.1063/1.2355320.

[141] K. M. Sundqvist. "Carrier Transport and Related Effects in Detectors of the Cryogenic Dark Matter Search". In: (2012). DOI: 10.2172/1128107. URL: https://www.osti.gov/biblio/1128107.

[142] B. A. Hines, K. M. Sundqvist, D. N. Seitz, and M. E. Huber. "Flux-Coupled Direct Feedback in a SQUID Amplifier". In: *IEEE Trans. Appl. Supercond.* 21.3 (2010). Ed. by B. Strauss, D. Gubser, M. Osofsky, M. Green, and S. Farinon, pp. 262–266. DOI: 10.1109/TASC.2010.2091617.

[143] Y. Hochberg, M. Pyle, Y. Zhao, and K. M. Zurek. "Detecting superlight dark matter with Fermi-degenerate materials". In: *J. High Energ. Phys.* 2016.8 (2016), p. 57. ISSN: 1029-8479. DOI: 10.1007/jhep08(2016)057. URL: http://dx.doi.org/10.1007/JHEP08(2016)057.

[144] S. Knapen, T. Lin, M. Pyle, and K. M. Zurek. "Detection of light dark matter with optical phonons in polar materials". In: *Phys. Lett. B* 785 (2018), pp. 386–390. ISSN: 0370-2693. DOI: 10.1016/j.physletb.2018.08.064.

[145] S. Griffin, S. Knapen, T. Lin, and K. M. Zurek. "Directional detection of light dark matter with polar materials". In: *Phys. Rev. D* 98 (11 2018), p. 115034. DOI: 10.1103/PhysRevD.98.115034.

[146] N. Kurinsky, T. C. Yu, Y. Hochberg, and B. Cabrera. "Diamond detectors for direct detection of sub-GeV dark matter". In: *Phys. Rev. D* 99 (12 2019), p. 123005. DOI: 10.1103/PhysRevD.99.123005.

[147] S. M. Griffin, K. Inzani, T. Trickle, Z. Zhang, and K. M. Zurek. "Multichannel direct detection of light dark matter: Target comparison". In: *Phys. Rev. D* 101 (5 2020), p. 055004. DOI: 10.1103/PhysRevD.101.055004.

[148] M. Baryakhtar, J. Huang, and R. Lasenby. "Axion and hidden photon dark matter detection with multilayer optical haloscopes". In: *Phys. Rev. D* 98 (3 2018), p. 035006. DOI: 10.1103/PhysRevD.98.035006.

[149] D. K. Papoulias, T. S. Kosmas, and Y. Kuno. "Recent Probes of Standard and Non-standard Neutrino Physics With Nuclei". In: *Front. Phys.* 7 (2019), p. 191. DOI: 10.3389/fphy.2019.00191.

[150] R. Agnese, Z. Ahmed, A. J. Anderson, S. Arrenberg, D. Balakishiyeva, R. Basu Thakur, D. A. Bauer, J. Billard, A. Borgland, D. Brandt, et al. "Silicon Detector Dark Matter Results from the Final Exposure of CDMS II". In: *Phys. Rev. Lett.* 111 (25 2013), p. 251301. DOI: 10.1103/PhysRevLett.111.251301.

[151] R. Agnese, T. Aralis, T. Aramaki, I. J. Arnquist, E. Azadbakht, W. Baker, S. Banik, D. Barker, D. A. Bauer, T. Binder, et al. "First Dark Matter Constraints from a SuperCDMS Single-Charge Sensitive Detector". In: *Phys. Rev. Lett.* 121 (5 2018), p. 051301. DOI: 10.1103/PhysRevLett.121.051301.

[152] A. H. Abdelhameed, G. Angloher, P. Bauer, A. Bento, E. Bertoldo, C. Bucci, L. Canonica, A. D'Addabbo, X. Defay, S. Di Lorenzo, et al. "First results from the CRESST-III low-mass dark matter program". In: 100 (10 2019), p. 102002. DOI: 10.1103/PhysRevD.100.102002. URL: https://link.aps.org/doi/10.1103/PhysRevD.100.102002.

[153] S. W. Nam, A. Lita, D. Rosenberg, and A. J. Miller. "Optical and near-infrared photon detection with superconducting transition-edge sensors". In: *2006 Digest of the LEOS Summer Topical Meetings*. Quebec City, Que., 2006, pp. 17–18. DOI: 10.1109/LEOSST.2006.1694046.

[154] M. Pyle, E. Figueroa-Feliciano, and B. Sadoulet. 2015. arXiv: 1503.01200.

[155] W. Knaak, T. Hauß, M. Kummrow, and M. Meißner. "Thermalization of Ballistic Phonon Pulses in Dielectric Crystals Below 1K Using Time-Resolved Thermometry". In: *Phonon Scattering in Condensed Matter V*. Ed. by A. C. Anderson and J. P. Wolfe. Berlin, Heidelberg: Springer Berlin Heidelberg, 1986, pp. 174–176. ISBN: 978-3-642-82912-3.

[156] S. Hansen, F. DeJongh, J. Hall, B. A. Hines, M. E. Huber, T. Kiper, V. Mandic, W. Rau, T. Saab, D. Seitz, et al. "The Cryogenic Dark Matter Search test stand warm electronics card". In: *IEEE Nuclear Science Symposium Medical Imaging Conference*. Knoxville, TN, 2010, pp. 1392–1395. DOI: 10.1109/NSSMIC.2010.5874000.

[157] J. T. Karvonen, L. J. Taskinen, and I. J. Maasilta. "Influence of Temperature Gradients on Tunnel Junction Thermometry below 1 K: Cooling and Electron–Phonon Coupling". In: *J. Low Temp. Phys.* 146.1 (2007), pp. 213–226. DOI: 10.1007/s10909-006-9264-y.

[158] C. Mancini-Terracciano and M. Vignati. "Noise correlation and decorrelation in arrays of bolometric detectors". In: *J. Instrum.* 7.06 (2012), P06013. DOI: 10.1088/1748-0221/7/06/p06013.

[159] I. J. Maasilta. "Complex impedance, responsivity and noise of transition-edge sensors: Analytical solutions for two- and three-block thermal models". In: *AIP Adv.* 2.4 (2012), p. 042110. DOI: 10.1063/1.4759111.

[160] N. A. Wakeham, J. S. Adams, S. R. Bandler, S. Beaumont, J. A. Chervenak, A. M. Datesman, M. E. Eckart, F. M. Finkbeiner, R. Hummatov, R. L. Kelley, et al. "Thermal fluctuation noise in Mo/Au superconducting transition-edge sensor microcalorimeters". In: *J. Appl. Phys.* 125.16 (2019), p. 164503. DOI: 10.1063/1.5086045.

[161] A. J. Miller, S. W. Nam, J. M. Martinis, and A. V. Sergienko. "Demonstration of a low-noise near-infrared photon counter with multiphoton discrimination". In: *Appl. Phys. Lett.* 83.4 (2003), pp. 791–793. DOI: 10.1063/1.1596723. URL: https://doi.org/10.1063/1.1596723.

[162] B. S. Karasik, S. V. Pereverzev, A. Soibel, D. F. Santavicca, D. E. Prober, D. Olaya, and M. E. Gershenson. "Energy-resolved detection of single infrared photons with $\lambda = 8\,\mu$m using a superconducting microbolometer". In: *Appl. Phys. Lett.* 101.5 (2012), p. 052601. DOI: 10.1063/1.4739839.

[163] D. J. Goldie, A. V. Velichko, D. M. Glowacka, and S. Withington. "Ultra-low-noise MoCu transition edge sensors for space applications". In: *J. Appl. Phys.* 109.8 (2011), p. 084507. DOI: 10.1063/1.3561432.

[164] L. Lolli, E. Taralli, C. Portesi, E. Monticone, and M. Rajteri. "High intrinsic energy resolution photon number resolving detectors". In: *Appl. Phys. Lett.* 103.4 (2013), p. 041107. DOI: 10.1063/1.4815922.

[165] P. Khosropanah, T. Suzuki, M. L. Ridder, R. A. Hijmering, H. Akamatsu, L. Gottardi, J. van der Kuur, J. R. Gao, and B. D. Jackson. "Ultra-low noise TES bolometer arrays for SAFARI instrument on SPICA". In: *Proc. SPIE* 9914 (2016), 99140B. DOI: 10.1117/12.2233472.

[166] Z. Hong, R. Ren, N. Kurinsky, E. Figueroa-Feliciano, L. Wills, S. Ganjam, R. Mahapatra, N. Mirabolfathi, B. Nebolsky, H. D. Pinckney, et al. "Single electron-hole pair sensitive silicon detector with surface event discrimination". In: *Nucl. Instrum. Methods Phys. Res. A* 963 (2020), p. 163757. ISSN: 0168-9002. DOI: 10.1016/j.nima.2020.163757.

[167] O. Abramoff, L. Barak, I. M. Bloch, L. Chaplinsky, M. Crisler, Dawa, A. Drlica-Wagner, R. Essig, J. Estrada, E. Etzion, et al. "SENSEI: Direct-Detection Constraints on Sub-GeV Dark Matter from a Shallow Underground Run Using a Prototype Skipper CCD". In: *Phys. Rev. Lett.* 122 (16 2019), p. 161801. DOI: 10.1103/PhysRevLett.122.161801.

[168] I. Alkhatib et al. "Light Dark Matter Search with a High-Resolution Athermal Phonon Detector Operated above Ground". In: *Phys. Rev. Lett.* 127 (6 2021), p. 061801. DOI: 10.1103/PhysRevLett.127.061801. URL: https://link.aps.org/doi/10.1103/PhysRevLett.127.061801.

[169] C. Alduino et al. "First Results from CUORE: A Search for Lepton Number Violation via $0\nu\beta\beta$ Decay of ^{130}Te". In: *Phys. Rev. Lett.* 120 (13 2018), p. 132501. DOI: 10.1103/PhysRevLett.120.132501.

[170] D. Q. Adams et al. "Improved Limit on Neutrinoless Double-Beta Decay in ^{130}Te with CUORE". In: *Phys. Rev. Lett.* 124 (12 2020), p. 122501. DOI: 10.1103/PhysRevLett.124.122501.

[171] E. Andreotti et al. "130Te Neutrinoless Double-Beta Decay with CUORICINO". In: *Astropart. Phys.* 34 (2011), pp. 822–831. DOI: 10.1016/j.astropartphys.2011.02.002.

[172] E. Armengaud et al. "Searching for low-mass dark matter particles with a massive Ge bolometer operated above ground". In: *Phys. Rev. D* 99 (8 2019), p. 082003. DOI: 10.1103/PhysRevD.99.082003.

[173] G. Angloher et al. "Results on MeV-scale dark matter from a gram-scale cryogenic calorimeter operated above ground". In: *Eur. Phys. J. C* 77.9 (2017), p. 637. ISSN: 1434-6052. DOI: 10.1140/epjc/s10052-017-5223-9.

[174] Q. Arnaud et al. "First Germanium-Based Constraints on Sub-MeV Dark Matter with the EDELWEISS Experiment". In: *Phys. Rev. Lett.* 125 (14 2020), p. 141301. DOI: 10.1103/PhysRevLett.125.141301.

[175] R. Agnese et al. "First Dark Matter Constraints from a SuperCDMS Single-Charge Sensitive Detector". In: *Phys. Rev. Lett.* 121 (5 2018), p. 051301. DOI: 10.1103/PhysRevLett.121.051301.

[176] O. Abramoff et al. "SENSEI: Direct-Detection Constraints on Sub-GeV Dark Matter from a Shallow Underground Run Using a Prototype Skipper CCD". In: *Phys. Rev. Lett.* 122 (16 2019), p. 161801. DOI: 10.1103/PhysRevLett.122.161801.

[177] A. Aguilar-Arevalo et al. "Constraints on Light Dark Matter Particles Interacting with Electrons from DAMIC at SNOLAB". In: *Phys. Rev. Lett.* 123 (18 2019), p. 181802. DOI: 10.1103/PhysRevLett.123.181802.

[178] A. H. Abdelhameed et al. "First results from the CRESST-III low-mass dark matter program". In: *Phys. Rev. D* 100 (10 2019), p. 102002. DOI: 10.1103/PhysRevD.100.102002.

[179] F. T. Avignone III, S. R. Elliott, and J. Engel. "Double beta decay, Majorana neutrinos, and neutrino mass". In: *Rev. Mod. Phys.* 80 (2 2008), pp. 481–516. DOI: 10.1103/RevModPhys.80.481. URL: https://link.aps.org/doi/10.1103/RevModPhys.80.481.

[180] W. R. Armstrong et al. 2019. arXiv: 1907.09376.

[181] V. Alenkov et al. "First results from the AMoRE-Pilot neutrinoless double beta decay experiment". In: *Eur. Phys. J. C* 79.9 (2019), p. 791. ISSN: 1434-6052. DOI: 10.1140/epjc/s10052-019-7279-1.

[182] O. Azzolini, J. W. Beeman, F. Bellini, M. Beretta, M. Biassoni, C. Brofferio, C. Bucci, S. Capelli, L. Cardani, P. Carniti, et al. "Background Model of the CUPID-0 Experiment". In: *Eur. Phys. J. C* 79.7 (2019), p. 583. DOI: 10.1140/epjc/s10052-019-7078-8.

[183] T. Tabarelli de Fatis. "Cerenkov emission as a positive tag of double beta decays in bolometric experiments". In: *Eur. Phys. J. C* 65.1 (2010), p. 359. DOI: 10.1140/epjc/s10052-009-1207-8.

[184] N. Casali, M. Vignati, J. W. Beeman, F. Bellini, L. Cardani, I. Dafinei, S. Di Domizio, F. Ferroni, L. Gironi, S. Nagorny, et al. "TeO$$_2$$2bolometers with Cherenkov signal tagging: towards next-generation neutrinoless double-beta decay experiments". In: *Eur. Phys. J. C* 75.1 (2015), p. 12. DOI: 10.1140/epjc/s10052-014-3225-4.

[185] M. Battaglieri et al. 2017. arXiv: 1707.04591.

[186] R. Essig, J. Mardon, and T. Volansky. "Direct detection of sub-GeV dark matter". In: *Phys. Rev. D* 85 (7 2012), p. 076007. DOI: 10.1103/PhysRevD.85.076007.

[187] R. Essig et al. 2013. arXiv: 1311.0029.

[188] J. Alexander et al. 2016. arXiv: 1608.08632.

[189] N. Kurinsky, D. Baxter, Y. Kahn, and G. Krnjaic. "Dark matter interpretation of excesses in multiple direct detection experiments". In: *Phys. Rev. D* 102 (1 2020), p. 015017. DOI: 10.1103/PhysRevD.102.015017. URL: https://link.aps.org/doi/10.1103/PhysRevD.102.015017.

[190] A. E. Robinson. "Coherent photon scattering background in sub-GeV/c^2 direct dark matter searches". In: *Phys. Rev. D* 95 (2 2017), p. 021301. DOI: 10.1103/PhysRevD.95.021301.

[191] S. Derenzo, R. Essig, A. Massari, A. Soto, and T.-T. Yu. "Direct detection of sub-GeV dark matter with scintillating targets". In: *Phys. Rev. D* 96 (1 2017), p. 016026. DOI: 10.1103/PhysRevD.96.016026.

[192] S. Knapen, T. Lin, M. Pyle, and K. M. Zurek. "Detection of light dark matter with optical phonons in polar materials". In: *Phys. Lett. B* 785 (2018), pp. 386–390. ISSN: 0370-2693. DOI: 10.1016/j.physletb.2018.08.064.

[193] S. A. Hertel, A. Biekert, J. Lin, V. Velan, and D. N. McKinsey. "Direct detection of sub-GeV dark matter using a superfluid ^{4}He target". In: *Phys. Rev. D* 100 (9 2019), p. 092007. DOI: 10.1103/PhysRevD.100.092007.

[194] A. G. Kozorezov, A. F. Volkov, J. K. Wigmore, A. Peacock, A. Poelaert, and R. den Hartog. "Quasiparticle-phonon downconversion in nonequilibrium superconductors". In: *Phys. Rev. B* 61 (17 2000), pp. 11807–11819. DOI: 10.1103/PhysRevB.61.11807. URL: https://link.aps.org/doi/10.1103/PhysRevB.61.11807.

[195] J. Schweppe, R. D. Deslattes, T. Mooney, and C. J. Powell. "Accurate measurement of Mg and Al $K\alpha_{1,2}$ X-ray energy profiles". In: *J. Electron Spectrosc.* 67.3 (1994), pp. 463–478. ISSN: 0368-2048. DOI: 10.1016/0368-2048(93)02059-U.

[196] G. Hölzer, M. Fritsch, M. Deutsch, J. Härtwig, and E. Förster. "$K\alpha_{1,2}$ and $K\beta_{1,3}$ x-ray emission lines of the 3d transition metals". In: *Phys. Rev. A* 56 (6 1997), pp. 4554–4568. DOI: 10.1103/PhysRevA.56.4554.

[197] C. W. Fink, S. L. Watkins, T. Aramaki, P. L. Brink, S. Ganjam, B. A. Hines, M. E. Huber, N. A. Kurinsky, R. Mahapatra, N. Mirabolfathi, et al. "Characterizing TES power noise for future single optical-phonon and infrared-photon detectors". In: *AIP Adv.* 10.8 (2020), p. 085221. DOI: 10.1063/5.0011130.

[198] B. Cabrera. "Introduction to TES Physics". In: *J. Low Temp. Phys.* 151.1-2 (2008), pp. 82–93. DOI: 10.1007/s10909-007-9632-2.

[199] I. J. Maasilta. "Complex impedance, responsivity and noise of transition-edge sensors: Analytical solutions for two- and three-block thermal models". In: *AIP Adv.* 2.4 (2012), p. 042110. DOI: 10.1063/1.4759111.

[200] S. R. Golwala. "Exclusion limits on the WIMP nucleon elastic scattering cross-section from the Cryogenic Dark Matter Search". PhD thesis. University of California, Berkeley, 2000. DOI: 10.2172/1421437.

[201] S. J. B. Reed and N. G. Ware. "Escape peaks and internal fluorescence in X-ray spectra recorded with lithium drifted silicon detectors". In: *J. Phys. E Sci. Instrum.* 5.6 (1972), pp. 582–583. DOI: 10.1088/0022-3735/5/6/029.

[202] D. M. Chernyak, F. A. Danevich, A. Giuliani, E. Olivieri, M. Tenconi, and V. I. Tretyak. "Random coincidence of $2\nu2\beta$ decay events as a background source in bolometric $0\nu2\beta$ decay experiments". In: *Eur. Phys. J. C* 72 (2012), p. 1989. DOI: 10.1140/epjc/s10052-012-1989-y.

[203] D. R. Artusa et al. "Exploring the neutrinoless double beta decay in the inverted neutrino hierarchy with bolometric detectors". In: *Eur. Phys. J. C* 74 (2014), p. 3096. DOI: 10.1140/epjc/s10052-014-3096-8.

[204] N. Casali, L. Cardani, I. Colantoni, A. Cruciani, S. Di Domizio, M. Martinez, G. Pettinari, and M. Vignati. In: *Eur. Phys. J. C* 79.8 (2019), p. 724. ISSN: 1434-6052. DOI: 10.1140/epjc/s10052-019-7242-1.

[205] B. S. Neganov and V. N. Trofimov. "Colorimetric method measuring ionizing radiation". In: *Otkryt. Izobret.* 146 (1985), p. 215.

[206] P. N. Luke. "Voltage-assisted calorimetric ionization detector". In: *J. Appl. Phys.* 64.12 (1988), pp. 6858–6860. DOI: 10.1063/1.341976.

[207] L. Cardani, N. Casali, A. Cruciani, H. le Sueur, M. Martinez, F. Bellini, M. Calvo, M. G. Castellano, I. Colantoni, C. Cosmelli, et al. "Al/Ti/Al phonon-mediated KIDs for UV–vis light detection over large areas". In: *Supercond. Sci. Technol.* 31.7 (2018), p. 075002. DOI: 10.1088/1361-6668/aac1d4.

[208] K. Schäffner, G. Angloher, F. Bellini, N. Casali, F. Ferroni, D. Hauff, S. S. Nagorny, L. Pattavina, F. Petricca, S. Pirro, et al. "Particle discrimination in TeO2 bolometers using light detectors read out by transition edge sensors". In: *Astropart. Phys.* 69 (2015), pp. 30–36. ISSN: 0927-6505. DOI: 10.1016/j.astropartphys.2015.03.008.

[209] M. Barucci, J. W. Beeman, V. Caracciolo, L. Pagnanini, L. Pattavina, G. Pessina, S. Pirro, C. Rusconi, and K. Schäffner. "Cryogenic light detectors with enhanced performance for rare event physics". In: *Nucl. Instrum. Methods Phys. Res. A* 935 (2019), pp. 150–155. ISSN: 0168-9002. DOI: 10.1016/j.nima.2019.05.019.

[210] L. Pattavina, N. Casali, L. Dumoulin, A. Giuliani, M. Mancuso, P. de Marcillac, S. Marnieros, S. S. Nagorny, C. Nones, E. Olivieri, et al. "Background Suppression in Massive TeO

2

2 Bolometers with Neganov–Luke Amplified Light Detectors". In: *J. Low Temp. Phys.* 184.1-2 (2015), pp. 286–291. ISSN: 1573-7357. DOI: 10.1007/s10909-015-1404-9.

[211] M. Willers, F. v. Feilitzsch, A. Gütlein, A. Münster, J.-C. Lanfranchi, L. Oberauer, W. Potzel, S. Roth, S. Schönert, M. v. Sivers, et al. "Neganov-Luke amplified cryogenic light detectors for the background discrimination in neutrinoless double beta decay search with TeO2bolometers". In: *J. Instrum.* 10.03 (2015), P03003–P03003. DOI: 10.1088/1748-0221/10/03/p03003.

[212] L. Bergé et al. "Complete event-by-event $\alpha/\gamma(\beta)$ separation in a full-size TeO_2 CUORE bolometer by Neganov-Luke-magnified light detection". In: *Phys. Rev. C* 97 (3 2018), p. 032501. DOI: 10.1103/PhysRevC.97.032501. URL: https://link.aps.org/doi/10.1103/PhysRevC.97.032501.

[213] V. Novati, L. Bergé, L. Dumoulin, A. Giuliani, M. Mancuso, P. de Marcillac, S. Marnieros, E. Olivieri, D. V. Poda, M. Tenconi, et al. "Charge-to-heat transducers exploiting the Neganov-Trofimov-Luke effect for light detection in rare-event searches". In: *Nucl. Instrum. Methods Phys. Res. A* 940 (2019), pp. 320–327. ISSN: 0168-9002. DOI: 10.1016/j.nima.2019.06.044.

[214] J. Rothe, G. Angloher, P. Bauer, A. Bento, C. Bucci, L. Canonica, A. D'Addabbo, X. Defay, A. Erb, F. v. Feilitzsch, et al. "TES-Based Light Detectors for the CRESST Direct Dark Matter Search". In: *J. Low Temp. Phys.* 193.5-6 (2018), pp. 1160–1166. DOI: 10.1007/s10909-018-1944-x.

[215] I. Alkhatib et al. 2020. arXiv: 2007.14289.

[216] J. Yen. "Phonon Sensor Dynamics for Cryogenic Dark Matter Search Experiment: A Study of Quasiparticle Transport in Aluminum Coupled to Tungsten Transition Edge Sensors". PhD thesis. Stanford U., 2015. DOI: 10.2172/1352050.

[217] *BICEP2 2014 RELEASE image gallery.* URL: http://bicepkeck.org/visuals.html.

[218] A. R. Liddle and D. H. Lyth. "INFLATION". In: *Cosmological Inflation and Large-Scale Structure*. Cambridge University Press, 2000, pp. 36–57. DOI: 10.1017/CBO9781139175180.004.

[219] D. Bodeker and W. Buchmuller. *Baryogenesis from the weak scale to the grand unification scale*. 2021. arXiv: 2009.07294 [hep-ph].

[220] S. Weinberg. "Universal Neutrino Degeneracy". In: *Phys. Rev.* 128 (3 1962), pp. 1457–1473. DOI: 10.1103/PhysRev.128.1457. URL: https://link.aps.org/doi/10.1103/PhysRev.128.1457.

[221] S. Betts et al. *Development of a Relic Neutrino Detection Experiment at PTOLEMY: Princeton Tritium Observatory for Light, Early-Universe, Massive-Neutrino Yield*. 2013. arXiv: 1307.4738 [astro-ph.IM].

[222] B. Follin, L. Knox, M. Millea, and Z. Pan. "First Detection of the Acoustic Oscillation Phase Shift Expected from the Cosmic Neutrino Background". In: *Phys. Rev. Lett.* 115 (9 2015), p. 091301. DOI: 10.1103/PhysRevLett.115.091301. URL: https://link.aps.org/doi/10.1103/PhysRevLett.115.091301.

[223] M. Pospelov and J. Pradler. "Big Bang Nucleosynthesis as a Probe of New Physics". In: *Annual Review of Nuclear and Particle Science* 60.1 (2010), pp. 539–568. DOI: 10.1146/annurev.nucl.012809.104521. eprint: https://doi.org/10.1146/annurev.nucl.012809.104521. URL: https://doi.org/10.1146/annurev.nucl.012809.104521.

[224] R. A. Sunyaev and J. Chluba. "Signals from the epoch of cosmological recombination - Karl Schwarzschild Award Lecture 2008". In: *Astronomische Nachrichten* 330.7 (2009), pp. 657–674. ISSN: 1521-3994. DOI: 10.1002/asna.200911237. URL: http://dx.doi.org/10.1002/asna.200911237.

[225] V. Desjacques, J. Chluba, J. Silk, F. de Bernardis, and O. Doré. *Detecting the cosmological recombination signal from space*. 2015. arXiv: 1503.05589 [astro-ph.CO].

[226] S. R. Golwala. "Exclusion limits on the WIMP nucleon elastic scattering cross-section from the Cryogenic Dark Matter Search". In: (2000). DOI: 10.2172/1421437. URL: https://www.osti.gov/biblio/1421437.

[227] C. W. Fink and S. L. Watkins. *QETpy*. Version 1.3.2. 2022. DOI: 10.5281/zenodo.5903353. URL: https://doi.org/10.5281/zenodo.5903353.

[228] G. E. Hinton and R. R. Salakhutdinov. "Reducing the Dimensionality of Data with Neural Networks". In: *Science* 313.5786 (2006), pp. 504–507. ISSN: 0036-8075. DOI: 10.1126/science.1127647. eprint: https://science.sciencemag.org/content/313/5786/504.full.pdf. URL: https://science.sciencemag.org/content/313/5786/504.

[229] D. P. Kingma and M. Welling. *Auto-Encoding Variational Bayes*. cite arxiv:1312.6114. 2013. URL: http://arxiv.org/abs/1312.6114.

[230] S. Kullback and R. A. Leibler. "On Information and Sufficiency". In: *Ann. Math. Statist.* 22.1 (1951), pp. 79–86. DOI: 10.1214/aoms/1177729694. URL: https://doi.org/10.1214/aoms/1177729694.

[231] E. Pinho and C. Costa. "Unsupervised Learning for Concept Detection in Medical Images: A Comparative Analysis". In: *Applied Sciences* 8 (2018). DOI: 10.3390/app8081213.

[232] L. Matthey, A. Pal, C. Burgess, X. Glorot, M. Botvinick, S. Mohamed, and A. Lerchner. "beta-VAE: Learning Basic Visual Concepts with a Constrained Variational Framework". In: *ICLR*. 2017.

Appendix A

Big-Bang Cosmology

In order to fully understand the 'dark matter problem', we first need a basic understanding of cosmology. What follows is a brief introduction to the standard big-bang model, closely following the summary in [10].

A.1 Intro to the ΛCDM Cosmological Model

The cosmological principle states that on very large scales, roughly 100 Mpc, the universe is homogeneous and isotropic. From this principle, the geometry of space-time can be described by the Robertson-Walker metric (setting $c = 1$):

$$ds^2 = dt^2 - a^2(t)\left[\frac{dr^2}{1-kr^2} + r^2(d\theta^2 + \sin^2\theta d\phi^2)\right], \tag{A.1}$$

where r is the radial comoving distance, ϕ and θ are the angular coordinates, and k is the curvature constant. $k = +1, 0, -1$ correspond to closed, flat, or open geometries. The expansion of space-time is accounted for with the dimensionless 'scale factor' $a(t)$, which is equal to $a(t_0) = 1$ for present time t_0. The evolution of this scale factor with time is of great importance in cosmology. The scale factor is related to the cosmological redshift z as

$$1 + z = \frac{a_0}{a(t)}, \tag{A.2}$$

To understand how the Robertson-Walker metric evolves, we turn to the Einstein field equations,

$$\mathcal{R}_{\mu\nu} - \frac{1}{2}\mathcal{R}g_{\mu\nu} + \Lambda g_{\mu\nu} = 8\pi G\mathcal{T}_{\mu\nu}, \tag{A.3}$$

where $\mathcal{R}_{\mu\nu}, \mathcal{R}$ are the Ricci curvature tensor and scalar, $\mathcal{T}_{\mu\nu}$ is the stress-energy tensor, G is the gravitational constant, Λ is the cosmological constant, and $g_{\mu\nu}$ is the metric tensor.

Eq. A.3 can be used to relate the scale factor $a(t)$ to the energy density of the universe by describing the cosmological matter as a perfect fluid for the stress-energy tensor $\mathcal{T}_{\mu\nu}$ and using Eq. A.1 to calculate $\mathcal{R}_{\mu\nu}, \mathcal{R}$ and $g_{\mu\nu}$. In doing so, we get what is known as the Friedmann equations,

$$H^2 \equiv \left(\frac{\dot{a}}{a}\right)^2 = \frac{8\pi}{3}G\rho - \frac{k}{a^2} + \frac{\Lambda}{3} \tag{A.4}$$

$$\frac{\ddot{a}}{a} = -\frac{4\pi}{3}G\left(\rho + 3p\right) + \frac{\Lambda}{3}, \tag{A.5}$$

where ρ is the energy density in the universe[1], p is the pressure, and we have defined the Hubble parameter H. We will see later that the age of the universe is the inverse of the Hubble parameter.

Equations A.4 and A.5 can be combined to make the following useful relation (which is also simply a direct consequence of the first law of thermodynamics)

$$\dot{\rho} = -3H(\rho + p). \tag{A.6}$$

The density and pressure are related for a perfect fluid with the equation of state,

$$p = w\rho, \tag{A.7}$$

where the factor w changes depending on content. For non-relativistic **matter**, the pressure is negligible, thus $w = 0$. For **radiation** (relativistic matter and photons) $w = 1/3$. For the energy of the **vacuum** (Λ), $w = -1$, since the pressure stays constant with the expanding universe.

The growth of the scale factor as a function of time can be determined by solving the Friedmann equations in the limit the energy density is dominated by a single source,

$$a \propto t^{1/2} \qquad \text{Radiation-dominated} \tag{A.8}$$

$$a \propto t^{2/3} \qquad \text{Matter-dominated} \tag{A.9}$$

$$a \propto e^{\sqrt{\Lambda/3}t} \qquad \Lambda\text{-dominated} \tag{A.10}$$

$$\tag{A.11}$$

The Friedmann equations can be refactored into a more useful form with the introduction of a few definitions. We first define the 'critical density' ρ_c which, ignoring the cosmological constant (Dark Energy), is the energy density that would be the inflection point between a

[1]Note, when no subscript is used, the total energy density is implied.

contracting and expanding universe. This can be determined from Eq. A.4 by setting $k = 0$ and $\Lambda = 0$,

$$H^2 = \frac{8\pi}{3} G\rho_c \tag{A.12}$$

$$\implies \rho_c = \frac{3H^2}{8\pi G} \tag{A.13}$$

$$\rho_c = 1.05 \times 10^{-5} h^2 \,\mathrm{GeV\,cm^{-3}} \tag{A.14}$$

where h, the scaled Hubble parameter is defined by $H \equiv 100h \,\mathrm{km\,s^{-1}\,Mpc^{-1}}$, and is measured to be roughly $h \approx 0.7$. This means that the critical density is approximately a few hydrogen atoms per cubic meter. With this parameter, we can now define the density parameter

$$\Omega \equiv \frac{\rho}{\rho_c}, \tag{A.15}$$

which is the ratio of the total measured energy density to the critical density. Furthermore, we can now relate the curvature parameter k to measurable quantities, H_0 and Ω_0 (where the 0 subscript denotes present day values)

$$k = H_0^2(\Omega_0 - 1). \tag{A.16}$$

We can now understand the curvature of the universe in terms of energy density. It is worth pausing for a moment to interpret what we have so far. From the form of Equation A.4, ignoring the cosmological constant term, in a flat or open universe ($\Omega_0 = 1, < 1$), the universe will expand forever, and in a closed universe ($\Omega_0 > 1$) it will collapse on itself, as shown in figure A.1.

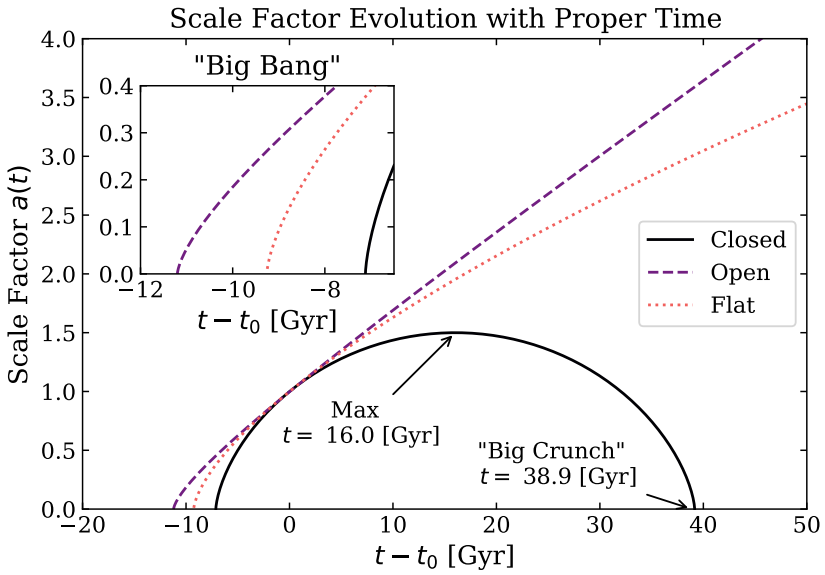

Figure A.1: Plot of scale Factor $a(t)$ vs proper time t for an open, flat, and closed universe (ignoring dark energy). Each model has been adjusted such that the present day time t_0 is at $t = 0$. The time of the maximum $a(t)$ and "Big Crunch" are shown on the plot assuming the present day time is zero.

From Equation A.16, we can now see how the curvature depends on the total mass density of the universe. Using the above relations, we can write the Hubble parameter in terms of the present day densities of the individual energy constituents of the universe,

$$H^2 = \left(\frac{\dot{a}}{a}\right)^2 = H_0^2 \left(\frac{\Omega_{0,m}}{a^3} + \Omega_{0,\Lambda} + \frac{\Omega_{0,r}}{a^4} + \frac{1 - \Omega_{0,m} - \Omega_{0,\Lambda} - \Omega_{0,r}}{a^2}\right). \tag{A.17}$$

where $\Omega_{0,m}$, $\Omega_{0,r}$, and $\Omega_{0,\Lambda}$ are the present day relative energy densities of all matter, radiation, and vacuum energy respectively. Observationally these parameters can be constrained in many ways, but most notably they have been measured by looking at a distance type metric of type 1A Supernovae as a function of cosmological redshift as shown in Fig. A.2. From this, we see that $\Omega_0 \approx 1$ and we live in a flat universe. Most surprising to astronomers at the time however, is the universe is dominated not by matter, but vacuum energy (Λ). This says that not only is the universe expanding, but at an accelerated rate! This is one of the major unanswered questions in cosmology, the next section will detail the other one. It is worth noting that the radiation density has been measured to be $\Omega_{0,r} \approx 10^{-4}$ and is often ignored in many calculations because of its low value.

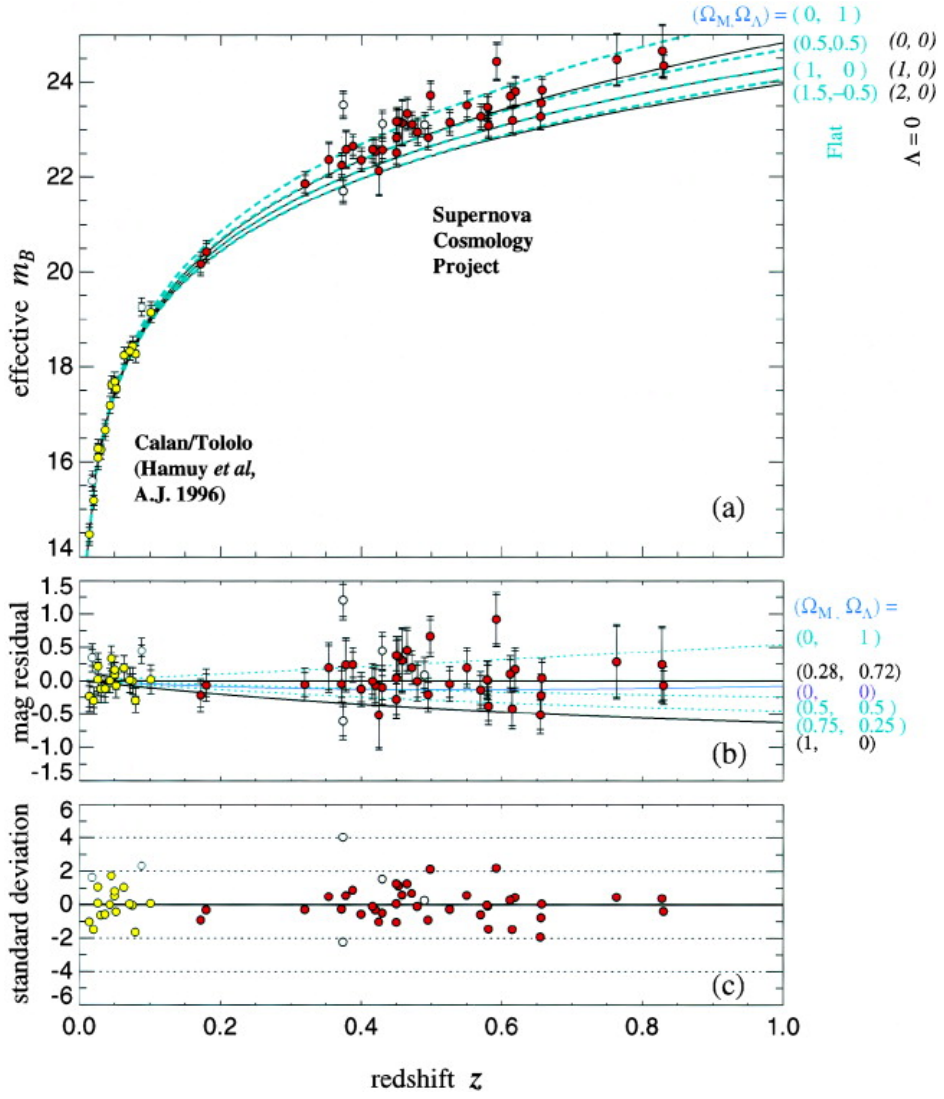

Figure A.2: Hubble diagram for type 1A Supernovae, from [1]

A.2 Thermal History of the Universe

We now step back in time to the very early universe to paint a picture of how the current universe came to be. After the big bang, the universe expanded and thus the equilibrium temperature decreased. The notable time frames of the early universe expansion are determined by which components of the universe are in thermal equilibrium. For example, for an interaction rate of a given particle species Γ_i, if

$$\begin{aligned} \Gamma_i \gg H \quad &\Longrightarrow \quad \text{Particles are in thermal equilibrium} \\ &\qquad\quad (\text{many interactions per Hubble time}) \\ \Gamma_i \ll H \quad &\Longrightarrow \quad \text{Particles have decoupled ('Feeze-out')} \end{aligned}$$

The process of freeze-out is also known as *chemical decoupling*. In short times after the big bang, the energy density of the universe was radiation dominated. In cosmological terms, 'radiation' includes any relativistic particles. For the radiation dominated era, temperature and time can be related with simple statistical mechanics techniques, with the result

$$k_B T = \frac{0.86\,\text{MeV}}{\sqrt{t\,\text{sec}}} \left(\frac{10\frac{3}{4}}{g^*}\right)^{\frac{1}{4}}. \tag{A.18}$$

The parameter g^* is the number of effective degrees of freedom for the radiation given by

$$g_* = \sum_{\text{bosons}} g_B \left(\frac{T_B}{T_{eq}}\right)^4 + \frac{7}{8} \sum_{\text{fermions}} g_F \left(\frac{T_F}{T_{eq}}\right)^4 \tag{A.19}$$

where $g_{B(F)}$ and $T_{B(F)}$ are the degrees of freedom and temperatures for the Bosons (Fermions), and T_{eq} is the equilibrium temperature. A similar quantity that is of use later on is the number of entropic relativistic degrees of freedom,

$$g_{*s} = \sum_{\text{bosons}} g_B \left(\frac{T_B}{T_{eq}}\right)^3 + \frac{7}{8} \sum_{\text{fermions}} g_F \left(\frac{T_F}{T_{eq}}\right)^3. \tag{A.20}$$

As a handy rule of thumb, for our purposes we can approximate

$$g_* \approx g_{*s} \approx \begin{cases} 100 & T > 300\,\text{MeV} \\ 10 & 300\,\text{MeV} > T > 1\,\text{MeV} \\ 3 & T < 1\,\text{MeV} \end{cases} \tag{A.21}$$

What follows is often referred to as **The First Three Minutes**. Throughout the following timeline, the reader should refer to figure A.3 for a helpful visual aid. The following times are considered from the beginning of the big-bang.

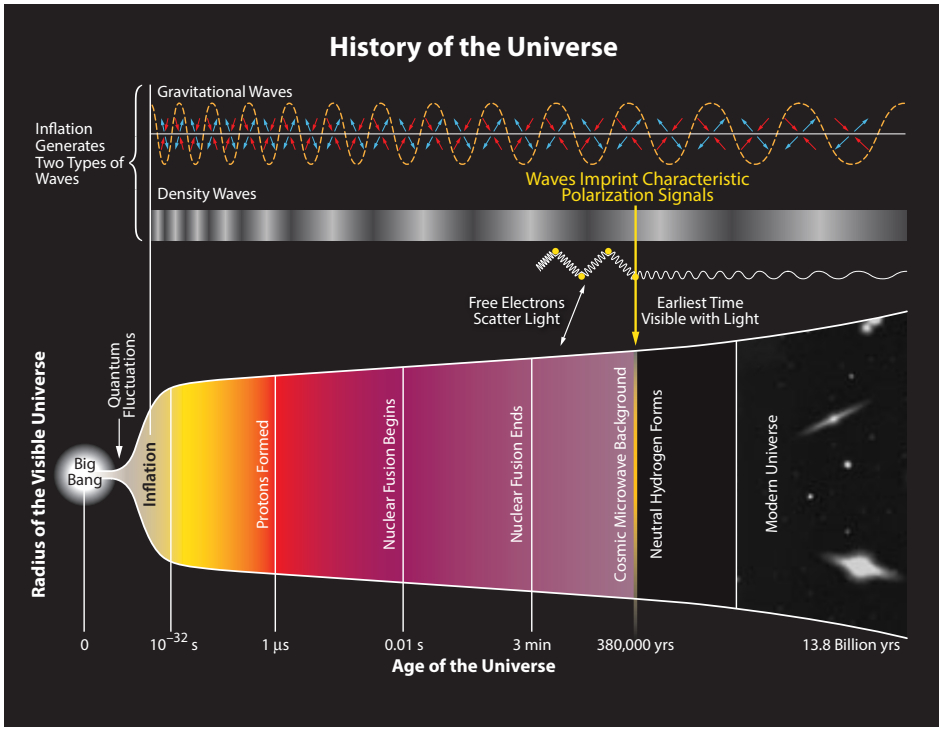

Figure A.3: Not to scale diagram of the history of the hot big bang expansion model from the BICEP2 Collaboration [217].

- $t \approx 10^{-36} - 10^{-32}\,\mathrm{s}$

  Experimentally little is known about this time period of the universe. However, the fairly well accepted theory of **cosmic inflation** states that during this time the universe expanded by a factor of 10^{26} [218]. After this period, the universe is left in a flat, isotropic, and largely homogeneous state. There are however, slight areas of over-densities and under-densities left by inflation.

- $t = 10^{-6}\,\mathrm{s} \implies T \approx 10^{11}\,\mathrm{K} \implies k_B T = 8.6\,\mathrm{MeV}$

  Quarks and gluons combined to form baryons and anti-baryons, primarily protons and neutrons and their anti-counterparts. At some time before this, a hypothetical process known as **baryogenesis** violated conservation of baryon number which resulted in a very small excess of quarks and leptons to anti-quarks and anti-leptons [219]. Once the universe cooled slightly, no new baryons were produced. The baryons and anti-baryons all annihilated, leaving no anti-baryons.

- $t = 0.01\,\mathrm{s} \implies T \approx 10^{10.5}\,\mathrm{K} \implies k_B T = 2.72\,\mathrm{MeV}$

  The mass of the proton is much larger than $k_B T$, thus the protons and neutrons have decoupled from the thermal bath. The photons, neutrinos, and electrons/positrons are

all in thermal equilibrium. The main reactions happening in this frame are

$$\mathrm{n} + \nu_e \longleftrightarrow \mathrm{p} + e^-$$
$$\mathrm{n} + e^+ \longleftrightarrow \mathrm{p} + \overline{\nu}_e$$

Due to the slightly lower mass of the proton than the neutron, the creation of protons was more energetically favorable, thus

$$\frac{n_n}{n_p} = \exp\left(-\frac{m_n - m_p}{k_B T}\right) = 0.86 \tag{A.22}$$

- $t = 1\,\mathrm{s} \implies T \approx 10^{10}\,\mathrm{K} \implies k_B T = 0.86\,\mathrm{MeV}$

  The temperature has now dropped below the proton-neutron mass difference, and the ratio is frozen out at $n_n/n_p \approx 0.24$. Even though thermally this ratio is fixed, the number of neutrons still continues to change via neutron decay,

  $$\mathrm{n} \longrightarrow \mathrm{p} + e^- + \overline{\nu}_e.$$

  The interaction rate of the weak scale is now less than the Hubble expansion rate, $\Gamma_{\mathrm{weak}} < H$, so the neutrinos have decoupled from the thermal bath. These neutrinos are now free streaming with a present day red-shifted temperature of $T_\nu \approx 1.9\,\mathrm{K}$ and are know as the **cosmic neutrino background** [220]. A number of experiments have been proposed to detect these neutrinos [221, 222].

- $t = 14\,\mathrm{s} \implies T \approx 10^{9.5}\,\mathrm{K} \implies k_B T = 0.272\,\mathrm{MeV}$

  Electrons and positrons have now become non-relativistic, thus annihilation is favored over pair production. The neutron/proton ratio continues to drop to $n_n/n_p = 0.2$. The neutron decay is slowed down by the combination of free protons and neutrons into ^{2}H (Deuterium).

  $$\mathrm{p} + \mathrm{n} \longleftrightarrow \mathrm{D} + \gamma$$

  However, the photon created in this reaction is more energetic than the binding energy of Deuterium ($\Delta_{\mathrm{D}} = 2.23\,\mathrm{MeV}$), and thus the Deuterium decays immediately. This is knows as the 'Deuterium Bottleneck'.

- $t \approx 3\,\mathrm{min} \implies T \approx 10^{9}\,\mathrm{K} \implies k_B T = 0.086\,\mathrm{MeV}$

  Most of the electrons and positrons have now disappeared. Free neutron decay has lowered the neutron to proton ration to $n_n/n_p \approx 0.16$. The temperature has now

dropped enough such that the number of photons per baryon above the deuterium binding energy,

$$\frac{n_\gamma}{n_B} \exp\left(-\frac{\Delta_{\mathrm{D}}}{T}\right), \tag{A.23}$$

is less than one. The deuterium has now become stable and the production of heavier elements begin. This process is known as **big-bang nucleosynthesis** or **BBN** (see [10–12] for a more detailed review). At this stage, the following reactions occur

$$\begin{aligned}
\mathrm{p} + \mathrm{n} &\longrightarrow \mathrm{D} + \gamma \\
\mathrm{p} + \mathrm{D} &\longrightarrow {}^3\mathrm{He} + \gamma \\
\mathrm{D} + \mathrm{D} &\longrightarrow {}^3\mathrm{He} + \mathrm{n} \\
\mathrm{D} + \mathrm{D} &\longrightarrow {}^3\mathrm{H} + \mathrm{p} \\
{}^3\mathrm{He} + \mathrm{D} &\longrightarrow {}^4\mathrm{He} + \mathrm{p} \\
{}^3\mathrm{H} + \mathrm{D} &\longrightarrow {}^4\mathrm{He} + \mathrm{n}
\end{aligned}$$

and less abundant reactions of

$${}^4\mathrm{He} + {}^3\mathrm{H} \longrightarrow {}^7\mathrm{Li} + \gamma$$

The production of these light elements occurs for a short time at which point the temperature is of the universe is too cold for nuclear fusion to happen. The amount of light elements stays relatively fixed except for radioactive decay of ^{3}H and ^{7}Li as seen in figure A.4.

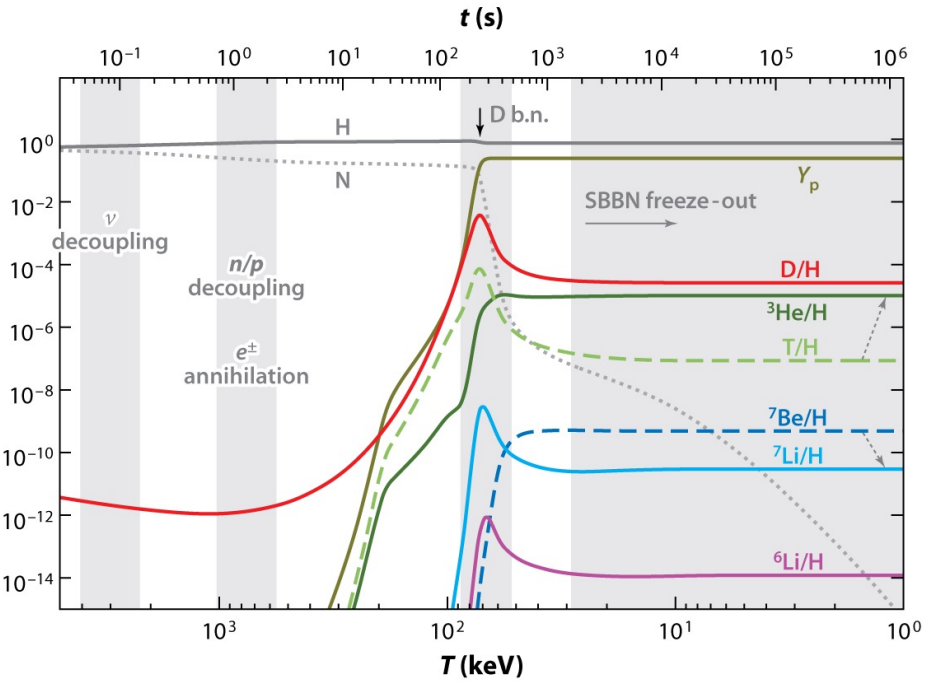

Figure A.4: Time and temperature evolution of all standard big bang nucleosynthesis (SBBN)- relevant nuclear abundances. The vertical arrow indicates the moment at T9 = 0.85 at which most of the helium nuclei are synthesized. The gray vertical bands indicate main BBN stages. From left to right: neutrino decoupling, electron-positron annihilation and n/p freeze-out, D bottleneck, and freeze-out of all nuclear reactions. Protons (H) and neutrons (N) are given relative to nb whereas Yp denotes the 4He mass fraction [223]

This provides a very interesting cosmological probe to measure. The abundance of these elements in the universe today sets the bound on the amount of baryonic matter in the universe.

- $t \approx 47000\,\text{years} \implies z \approx 3600 \implies k_B T = \mathcal{O}(\text{eV})$

  The Universe has cooled to the point that it has transitioned from being dominated by radiation energy to being matter dominated as shown in Fig. A.5. This means that the gravitational potential between small over-densities is now greater than the thermal radiation pressure and baryonic structure formation is able to begin.

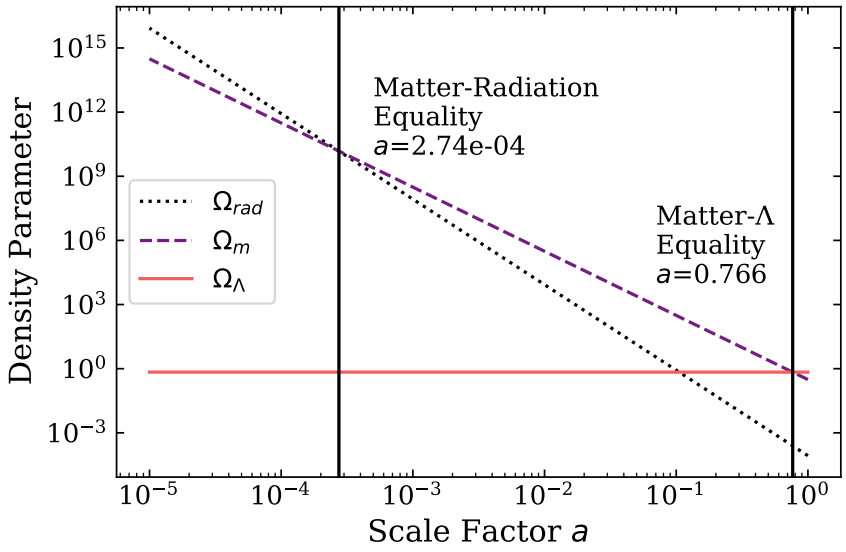

Figure A.5: Density parameters Ω_m, Ω_{rad}, and Ω_Λ as a function of scale factor a.

The time at which this structure formation takes place is largely dependent on the total matter density of the universe, defined as the point at which $\Omega_m(z_{eq}) = \Omega_r(z_{eq}) + \Omega_\Lambda(z_{eq})$. If we only consider the baryonic component of the matter energy density, then baryonic structure formation would begin much too late to account for the complex structures we observe today. So there is clearly already a strong dependence on the remaining non-baryonic component of the matter density, There is also a much larger dependence on structure formation from this DM component that we will discuss later.

- $t \approx 288,000$ years $\implies z \approx 1320$

  As the universe cools, it becomes energetically favorable for charged light element nuclei created in the BBN to form neutral atoms with free electrons. The process has been happening for some time, but peaks at about this time [10] (see Fig. A.6). Said more quantitatively, the free electron fraction x_e defined as

$$x_e = \frac{n_e}{n_p + n_H} \tag{A.24}$$

  where n_e is the number density of free electrons, n_H is the number density of atomic hydrogen and n_p is the number density of ionized hydrogen, drops from unity to roughly $x_e \approx 0.1$, and this epoch is know as **recombination** [224]. Once the free electron fraction dropped, the optical depth of the universe greatly increases as photons were no longer constantly Thompson scattering off of free electrons.

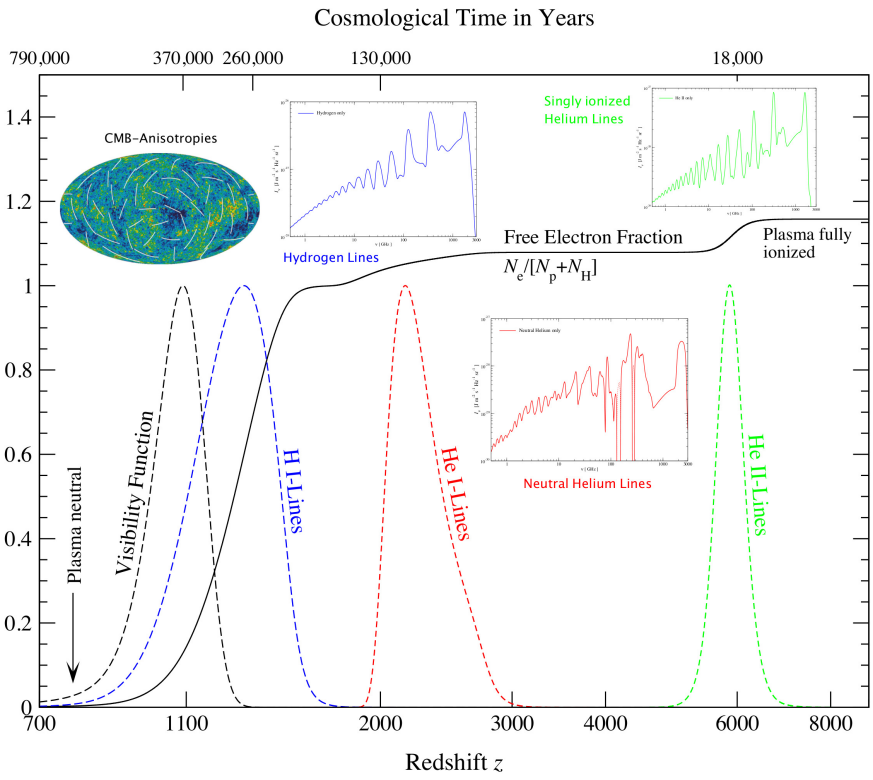

Figure A.6: Ionization history of the Universe (solid black curve) and the origin of different CMB signals (dashed lines and inlays). The observed temperature anisotropies in the CMB temperature are created close to the maximum of the Thomson visibility function around $z \approx 1089$, whereas the direct information carried by the photons in the cosmological hydrogen recombination spectrum is from slightly earlier times. The photons associated with the two recombinations of helium were released at even higher redshifts. Finding the traces of these signals in the cosmological recombination spectrum will therefore allow us to learn about the state of the Universe at $\approx 130,000$ yrs and $\approx 18,000$ yrs after the big bang. Furthermore, the cosmological recombination radiation may offer a way to tell if something unexpected (e.g. energy release due to annihilating dark matter particles) occurred before the end of cosmological recombination, from [224]

When these early neutral atoms formed, the electrons were bound to excited states. These electrons eventually dropped to the ground state and became decoupled from the bath. The feasibility of detecting the photons released from the Helium and Hydrogen recombination process, which would allow for a cosmological probe at an incredibly high redshift, is currently being explored [225].

- $t \approx 370,000\,\text{years} \implies z \approx 1100$

The process of recombination drastically increases the mean free path of photons, however the universe has not yet become 'transparent'. This happens when the Thomson scattering rate Γ_{th} is less than the Hubble expansion. During the matter dominated era, the Hubble parameter can be written as

$$H = H_0\sqrt{\Omega_{0,m}}\left(\frac{T}{T_0}\right)^{\frac{3}{2}}, \tag{A.25}$$

and the Thomson scattering rate is

$$\Gamma_{th} = n_e\frac{8\pi\alpha^2}{3m_e} = x_e n_B\frac{8\pi\alpha^2}{3m_e} \tag{A.26}$$

where α is the fine structure constant [10], and we can see that the scattering rate depends on the free electron fraction. Equating these two expressions, one finds that the temperature of the **photon decoupling** is $T_{dec} \approx 3000\,\mathrm{K}$. These free-streaming photons have been red-shifted to $\sim 2.7\,\mathrm{K}$ and is known as the **cosmic microwave background** or (**CMB**). This epoch is also referred to as **last scattering**. These photons are the closest approximation to a perfect black body ever measured, with temperature anisotropies at the 10^{-5} level. An image of the CMB sky can be seen in Fig. A.7. The observations of the CMB is rich with information, and the measurements will be discussed in a later section.

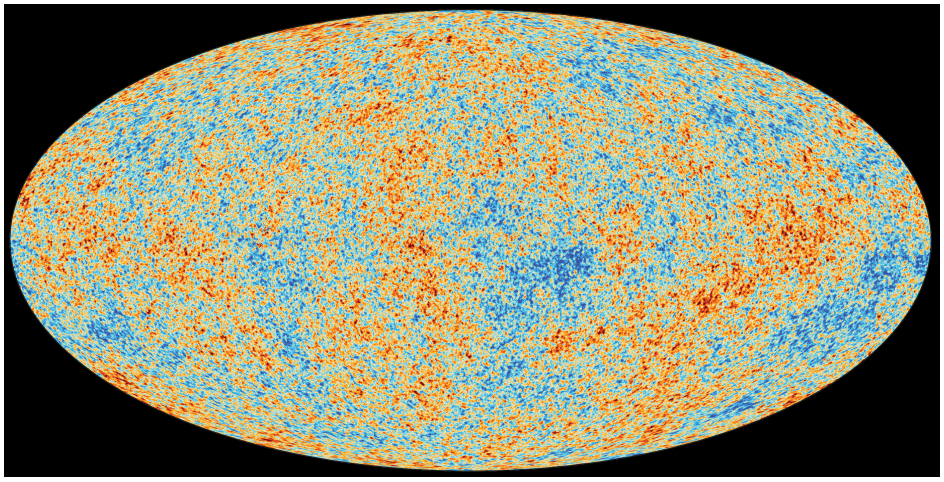

Figure A.7: Picture of the CMB sky from [14] with data from [15, 16]. The color gradient represents temperature. No scale is given, this is simply to illustrate the temperature anisotropies.

- $t \approx 370,000\,\mathrm{years} \rightarrow t \approx 100\,\mathrm{million\ years}$

The only light sources at this time were the relic CMB photons and small amounts of light released by neutral hydrogen, known as the **21 centimeter line**. This period is known as the **Dark Ages**

- $t \approx 100\,\text{million years} \rightarrow t \approx 1\,\text{billion years}$

  Large structures (stars, galaxies, clusters) begin to form from gravitational collapse.

- $t \approx 10\,\text{billion years}$

  The energy density in the universe due to matter has now dropped below that of dark energy (see Fig. A.5), and consequently the universe is now expanding at an accelerated rate (see Fig. A.3).

This ends the thermal history of the universe, as it pertains to this thesis. We have learned that we live in a nearly flat universe ($\Omega_0 \approx 1$) and that the energy density is dominated by dark energy ($\Omega_\Lambda \approx 0.7$), with a matter content of $\Omega_m \approx 0.3$. Most important for the remainder of this thesis, is that the of the measured matter density, only $\sim 5\%$ of it is understood. The rest of this chapter is dedicated to what we do know about the missing dark matter.

Appendix B

TES Energy Resolution Derivation

Given that we know the intrinsic noise sources of a TES and understand the dynamics, we can estimate the expected energy resolution. For a known noise and pulse template shape, the optimal resolution is achieved with the 'matched filter', also often called an 'optimum filter' [76, 93].

The expected power pulse shape $p(\omega)$ in will depend on the type of detector. If the TES is directly measuring a photon, than the pulse shape will simply be a dirac-delta impulse of energy, with some efficiency factor for absorption. If operated as the sensor in a thermal (athermal) calorimeter, the the pulse shape can be approximated by

$$p(\omega) = \frac{\varepsilon}{1 + i\omega\tau_{ph}}, \tag{B.1}$$

where ε is an efficiency factor accounting for energy losses, and τ_{ph} is the time scale for collecting the thermal (athermal) phonons. The nature of the excitation for our purpose will be athermal phonons as will be discussed in later chapters, but the framework is the same regardless of thermal or athermal excitations.

Using an Optimum Filter with known pulse shape, the theoretical resolution of a TES is given by

$$\sigma^2 = \left[\int_0^\infty \frac{d\omega}{2\pi} \frac{4|p(\omega)|^2}{S_{P_{tot}}(\omega)}\right]^{-1} \tag{B.2}$$

previously, we derived the total input power referred noise spectrum in Eq. 2.91, with constituent components of

$$S_{V_{TES}} = 4k_B T_0 R_0(1 + 2\beta) \tag{B.3}$$
$$S_{V_\ell} = 4k_B T_\ell R_\ell \tag{B.4}$$
$$S_{P_{TFN}} = 4k_B T_0^2 G F(T_0, T_{\text{bath}}) \tag{B.5}$$

In principle, in a well designed experiment the SQUID noise can be made negligible and we can thus ignore the $S_{I_{\text{SQUID}}}$ term. Also, to make the result more general, we can include a 'power-like' parasitic source $S_{P_{\text{par}}}$ that presents like excess TFN. We can thus change the expression to $S_{P_{TFN}} \rightarrow S_{P_{\text{TFN-like}}} = S_{P_{TFN}} + S_{P_{\text{par}}}$. Lastly, we assume the value of the inductance is small, and we thus ignore L. We insert these changes and re-arrange the expression into pole-zero form

$$S_{P_{tot}}(\omega) = S_{P_{TFN}} + \frac{I_0^2}{\mathscr{L}^2}\left[S_{V_{TES}}(1+\omega^2\tau^2) + \underbrace{S_{V_\ell}(\mathscr{L}-1)^2\left(1+\omega^2\tau^2\frac{1}{(1-\mathscr{L})^2}\right)}_{B}\right] \tag{B.6}$$

We next simplify the second term in the expression labeled 'B' above.

$$B \equiv S_{V_\ell}(\mathscr{L}-1)^2\left(1+\omega^2\tau^2\frac{1}{(1-\mathscr{L})^2}\right) \tag{B.7}$$

$$\implies S_{V_\ell}\left((\mathscr{L}-1)^2+\omega^2\tau^2\right) \tag{B.8}$$

$$\implies S_{V_\ell}\left(\mathscr{L}^2-2\mathscr{L}+1+\omega^2\tau^2\right) \tag{B.9}$$

$$\implies S_{V_\ell}\mathscr{L}\left(\mathscr{L}-2\right)+S_{V_\ell}\left(1+\omega^2\tau^2\right) \tag{B.10}$$

Combing back with Eq. B.6, we get

$$S_{P_{tot}}(\omega) = S_{P_{\text{TFN-like}}} + \frac{I_0^2}{\mathscr{L}^2}\left[(S_{V_{TES}}+S_{V_\ell})(1+\omega^2\tau^2) + S_{V_\ell}\mathscr{L}\left(\mathscr{L}-2\right)\right] \tag{B.11}$$

$$S_{P_{tot}}(\omega) = S_{P_{\text{TFN-like}}} + \underbrace{S_{V_\ell}I_0^2\frac{\mathscr{L}-2}{\mathscr{L}}}_{X} + \underbrace{(S_{V_{TES}}+S_{V_\ell})\frac{I_0^2}{\mathscr{L}^2}}_{A}(1+\omega^2\tau^2) \tag{B.12}$$

$$S_{P_{tot}}(\omega) = S_{P_{\text{TFN-like}}} + X + A(1+\omega^2\tau^2) \tag{B.13}$$

$$S_{P_{tot}}(\omega) = S_{P_{\text{TFN-like}}} + X + A + \omega^2\tau^2 A \tag{B.14}$$

$$S_{P_{tot}}(\omega) = (S_{P_{\text{TFN-like}}} + X + A)\left(1 + \omega^2\tau^2 \frac{A}{S_{P_{\text{TFN-like}}} + X + A}\right) \tag{B.15}$$

We now calculate $X + A$,

$$X + A = S_{V_\ell} I_0^2 \frac{\mathscr{L} - 2}{\mathscr{L}} + (S_{V_{TES}} + S_{V_\ell}) \frac{I_0^2}{\mathscr{L}^2} \tag{B.16}$$

$$\implies \frac{I_0^2}{\mathscr{L}^2}\left(S_{V_{TES}} + S_{V_\ell}(\mathscr{L} - 1)^2\right) \tag{B.17}$$

Plugging this back into Eq. B.15,

$$\begin{aligned} S_{P_{tot}}(\omega) = &\left[S_{P_{\text{TFN-like}}} + \frac{I_0^2}{\mathscr{L}^2}\left(S_{V_{TES}} + S_{V_\ell}(\mathscr{L} - 1)^2\right)\right] \\ &\times \left[1 + \omega^2\tau^2 \frac{(S_{V_{TES}} + S_{V_\ell})\frac{I_0^2}{\mathscr{L}^2}}{S_{P_{\text{TFN-like}}} + \frac{I_0^2}{\mathscr{L}^2}\left(S_{V_{TES}} + S_{V_\ell}(\mathscr{L} - 1)^2\right)}\right] \end{aligned} \tag{B.18}$$

$$\begin{aligned} S_{P_{tot}}(\omega) = &\left[\underbrace{S_{P_{\text{TFN-like}}} + \frac{I_0^2}{\mathscr{L}^2}\left(S_{V_{TES}} + S_{V_\ell}(\mathscr{L} - 1)^2\right)}_{S_{P_{tot}}(\omega=0)}\right] \\ &\times \left[1 + \omega^2\,\tau^2 \underbrace{\frac{S_{V_{TES}} + S_{V_\ell}}{\frac{\mathscr{L}^2}{I_0^2} S_{P_{\text{TFN-like}}} + S_{V_{TES}} + S_{V_\ell}(\mathscr{L} - 1)^2}}_{\tau_*^2}\right] \end{aligned} \tag{B.19}$$

$$S_{P_{tot}}(\omega) = S_{P_{tot}}(\omega = 0)\left(1 + \omega^2\tau_*^2\right) \tag{B.20}$$

We can now consider how this impacts our energy resolution in Eq. B.2. Using the power pulse from Eq. B.1 and the noise PSD in Eq. B.20, Eq. B.2 becomes

$$\sigma^2 = \left[\frac{\varepsilon^2}{S_{P_{tot}}(\omega = 0)} \underbrace{\int_0^\infty d\omega \frac{2}{\pi} \frac{1}{(1 + \omega^2\tau_{ph}^2)(1 + \omega^2\tau_*^2)}}_{\frac{1}{\tau_{ph} + \tau_*}}\right]^{-1} \tag{B.21}$$

$$\sigma^2 = \frac{1}{\varepsilon^2} S_{P_{tot}}(0)\left(\tau_{ph} + \tau_*\right) \tag{B.22}$$

We note the introduction of a new time constant τ_*, which we will now simplify.

$$\tau_*^2 = \tau^2 \frac{S_{V_{TES}} + S_{V_\ell}}{\frac{\mathscr{L}^2}{I_0^2} S_{P_{\text{TFN-like}}} + S_{V_{TES}} + S_{V_\ell}(\mathscr{L}-1)^2} \tag{B.23}$$

$$= \tau^2 \frac{4k_B T_0 R_0(1+2\beta) + 4k_B T_\ell R_\ell}{\frac{\mathscr{L}^2}{I_0^2} 4k_B T_0^2 G F(T_0, T_{\text{bath}}) \left(1 + \frac{S_{P_{\text{par}}}}{S_{P_{\text{TFN}}}}\right) + 4k_B T_0 R_0(1+2\beta) + 4k_B T_\ell R_\ell(\mathscr{L}-1)^2} \tag{B.24}$$

$$= \tau^2 \frac{(1+2\beta) + \frac{T_\ell}{T_0}\frac{R_\ell}{R_0}}{\frac{\mathscr{L}^2}{I_0^2 R_0} T_0 G F(T_0, T_{\text{bath}}) \left(1 + \frac{S_{P_{\text{par}}}}{S_{P_{\text{TFN}}}}\right) + (1+2\beta) + \frac{T_\ell}{T_0}\frac{R_\ell}{R_0}(\mathscr{L}-1)^2} \tag{B.25}$$

We use the fact that

$$I_0^2 R_0 = P_0 = \frac{\mathscr{L} G T_0}{\alpha}, \quad \text{and} \quad \mathscr{L} = \alpha \frac{\left(1 - \frac{T_{\text{bath}}^n}{T_0^n}\right)}{n} \tag{B.26}$$

$$\implies P_0 = \frac{G T_0}{n}\left(1 - \frac{T_{\text{bath}}^n}{T_0^n}\right) \tag{B.27}$$

Substituting this into the above equation we get

$$\tau_*^2 = \tau^2 \frac{1 + 2\beta + \frac{T_\ell}{T_0}\frac{R_\ell}{R_0}}{\frac{\alpha^2}{n} F(T_0, T_{\text{bath}}) \left(1 - \frac{T_{\text{bath}}^n}{T_0^n}\right)\left[1 + \frac{S_{P_{\text{par}}}}{S_{P_{TFN}}}\right] + 1 + 2\beta + \frac{T_\ell}{T_0}\frac{R_\ell}{R_0}(\mathscr{L}-1)^2}. \tag{B.28}$$

Let us factor out the T_ℓ/T_0 term and define

$$Y \equiv \frac{\alpha^2}{n}\frac{T_0}{T_\ell} F(T_0, T_{\text{bath}}) \left(1 - \frac{T_{\text{bath}}^n}{T_0^n}\right)\left[1 + \frac{S_{P_{\text{par}}}}{S_{P_{TFN}}}\right]. \tag{B.29}$$

Our definition of τ_* becomes,

$$\tau_*^2 \approx \tau^2 \frac{1 + 2\beta + \frac{R_\ell}{R_0}}{Y + 1 + 2\beta + \frac{R_\ell}{R_0}(\mathscr{L}-1)^2}. \tag{B.30}$$

This can be expressed in terms of τ_{ETF}^2. Squaring Eq. 2.53 and dropping second order terms in β and R_ℓ/R_0, (since these are both ideally quite small, however in practice this is

not always the case) and keeping only higher order terms in $\mathscr{L}$ (since loopgain should be large), we can write

$$\tau_{\mathrm{ETF}}^2 \approx \tau^2 \frac{1+2\beta+2\frac{R_\ell}{R_0}+\mathcal{O}\left(\beta^2,\frac{R_\ell}{R_0}^2\right)}{1+2\beta+2\frac{R_\ell}{R_0}+\left(1-2\frac{R_\ell}{R_0}\right)\mathscr{L}^2+\mathcal{O}\left(\beta^2,\frac{R_\ell}{R_0}^2\right)} \tag{B.31}$$

Pulling out a factor of τ_{ETF}, we can write τ_* as

$$\tau_*^2 \approx \tau_{\mathrm{ETF}}^2 \frac{1}{\frac{Y+\mathscr{L}^2}{1+2\beta+2\frac{R_\ell}{R_0}+\left(1-2\frac{R_\ell}{R_0}\right)\mathscr{L}^2}+1} \tag{B.32}$$

$$\tau_*^2 \approx \tau_{\mathrm{ETF}}^2 \frac{1+2\beta+2\frac{R_\ell}{R_0}+\left(1-2\frac{R_\ell}{R_0}\right)\mathscr{L}^2}{Y+\mathscr{L}^2}. \tag{B.33}$$

Assuming the loopgain is large ($\mathscr{L} \gg 1$), and beta is small $\beta, R_\ell/R_0 < 1$, this becomes

$$\tau_*^2 \approx \tau_{\mathrm{ETF}}^2 \frac{\mathscr{L}^2}{Y+\mathscr{L}^2}. \tag{B.34}$$

$$\tau_*^2 \approx \tau_{\mathrm{ETF}}^2 \frac{\frac{\alpha^2}{n^2}\left(1-\frac{T_{\mathrm{bath}}^n}{T_0^n}\right)^2}{Y+\frac{\alpha^2}{n^2}\left(1-\frac{T_{\mathrm{bath}}^n}{T_0^n}\right)^2}. \tag{B.35}$$

Plugging back in our definition for Y, this becomes

$$\tau_*^2 \approx \tau_{\mathrm{ETF}}^2 \frac{1}{\frac{T_0}{T_\ell} nF(T_0,T_{\mathrm{bath}})\left[1+\frac{S_{P_{\mathrm{par}}}}{S_{P_{TFN}}}\right]\left(1-\frac{T_{\mathrm{bath}}^n}{T_0^n}\right)^{-1}+1}. \tag{B.36}$$

$$\tau_*^2 \approx \tau_{\mathrm{ETF}}^2 \frac{T_\ell}{T_0} \frac{\left(1-\frac{T_{\mathrm{bath}}^n}{T_0^n}\right)}{nF(T_0,T_{\mathrm{bath}})\left[1+\frac{S_{P_{\mathrm{par}}}}{S_{P_{TFN}}}\right]}. \tag{B.37}$$

$$\tau_* \approx \tau_{\mathrm{ETF}} \sqrt{\frac{T_\ell}{T_0} \frac{\left(1-\frac{T_{\mathrm{bath}}^n}{T_0^n}\right)}{nF(T_0,T_{\mathrm{bath}})\left[1+\frac{S_{P_{\mathrm{par}}}}{S_{P_{TFN}}}\right]}}. \tag{B.38}$$

Combining this back to the energy variance result in Eq. B.22, we finally arrive at

$$\sigma^2 = \frac{1}{\varepsilon^2} S_{P_{tot}}(0) \left(\tau_{ph} + \tau_{\mathrm{ETF}} \sqrt{\frac{T_\ell}{T_0} \frac{\left(1 - \frac{T_{\mathrm{bath}}^n}{T_0^n}\right)}{nF(T_0, T_{\mathrm{bath}}) \left[1 + \frac{S_{P_{\mathrm{par}}}}{S_{P_{TFN}}}\right]}} \right), \tag{B.39}$$

where

$$S_{P_{tot}} = S_{P_{\mathrm{TFN}}} + S_{P_{\mathrm{par}}} + \frac{I_0^2}{\mathscr{L}^2} \left(S_{V_{TES}} + S_{V_\ell} (\mathscr{L} - 1)^2 \right). \tag{B.40}$$

It is interesting the note that the addition of an excess TFN-like power noise will actually slightly decrease the effective falltime. However, this effect on the overall baseline energy variance will be much smaller than the increase in $S_{P_{tot}}(0)$ that an excess TFN-like power noise would add. This false increase in bandwidth can also be used as a diagnostic tool when looking at excess noise.

Appendix C

TES Response to Square Wave Impulse

In this appendix, the TES response to a small amplitude square wave voltage source is derived. Note, this was written my first summer as a grad student, so the some of the explanations may be a bit basic. Recall that the complex impedance of a TES in the low inductance limit can be written as

$$Z(\omega)_{tot} = \frac{\partial I_{TES}}{\partial V_b}(\omega)^{-1} = R_L + i\omega L + Z(\omega)_{TES}, \tag{C.1}$$

where $Z(\omega)_{TES}$ is defined as

$$Z(\omega)_{TES} = R_0(1+\beta) + \frac{R_0\mathscr{L}}{1-\mathscr{L}}\frac{(2+\beta)}{1+i\omega\frac{C}{G(1-\mathscr{L})}}. \tag{C.2}$$

To understand how the TES responds to a test input, we can place a small voltage excitation (δV_b) down the QET bias line and measure the change in current though the TES (δI_{TES}). We thus arrive at,

$$\frac{\delta I(\omega)_{TES}}{\delta V_b(\omega)} = \frac{\partial I_{TES}}{\partial V_b}(\omega), \tag{C.3}$$

which can be rearranged to

$$\delta I(\omega)_{TES} = \frac{\partial I_{TES}}{\partial V_b}(\omega)\delta V_b(\omega), \tag{C.4}$$

where $\frac{\partial I_{TES}}{\partial V_b}(\omega)$ is defined as the inverse of Eq. **??**.

A square wave is used for the voltage excitation, . If the period is much larger than the fall time of the TES, then $\delta V_b(\omega)$ can be modeled as a step function $\mathcal{H}(t-t_0)$ multiplied by

an amplitude factor δV_{pp}. This step function must be transformed into Fourier space to be used in Eq. . To do this, recall that the Fourier transform of a Dirac delta function is

$$\mathcal{F}[\delta(t-t_0)] = \int_{-\infty}^{\infty} e^{-i\omega t}\delta(t-t_0)dt = e^{-i\omega t_0}. \tag{C.5}$$

We know that a step function is defined as such

$$\mathcal{H}(t-t_0) = \int_{-\infty}^{t} \delta(t'-t_0)dt'. \tag{C.6}$$

We can substitute in the inverse Fourier transform of the result of Eq. C.5 into the delta function in Eq. C.6

$$\mathcal{H}(t-t_0) = \int_{-\infty}^{t} \mathcal{F}^{-1}[\delta(t'-t_0)]dt' = \mathcal{H}(t-t_0) = \int_{-\infty}^{t} \Big[\int_{-\infty}^{\infty} \frac{d\omega}{2\pi} e^{i\omega(t'-t_0)}\Big]dt'. \tag{C.7}$$

Simplifying,

$$\mathcal{H}(t-t_0) = \int_{-\infty}^{\infty} \frac{d\omega}{2\pi} e^{-i\omega t_0} \int_{-\infty}^{t} e^{i\omega t'}dt' = \int_{-\infty}^{\infty} \frac{d\omega}{2\pi} e^{-i\omega t_0}\Big[\frac{1}{i\omega}e^{i\omega t'}\Big]\Big|_{-\infty}^{t} = \int_{-\infty}^{\infty} \frac{d\omega}{2\pi}\frac{e^{-i\omega t_0}}{i\omega}e^{i\omega t}, \tag{C.8}$$

where $e^{i\omega t'}$ goes to zero in the limit that t' goes to negative infinity, as it is periodic and averages to zero. In doing the contour integral, it is clear that the the $i\omega$ pole will be directly on the integration loop. We must therefore shift the pole by amount ε such that the pole is in the loop. Eq. C.8 then becomes

$$\mathcal{H}(t-t_0) = \lim_{\varepsilon\to 0}\int_{-\infty}^{\infty} \frac{d\omega}{2\pi} e^{i\omega t}\frac{e^{-i\omega t_0}}{i[\omega - i\varepsilon]} = \mathcal{F}^{-1}\Big[\lim_{\varepsilon\to 0}\frac{e^{-i\omega t_0}}{i[\omega - i\varepsilon]}\Big]. \tag{C.9}$$

Thus,

$$\mathcal{H}(\omega) = \mathcal{F}[\mathcal{H}(t-t_0)] = \lim_{\varepsilon\to 0}\frac{e^{-i\omega t_0}}{i[\omega - i\varepsilon]} \tag{C.10}$$

For the case where $t_0 = 0$, the voltage jitter becomes,

$$\delta V_b(\omega) = \lim_{\varepsilon\to 0}\frac{1}{i[\omega - i\varepsilon]}\delta V_{pp} \tag{C.11}$$

The next step in determining the impulse response of the TES is to put $\frac{\partial I_{TES}}{\partial V_b}(\omega)$ in pole-zero form.

$$\frac{\partial I_{TES}}{\partial V_b}(\omega) = \frac{1}{Z(\omega)_{TES}} = \Big(R_L + i\omega L + R_0(1+\beta) + \frac{R_0\mathscr{L}}{1-\mathscr{L}}\frac{(2+\beta)}{1+i\omega\frac{C}{G(1-\mathscr{L})}}\Big)^{-1} \tag{C.12}$$

Multiplying top and bottom by $(1 + i\omega\frac{C}{G(1-\mathscr{L})})$, we get

$$\frac{\partial I_{TES}}{\partial V_b}(\omega) = \frac{1 + i\omega\frac{C}{G(1-\mathscr{L}}}{(R_L + R_)(1+\beta) + i\omega L)(1 + i\omega\frac{C}{G(1-\mathscr{L})}) + \frac{R_O\mathscr{L}}{1-\mathscr{L}}(2+\beta)}. \tag{C.13}$$

Expanding and multiplying the top and bottom by $\frac{G(1-\mathscr{L})}{LC}$ we get,

$$\frac{\partial I_{TES}}{\partial V_b}(\omega) = \frac{-\frac{G(1-\mathscr{L})}{LC} - \frac{i\omega}{L}}{\omega^2 - \Big(\frac{G(1-\mathscr{L})}{C} + L(R_L + R_0(1+\beta))\Big)i\omega - \Big(\frac{G(1-\mathscr{L})}{LC}(R_l + R_0(1+\beta)) + \frac{R_0\mathscr{L}}{(1-\mathscr{L})}(2+\beta)\Big)}. \tag{C.14}$$

Factoring the numerator we get,

$$\frac{\partial I_{TES}}{\partial V_b}(\omega) = \frac{-\frac{i}{L}(\omega + \frac{G(1-\mathscr{L})}{LC})}{\omega^2 - \Big(\frac{G(1-\mathscr{L})}{C} + L(R_L + R_0(1+\beta))\Big)i\omega - \Big(\frac{G(1-\mathscr{L})}{LC}(R_l + R_0(1+\beta)) + \frac{R_0\mathscr{L}}{(1-\mathscr{L})}(2+\beta)\Big)}. \tag{C.15}$$

It is now clear that $\frac{\partial I_{TES}}{\partial V_b}(\omega)$ will have one zero and two poles and can thus be expressed in the general form

$$\frac{\partial I_{TES}}{\partial V_b}(\omega) = \frac{a(\omega - z)}{(\omega - P_1)(\omega - P_2)}. \tag{C.16}$$

The constant a, the zero, and two poles can be determined from Eq. C.15. The zero and a can simply be read off and completing the square of the denominator gives the poles,

$$a = -\frac{i}{L}, \tag{C.17}$$

$$z = \frac{G(1-\mathscr{L})}{LC}, \tag{C.18}$$

For simplicity, the time domain analysis will be continued from Eq. C.16, where the poles can be found simply by using the quadratic formula. Eq. C.16 and Eq. C.11 can be substituted into Eq. C.4 and it can be inverse Fourier transformed,

$$\delta I(t)_{TES} = \int_{-\infty}^{\infty} \frac{d\omega}{2\pi} \frac{\partial I_{TES}}{\partial V_b}(\omega)\mathcal{H}(\omega)e^{i\omega t} \tag{C.19}$$

$$\delta I(t)_{TES} = \lim_{\varepsilon\to 0}\int_{-\infty}^{\infty} \frac{d\omega}{2\pi} \frac{a'(\omega - z)}{(\omega - P_1)(\omega - P_2)} \frac{1}{i[\omega - i\varepsilon]} e^{i\omega t} \tag{C.20}$$

where $a' = a\delta V_{pp}$. From the residue theorem, we know that the solution to Eq. C.20 will be

$$\delta I(t)_{TES} = 2\pi i\Big[\sum_n R(P_n)\Big]. \tag{C.21}$$

$$R_{i\varepsilon} = \lim_{\varepsilon\to 0}\frac{1}{2\pi i}\frac{a(i\varepsilon - z)e^{i(i\varepsilon)t}}{(i\varepsilon - P_1)(i\varepsilon - P_2)} = \frac{1}{2\pi i}\frac{-az}{P_1P_2} \tag{C.22}$$

$$R_1 = \frac{1}{2\pi i}\frac{a(P_1 - z)e^{iP_1t}}{P_1(P_1 - P_2)} \tag{C.23}$$

$$R_2 = \frac{1}{2\pi i}\frac{a(P_2 - z)e^{iP_2t}}{P_2(P_2 - P_1)} \tag{C.24}$$

Thus, we arrive at

$$\delta I(t)_{TES} = a\Big(\frac{z}{P_1P_2} + \frac{(P_1 - z)}{P_1(P_1 - P_2)}e^{iP_1t} + \frac{(P_2 - z)}{P_2(P_2 - P_1)}e^{iP_2t}\Big). \tag{C.25}$$

Applying the boundary condition that for $t \le 0$, $\delta I(t)_{TES} = 0$, we get

$$\frac{z}{P_1P_2} = \frac{(P_1 - z)}{P_1(P_1 - P_2)} + \frac{(P_2 - z)}{P_2(P_2 - P_1)} \tag{C.26}$$

Plugging this back into Eq. C.25 results in

$$\delta I(t)_{TES} = a\Big(\frac{(P_1 - z)}{P_1(P_1 - P_2)}(e^{iP_1t} - 1) + \frac{(P_2 - z)}{P_2(P_2 - P_1)}(e^{iP_2t} - 1)\Big) \tag{C.27}$$

We can see that since our poles P_1 and P_2 are imaginary, Eq. C.27 will be a sum of two exponential functions. When one pole is much larger than the other, this means that one of time time constants of the exponentials will be very large, and the other time constant will be very small. This means that the function $\delta I(t)_{TES}$ will look like a step function decrease (very small time constant) and a slow exponential rise.

It is of interest to look at limiting cases of this expression. Taking the limit when t goes to infinity will give us the zero frequency signal level of the TES. For $P_2 \gg P_1$,

$$\lim_{t\to\infty}\delta I(t)_{TES} = -a\Big(\frac{(P_1 - z)}{P_1(P_1 - P_2)} + \frac{(P_2 - z)}{P_2(P_2 - P_1)}\Big) = -\frac{az}{P_1P_2}. \tag{C.28}$$

To understand the effect of the short time constant, which in turn will tell us about β, we need to look at the case of $\frac{i}{P_1} < t < \frac{i}{P_2}$, resulting in

$$\delta I\left(\frac{i}{P_1} < t < \frac{i}{P_2}\right)_{TES} = \frac{a(P_2 - z)}{P_2(P_2 - P_1)}. \tag{C.29}$$

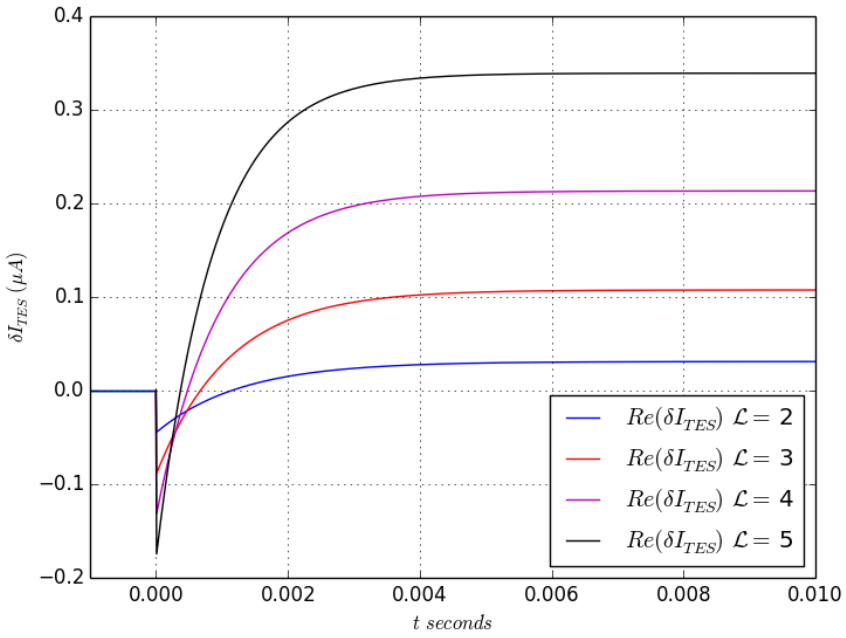

Figure C.1: Plot of $\delta I(t)_{TES}$ for various values of loop gain

Taking the absolute value of the ratio of Eq. C.29 to Eq. C.28 gives us the ratio of initial response peak to signal peak. Doing so results in the following,

$$\frac{\frac{a(P_2-z)}{P_2(P_2-P_1)}}{\frac{az}{P_1P_2}} = \frac{P_1(P_2-z)}{z(P_2-P_1)}. \tag{C.30}$$

In the limit that $P_2 >> P_1$ and $P_2 >> z$, this becomes

$$\left|\frac{P_1}{z}\right| \tag{C.31}$$

From this point on, let us refer to P_2 as P_L and P_1 as P_{eff}. We note that the justification for $P_L >> P_{eff}$ is for the limit of the inductor L being very small. In the limit of Small L, P_{eff} becomes:

A plot δI as a function of Loop gain $\mathscr{L}$, using standard TES parameters from this thesis, can is shown in Fig. C.1.

Appendix D

Design of Cryogenic Electronics

For all electronics going into the fridge, there are two important factors to consider: the noise contributions and the power dissipated. There are of course second order design factors like parasitic resistance/inductance, and cross-talk, but these can be designed away.

The cooling powers of all stages of the DR are given in Table D.1.

	4K	Still	Cold Plate	Mixing Chamber
P_{cool}	1.5 W	1 mW	10 μW	1 μW
T	4K	850 mK	150 mK	10 mK

Table D.1: New fridge cooling power

D.1 Noise Modeling

The CDMS II FEB's have been used for decades at this point, and their noise performance is discussed in numerous papers [141]. The noise floor of the SQUIDs is limited to roughly $2.5\,\mathrm{pA}/\sqrt{\mathrm{Hz}}$ (when referenced to the TES), which sets the lower limit on noise performance of our system. To ensure that this limit is reached, we need to choose the temperature stage to place the SQUID feedback amplifier's feedback resistor and the shunt resistor such that their Johnson noise is less than the SQUID noise.

D.1.1 SQUID Feedback Resistor

We model the the CDMS II FEB SQUID amplifier as a standard feedback network (see Fig. D.1), where A_{OL} is the combination of all the amplifiers in the FB loop, and β is the ratio of signal feed back into the system, $\beta = Z_{FB}/R_{FB}$. For the trans-impedance of the SQUIDS we use the following values, $Z_{TES} = 800\ \Omega$ and $Z_{FB} = 80\ \Omega$.

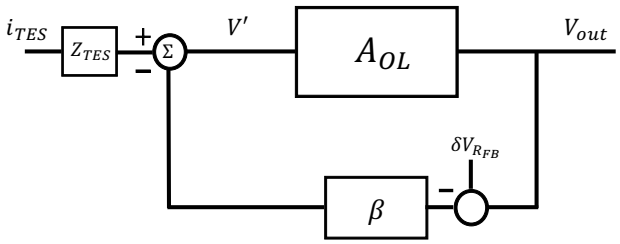

Figure D.1: Simplified model of SQUID feedback loop.

We now consider a noise source $\delta V_{R_{FB}}$ after the β component, which is simply the Johnson noise of the feedback resistor at temperature T_{FB}

$$\delta V_{R_{FB}}^2 = 4k_{bT}R_{FB}T_{FB}. \tag{D.1}$$

We now propagate the noise source $\delta V_{R_{FB}}$ through the FB loop.

$$\left.\begin{array}{l} V_{out} = V'A_{OL} + \delta V_{R_{FB}} \\ V' = \delta V_{R_{FB}}\beta \end{array}\right\} \implies V_{out} = V_{R_{FB}}(1 + \beta A_{OL}) \tag{D.2}$$

We can now reference this to the equivalent input current using the total gain of the FB loop,

$$G_{FB} = \frac{A_{OL}}{1 + \beta A_{OL}} Z_{TES} \tag{D.3}$$

$$\delta i_{R_{FB}}^{TES} = \frac{V_{out}}{G_{FB}} = \frac{(1 + \beta A_{OL})^2}{A_{OL}Z_{TES}} \delta V_{R_{FB}} \tag{D.4}$$

The open loop gain of the FEB, A_{OL} ranges between $226 - 5658$. We can model the noise of the feedback resistor for various values of R_{FB} as a function of temperature for across the two limits of the FEB open-loop feedback gain. A plot of this model is shown in Fig. D.2

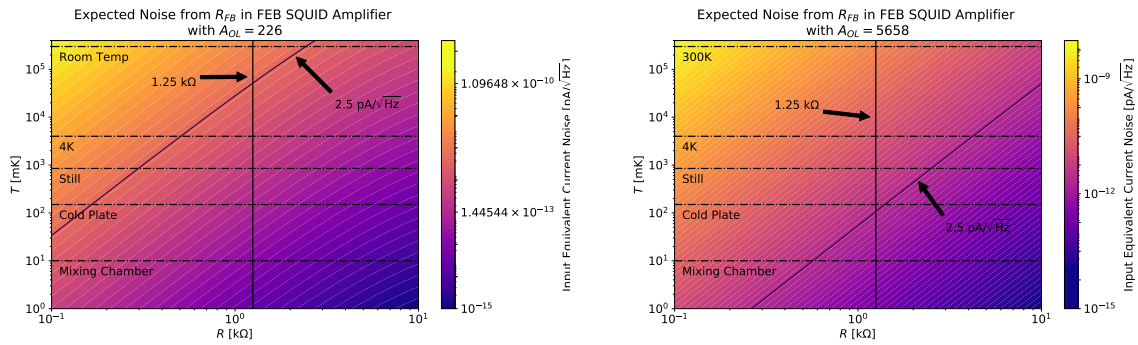

Figure D.2: Input reference current noise of the Johnson noise of the feedback resistor as a function of R_{FB} and temperature for the minimum/maximum values of A_{OL} (left/right). Shown is the current value of the feedback resistor of 1.25 kΩ as well as the available temperature stages. Also shown is the the contour corresponding to 2.5 pA/$\sqrt{\text{Hz}}$.

For the nominal value of $R_{FB} = 1.25\,\text{k}\Omega$, we can see that when the amplifier is operated with the maximum open-loop gain, then the feedback resistor must be placed on the cold plate ($\sim 100\,\text{mK}$) in order to meet the noise requirements. However, for lower feedback gains, we could easily get away with placing the feedback resistor on the 4K plate.

D.1.2 TES Shunt Resistor

The noise contribution from the shunt resistor was modeled in chapter 2. As long as the parasitic resistances R_p are kept low, this noise term can be made negligible as long as it sufficiently cold.

D.2 Heat Loads

D.2.1 SQUID Feedback Resistor

To estimate the power through the feedback resistor, we first relate the current through R_{FB} to the input current in the TES. Recall that the output voltage of the FB loop in Fig. D.1 is,

$$V_{out} = \frac{A_{OL}}{1+\beta A_{OL}} Z_{TES}\ I_{TES} \tag{D.5}$$

$$\approx \frac{Z_{TES}}{\beta}\ I_{TES} \tag{D.6}$$

$$\implies \frac{Z_{TES}}{Z_{FB}} R_{FB}\ I_{TES} \tag{D.7}$$

$$\implies 10 R_{FB}\ I_{TES} \tag{D.8}$$

Thus the current through the feedback resistor is simply 10 times the current through the TES. For the MELANGE devices, we would expect a TES current of roughly a few μA

$$P_{R_{FB}} \approx (10 i_{TES})^2 R_{FB} \approx .5\ \mu\text{W} \tag{D.9}$$

For 12 channels, this would be $\approx 6\ \mu$W. Similarly, for 12 CPD-like detectors, we would have about 150μW of power loading.

From a power loading perspective, placing the feedback resistors on the CP would be problematic. We thus made the compromise to place the feedback resistor on the 4K plate.

D.2.2 TES Shunt Resistor

Given the Joule heating of the TES, we can calculate the power dissipated by the shunt resistance via,

$$\left.\begin{aligned} P_{TES} &= \frac{V^2}{R_{TES}} \\ P_{shunt} &= \frac{V^2}{R_{shunt}} \end{aligned}\right\} \implies P_{shunt} = \frac{P_{TES} R_{TES}}{R_{shunt}}. \tag{D.10}$$

Plugging in approximate values for the MALANGE and CPD-like devices, this gives anywhere from $2 - 50\,$pW per detector. Compared to the cooling powers of the DR, placing these on any stage should be fine.

D.2.3 SQUID Arrays

Lastly, we consider the power load from the biasing of the SQUID arrays. We have the following properties for the each CDMSII SQUID array

R_{shunt}	N_{SQUID}	V_{SQUID}
2 Ω	100	50 μV

Table D.2: SQUID array parameters

This gives a heat load per SQUID array of

$$P = N_{SQUID}\frac{V_{SQUID}^2}{R_{shunt}} = 0.125 \text{ pW}. \tag{D.11}$$

To operate 12 channels at a time, this gives 1.5 pW of power dissipated by the SQUID arrays. Like the shunt resistors, this power is negligible compared with the cooling power of the fridge. However, when zapping the SQUIDs, or if a SQUID lost lock and went into a possitive feedback loop, this could cause significant warming of the fridge if they were put on the mixing chamber.

D.3 Wiring Layout

From noise considerations and power loading, we have learned the following:

- The SQUID feedback resistor must go on the 4K plate.
- Shunt resistors should be placed on CP or MC.
- SQUID arrays can be placed on CP or Still.

Since placing the SQUIDs on a colder temperature stage would have the best noise performance, we chose to place them on the CP. And due to difficulty in logistically placing the shunt resistors on the MC with the detectors, it was decided to place the shunt resistors on the same PCB as the SQUIDs.

D.3.1 Wiring

In order to push to lower energy thresholds, it is necessary to operate at much lower TES resistances. To remain in the strong ETF limit, this requires small load resistances. All of this necessitates having minimal parasitic resistances on the TES bias lines. All wiring used in the fridge is in the form of NbTi PhBr weaves, such that all wiring is superconducting below 4K. The remaining source of parasitic resistance is from the connection points. We decided on using Micro-D style connectors, which typically have about $1 - 2\,\text{m}\Omega$ of contact resistance per pin. To reduce this contact resistance further, we deiced to double up pins for the TES lines, reducing the contact resistance in half. In order to reduce cross-talk, ground lines were placed between channels in the wiring weave. The channel mapping at the face of the micro-D connector can be see in Fig. D.3.

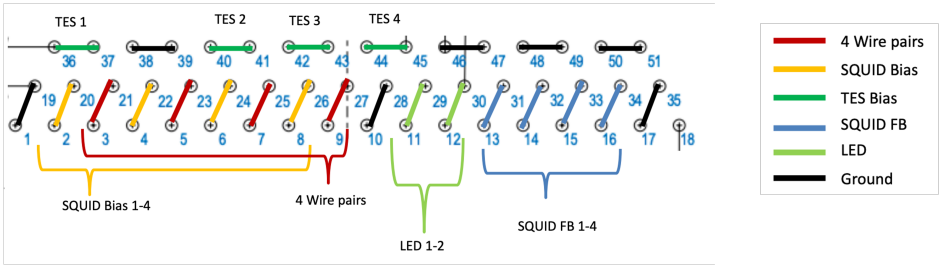

Figure D.3: Channel layout in the cryogenic wiring weaves.

D.4 PCB Designs

In total the wiring design required 4 PCB to be designed. One set of PCBs and wiring allow 4 TES channels to be operated. Additionally, optional wiring was included to perform 4-wire measurements of the TES shunt resistors. A schematic of location of the PCBs and wiring can be seen in Fig. D.4.

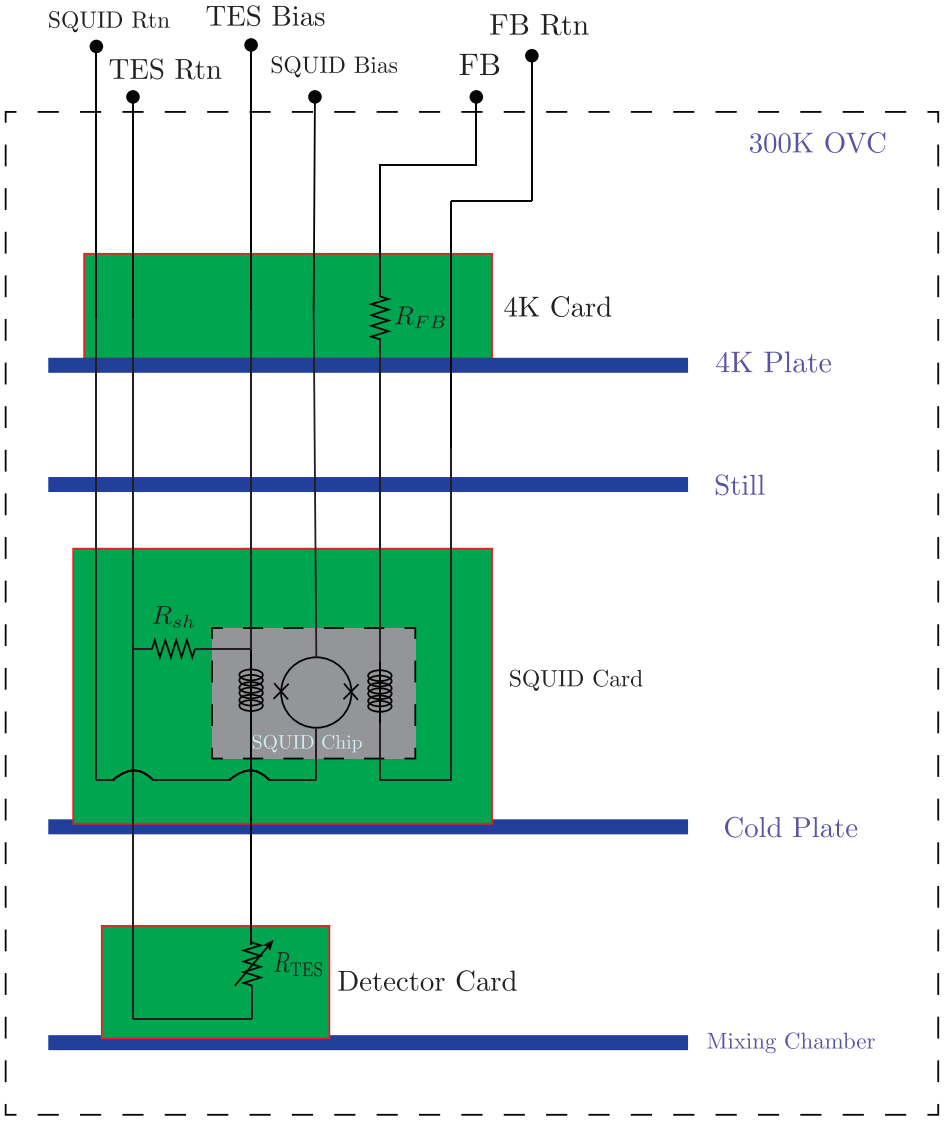

Figure D.4: Schematic model of wiring in fridge showing the various cryogenic electronic components and the corresponding PCB cards.

- **300K Card**
  - 50 pin DSUB connector to 51 pin Micro-D
  - Maps the CDMSII FEB channel to UCB Cryo wiring
  - Optional routing to be compatible with the SuperCDMS DCRC
  - Located inside directly inside e-stem.
- **4K Card**

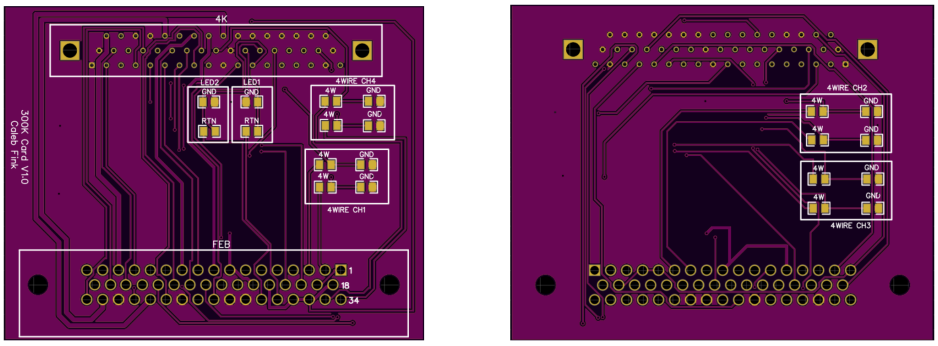

Figure D.5: Image of the design of the 300K PCB.

- 51 pin Micro-D to 51 pin Micro-D
- Holds the SQUID amp feedback resistors
- Located on 4K plate

- **SQUID Card**
  - 51 pin Micro-D to 25 pin Micro-D
  - Holds the CDMSII SQUIDs and the TES shunt resistors
  - Located on the cold plate

- **Detector Card (DIB)**
  - 25 pin Micro-D
  - 4 TES channels, 2 LED channels
  - Located on Mixing Chamber

D.4.1 300K Card

The primary function of the 300K card is to route the channel mapping from the FEB or SuperCDMS DCRC to the channel mapping we used inside the UCB fridge. The LED return/grounding scheme changed between the FEB and DCRC, so there are optional jumper on the 300K card that can be moved depending on which readout is being used. Additionally if a 4-wire measurement of the TES shunt resistors is to be done, there are more jumpers that can be placed on this card to change from standard readout, to 4-wire readout. An image of the can can be seen in Fig. D.5.

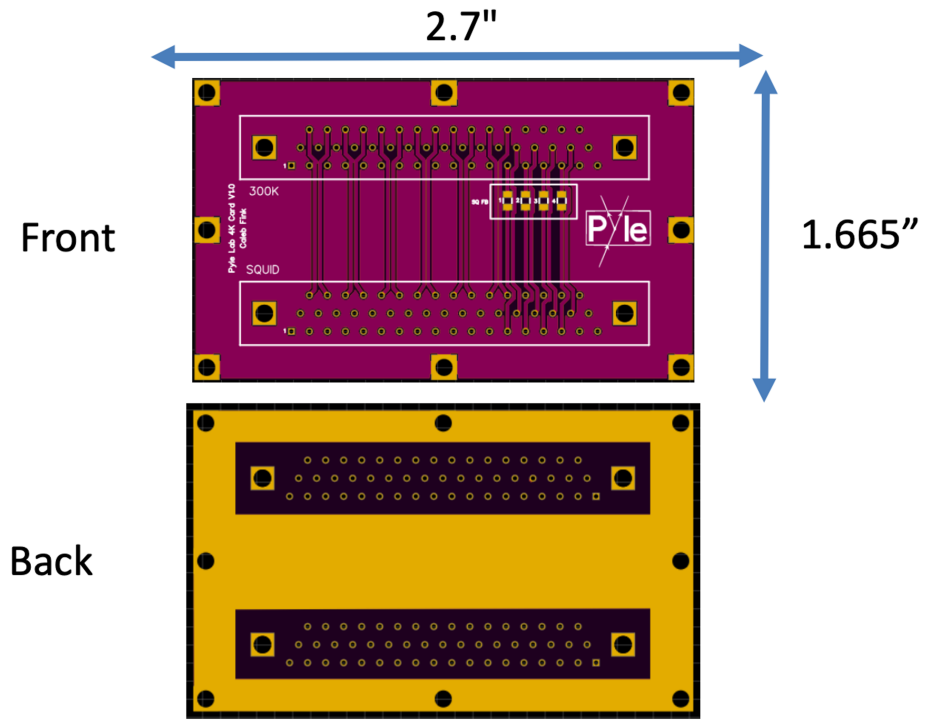

Figure D.6: Image of the design of the 300K PCB.

D.4.2 4K Card

The 4K card is the simplest of the PCBs in the fridge. It's only purpose is to help thermalize the wiring, and holds the SQUID amp feedback resistors. It consists of a 6 layer board, with full copper ground planes on the outer layers. All twisted pairs in the cabling are kept as close pairs on the PCB, and sensitive lines are separated by internal ground planes. An image of the PCB can be seen in Fig. D.6. In order to thermalize the PCB, it was placed in a copper housing and securely bolted to the 4K plate. @ add pic @

D.4.3 SQUID Card

The SQUID card consists of a 4 layer board with SQUID Bias and TES lines separated by the SQUID FB lines via and internal ground plane. To reduce the parasitics on the SQUID Bias and TES lines, they were left as exposed Cu, and were later coated in solder to make the superconducting. A diagram of the PCB can be seen in Fig. D.7.To help with thermalization the board was gold-plated with a nickel-less process to ensure there were no stray magnetic fields near the SQUIDs. To thermalize the board and SQUID arrays the board was mounted vertically in a Cu housing. To Shield the SQUIDs from stray magnetic fields, an Aluminum box was fabricated that can be slid over the SQUID arrays. The Housing, Al shield, and close up of the mounted SQUIDs can be seen in Fig. D.8

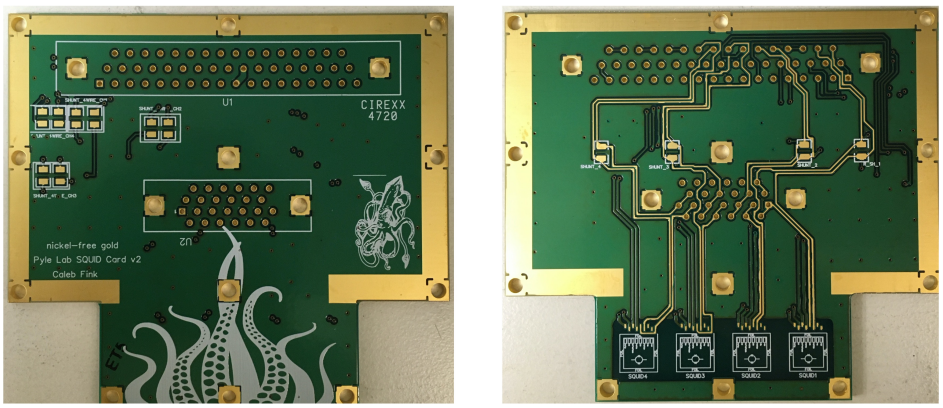

Figure D.7: Image of the front (left) and back (right) of the SQUID PCB.

The SQUIDs were mounted to the board in the following manner:

1. the Micro-D connectors are soldered to the board (note: it is important that this step be done BEFORE the SQUIDs are placed on the board so as not to heat up the SQUIDs too much and degrade thier performance)
2. a piece of superconducting Nb foil was epoxied to the PCB
3. Four SQUIDs were then epoxied with single dot of epoxy to the Nb foil
4. the SQUIDs were wire-bonded to pads on the PCB

D.4.4 Detector Card (DIB)

For the detector housing, we re-purposed CMDSII Cu 'hex' style housings. We created a new opening and silver epoxied a straight angle 25-pin micro-D connector into the opening, making the housing a Faraday cage. The PCB is screwed vertically to the housing for thermalization and soldered to the micro-D pins. Since the DIB is mounted perpendicular to the detector holders, castellated holes[1] are used for the bond pads. Similar to the SQUID card, the DIB was plated with a nickle-less gold, and the signal lines were left exposed so that they could be solder coated. A picture of the DIB, a schematic of the housing, and a picture of a DIB mounted in a housing are shown in Fig. D.9.

@ show thermal wiring diagram

@ talk about different PCBs

[1]Castellated holes are essentially plated through holes on the edge of the PCB that have been cut in half.

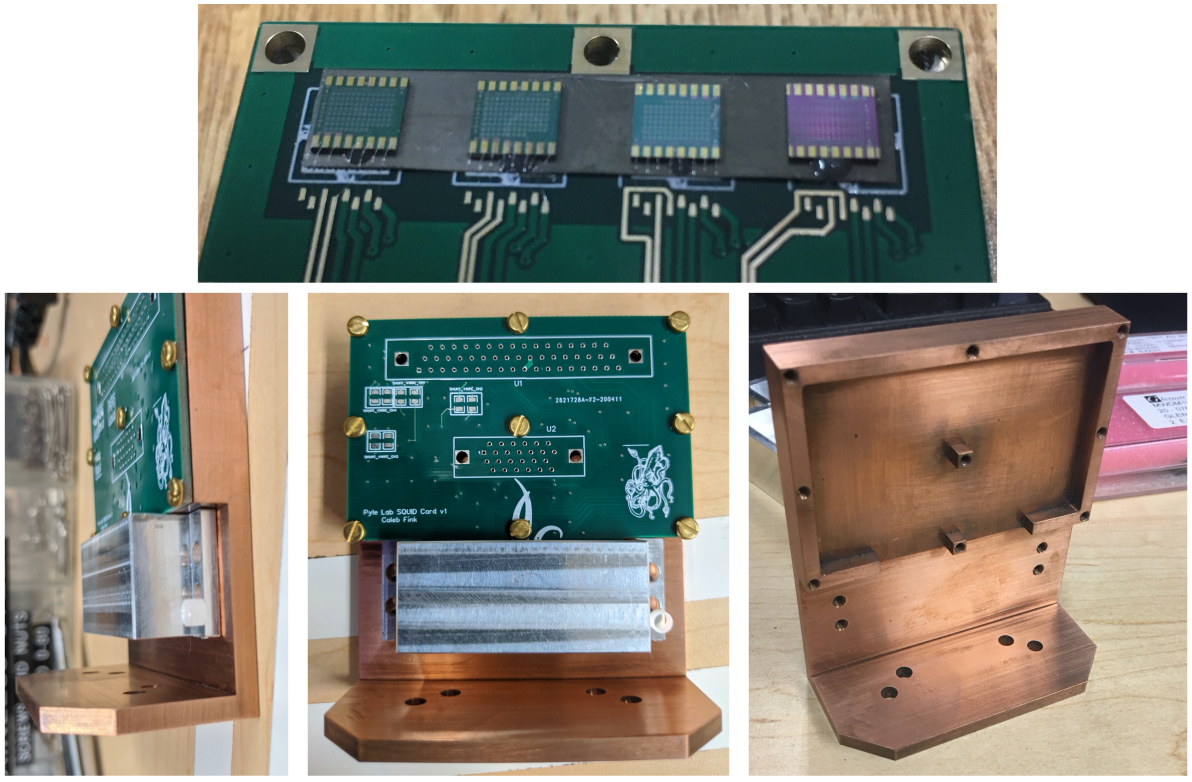

Figure D.8: Clockwise from top: Close up of SQUID arrays epoxied onto Nb foil on SQUID PCB, Cu housing for SQUID PCB, SQUID card mounted to Cu housing with SC Al SQUID shield in place, Side view of SQUID card mounted to Cu housing with SC Al SQUID shield in place.

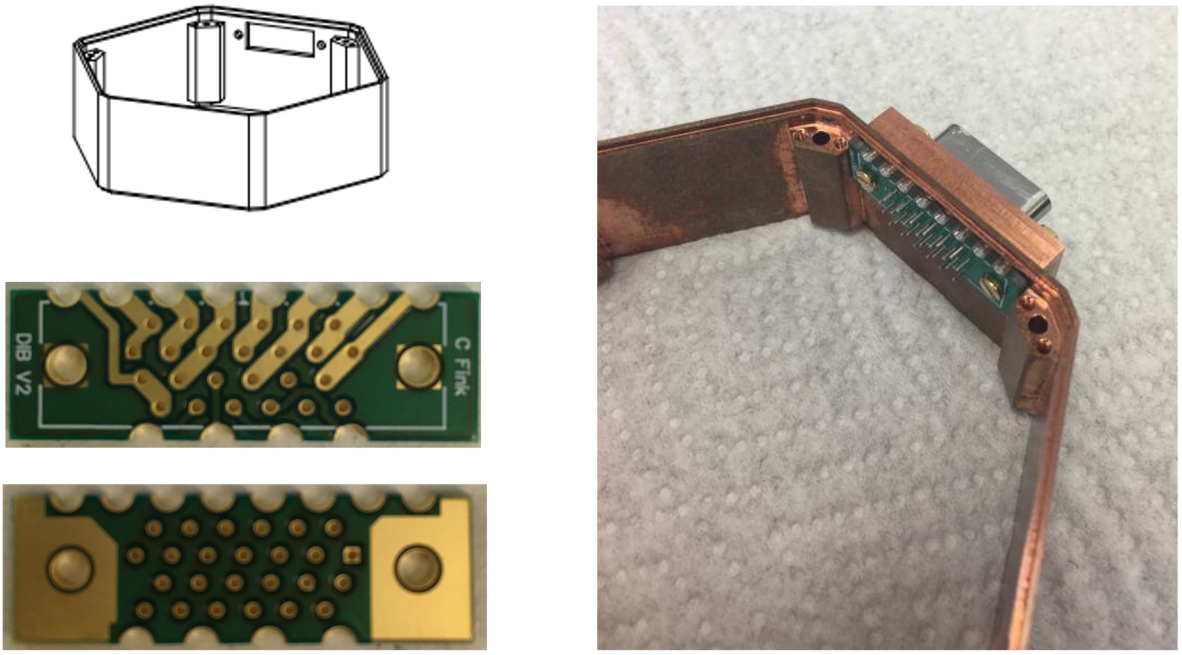

Figure D.9: Clockwise from top: Schematic of housing, DIB mounted in housing with micro-D in place, back side of DIB, front side of DIB.

Appendix E

Noise studies of DCRC rev D.0 at SLAC

This appendix is a slightly modified version of a presentation detailing the noise diagnostics that I performed for the SuperCDMS DCRC warm electronics at SLAC during my first summer in grad school. The presentation was aimed at an internal CDMS audience, so it will be somewhat specific to CDMS. This work was crucial to helping SuperCDMS reach their warm electronics noise goals at the time. The actual results of this study are irrelevant at this point in time, but the reader should find this as a useful general guide to tracking down problematic noise sources in a multi-stage amplifier. All noise studies here were done with the TES biased in the normal state, so as only to study the noise in the SQUID and downstream electronics.

E.1 Closed Loop Noise Model

A block diagram for the DCRC phonon amplifier circuit can be seen in Fig. E.1. We will first construct a model for this amplifier in the closed loop mode, using standard feedback control theory. This amplifier is operating in closed loop when the switch at the input of the Opamp labeled 'PGA' in Fig. E.1 is connected to the lower node, as it currently is in the schematic. For this noise analysis, we include a potential noise source at the input of each amplifier. Each noise term is used as a general representation for either the intrinsic input noise of the amplifier, or some environmental noise that is coupling in at that point in the circuit. A schematic of this closed loop model with noise sources included can be seen in Fig. E.2.

In the closed loop model in Fig. E.2, we introduce the following gain factors from the SQUID input and feedback coils, as well as the amplifier feedback factor β. Note that this has nothing to do with the logarithmic current sensitivity of the TES which we have used throughout this whole thesis.

- $G_{TES} = \frac{\partial V}{\partial I_{TES}}$, Responsivity with respect to input coil

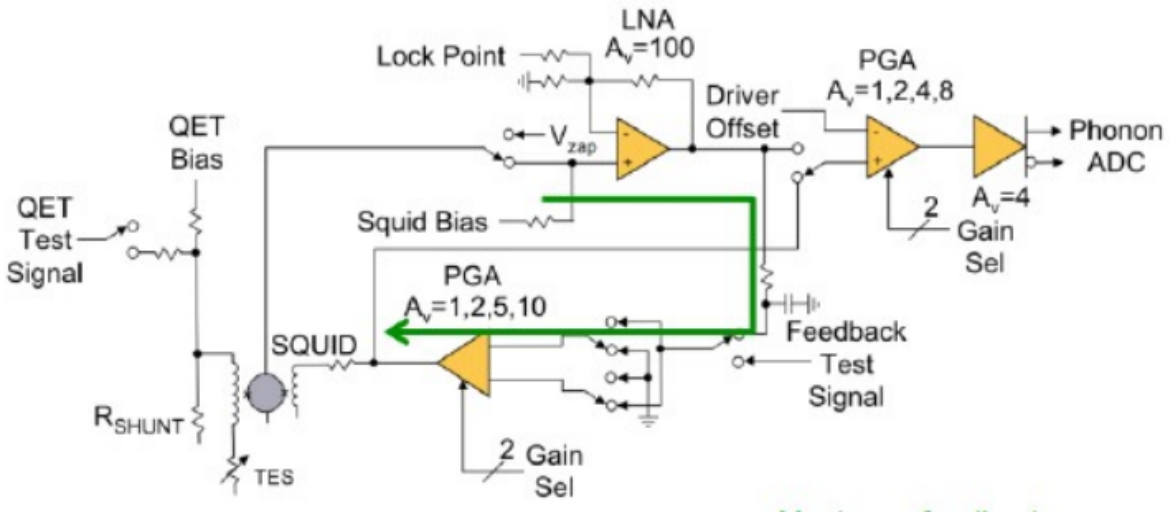

Figure E.1: Block Diagram for DCRC revD.0

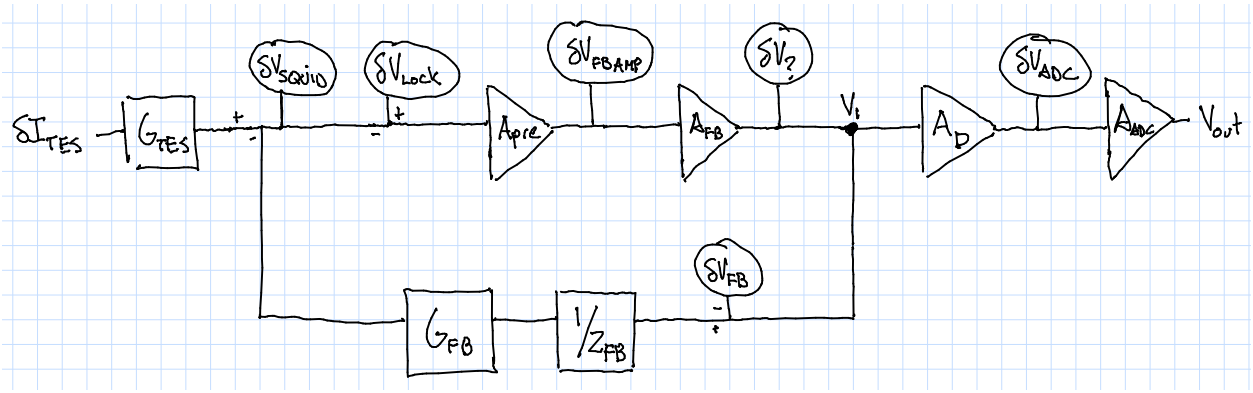

Figure E.2: Closed loop model for the DCRC revD.0 with noise sources included.

- $G_{FB} = \frac{\partial V}{\partial I_{FB}}$, Responsivity with respect to feedback coil
- $\beta \equiv G_{FB}/Z_{FB}$

The noise sources we consider in this analysis are listed below:

- δI_{TES} : Current noise down TES line
- δV_{lock} : Voltage noise at input of preamplifier
- δV_{FBamp} : Voltage noise at input of feedback amplifier
- $\delta V_?$: Unknown noise source inside the loop between FB amp and driver amp

- δV_D : Voltage noise at input of driver amplifier
- δV_{ADC} : Voltage noise at input of digitizer
- δV_{FB} : Johnson noise from feedback resistor
- δV_{sq} : Voltage noise at squid (Dependence on SQUID parameters not fully understood)

E.1.1 Calculation of Noise/Signal Transfer Function

Let us first write the transfer function relating the input current to the voltage at node V_1 in Fig. E.2.

$$\left[\delta I_{TES} G_{TES} + \delta V_{lock} + \delta V_{sq} + \frac{\delta V_{FBamp}}{A_{pre}} + \delta V_{FB}\beta - \beta V_1\right] A_{pre} A_{FB} + \delta V_? = V_1 \tag{E.1}$$

$$\left[\delta I_{TES} G_{TES} + \delta V_{lock} + \delta V_{sq} + \frac{\delta V_{FBamp}}{A_{pre}} + \delta V_{FB}\beta\right] A_{pre} A_{FB} + \delta V_? = V_1 \left(1 + \beta A_{pre} A_{FB}\right) \tag{E.2}$$

$$V_1 = \frac{A_{pre} A_{FB}}{1 + \beta A_{pre} A_{FB}} \left[\delta I_{TES} G_{TES} + \delta V_{lock} + \delta V_{sq} + \frac{\delta V_{FBamp}}{A_{pre}} + \delta V_{FB}\beta\right] + \frac{\delta V_?}{1 + \beta A_{pre} A_{FB}} \tag{E.3}$$

Referencing this to the output voltage V_{out} this becomes

$$V_{out} = \left[V_1 A_D + \delta V_D A_D + \delta V_{ADC}\right] A_{ADC} \tag{E.4}$$

$$V_{out} = \frac{A_{pre} A_{FB} A_D A_{ADC}}{1 + \beta A_{pre} A_{FB}} \left[\delta I_{TES} G_{TES} + \delta V_{lock} + \delta V_{sq} + \frac{\delta V_{FBamp}}{A_{pre}} + \delta V_{FB}\beta + \frac{\delta V_?}{A_{pre} A_{FB}}\right] + \delta V_D A_D A_{ADC} + \delta V_{ADC} A_{ADC} \tag{E.5}$$

Finally, we reference this to the input current at the TES. We do this using the transfer function below.

$$\delta I_{in} = V_{out} \left(\frac{1 + A_{pre} A_{FB} \beta}{A_{ADC} A_D A_{pre} A_{FB} G_{TES}}\right) \tag{E.6}$$

Plugging in our definition of V_{out} with the noise terms included we get

$$\begin{aligned} \delta I_{in} =& \delta I_{TES} + G_{TES}^{-1} \left[\delta V_{lock} + \delta V_{sq} + \delta V_{FB}\beta + \frac{\delta V_{FBamp}}{A_{pre}} + \frac{\delta V_?}{A_{pre} A_{FB}}\right] \\ &+ \frac{1 + A_{pre} A_{FB} \beta}{A_{pre} A_{FB} G_{TES}} \left(\delta V_D + \frac{\delta V_{ADC}}{A_D}\right) \end{aligned} \tag{E.7}$$

E.2 Identifying Dominant Noise Sources

With an understanding of how different noise sources couple into the circuit, we can now turn to trying to determine which ones are the largest. The general idea for this is as follows:

1. Measure noise PSD and reference to units of the input (TES current in our case)
2. Increase the gain for a single amplifier in the signal chain
    - If input referred noise stays the same → the noise at the input of this amplifier is sub-dominant
    - If input referred noise decreases → the noise at the input of this amplifier is dominant

The above logic can be slightly confusing when first doing these types of studies. I encourage the reader to work this out with a simplified version of this circuit to convince themselves that it is true. The following will go through all of the amplifiers that we have control over and discuss what information we can learn from it.

E.2.1 Vary Driver Gain (A_D) in Closed Loop

We can see from Eq. E.7 that by varying the driver gain, we can study δV_{ADC} (this is the only term that depends on driver gain). As shown in Fig. E.3, there is virtually no difference between the noise with the minimum and maximum values for the driver gain. This tells us that the ADC Noise Is Sub-Dominant.

E.2.2 Vary Feedback Gain (A_{FB}) in Closed Loop

Let's plot V_{out} for various A_{FB}.

From Fig. E.4 and Eq. E.5, we see that for sufficiently large feedback gain, $\delta V_?$ becomes sub-dominant, as evidenced by the fact that the noise for $A_{FB} = 5$ is the same as for $A_{FB} = 10$. This should be a non issue for D.1 since the lowest feedback gain is 800 (40x20x1) vs 100 (100x1) for the D.0

At this point, we have learned most of what we can from the closed loop data, we just don't have anymore knobs to turn.

E.3 Open Loop Model

We now look at the amplifier in 'open loop' mode. This amplifier is operating in open loop when the switch at the input of the Opamp labeled 'PGA' in Fig. E.1 is connected to the upper node, the opposite as it currently is in the schematic. We write out a gain diagram for the amplifier in open loop shown in Fig. **??**.

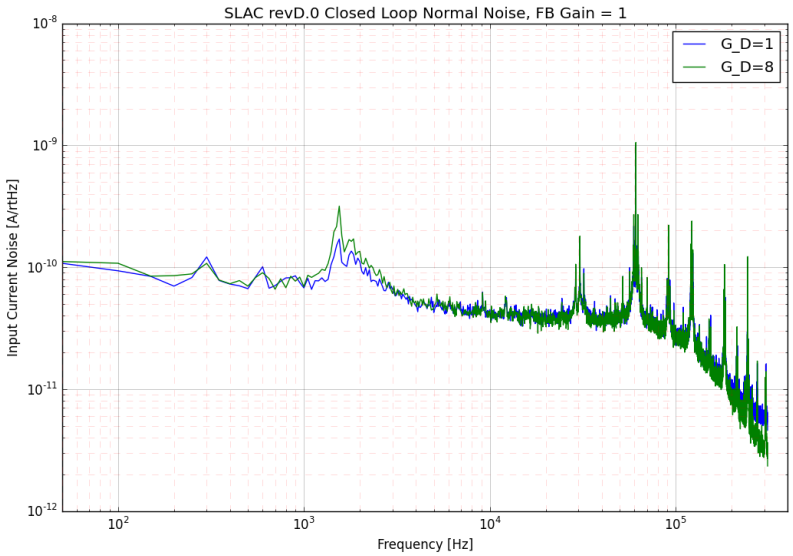

Figure E.3: Input referenced current noise as a function of driver gain

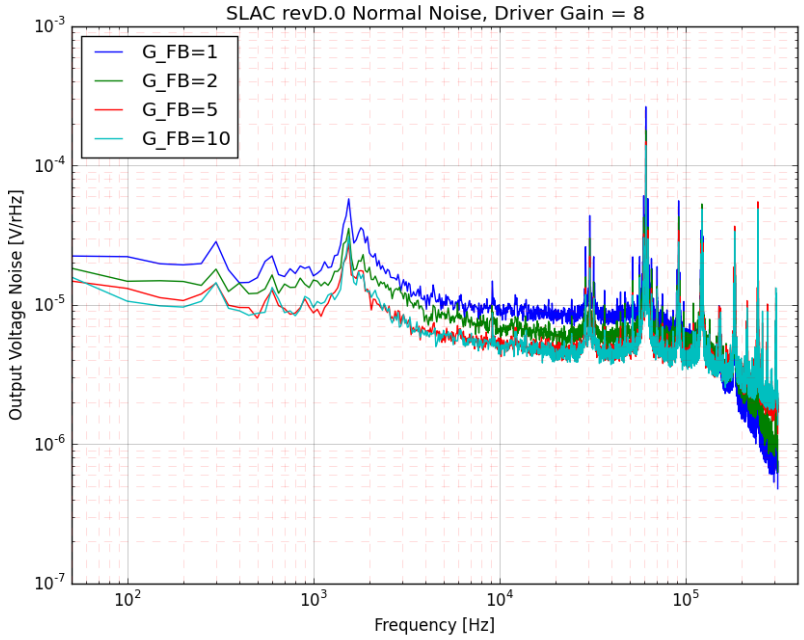

Figure E.4: Output voltage noise as a function of feedback gain

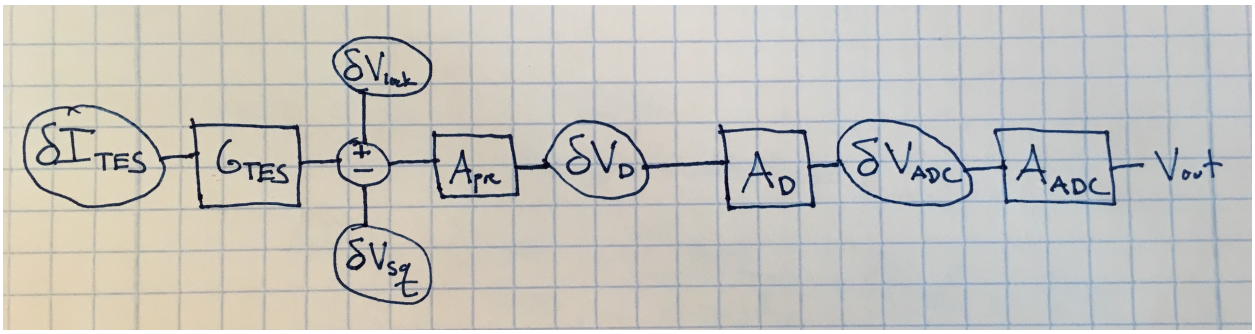

In the open loop mode, we do not have any new noise sources. We have the same noise sources except we no longer have the Johnson noise from the feedback resistor (δV_{FB}), the noise source at the input of the feedback amplifier (δV_{FBamp}), and the unknown noise source $\delta V_?$.

E.3.1 Open Loop Transfer Function

Same as for before, we can work out how the noise sources will be measured as V_{out}, as well as how they will appear when referenced to the TES input current.

$$V_{out} = \{[(\delta I_{TES} G_{TES} + \delta V_{lock} + \delta V_{sq})\, A_{pre} + \delta V_D]\, A_D + \delta V_{ADC}\}\, A_{ADC} \tag{E.8}$$

Referencing to input current,

$$\delta I_{in} = \delta I_{TES} + G_{TES}^{-1} \left[\delta V_{lock} + \delta V_{sq} + \frac{\delta V_D}{A_{pre}} + \frac{\delta V_{ADC}}{A_D A_{pre}}\right] \tag{E.9}$$

E.3.2 Closed loop vs Open loop noise

Since we previously showed that δV_{ADC} is sub-dominant always and $\delta V_?$ is sub-dominant for $A_{FB} = 10$, let's ignore these term in the closed loop Equation (Eq. E.7). Comparing closed vs open loop we find

- Closed loop noise

$$\delta I_{in} \approx \delta I_{TES} + \frac{1}{G_{TES}} \left[\delta V_{lock} + \delta V_{sq} + \delta V_{FB}\beta + \frac{\delta V_{FBamp}}{A_{pre}} + \frac{1 + A_{pre} A_{FB} \beta}{A_{pre} A_{FB}} \delta V_D\right] \tag{E.10}$$

- Open loop noise

$$\delta I_{in} \approx \delta I_{TES} + \frac{1}{G_{TES}} \left[\delta V_{lock} + \delta V_{sq} + \frac{\delta V_D}{A_{pre}}\right] \tag{E.11}$$

E.3.3 Closed loop vs Open loop noise: δV_D

Let us look now at the noise at the input of the driver gain amplifier. From the equations above, we can see that we have

$$\frac{1 + A_{pre}A_{FB}\beta}{A_{pre}A_{FB}}\delta V_D \approx \frac{1}{20}\delta V_D, \quad \text{closed loop} \tag{E.12}$$

$$\frac{\delta V_D}{A_{pre}} \approx \frac{1}{100}\delta V_D, \quad \text{open loop.} \tag{E.13}$$

Thus we can see how the δV_D is suppressed for the two cases. We now plot the noise in open loop vs closed loop in Fig. E.5. From this plot we see that the closed loop noise is approximately x1.5 higher than for open loop at low frequency. δV_{FB} is the Johnson noise of the feedback resistor, and it is scaled by β, so this term should be small. This suggests that we are dominated by either δV_{FBamp} or δV_D.

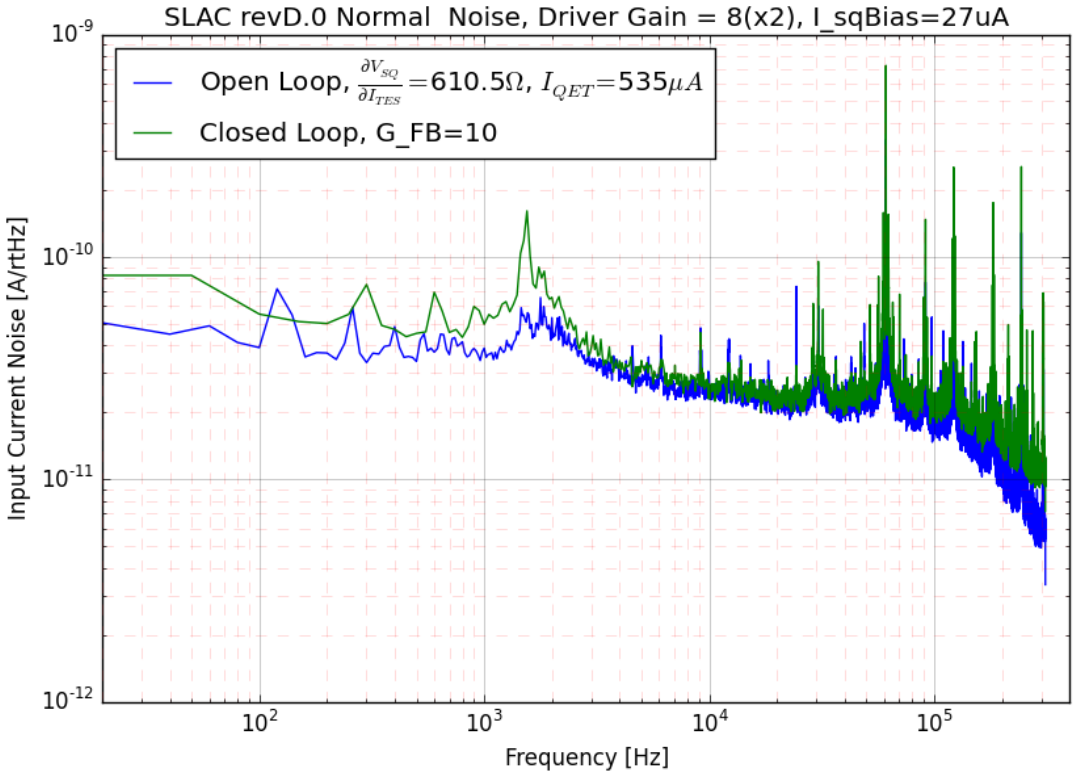

Figure E.5: Open loop noise vs Closed loop noise for FB gain of 10

E.3.4 Varying Squid Bias (G_{TES}) In Open Loop: Is Flux Coupled Noise Dominant?

The responsivity of the squid is varied by changing the squid bias. This keeps δI_{TES} constant between all the trials.

It's easiest to see this effect when referencing to output. After simplifications,

$$V_{out} = \left[\left(\delta I_{TES} G_{TES} + \delta V_{lock} + \delta V_{sq}\right) A_{pre} + \delta V_D\right] A_D A_{ADC} \tag{E.14}$$

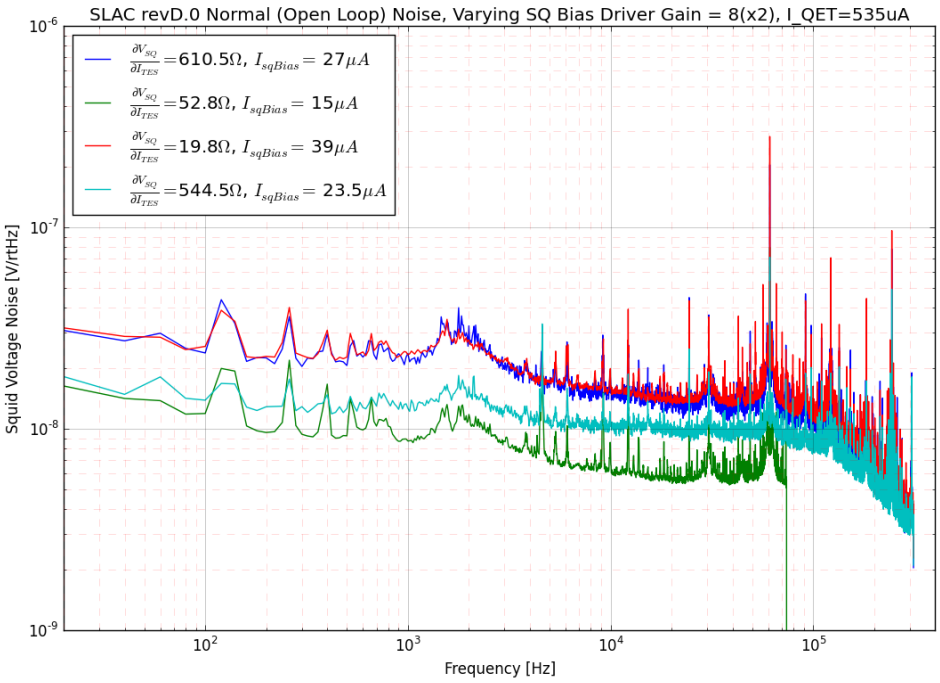

Figure E.6: DCRC input referenced voltage noise as a function of G_{TES} (Open Loop)

We can now look at the the open loop noise, referenced to SQUID input voltage, as a function of G_{TES} in Fig. E.6 to see if flux coupled noise is dominant. From looking at the plot, we would say no - the red and blue have vastly different G_{TES}, but have identical noise when referenced to output. All noise that is flux coupled to the SQUID is sub-dominant.

δV_{SQUID} must be a function of something other than $\frac{\partial V_{SQUID}}{\partial I_{TES}}$. Perhaps I_{bias}? Z_{SQUID} ?

E.4 Conclusions

This work was the first of a few deeper dives into understanding how excess noise was coupling into the DCRC, and resulted in a re-design with better shielding/filtering. This also prompted the study of understanding how the SQUID parameters should be optimized for the best noise performance. These were all studies that I was a major part of, but I only include this section of the noise analysis for educational purposes on how to track down problematic sources.

Appendix F

Estimation of Phonon Collection Time Constant

In this appendix, I describe a general algorithm I developed to extract the phonon collection time constant(s) from measured QET event pulses.

F.1 Athermal Phonon Signal

In a given particle interaction in the substrate, a large number of acoustic phonons will be generated. Since we measure the phonon interaction with all the QETs in parallel, the amount of phonons hitting any of the QETs is governed by a Poissonian processes. As such, the time intervals between arriving phonons will be exponential, and the normalized athermal phonon signal will be a single pole exponential approximated by

$$p_P(\omega) = \frac{1}{1 + i\omega\tau_{ph}}, \tag{F.1}$$

where the 'P' subscript denotes that we are in units of power and τ_{ph} is the characteristic phonon collection time. For a perfectly long lived ballistic phonons, this collection time should be given by

$$\tau_{\text{collect}} = \frac{A_{\text{absorber}} h_{\text{absorber}}}{\langle c_s \rangle A_{\text{Al}} f_{abs}} = \frac{V_{\text{absorber}}}{\langle c_s \rangle A_{\text{Al}} f_{abs}}. \tag{F.2}$$

See section 3.4.2 for more details about considerations that go into these phonon time constants. For the purpose of this appendix, we take Eq. F.1 at face value.

F.2 QET Signal

The phonon signal can be thought of in two equivalent ways: the phonons are delta function impulses of energy into the QETs at exponentially distributed times, or that the phonon pulse

from Eq. F.1 hits a single 'effective' QET at a single time. The two are mathematically equivalent, but I prefer the latter. This phonon signal now gets convolved with the TES power-to-current resonsivity transfer function into the current signal that is read out by our DAQ,

$$p_{I_{\mathrm{TES}}}(\omega) = p_P(\omega)\frac{\partial I}{\partial P}(\omega) \tag{F.3}$$

where the 'TES' subscript is to show that we are now in units of current referenced to the TES. Finally, taking the inverse Fourier transform, we get the time domain phonon pulse convolved with the TES transfer function

$$I_{\mathrm{TES}}(t) = \mathcal{F}^{-1}\left[p_P(\omega)\frac{\partial I}{\partial P}(\omega)\right], \tag{F.4}$$

which is what we measure. In a perfect world we could simply undo all the steps we just applied to return to the idea phonon power pulse and measure τ_{ph}. Unfortunately things are never that simple, what we actually measure is $I_{\mathrm{TES}}(t)$ in addition to fundamental noise

$$I_{\mathrm{TES}}^{\mathrm{measured}}(t) = I_{\mathrm{TES}}(t) + \mathcal{N}_{\mathrm{noise}}(t). \tag{F.5}$$

Now, when we deconvolve this signal, we effectively boost the white noise above the ETF pole making the signal almost unrecognizable by eye. The saving grace is that we understand the noise, because we measure it!

F.3 Toy Model

We can now construct a toy model from fake data to test an algorithm from extracting τ_{ph}. Using the measured TES parameters from the CPDv1 detector in table 6.5, we can generate the TES power-to-current transfer function, as well as the current reference PSD. The PSD can then be used to generate fake time domain noise data.

We generate the fake data in the following steps:

1. choose value for τ_{ph}
2. create time domain phonon pulse from

$$p(t) = A(1 - e^{-t/\tau_{ph}})e^{t_0} \tag{F.6}$$

3. Take Fourier transform of power pulse to put in form of Eq. F.1.
4. Calculate current-to-power transfer function given by Eq. 2.40 from values in table 6.5.
5. convolve power pulse and current-to-power transfer function

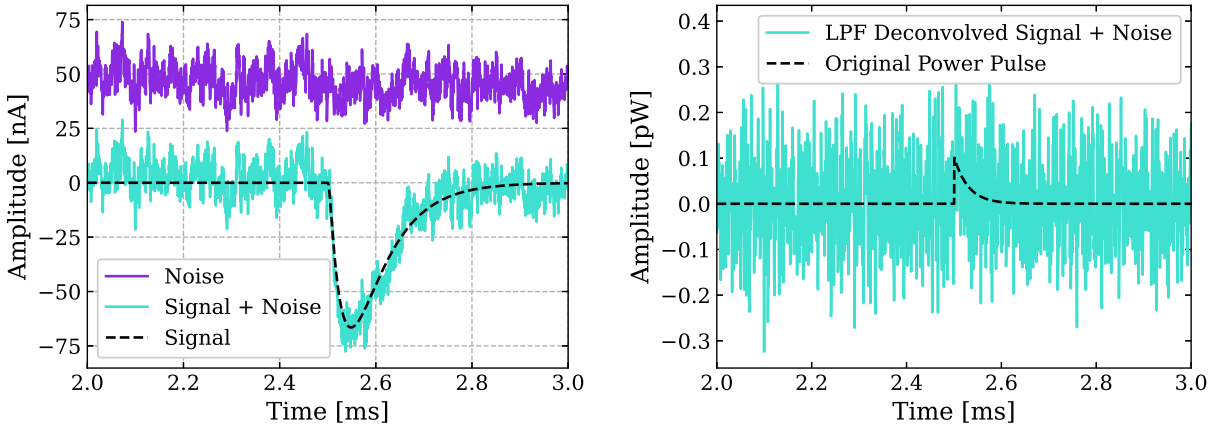

Figure F.1: Left: The ideal power pulse convolved with the TES response is shown in black, the simulated noise in purple, and the combined signal and noise is shown in turquoise. Note the offset between the nosie and the signal added for clarity. Right: In black the ideal power pulse is shown, and in turquoise the fully deconvolved signal + noise is shown

6. take inverse Fourier transform of convolved pulse to reference to TES current in time domain
7. Calculate noise PSD from values in table 6.5
8. Use noise PSD to generate random noise trace in time domain
9. Sum noise trance with convolved TES current pulse

The fake data can be seen in the left plot of Fig. F.1. Now that we have the fake data generated, we do the following steps to 'process' and fit the data:

1. Take Fourier transform of fake TES + noise pulse.
2. divide by the current-to-power transfer function.
3. take inverse Fourier transform to return to time domain power pulse.
4. use non-linear pulse fitting method (described below) to fit athermal phonon time constant.

The noise fake data that has been de-convolved back to the phonon power pulse can be seen in the right plot of Fig. F.1.

F.3.1 Pulse Fitting

This non-linear pulse fitting method uses the same optimal filtering setup as described in almost every CDMS thesis appendix, so I will not re-describe it here. For the best reference, see Sunil's thesis [226]. The basic motivation is that since the time domain noise is highly correlated, the optimization becomes much more straight forward by working in the frequency domain. Thus, we wish to minimize

$$\chi^2 = \int_{-\infty}^{\infty} \frac{(y_{data} - \tilde{p}(\omega))^2}{J(f)} \frac{d\omega}{2\pi}, \tag{F.7}$$

where y_{data} is the measured data, $\tilde{p}(\omega)$ is the functional form of the pulse, and $J(f)$ in this case is the squared NEP.

In time domain, we define the pulse function

$$p(t) = A\left(e^{-t/\tau_{ph}} - e^{t/\tau_r}\right) e^{t_0}. \tag{F.8}$$

Note that a 'rise' time is added to this function to account for the fact that due to finite sampling rate (and other physical limitations) we can never truly have a single pole exponential function. We simply set this rise time to be very short in the fit (sub μs).

Switching to frequency domain, this becomes

$$\tilde{p}(\omega) = \frac{A(\tau_f - \tau_r)}{(1 + i\omega\tau_f)(1 + i\omega\tau_r)} e^{-i\omega t_0} \tag{F.9}$$

We define a residual

$$R = \frac{(y_{data} - \tilde{p}(\omega))}{\sigma_{in}} \tag{F.10}$$

where $\sigma_{in} = \sqrt{J(f)}$. The real and imaginary parts of this residual are numerically minimized via `scipy.optimize.least_squares()`, letting the amplitude A, τ_{ph} and the time offset τ_0 be free parameters. All of these functions can be found in the python package `QETpy` [227] written by myself and fellow grad student Samuel Watkins.

F.3.2 Results

After the creation of fake data, and the processing and fiting as defined in the previous section, we find that we are able to recover the original power signal quite well. For a generated athermal phonon collection time of $\tau_{ph} = 100\,\mu$s, we get a reconstructed value of $\tau_{ph}^{\text{reconstructed}} = 99.8 \pm 0.2\,\mu$s. The frequency space fit can be seen in the left plot of Fig. F.2 and the best fit parameters plotted in time domain shown with a low pass filtered signal are shown in the right plot of the same figure.

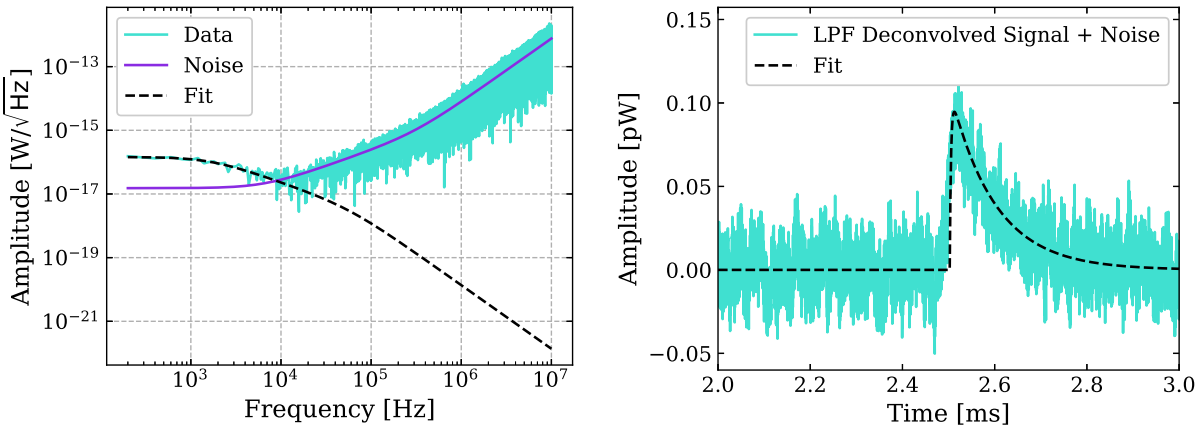

Figure F.2: Left: Fit to the deconvolved signal plus noise in power done in the frequency domain. Right: the best fit parameters from the frequency domain fit shown in time domain with the low pass filtered noisy signal.

F.3.3 Accounting For TES Saturation

One problem that we often face with highly sensitive detectors, is that they easily locally saturate which manifests as a longer effective electrothermal time constant (see section 6.2). We wish to simulate this to understand how it will effect our estimation of τ_{ph}. This can be done by simulating data and using a variety of τ_{ETF} time constants when convolving the power pulse to current via Eq. F.3. Then using the true τ_{ETF} when de-convolving the noise signal back to units of power before fitting. This matches reality in that the local saturation will take the power phonon pulse and add a longer τ_{ETF} to it, then we will de-convolve with the measured $\partial I/\partial P$ with the ideal τ_{ETF} time constant.

We do this simulation for a range of saturated effective τ_{ETF}'s both above and below the true τ_{ETF}, and put each simulated trace through the same fitting routine. The results are shown in Fig. F.3. We see that for saturated τ_{ETF}'s that are longer than the true τ_{ETF}, the reconstructed phonon collection times are also longer, scaling roughly linearly. This simulation implies that even when only saturated pulses are available to analyze, this method still allows one to set an upper bound on τ_{ph}. Additionally one could extrapolate down to the true τ_{ETF} as measured from the dIdV.

There is an caveat though, in that for many detectors, measuring the variation in τ_{ETF} is a difficult task. For the CPDv1 it was possible because the ideal τ_{ETF} value was decently larger than the expected τ_{ph}. In this scenario, the measured current pulse will have a rise time given by τ_{ph} and a fall time given by τ_{ETF}. In this case, this deconvolution isn't necessary and one can then simply fit this fall time as a function of energy to see how it varies for large energy deposits that begin to locally saturate the detector. From Fig. F.4 we can see that the τ_{ETF} fall time varies roughly linearly with the energy of the event (above the energy

threshold at which saturation begins). Thus, in some sense we can use event energy as a proxy for pulse saturation for higher energies. We will see in most of the 'low coverage' devices, we will be in the opposite limit

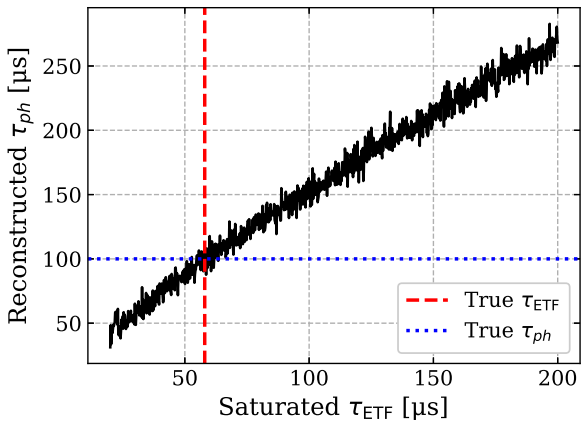

Figure F.3: Plot of the reconstructed τ_{ph} as a function of the τ_{ETF} used in the $\partial I/\partial P$ deconvolution. The True τ_{ETF} and τ_{ph} are also shown.

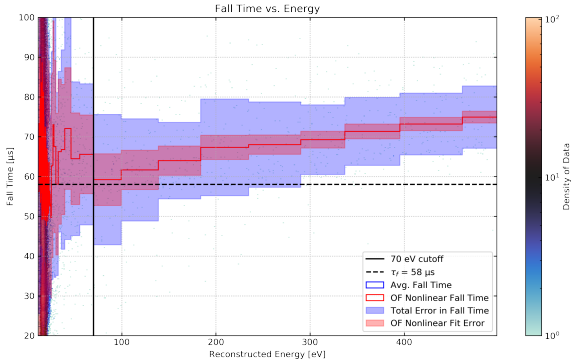

Figure F.4: Plot of the reconstructed τ_{ph} as a function of the τ_{ETF} used in the $\partial I/\partial P$ deconvolution. The True τ_{ETF} and τ_{ph} are also shown.

Appendix G

Event Reconstruction with a Variational Autoencoder

This contents of this appendix were originally a project for a machine learning course I took. As such, the material as it pertains to dark matter detectors is written for a very general audience. However, the machine learning tools discussed might be of use as a jumping off point for future students interested in new ideas in event reconstruction, so I've decided to include this project 'as is' as an appendix.

In this project, a Variational Autoencoder was built and used to extract features from Dark Matter (DM) search data. The data consist of single channel traces of recorded detector voltage as a function of time. The VAE was trained to learn interesting features within the traces and map a 32500 dimensional space to a 30 dimensional space. It is shown that variables within this latent space are strongly correlated with known physical quantities of interest. A regression model will be built (in progress, but not finished in time for this project) to fit the latent variables of the 30 dim space to the known energy of each event for the data that the energies are know.

G.1 Introduction

The Cryogenic Dark Matter Search (CDMS) project is a high precision experiment searching for low mass dark matter (sub eV-GeV mass range). The experiment uses Transition Edge sensors [81] operated at 20mK to measure athermal phonons produced by the interaction of cosmogenic particles with the nucleons of Si and Ge detector targets.

Rare event searches require (among many other things) a good understanding of the energy of each event detected, and the location in the detector where the event occurred. The current method for energy reconstruction is to use a frequency domain matched filter with a known signal shape, which is calculated based on the physics of the detector. When the shape of detector energy transfer function is constant and only the amplitude is allowed to change, this method works well and is computationally efficient. However, as the detectors get more

complicated, understanding the detector response becomes prohibitively challenging. In the next generation of DM detectors, the pulse shape of an event changes in non-trivial ways with both the energy deposited, and the location of the event in the detector. This is illustrated in Fig. G.1

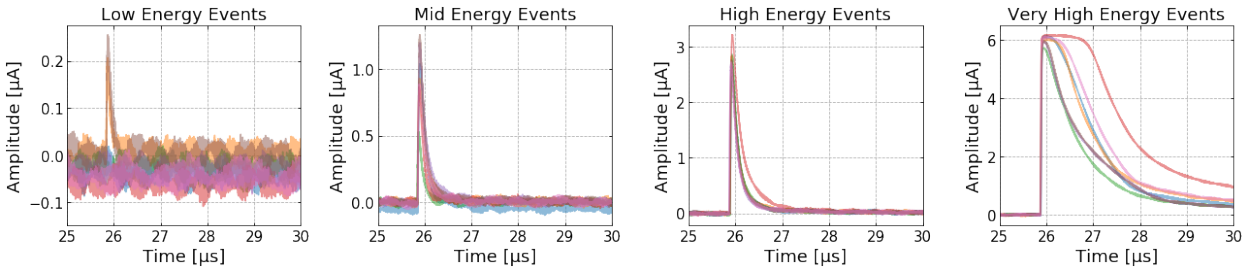

Figure G.1: Examples of raw events at various energy ranges, from 100's of eV (left) to 10+ keV (right). Each colored trace in the subplots represents a different triggered event occurring at different a time.

This motivates the search for new methods to classify events. This problem can be simplified to two key parts: What features of an event are necessary to correctly classify it? How do you then relate those features to true physical quantities (ie. Energy, position, particle type, etc). This project will attempt to tackle the former of these parts, with the intention of continuing the latter part after the completion of this class.

G.2 Method

A big challenge with this problem is the lack of a robust Detector Monte Carlo simulation, or abundant well calibrated data. We do have lots of data, some of it previously calibrated from a recent dark matter search. This suggests at using a semi-supervised method. Using unsupervised learning to perform feature extraction, and then using a supervised process to calibrate those features. The natural choice for this first step is to use a self-supervised generative model, such as a Variational Autoencoder, which is described in detail in section G.2.1.

G.2.1 Variational Autoencoder

I will now take a small aside to introduce the Variational Autoencoder (VAE). A VAE is a self-supervised method used for dimentionality reduction and feature extraction. Unlike popular methods like PCA, t-SNE, etc, autoencoders typically use neural networks to learn 'interesting' features of the data. The basic idea of a general autoencoder is the following: It takes in a input vector, passes it through an 'encoder' that maps input variables to latent space (typically much smaller than the number of input variables), then 'decodes' the

latent variables back into an output the same shape of the input. The input vector is then compared with the output and a loss function is constructed based on the difference between the output and input, this is usually the Mean Squared Error. The model is then trained by tuning the weights of the encoder and decoder until the input and output match as closely as possible. For more details on the use of autoencoders, see the seminal paper by Hinton and Salakhutdinov [228].

As it stands, an autoencoder can easily over-fit the data since the loss function is encouraging an exact reconstruction of the original data. Many alternatives have since been introduced, but the Variational autoencoder proposed by Kingma and Welling in [229] has perhaps been the most popular. The VAE rephrases the original problem into a probabilistic one. We assume that the latent variables z come from a prior probability distribution $p_\theta(z)$ which is a function of weights θ. We then assume that there is a probability distribution $p_\theta(z|x)$ that given an input vector x, describes latent variable z, and a $p_\theta(x|z)$ that given a z, describes x. The goal of the VAE is to learn $p_\theta(z)$ by using $p_\theta(z|x)$, which we also don't know. To overcome this problem, Variational Inference is used to model $p_\theta(z|x)$ as a Gaussian $q_\phi(z|x)$. This is done by stating the above as an optimization problem. $p_\theta(z|x)$ can be inferred by $q_\phi(z|x)$ by minimizing the Kullback-Leibler divergence [230], which is a measure of how two probability distributions differ from each other. For completeness, and for my own benefit, I will re-derive the objective function and explain how it relates to the autoencoder.

Starting with the definition of D_{KL}

$$D_{\mathrm{KL}}\left((q_\phi(z|x)||p_\theta(z|x))\right) = \sum_z q_\phi(z|x)\log\frac{q_\phi(z|x)}{p_\theta(z|x)} \tag{G.1}$$

$$= \sum_z q_\phi(z|x)\left[\log q_\phi(z|x) - \log p_\theta(z|x)\right] \tag{G.2}$$

$$= \mathbb{E}_{q_\phi(z|x)}\left[\log q_\phi(z|x) - \log p_\theta(z|x)\right] \tag{G.3}$$

Using Bayes theorem, we can write $p(z|x) = \frac{p(x|z)p(z)}{p(x)}$,

$$D_{\mathrm{KL}}\left((q_\phi(z|x)||p_\theta(z|x))\right) = \mathbb{E}_{q_\phi(z|x)}\left[\log q_\phi(z|x) - \log\frac{p_\theta(x|z)p_\theta(z)}{p_\phi(x)}\right] \tag{G.4}$$

$$= \mathbb{E}_{q_\phi(z|x)}\left[\log q_\phi(z|x) - \log\frac{p_\theta(x|z)p_\theta(z)}{p_\phi(x)}\right] \tag{G.5}$$

$$= \mathbb{E}_{q_\phi(z|x)}\left[\log q_\phi(z|x) - \log p_\theta(x|z) - \log p_\theta(z) + \log p_\theta(x)\right] \tag{G.6}$$

$$= \mathbb{E}_{q_\phi(z|x)}\left[\frac{\log q_\phi(z|x)}{\log p_\theta(z)} - \log p_\theta(x|z)\right] + \log p_\theta(x) \tag{G.7}$$

$$= \log p_\theta(x) - \mathbb{E}_{q_\phi(z|x)}\left[\log p_\theta(x|z)\right] + \mathbb{E}_{q_\phi(z|x)}\left[\frac{\log q_\phi(z|x)}{\log p_\theta(z)}\right] \tag{G.8}$$

$$= \log p_\theta(x) - \mathbb{E}_{q_\phi(z|x)}\left[\log p_\theta(x|z)\right] + D_{\mathrm{KL}}\left((q_\phi(z|x)||p_\theta(z))\right) \tag{G.9}$$

$$\tag{G.10}$$

Re-arranging,

$$\log p_\theta(x) = D_{\mathrm{KL}}\left((q_\phi(z|x)||p_\theta(z|x))\right) + \underbrace{\mathbb{E}_{q_\phi(z|x)}\left[\log p_\theta(x|z)\right] - D_{\mathrm{KL}}\left((q_\phi(z|x)||p_\theta(z))\right)}_{\mathcal{L}(\theta,\phi,x)} \tag{G.11}$$

where $\mathcal{L}(\theta, \phi, x)$ is called the variational lower bound because $\log p_\theta(x) \geq \mathcal{L}(\theta, \phi, x)$ since D_{KL} is always a positive quantity. So the optimization problem now becomes

$$\boxed{\begin{array}{l}\text{Find the } \theta \text{ and } \phi \text{ that maximizes:} \\ \log p_\theta(x|z), \text{ and minimizes } D_{\mathrm{KL}}\left((q_\phi(z|x)||p_\theta(z))\right)\end{array}}. \tag{G.12}$$

We assert that $z \sim \mathcal{N}(0, 1)$ and approximate $q_\phi(z|x)$ as a multivariate normal distribution with a diagonal covariance matrix, $q_\phi(z|x) = \mathcal{N}(z; \mu(x), I\sigma^2(x))$. By doing this, we can easily work out the KL divergence term.

$$D_{\mathrm{KL}}\left((q_\phi(z|x)||p_\theta(z))\right) = \mathbb{E}_{(q_\phi(z|x)}\left[\log \mathcal{N}(z; \mu(x), I\sigma^2(x)) - \log \mathcal{N}(0, 1)\right] \tag{G.13}$$

$$= \frac{1}{2}\mathbb{E}_{(q_\phi(z|x)}\left[-\log \prod_i \sigma_i^2 - (x-\mu)^T\sigma^{-2}(x-\mu) + x^T I x\right] \tag{G.14}$$

$$= -\frac{1}{2}\sum_i \log \sigma_i^2 - \frac{1}{2}\mathbb{E}_{(q_\phi(z|x)}\left[\mathrm{Tr}\left(\sigma^{-2}\underbrace{(x-\mu)^T(x-\mu)}_{\sigma^2}\right)\right] + \frac{1}{2}\underbrace{\mathbb{E}_{(q_\phi(z|x)}\left[\mathrm{Tr}\left(x^T x\right)\right]}_{\mathrm{Tr}(\mu^2+\sigma^2)} \tag{G.15}$$

$$= \underline{\frac{1}{2}\sum_i \left[\mu_i^2 + \sigma_i^2 - \log \sigma_i^2 - 1\right]}. \tag{G.16}$$

Arriving at the loss function for the VAE:

$$\mathcal{L}_{VAE}(\theta, \phi, x) = \mathbb{E}_{q_\phi(z|x)}\left[\log p_\theta(x|z)\right] + \frac{1}{2}\sum_i \left[1 + \log \sigma_i^2 - \mu_i^2 - \sigma_i^2\right] \tag{G.17}$$

To train this model, you take an input x, encode the input down to a mean μ and variance σ^2, use these variables to generate at Gaussian RV z, then decode this z back into x, evaluate the loss function and repeat. There is however one problem with the above method. In generating the RV z after the encoding step, back propagation will not work. This leads to what is called the 'reparameterization trick'. Rather than randomly sample from a distribution with μ and σ^2, generate values of z from

$$z = \mu + \sigma * \varepsilon, \quad \text{where} \quad \varepsilon \sim \mathcal{N}(0, 1). \tag{G.18}$$

(where $*$ is element-wise multiplication.) By doing this, the random sampling takes place at a step outside of the network, so backpropagation will still work. A cartoon diagram of a VAE can been seen in Fig. G.2.

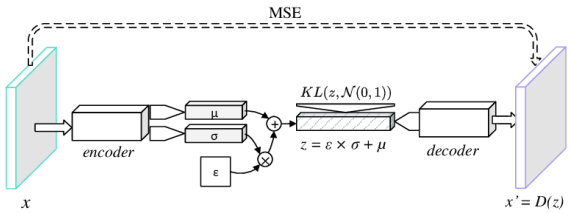

Figure G.2: Diagram of a Variational Autoencoder, taken from [231]

Lastly, a further modification to the VAE can be made. In the loss function in Eq. G.17, the D_{KL} term can be thought of as a regularization term. Higgins *et al.* [232] proposed introducing a hyperparameter β to this term, where a value of $\beta > 1$ encourages the latent variables to become disentangled from each other, and perhaps more human interpretable (at the potential trade off of decreasing the model's ability to better reproduce its original input). This is commonly referred to as the $\beta-$VAE or the disentangled VAE, with loss function,

$$\mathcal{L}_{\beta VAE}(\theta, \phi, x) = \mathbb{E}_{q_\phi(z|x)} \left[\log p_\theta(x|z)\right] + \frac{1}{2}\beta \sum_i \left[1 + \log \sigma_i^2 - \mu_i^2 - \sigma_i^2\right] \tag{G.19}$$

G.2.2 Data Processing

For this project, a data set from my research group's recent Dark Matter search was used. The data were taken with a single channel R&D detector. In total, there are 482743 threshold triggered events and 79458 randomly triggered events in this data. Each event has 32500 time domain data points (52ms tracelength with 625kHz sampling rate). The first processing step was to 'clean' the data so that only good events remained. Only races that had a single event and were not contaminated with non-stationary environmental noise were included. A few examples of the types of traces that were removed can be seen in Fig. G.3. The details of how these events were removed is beyond the scope of this paper, but is standard practice in these types of astrophysical analyses.

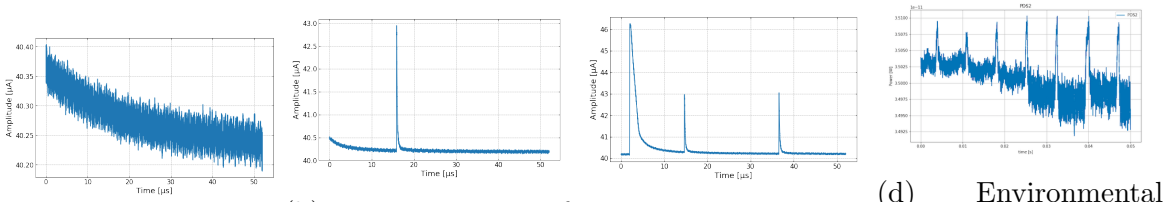

(a) Muon tail event (b) Event on top of muon tail (c) Multiple pulse pileup (d) Environmental noise due to readout electronics

Figure G.3: A variety of rejected events from the data set. The left three figures show events that were rejected due to multiple pulse pileup, where as the figure on the right is rejected due to environmental noise.

The data set had an Fe55 X-ray source with Al foil for fluorescence, incident on the detector to be used for energy calibration. Due to the high energies (relative to the dynamic range of the detector) the $K\alpha$ and $K\beta$ lines saturated the sensors of the detector to a large degree. This energy is well above the energy range that we are interested in for the DM search, so for these reasons It decided to first optimize a VAE model that did not include these events. The calibrated spectrum and region of data used for training can be seen in Fig. G.4. To be clear, the dataset used for the project consists of the triggered events in the blue shaded region, which is about 7000 good events. This was then divided up into 80% training data and 20% validation data. For the current task of this model, further dividing into a test set did not make sense, as there is more data that can be used for testing later on.

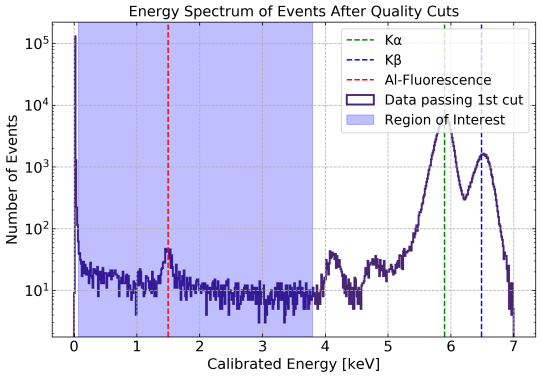

Figure G.4: Known energy spectrum of events after bad events are removed. The shaded region showns the events used for training the model.

After the good events were selected, each trace then went through a normalization process. Many different schemes were tried, but the final normalization used was the following:

1. Subtract the pre-pulse baseline from the whole trace to center the event at zero Volts.
2. Truncate the traces to be 1624 bins long, centered about the triggered event.
3. Low-pass filter all the traces with a single pole filter at 50kHz (well above the signal bandwidth of the detector).
4. Divide every trace by a factor of ∼1.25 times the maximum of the largest event in the training dataset.
5. Add an offset of 0.25, so that the range of all the data is roughly between 0.25 and 0.85

An example visualization of a raw and processed trace can be seen in Fig. G.5.

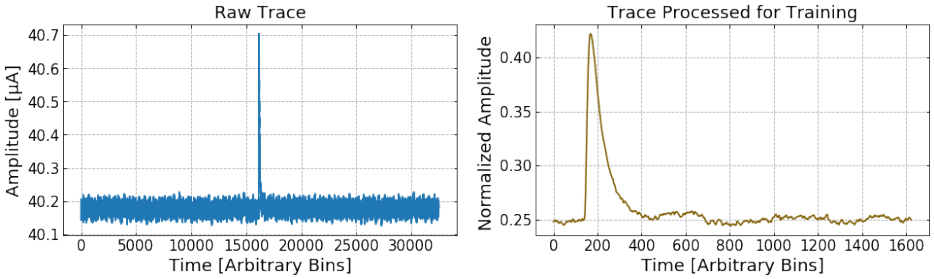

Figure G.5: Visualization of an event before (left) and after pre-processing step (right).

G.2.3 Design of Model

The Encoder model consisted of a Neural Network with four one dimensional convolutional layers, each with kernels of size 3 and stride 2. These were then followed by two fully connected layers. ReLU activation functions were used after every layer, as well as batch normalization and (optional) dropout layers. The last layer was connected to two separate fully connected layers, one for μ and one for σ^2 from section G.2.1. The 'reparameterization trick' was then applied before the decoding model. The Decoder essentially copied the Encoder, but in reverse, using transposed convolutional layers to 'undo' the convolution layers. There was one additional transposed convolutional layer in the decoder in order to make the output shapes match the original input. A summary of the encoder and decoder can be in Fig G.6.

A module was written in `python` to handle data processing, plotting, io, and training. The package uses `PyTorch` for model development and training. The module can be downloaded and installed from the project GitHub page: link. Python scripts for training models, and a template `Jupyter` notebook for evaluating models are also included in the repository.

Layer (type)	Output Shape	Param #
Conv1d-1	[-1, 16, 812]	64
BatchNorm1d-2	[-1, 16, 812]	32
Conv1d-3	[-1, 16, 405]	784
BatchNorm1d-4	[-1, 16, 405]	32
Conv1d-5	[-1, 32, 202]	1,568
BatchNorm1d-6	[-1, 32, 202]	64
Conv1d-7	[-1, 32, 100]	3,104
BatchNorm1d-8	[-1, 32, 100]	64
Linear-9	[-1, 64]	204,864
BatchNorm1d-10	[-1, 64]	128
Linear-11	[-1, 16]	1,040
Linear-12	[-1, 30]	510
Linear-13	[-1, 30]	510

Total params: 212,764
Trainable params: 212,764
Non-trainable params: 0

Input size (MB): 0.01
Forward/backward pass size (MB): 0.45
Params size (MB): 0.81
Estimated Total Size (MB): 1.26

(a) Summary of VAE Encoder model.

Layer (type)	Output Shape	Param #
Linear-1	[-1, 1, 3200]	99,200
ConvTranspose1d-2	[-1, 32, 201]	3,104
BatchNorm1d-3	[-1, 32, 201]	64
ConvTranspose1d-4	[-1, 32, 403]	3,104
BatchNorm1d-5	[-1, 32, 403]	64
ConvTranspose1d-6	[-1, 16, 807]	1,552
BatchNorm1d-7	[-1, 16, 807]	32
ConvTranspose1d-8	[-1, 16, 1615]	784
BatchNorm1d-9	[-1, 16, 1615]	32
ConvTranspose1d-10	[-1, 1, 1624]	161

Total params: 108,097
Trainable params: 108,097
Non-trainable params: 0

Input size (MB): 0.00
Forward/backward pass size (MB): 0.92
Params size (MB): 0.41
Estimated Total Size (MB): 1.34

(b) Summary of VAE Decoder model.

Figure G.6: Summaries of the VAE Encoder and Decoder models implemented in PyTorch.

G.3 Training

In order to confirm the model was working correctly, it was first tested by training on a single batch of 16 events with a 30 dim latent space and β set to zero so the D_{KL} term was ignored. Training was continued for ~ 4500 epochs, enough to show the model was working correctly, but judging from the loss function in Fig. G.7, it looks like the fit would have kept improving. A few of the reconstructed pulses from the model can be seen in Fig. G.8.

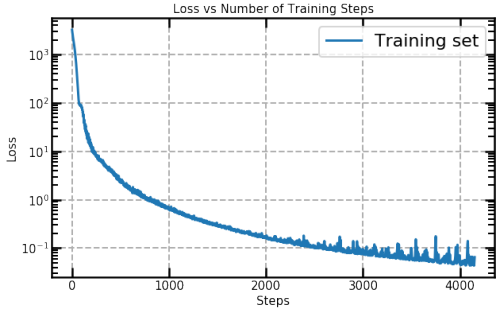

Figure G.7: Training loss for single batch vs training step.

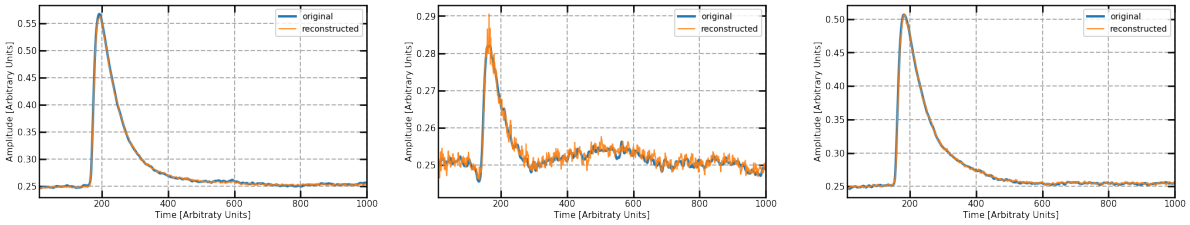

Figure G.8: Various reconstructed pulses when 'overfitting' on single batch and setting $\beta = 0$ in the loss function to check that model is working.

The above test was then repeated, but now with β included. It was found that if $\beta \approx 1$, it was seemingly impossible to overfit the data, at least for the time I was able to put into training. This makes sense, as the VAE is introducing a random sampling step that would make it incredibly difficult for a model to memorize the input. This means that β needs to be tuned such that the model can reconstruct the relevant features (pulse shape/height type parameters) reliably, but not overfit the noise. This however is a difficult thing to define.

When training the model on the training set described in section G.2.2, I used the following method to tune β. If β was too large, then the model would have a difficult time reconstructing the input and the training loss would oscillate. If β was too small, the loss function for the training data would decrease rapidly, but the validation loss would oscillate wildly. A small β means that the model will just start memorizing the input and will not generalize well. The final value of β was chosen such that the loss function for both the training data and validation data decreased monotonically at similar rates. Then a final visual check is done to make sure the traces are being reconstructed well. The loss function and hyperparameters for the final model can be seen in Fig. G.9 and the Table below.

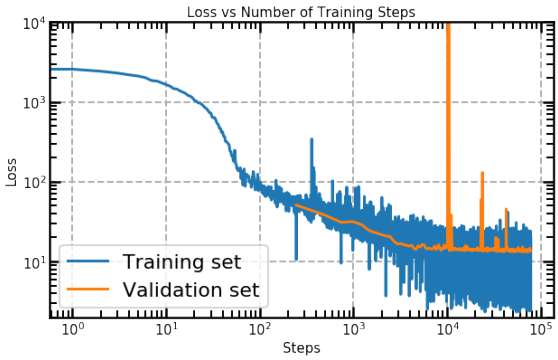

Figure G.9: Training and Validation loss during training of 315 epochs

Model Hyperparameters

lr	1e-3
β	0.5
z_dim	30
batch size	16
epochs	344

G.4 Results

Using the trained model, traces from both the training set and validation set can be compared against their reconstructed versions. The training and testing events can be seen in Fig. G.10 and Fig. G.11 respectively.

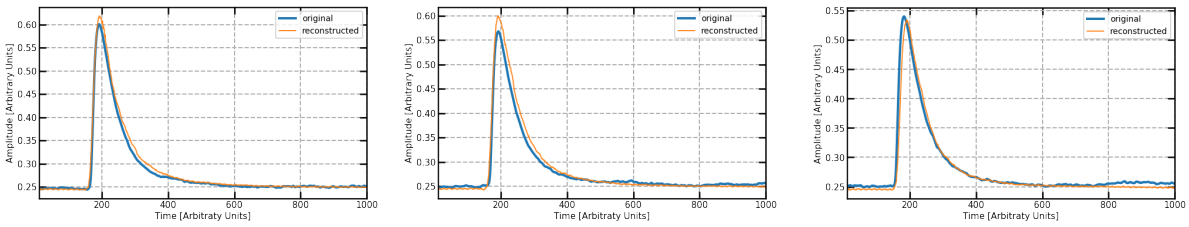

Figure G.10: Various reconstructed pulses from training data after model training.

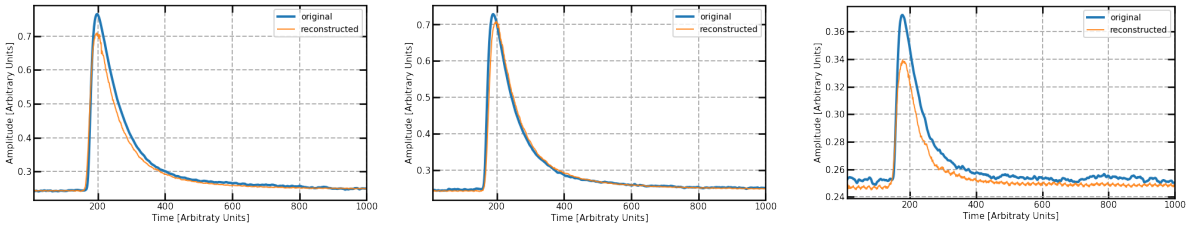

Figure G.11: Various reconstructed pulses from validation data after model training.

It is now interesting to see if the features (latent variables) found by the VAE model will be of any use for quantifying physical quantities. In order to visualize the 30 dimensional latent space, PCA was used to project down to a 2 dimensional space[1], where color is used to indicate the known energy value of every event in the training/validation data. It is clear from the results in Fig. G.12 that there is a continuous monotonic distribution of the energy in this latent space. This strongly implies that these features found by the VAE will be able to fit to true physical quantities. The fact that the results are still so clear after reducing the 30 latent dimensions down to 2, suggests that some of these 30 dimensions may be degenerate/unnecessary and can be further reduced in future models.

[1]The t-SNE algorithm was tried as well, but the conclusions of the results were similar to PCA so plots of those projections are not included

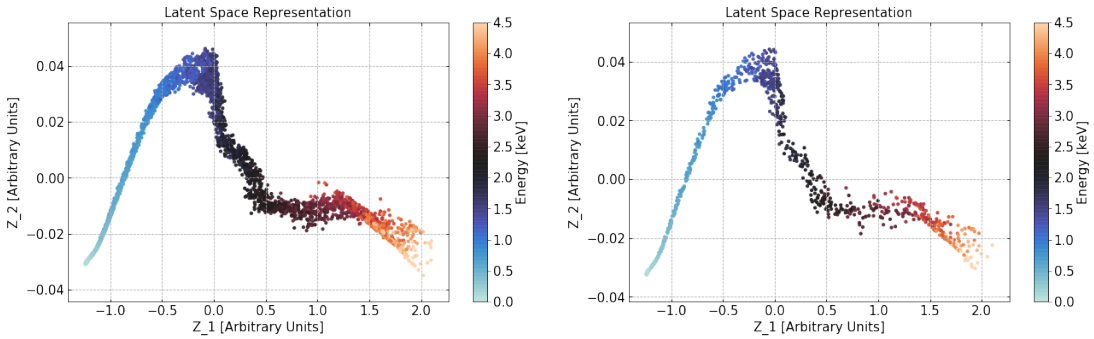

(a) Latent space of training data. (b) Latent space of validation data.

Figure G.12: Two dimensional visualization of the 30 dimensional latent space of the training and testing data. The color of the data corresponds to the True energy of each event.

Finally, various latent variables can be plotted against known quantities. For example, it can be seen in Fig. G.13 that certain latent variables are highly correlated with the pulse energy, the starting time of the pulse within the trace, and the fall time of the pulse.

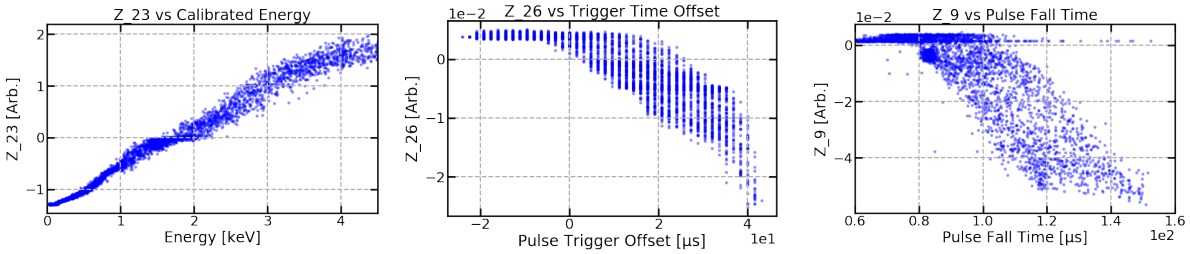

Figure G.13: Selected latent variables plotted against some of the know physical quantities for the training data.

G.5 Conclusion and Future Work

It has been shown that this Variational Autoencoder model has great potential as a method for feature extraction. Certain latent variables correlate strongly with physically meaningful quantities. Also, when visualising the latent variables in a 2 dimensional space, the structure of the data suggests that it is possible to fit the latent variables to the true energy of the events.

The next step in this analysis are to further develop the VAE model by expanding the types of events that are included in the training/testing. I would like to allow purely noise traces, highly saturated events, and multi-pulse pileups. Additionally, a regression model to fit the latent variables to physical quantities needs to be implemented.